Programa de Pós-Graduação em Engenharia Mecânica
Centro Tecnológico
Pró-Reitoria de Pesquisa e Pós-Graduação
Universidade Federal do Espírito Santo

Lucas Henrique Pagoto Deoclecio

Drop Rise and Interfacial Coalescence Initiation in Complex Materials

Vitória
November, 2023

Programa de Pós-Graduação em Engenharia Mecânica
Centro Tecnológico
Pró-Reitoria de Pesquisa e Pós-Graduação
Universidade Federal do Espírito Santo

Lucas Henrique Pagoto Deoclecio

Drop Rise and Interfacial Coalescence Initiation in Complex Materials

Thesis presented to the Graduate Program in Mechanical Engineering of the Federal University of Espírito Santo, as a partial requirement for obtaining the title of Doctor in Mechanical Engineering.
Supervisor: Prof. Dr. Edson José Soares

Vitória
November, 2023

PROGRAMA DE PÓS-GRADUAÇÃO EM ENGENHARIA MECÂNICA
CENTRO TECNOLÓGICO
UNIVERSIDADE FEDERAL DO ESPÍRITO SANTO

DROP RISE AND INTERFACIAL COALESCENCE INITIATION IN COMPLEX MATERIALS

LUCAS HENRIQUE PAGOTO DEOCLECIO

COMISSÃO EXAMINADORA

Prof. Dr. Edson José Soares
(Orientador – PPGEM/UFES)

Prof. Dr. Renato do Nascimento Siqueira
(Examinador Interno – PPGEM/UFES)

Prof. Dr. Rogério Ramos
(Examinador Interno – PPGEM/UFES)

Prof. Dr. Francisco Ricardo da Cunha
(Examinador Externo – ENM/FT/UnB)

Prof. Dr. Roney Leon Thompson
(Examinador Interno – PEM-COPPE/UFRJ)

Tese apresentada ao Programa de Pós-Graduação em Engenharia Mecânica da Universidade Federal do Espírito Santo como parte dos requisitos necessários à obtenção do título de Doutor em Engenharia Mecânica

Vitória/ES, 10 de novembro de 2023

Datas e horários baseados em Brasília, Brasil
Sincronizado com o NTP.br e Observatório Nacional (ON) em 13/11/2023 às 20:06:47

Doctos TESE DE DOUTORADO Lucas Henrique Pagoto Deoclecio PPGEM UFES

Data e Hora de Criação: 13/11/2023 às 15:17:53

Documentos que originaram esse envelope:
- AVALIAÇÃO DA TESE DE DOUTORADO CAPES Lucas Henrique Pagoto Deoclecio.pdf (Arquivo PDF) - 2 página(s)
- Ata 23 TESE Lucas Henrique Pagoto Deoclecio.pdf (Arquivo PDF) - 1 página(s)
- Folha aprovação TESE Lucas Henrique Pagoto Deoclecio.pdf (Arquivo PDF) - 1 página(s)

Hashs únicas referente à esse envelope de documentos

[SHA256]: de0e1db96c4f5c2d65dfe19665148c31e832c9e948113fda15b89a1c465dae82
[SHA512]: 966d990e9601b853712a5201bf1ff6c0ff2934abbb104cebebc8a17cf326d32f9d7a605c1eee1ce47ce05cc928112bb30f7506832a119d98e5a55093dd7e4e8a

Lista de assinaturas solicitadas e associadas à esse envelope

ASSINADO - Edson José Soares (edson.soares@ufes.br)
Data/Hora: 13/11/2023 - 16:02:20, IP: 187.36.235.237
[SHA256]: 45a2266b268e69c830da01f763ea0d37d0d4f1514ae6a44832d5d9a324093f3f

ASSINADO - Francisco Ricardo da Cunha (frcunha@unb.br)
Data/Hora: 13/11/2023 - 17:46:55, IP: 164.41.16.61
[SHA256]: 4b3f6f67e66786757d60c8539a06449a23933894ce48e5cc469b16d68acff855

ASSINADO - Rogério Ramos (ramosrogerio@hotmail.com)
Data/Hora: 13/11/2023 - 15:35:33, IP: 200.137.65.104, Geolocalização: [-20.278950, -40.302710]
[SHA256]: 8e3940fafd459f881212c87ba8b80744853ec653a2bb6ac85ac44f0a365ee88c

ASSINADO - Renato do Nascimento Siqueira (renatons.ifes@gmail.com)
Data/Hora: 13/11/2023 - 16:23:51, IP: 189.91.158.155
[SHA256]: f7b6b24a6c7ad60bf82b314b9a087e973d23539010217a19310b61fce722506e

ASSINADO - Roney Leon Thompson (rthompson@mecanica.coppe.ufrj.br)
Data/Hora: 13/11/2023 - 20:06:47, IP: 177.26.78.157
[SHA256]: a6154b10f095f05af7273a0e35c3499bee9a1b82fee7d6788676bec883cfff9b

Histórico de eventos registrados neste envelope

13/11/2023 20:06:47 - Envelope finalizado por rthompson@mecanica.coppe.ufrj.br, IP 177.26.78.157
13/11/2023 20:06:47 - Assinatura realizada por rthompson@mecanica.coppe.ufrj.br, IP 177.26.78.157
13/11/2023 17:46:55 - Assinatura realizada por frcunha@unb.br, IP 164.41.16.61
13/11/2023 16:23:51 - Assinatura realizada por renatons.ifes@gmail.com, IP 189.91.158.155
13/11/2023 16:02:20 - Assinatura realizada por edson.soares@ufes.br, IP 187.36.235.237
13/11/2023 15:35:33 - Assinatura realizada por ramosrogerio@hotmail.com, IP 200.137.65.104
13/11/2023 15:35:07 - Envelope visualizado por ramosrogerio@hotmail.com, IP 200.137.65.104
13/11/2023 15:20:48 - Envelope registrado na Blockchain por andreia.eyng@ufes.br, IP 200.137.65.106
13/11/2023 15:20:46 - Envelope encaminhado para assinaturas por andreia.eyng@ufes.br, IP 200.137.65.106
13/11/2023 15:17:55 - Envelope criado por andreia.eyng@ufes.br, IP 200.137.65.106

Publications

This thesis has resulted in one publication in a conference proceedings and two articles published in indexed journals:

- Deoclecio, L.H.P., Soares, E.J., 2021. Drop interfacial coalescence in Bingham materials. In: JEM - Jornada de Escoamentos Multifásicos, 2021, Vitória. 6th Multiphase Flow Journeys;
- Deoclecio, L.H.P., Soares, E.J., Deka, H., Pierson, J.L., 2021. Bubble entrapment condition in Bingham materials. Journal of Non-Newtonian Fluid Mechanics, 295, 104616;
- Deoclecio, L.H.P., Soares, E.J., Popinet, S., 2023. Drop rise and interfacial coalescence initiation in Bingham materials. Journal of Non-Newtonian Fluid Mechanics. 319, 105075.

A third article, entitled "Drop rise and interfacial coalescence initiation in viscoelastic and elasto-viscoplastic materials" is currently being written and will be sent to the Journal of Non-Newtonian Fluid Mechanics.

Dedication

To God, my wife Letícia, and my daughter Beatriz.

Acknowledgment

I am immensely grateful for all the assistance and support received from several individuals and organizations involved in the execution of this work.

In particular, I would like to thank:

- My supervisor, prof. Dr. Edson José Soares, from whom I have learned a lot about being a researcher and for trying to extract the best of me;
- Prof. Dr. Roney Leon Thompson, for sharing, patiently and regardless of the moment, his deep knowledge of the rheology of complex materials;
- Prof. Ph.D. Stéphane Popinet, for his invaluable support, assistance, and shared knowledge in the implementation of the numerical code. I am also grateful for his guidance in cultivating a researcher mindset. And also for the warm welcome at the Institut Jean Le Rond d'Alembert;
- Prof. Ph.D. Anthony Wachs, for the help in the numerical implementation of the constitutive equations;
- The Federal University of Espírito Santo (UFES), for the excellent training and the doctoral degree;
- The Federal Institute of Espírito Santo (IFES), for the license granted to me to carry out my doctorate;
- The Higher Education Personnel Improvement Coordination (CAPES), for the financial support of the sandwich scholarship;
- Welington Mothé de Oliveira and Pascal Ray, from the IT teams of IFES and Institut d'Alembert, for their assistance and support in running the simulations.

Abstract

Drop rise and coalescence phenomena in complex materials hold significant relevance for various environmental and industrial processes. The intricate dynamics of the sequential steps of drop rise, collision, and film drainage are influenced by non-Newtonian behaviors such as plasticity and elasticity exhibited by the surrounding material. A comprehensive understanding of these processes is crucial for the efficient design and operation of industrial mixing and separating units. However, despite their importance, the underlying mechanisms governing these phenomena are not entirely comprehended. The primary objective of this thesis is to investigate the rise and interfacial coalescence initiation of a Newtonian drop in complex materials using time-dependent direct numerical simulations. The surrounding material is progressively modeled with formulations of increasing complexity, namely, Newtonian, inelastic viscoplastic, viscoelastic, and elasto-viscoplastic. To conduct the study, the elasto-viscoplastic Saramito model is implemented and validated. The investigation focuses on elucidating the influence of plastic, elastic, inertial, viscous, and surface tension effects, as well as their interaction on the dynamics of drop rise and coalescence initiation. Initially, the entrapment condition of spherical and non-spherical drops in inelastic viscoplastic materials is assessed in terms of the ratio of the force exerted by the yield stress and the buoyancy force. It is found that when determining the force exerted by the yield stress based on the radius of the maximum cross-sectional area of the drop (normal to buoyancy), this ratio remains constant for drops with low viscosity. However, for highly viscous drops, the ratio decreases asymptotically until it reaches the limit for solid spheres. For non-spherical drops, surface tension may yield the surrounding material to minimize the surface energy of the drop, making the drop to be permanently or only temporally mobile. For elasto-viscoplastic materials, elasticity increases the level of plasticity required for entrapment. Drop rise plays an important role in the initiation of the coalescence process. Inertial effects tend to increase the drop velocity and width, while an increase in the drop's viscosity increases viscous dissipation and slows down the drop. The influence of surface tension on the droplet velocity and width depends on the dominant forces in the flow, which can cause both an increase or decrease in these quantities. Plastic effects result in a reduction of droplet velocity and

width. Drop rise in viscoelastic materials is a dynamic process, influenced by the ratio of the relaxation time of the material to the characteristic rise time of the drop. Elastic effects also contribute to a reduction in drop width, facilitating its rise. In the case of elasto-viscoplastic materials, the interplay between elastic and plastic effects gives rise to intriguing behaviors. Plastic effects enhance the elastic behavior of the material, resulting in the appearance of the negative wake and teardrop shape (both characteristic of elastic behavior) for lower values of the elastic modulus when increasing the level of plasticity. Conversely, elastic effects suppress the plastic response of the material, leading to an expanded yielded region and reduced restriction on drop mobility by plasticity with increasing levels of elasticity. Regarding the coalescence phenomenon, plasticity manifests two main effects on the film drainage process. Firstly, it induces the formation of shorter and more spherical films, and secondly, it increases the resistance of the film to flow. The effect on the film shape facilitates the film drainage process, while the effect on the resistance of the film to flow hinders it. In regimes characterized by low surface tension, the influence of plasticity on the film geometry becomes more prominent than the resistance effect, resulting in a reduction in the drainage time. Conversely, in regimes characterized by high surface tension, where the interfaces between the fluids are less deformable, the resistance effect becomes more dominant compared to the effect of film shape, leading to an increase in the drainage time with the level of plasticity. Elastic effects also contribute to the formation of shorter films, thereby facilitating the drainage process. The partial or over activation of the viscosity of the elastic material further affects the rate of film drainage. Specifically, the partial activation of viscosity increases the drainage rate, while over-activation decreases it. In the case of elasto-viscoplastic materials, plastic effects enhance the partial activation of the material's viscosity, facilitating the initial stage of the drainage process. Additionally, elastic deformation makes it more difficult for the drainage film to freeze due to yield stress.

Keywords: Drop Rise; Drop Coalescence; Film Drainage Time; Plasticity; Elasticity; Elasto-viscoplastic materials.

Resumo

Os fenômenos de ascensão e coalescência de gotas em materiais complexos são relevantes para vários fenômenos naturais e processos industriais. A dinâmica intricada das etapas sequenciais de ascensão, colisão e drenagem do filme é influenciada por comportamentos não newtonianos, como plasticidade e elasticidade exibidos pelo material circundante. Uma compreensão abrangente desses processos é crucial para um eficiente projeto e operação de unidades de mistura e separação industriais. No entanto, apesar de sua importância, os mecanismos subjacentes que governam esses fenômenos não são totalmente compreendidos. O objetivo principal desta tese é investigar a ascensão e a iniciação da coalescência interfacial de uma gota newtoniana em materiais complexos usando simulações numéricas diretas transientes. O material circundante é progressivamente modelado com formulações de crescente complexidade, a saber, newtoniano, inelástico viscoplástico, viscoelástico e elasto-viscoplástico. Para conduzir o estudo, o modelo elasto-viscoplástico de Saramito é implementado e validado. A investigação se concentra em elucidar a influência dos efeitos plásticos, elásticos, inerciais, viscosos e de tensão superficial, bem como suas interações na dinâmica da ascensão e iniciação da coalescência de gotas. Inicialmente, a condição de aprisionamento de gotas esféricas e não esféricas em materiais inelásticos viscoplásticos é avaliada em termos da razão entre a força exercida pela tensão limite de escoamento e a força de empuxo. Verifica-se que, ao determinar a força exercida pela tensão limite de escoamento com base no raio da área transversal máxima da gota (normal ao empuxo), essa razão permanece constante para gotas com baixa viscosidade. No entanto, para gotas altamente viscosas, a razão diminui assintoticamente até atingir o limite para esferas sólidas. Para gotas não esféricas, a tensão superficial pode fazer com que o material circundante minimize a energia superficial da gota, tornando-a permanentemente ou apenas temporariamente móvel. Para materiais elasto-viscoplásticos, a elasticidade aumenta o nível de plasticidade necessário para o aprisionamento. A ascensão da gota desempenha um papel importante na iniciação do processo de coalescência. Efeitos inerciais tendem a aumentar a velocidade e a largura da gota, enquanto um aumento na viscosidade da gota aumenta a dissipação viscosa e diminui a sua velocidade. A influência da tensão superficial na velocidade e largura da gota de-

pende das forças que dominam o escoamento, que podem causar tanto um aumento quanto uma diminuição nessas variares. Efeitos plásticos resultam em uma redução na velocidade e largura da gota. A ascensão da gota em materiais viscoelásticos é um processo dinâmico, influenciado pela razão entre o tempo de relaxação do material e o tempo de ascensão característico da gota. Efeitos elásticos também contribuem para uma redução na largura da gota, facilitando sua ascensão. No caso de materiais elasto-viscoplásticos, a interação entre efeitos elásticos e plásticos resulta em comportamentos intrigantes. Efeitos plásticos intensificam o comportamento elástico do material, resultando no surgimento da esteira negativa e do formato de lágrima (ambos característicos do comportamento elástico) para valores mais baixos do módulo de elasticidade com um aumento no nível de plasticidade. Por outro lado, efeitos elásticos suprimem a resposta plástica do material, levando a uma região cedida expandida e menor restrição à mobilidade da gota pela plasticidade com o aumento da elasticidade. Em relação ao fenômeno de coalescência, a plasticidade manifesta dois efeitos principais no processo de drenagem do filme. Primeiramente, induz a formação de filmes mais curtos e esféricos, e, em segundo lugar, aumenta a resistência do filme ao escoamento. O efeito na forma do filme facilita o processo de drenagem, enquanto o efeito na resistência do filme ao escoamento o prejudica. Em regimes caracterizados por baixa tensão superficial, a influência da plasticidade na geometria do filme torna-se mais proeminente do que o efeito de resistência, resultando em uma redução no tempo de drenagem. Por outro lado, em regimes caracterizados por alta tensão superficial, onde as interfaces entre os fluidos são menos deformáveis, o efeito de resistência torna-se mais dominante em comparação com o efeito da forma do filme, levando a um aumento no tempo de drenagem com o nível de plasticidade. Efeitos elásticos também contribuem para a formação de filmes mais curtos, facilitando assim o processo de drenagem. A ativação parcial ou excessiva da viscosidade do material elástico também afeta a taxa de drenagem do filme. Especificamente, a ativação parcial da viscosidade aumenta a taxa de drenagem, enquanto a ativação excessiva a diminui. No caso de materiais elasto-viscoplásticos, os efeitos plásticos intensificam a ativação parcial da viscosidade do material, facilitando a etapa inicial do processo de drenagem. Além disso, a deformação elástica dificulta a paralisação da drenagem do filme pela tensão limite de escoamento.

Palavras-chave: Ascensão de Gota; Coalescência de Gota; Tempo de Drenagem do Filme; Plasticidade; Elasticidade; Materiais Elasto-viscoplástico.

List of Figures

List of Tables

List of Symbols and Acronyms

Greek letters

$\alpha_{i,j}$	Parameter to set the location of the line segment representing an interface numerically
$\alpha_{\mathcal{L}}$	Empirical coefficient for the Level-Set Method
β	Solvent to total viscosity in a polymer solution
$\boldsymbol{\gamma}$	Strain tensor
$\dot{\boldsymbol{\gamma}}$	Strain rate tensor
$\dot{\gamma}$	Strain rate
δ	Dirac delta function
Δ	Delta
Δt	Computational drainage time
$\underline{\Delta}$	Delta function for numerical discretization
ϵ	Regularization parameter
η	Viscosity
η'	Second coefficient of viscosity
η_c	Characteristic viscosity
η_p	Polymeric viscosity
η_r	Viscosity ratio
η_s	Solvent viscosity
θ	Retardation time
λ	Relaxation time
λ_c	Characteristic relaxation time
κ	Curvature
μ_p	Plastic viscosity
Π	Disjoining pressure
ρ	Density
σ	Surface tension coefficient

τ	Extra stress
$\boldsymbol{\tau}$	Extra stress tensor
$\boldsymbol{\tau}_d$	Deviatoric part of the extra stress tensor
$\boldsymbol{\tau}_p$	Polymeric stress tensor
$\boldsymbol{\tau}_{pd}$	Deviatoric part of the polymeric stress tensor
$\boldsymbol{\tau}_s$	Solvent stress tensor
ξ	Generic field variable
ξ_p	Ratio of unyielded radius to pipe radius
$\phi(\mathsf{r})$	Slope-limiter

Latin letters

A	Area
A_H	Hamaker constant
$\mathbf{A}$	Generic tensor
c	Volume fraction
$\tilde{c}$	Smoothed volume fraction
C	Perimeter of a surface element
C_D	Drag coefficient
$\mathcal{C}$	Minimum number of cells in the draining film
d	Distance
E	Surface free energy
$\mathcal{E}$	Error margin
f	function, functional
$\mathbf{f}$	Body forces per unit volume
F	Flux
F_{id}	Film region identification scalar
$\mathtt{F}$	Force
$\mathbf{g}$	Gravity acceleration vector
G	Elastic modulus
G''	Dissipation modulus
h	Film thickness
h_{min}	Minimum film thickness
$\mathtt{h}$	Height function
H	Domain height

$\mathcal{H}$	Heaviside function
$\mathbf{I}$	Identity tensor
$\mathtt{i}$	Grid stencil index
$\mathtt{j}$	Grid stencil index
K	Consistency index
l	Arc length
$\mathbf{l}$	Unit tangential vector
L	Mesh refinement level
L_{max}	Mesh maximum refinement level
$\mathcal{L}$	Level-Set function
$\mathtt{L}$	Characteristic length
$\mathbf{m}_{i,j}$	Local unit normal vector to the line segment representing the interface numerically
n	Level of refinement
$\mathtt{n}$	Power-law index
$\mathtt{n}$	Timestep index
N	Dimensionless regularization parameter
p	Pressure
P	Point in the domain
$\mathbf{q}$	unit normal vector normal to a contour C and tangent to a surface S
r	Radial position
R	Drop radius
s	Surface length
S	Surface
t	Time
T_σ	Time period of the smallest capillary wave
$\mathbf{T}$	Total stress tensor
$\mathbf{T}_d$	Deviatoric part of the total stress tensor
$\mathbf{T}_S^\sigma$	Surface tension tensor
u	Velocity
$\mathbf{u}$	Velocity vector
U	Characteristic velocity
V	Volume
W	Mechanical work
x	Direction in the Cartesian coordinate system
$\mathbf{x}$	Position vector

y	Direction in the Cartesian coordinate system
Y_g	Yield stress parameter
Y_{gc}	Critical yield stress parameters
z	Axial position

Subscripts

1	Fluid 1
2	Fluid 2
σ	Surface tension
θ	Azimuthal direction
AR	Aspect ratio
c	Characteristic
c	Critical
d	Deviatoric
d	Drop
e	Elastic
eq	Equivalent
h	Discretized
h	Hidden
H	Height
HR	Hadamard and Rybczynski
i	Interface
i	Grid stencil index
I	Interface position
j	Grid stencil index
m	Materials
m	Mean
max	Maximum
min	Minimum
o	Observation
o	Initial
p	Polymeric
p	Pressure
r	Ratio

$\mathtt{r}$	Rise
s	Solvent
$\mathtt{s}$	Surrounding
S	Surface
ST	Stokes
t	Terminal
v	Viscous
vdW	van der Waals
w	Wall
W	Width

Superscripts

$-$	Dimensionless variable
σ	Surface tension
$\cdot$	Time rate
$\sim$	Smoothed variable averaged over eight neighboring cells
T	Transposed

Mathematical Operators

$\cdot$	Scalar product
$\|\|$	Frobenius norm of a tensor
∇	Nabla operator
∇_h	Numerical discrete gradient operator
$\triangledown$	Upper Convected Derivative
d	Derivative
∂	Partial derivative
D	Material derivative
tr	Trace of a tensor

Acronyms

ALM	Augmented Lagrangian Method
BF	Balance-force
CFL	Courant–Friedrichs–Lewy number

CSF	Continuum-Surface-Force
DNS	Direct Numerical Simulations
EDL	Electrical Double Layer
EVP	Elasto-viscoplastic
FT	Front-Tracking
HF	Height function
IV	Inelastic viscoplastic
LLPS	Liquid-liquid Phase Separation
LS	Level-Set
UCM	Upper Convected Maxwell
PBE	Population Balance Equations
PIV	Particle Image Velocimetry
PTV	Particle Tracking Velocimetry
VE	Viscoelastic
VOF	Volume-of-Fluid

Dimensionless Numbers

Ar	Archimedes number
Bi	Bingham number
Bo	Bond number
Ca	Capillary number
De	Deborah number
El	Elastic number
Fr	Froude number
Ga	Galilei number
Pl	Plastic number
Re	Reynolds number
We	Weber number
Wi	Weissenberg number
Wi_c	Characteristic Weissenberg number
β	Solvent to total viscosity ratio
η_r	Viscosity ratio
ρ_r	Density ratio

Contents

Chapter 1

Introduction

Drop rise and coalescence phenomena are fundamental problems in fluid mechanics, holding significant relevance in various environmental and industrial mixing and separation processes. The surrounding fluid often exhibits non-Newtonian behaviors such as plasticity and elasticity; for instance, in the processing of food, cosmetics, medicines, waste, slurries, inks, polymer solutions, and crude oil (Dubash and Frigaard, 2004, 2007; Potapov et al., 2006; Tripathi et al., 2015b; Mendes, 2011). Depending on the specific application, phase separation, or more precisely, the phenomena of drop rise and coalescence, may be considered desirable or undesirable. For instance, the mobility of bubbles and drops plays a crucial role in water treatment, fermentation, and liquid-liquid extraction processes, wherein their dynamic behavior (including velocity and shape) can significantly impact the diffusion of gases and solutes. Consequently, these dynamics directly influence the overall efficiency of physical and chemical processes. In the treatment of crude oil and liquid–liquid extraction, drop rise and coalescence is desirable in order to recover valuable components and discard treated residues. Conversely, the entrapment of bubbles and drops is highly desirable in food processing applications, such as chocolate, ketchup, and mayonnaise in order to improve their taste. Furthermore, the stability of bubbles and drops is a sought-after property in the production of cosmetic lotions and medicines. Throughout this study, the term "drop" is utilized as a general reference, irrespective of density and viscosity ratios. Conversely, the term "bubble" is specifically reserved for situations where the internal phase consists of a gas, characterized by small density and viscosity ratios.

The management of multiphase flows in situations of practical interest poses considerable challenges, and potential monetary benefits derived from a more profound comprehension of these flow dynamics are substantial. Much of the knowledge regarding multiphase flows comes from experimental investigations and scaling analysis, which despite their significance, encounter numerous challenges. Therefore, the utilization of numerical tools capable of pro-

viding precise solutions for multiphase flows holds immense value in aiding a more comprehensive understanding of these intricate flows (Tryggvason et al., 2011). However, numerical studies regarding the flow of yield stress materials commonly rely on inelastic viscoplastic models that do not incorporate elastic effects. Consequently, there is a lack of agreement in the existing literature between experimental observations and numerical simulations pertaining to the rise of drops and bubbles within complex fluids (Lopez et al., 2018).

Drop rise and coalescence are intricate and not fully comprehended phenomena, encompassing a wide range of length and time scales. Investigating these phenomena within a fully dispersed system, characterized by a swarm of drops, can be laborious, time-consuming, and demanding in terms of resources. Therefore, focusing on the study of single-drop systems is of great importance for scaling up industrial processes involving dispersed systems (Charin et al., 2019; Saien and Jafari, 2019). For instance, developing coalescence models based on single-drop systems holds significant potential as an input for predicting particle size distribution in industrial oil/water separators using the Population Balance Equations (PBE) approach (Deoclecio et al., 2020). The occurrence of coalescence depends on a sequence of events (Goel and Ramachandran, 2017; Liao and Lucas, 2010; Mohamed-Kassim and Longmire, 2003; Chesters, 1991). For gravity-driven phase separation, drop rise leads to collisions, resulting in the entrapment and draining of a film of the surrounding material. The film drainage process governs the rate of coalescence (Chesters, 1991; Kamp et al., 2017; De Malmazet et al., 2015), thereby highlighting the importance of comprehending this step for improving mixing and separation processes. If the film thickness reaches the critical rupture thickness, non-hydrodynamic short-range forces (*e.g.* van der Waals and electric double layer) destabilize and break the film. A bridge is then formed and the bulk fluids of the internal phase merge. Most strategies to render a dispersed system stable or unstable focus on the modification of the fluid-fluid interfaces by the addition or removal of surfactants, respectively. These surfactants control the resultant non-hydrodynamic short-range forces, which play a crucial role in film rupture (Goel and Ramachandran, 2017; Zawala et al., 2020).

However, phase separation kinetics are also governed by the bulk properties. A lack of understanding regarding how non-Newtonian effects influence drop rise and coalescence dynamics can result in the inadequate strategy to deal with multiphase dispersed systems; for example, unnecessary use of emulsifier or demulsifier when the coalescence process is primarily controlled by the rheological parameters of the phases (Tchoukov et al., 2014). For instance, large molecules such as asphaltenes, cellulose microfibrils, and polymers can form networks around drops and contribute to the stabilization of emulsions by imparting yield stress. Emulsions stabilized by asphaltenes are of particular relevance in the oil industry, where the presence of micrometer-sized water drops with dissolved salts can lead to severe

corrosion problems in refinery equipment and pipelines (Tchoukov et al., 2014). Asphaltenes can stabilize films at thicknesses larger ($\sim$ 100 nm) than the range where intermolecular forces become significant ($\sim$ 10-50 nm) (Yiantsios and Davis, 1990; Kamp et al., 2017; Liu et al., 2019; Chatzigiannakis et al., 2021). The formation of such three-dimensional structures alters the rheological properties of the liquid film to become non-Newtonian with yield stress, resembling a gel-like material (viscous, plastic, and elastic behavior) (Tchoukov et al., 2014). Cellulose microfibrils are another example of agents that can stabilize emulsions. They are biodegradable and readily available, making them suitable for applications in the food and cosmetic industries (Nomena et al., 2018). Hydrogels, which are formed by hydrophilic polymer networks in aqueous media, are extensively used in tissue regeneration, drug delivery, and wound healing. The fabrication of hydrogels often involves the liquid-liquid phase separation technique, where gelation imparts yield stress to the dispersing phase, making it resistant to drainage and thereby slowing down coalescence (Garcia and Kiick, 2019). Additionally, the use of polymers, such as polyacrylamide, in enhanced oil recovery processes can introduce difficulties in emulsion treatment. The polymers can alter the physical and chemical characteristics of the produced emulsion, and their presence at the oil-water interface can act as surfactants (Zheng et al., 2011; Wang et al., 2020). Moreover, polymer solutions may induce increased viscosity and elastic effects, such as normal stresses, which significantly increase the resistance of the film to flow due to the presence of polymeric molecules (Chatzigiannakis and Vermant, 2021).

Despite its significance in optimizing mixing and separation processes, the investigation of drop rise and coalescence phenomena in elasto-viscoplastic (EVP) materials has not yet received much attention in the existing literature. Thus, the primary objective of this thesis is to examine the influence of the rheological parameters of elasto-viscoplastic materials on the dynamics of drop rise and initiation of interfacial coalescence through the utilization of direct numerical simulations. To accomplish this objective, an elasto-viscoplastic constitutive model is implemented and validated. Subsequently, the sequential problems of a Newtonian drop entrapment, rise, interfacial collision, and film drainage initiation are solved numerically. Then, a parametric study is conducted to evaluate the effects of the surrounding phase plasticity and elasticity, as well as their combined effects with inertial, viscous, and surface tension effects on the rise of drops and their subsequent interfacial collision.

The remainder of this thesis is organized as follows. Chapter 2 presents a literature review on interfacial phenomena, numerical modeling of flows with free interfaces, modeling of non-Newtonian materials, and the phenomena of drop rise and coalescence, in both Newtonian and non-Newtonian materials. Chapter 3 formulates the physics of the studied problem, where the flow domain and boundary conditions, governing and constitutive equations, and

dimensionless numbers are presented. Chapter 4 introduces the employed numerical methodology and validation tests of the numerical code. Chapter 5 presents and discusses the results regarding the entrapment, rise, collision, and film drainage initiation of Newtonian drops in different material formulations. Finally, the concluding remarks are drawn in Chapter 6.

Chapter 2

Literature Review

The study of flows involving elasto-viscoplastic materials and the phenomena of drop rise and coalescence poses considerable complexity, which is further compounded when these aspects are examined together. This chapter aims to provide a literature review encompassing these subjects, first addressing them individually and subsequently together. The chapter initiates with a review of interfacial phenomena and numerical modeling of flows with free interfaces. Following this, the concepts of non-Newtonian fluids and their modeling are introduced, starting with inelastic viscoplastic (IV) models, progressing to viscoelastic (VE) models, and culminating with elasto-viscoplastic (EVP) models. Lastly, the literature on the phenomena of drop rise and drop coalescence, encompassing both Newtonian and non-Newtonian mediums, is reviewed. Throughout the review, relevant dimensionless numbers pertaining to each topic are introduced and discussed in conjunction with the corresponding text.

2.1 Interfacial Phenomena

Interfaces are present everywhere, and every physical entity may be considered to have an interface at its boundary with its surroundings. This thesis focuses on liquid-liquid and liquid-gas interfaces, which are relevant to phenomena involving drops and bubbles, respectively. The term "surface tension" is sometimes used to refer to the interface between a liquid and a gas, while "interfacial tension" pertains to the interface between two liquid phases (Bush, 2013). In this work, the terms "surface" and "interface" will be used interchangeably. Additionally, the term "drop" will be employed as a general reference, irrespective of density and viscosity ratios, whereas "bubble" will be reserved for scenarios in which the internal phase is a gas (characterized by small density and viscosity ratios).

Interfacial phenomena arise from intermolecular forces between molecules in the bulk

and at the interface. To achieve a stable electron arrangement, atoms form chemical bonds (form molecules) by gaining, losing, or sharing electrons, so they acquire the same number of electrons as the noble gas closest to them in the periodic table. The electron distribution in a molecule depends on the electronegativity of its constituent atoms. Electronegativity is defined as the ability of an atom in a molecule to attract electrons to itself (Brown et al., 2012). In a molecule composed of two identical atoms (*e.g.*, H_2), electrons are equally shared between them since they have the same electronegativity, resulting in a non-polar covalent bond. The molecule is considered non-polar because it possesses a symmetric distribution of electrical charges and lacks permanent electrical poles. Conversely, molecules formed by atoms from opposing sides of the periodic table, typically involving metals and non-metals (e.g., NaCl), exhibit minimal electron sharing, as one atom effectively transfers its electrons entirely to the other atom, thus forming an ionic bond. For molecules falling between these two scenarios, electrons are shared between the atoms in an unequal manner (e.g., H_2O), leading to a polar covalent bond. In this case, one of the atoms exerts a greater attraction on the electrons, creating a dipole with two electrical poles possessing opposite charges. Therefore, although the molecule as a whole remains electrically neutral, one region of the molecule becomes more negatively charged due to a higher electron concentration, while the other region becomes more positively charged owing to a deficit of electrons. Polar molecules have a propensity to align with one another, analogous to a set of magnets, as the positive region of one molecule is attracted to the negative region of an adjacent molecule, and vice versa. They also exhibit attraction towards ions. On the other hand, non-polar molecules lack permanent poles, but they can transiently acquire polarity since electrons are in constant motion. These temporary electrical poles induce electrical charges in neighboring molecules, causing them to temporarily exhibit polarity as well (Brown et al., 2012).

Due to the presence of molecular dipoles and their associated electric fields, molecules are attracted to one another through electrostatic forces. These forces become stronger as the charges' magnitude increases and weaken as the distance between charges increases. Intermolecular forces, which are considerably weaker than intramolecular forces, come into play when molecules are in close proximity. In the case of neutral molecules, these non-ionic intermolecular forces are referred to as van der Waals forces, which can be further categorized as dispersion forces and dipole-dipole attractions. An additional type of attractive force is the ion-dipole force, which holds particular importance in solutions, such as a solution of NaCl in water. Dispersion forces arise from the transient polarization of molecules and are present in all substances. The momentary dipole in one molecule induces an instantaneous dipole in neighboring atoms, resulting in an attractive force between them. Dipole-dipole attractions occur between polar molecules, which are characterized by permanent dipoles. Generally,

these forces are less significant than dispersion forces in terms of overall intermolecular attraction. However, a special case of dipole-dipole attraction forces is the hydrogen bonds. In case hydrogen forms molecules with highly electronegative atoms such as oxygen (H_2O), nitrogen (NH3), or fluorine (HF), the resulting molecules become highly polarized. The positive end of the dipole, which is nearly a bare hydrogen nucleus (a positive proton), experiences a strong attractive force due to the close proximity of the hydrogen atom with the electronegative atom in an adjacent molecule. This is because hydrogen is small in size, particularly when it lacks electrons. Hydrogen bonding can also occur between the hydrogen in a polar bond and ions, leading to a strong attraction (Brown et al., 2012).

As a result of these intermolecular forces, molecules within the interior of a liquid experience mutual attractive forces known as cohesion. This cohesive force acts equally in all directions, resulting in a net force of zero on an individual molecule. In contrast, molecules at an interface between two fluids lose half of their same-phase neighboring molecules. While they can still experience attractive forces with neighboring molecules from the other phase, the net attractive force is non-zero. Consequently, a net inward pulling force arises between the molecules at the interface and the adjacent molecules in the bulk. This phenomenon is depicted in Fig. 2.1. The collective effect of this net force causes the surface to contract as the molecules at the interface are drawn together. The fluctuations in surface thickness are of the order of a mere Angstrom (de Gennes et al., 2004). This leads to the emergence of surface tension, denoted as σ, which can be understood as a force per unit length acting at the interface (Martin et al., 2006). It is similar to the surface tension in a stretched membrane that opposes its distortion (de Gennes et al., 2004). The dynamics of drop rise and coalescence are primarily governed by the effects of surface tension. To increase the area of a surface, a stretching force parallel to the surface must be applied. This force needs to be sufficiently strong to overcome the net inward force acting on the molecules at the interface and bring molecules from the bulk to the surface. Upon removal of the stretching force, the surface reverts to its "resting" position, and the molecules return to the bulk. Surface tension can be viewed as a negative surface pressure or a line tension acting in all directions parallel to the surface. However, unlike pressure, which explicitly appears in the Navier-Stokes equations with units of force per unit volume, surface tension is confined to the interface (Bush, 2013).

The surface tension between two liquids is typically lower than the surface tension between a liquid and a gas. This is because the adhesive forces between two liquids generally are greater than that of a liquid and a gas forming an interface. In the case of two completely miscible liquids, there is no surface tension between them. For example, fresh and saltwater are miscible and salt molecules can freely diffuse across their boundary (Bush, 2013).

Surface tension can also be related to the work per unit area needed to increase the

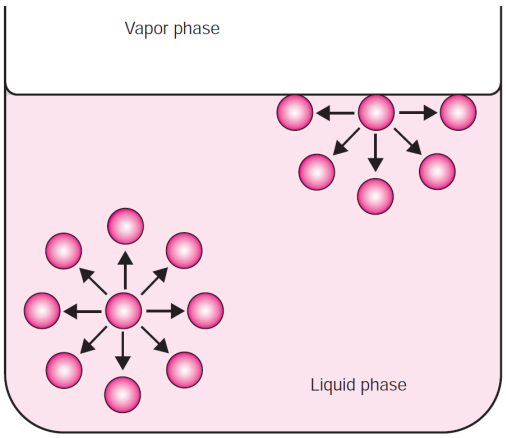

Figure 2.1: Illustration of the attraction forces between molecules in the bulk of a liquid and at the interface.
Source.: Martin et al. (2006).

surface area. Work is done to bring a molecule from the fluid interior to the surface, and it is proportional to the number of molecules brought up. Hence, each molecule at the interface possesses excess potential energy compared to molecules in the interior. Due to the deformable nature of fluid interfaces, they have the ability to change their shape in order to minimize their surface energy (de Gennes et al., 2004). This phenomenon leads liquids to adopt a form that minimizes their surface area, thereby reducing their surface free energy. It explains why bubbles and drops tend to exhibit a spherical shape (Martin et al., 2006), and why a thin fluid jet emerging from a sink typically breaks up into spherical drops (Bush, 2013). On the other hand, energy is required to disperse water into a fine spray, as this process increases the surface area and therefore the surface free energy.

For a spherical bubble of radius R, the total surface free energy is $E = \sigma A$, where $A = 4\pi R^2$ is the bubble's surface area. If the bubble radius varies by dR, the final surface free energy becomes $E = 4\pi\sigma(R + dR)^2$. By expanding this expression and neglecting the term containing dR^2, the variation in surface free energy is given by $dE = \sigma dA = 8\pi\sigma R dR$. The change in bubble volume is accompanied by a difference between the pressure inside and outside of the bubble, Δp. Therefore, the work required to change the bubble radius associated with the pressure change is $dW = 4\pi\Delta p R^2 dR$. At equilibrium, this is equal to the change in surface free energy, so $8\pi\sigma dR = 4\pi\Delta p R^2 dR$. Rewriting for the pressure difference,

$$\Delta p = \frac{2\sigma}{R}. \tag{2.1}$$

Equation 2.1 is a simplification of the Young-Laplace equation, and it states that the bubble radius and the pressure inside the bubble relative to the pressure outside are inversely pro-

portional. Therefore, during the coalescence of two bubbles of different sizes, the smaller one disappears in favor of the large one because the former possesses a higher Laplace pressure compared to the latter (Bush, 2013). The Laplace theorem states that an increase in hydrostatic pressure occurs across the boundary between two fluids, and it is equal to the product of the surface tension σ and the curvature of the surface $\kappa = 1/R_1 + 1/R_2$, where R_1 and R_2 are the radii of curvature of the surface. Thus, the pressure difference across the interface is given by

$$\Delta p = \sigma\kappa. \tag{2.2}$$

For the case of a spherical bubble ($R_1 = R_2$), Eq. 2.2 simplifies to Eq. 2.1. If the interface is flat, both the curvature and the pressure jump are zero. The radii R_1 and R_2 are algebraic quantities, and thus, they are positive or negative depending on which side of the interface the center of the radius of curvature is. In the case of a spherical bubble, both centers are located inside the bubble, resulting in an increase in pressure from the outside to the inside. This is illustrated in Figure 2.2 for a drop of radius R deposited on a fiber with radius b. For $R >> b$, the pressure inside the drop can be approximated as $\Delta p \approx 2\sigma/R$. At point A (Fig. 2.2(a)), as $z \to 0$ and $r \to b$, R_2 tends towards b. However, since $\kappa \approx 2/R$, R_1 becomes negative and of the same order of magnitude as R_2. Conversely, at point B (Fig. 2.2(b)), both R_1 and R_2 are positive and approximately equal to R in terms of magnitude.

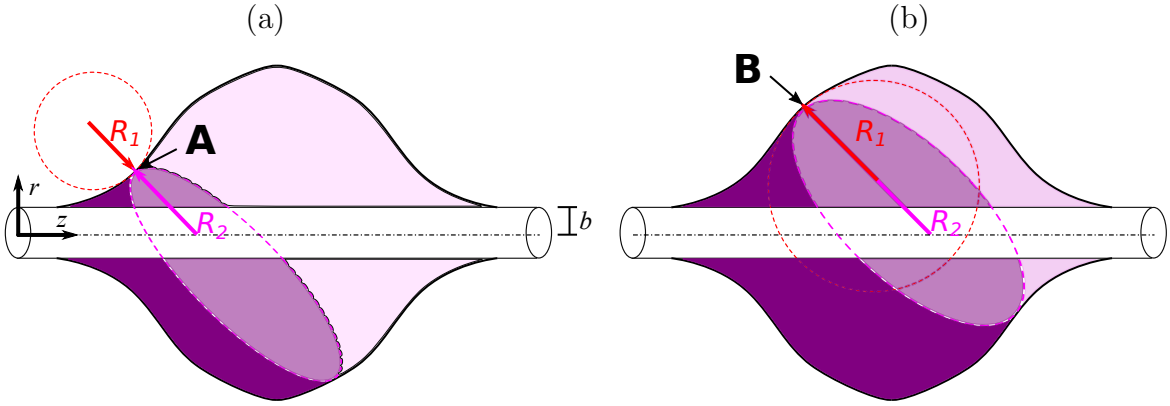

Figure 2.2: Radii of curvature, R_1 and R_2, of the surface of a drop deposited on a fiber. (a) R_1 is outside the drop (negative) and R_2 is inside the drop (positive) at point A, and (b) both radii are inside the drop and are positive at point B.

Despite the energy required to transport a molecule from the bulk to the surface, certain molecules and ions have a natural tendency to accumulate at the interface when dispersed in a liquid. This phenomenon is referred to as adsorption, which leads to a reduction in the system's surface tension. These molecules and ions are commonly known as surfactants,

surface-active agents, or amphiphiles, as they exhibit an affinity for both fluids that comprise the interface. Typically, one of the fluids is polar (e.g., water) while the other is non-polar (e.g., oil). For instance, in a water-air or water-oil interface, the polar head of the surfactant interacts with water molecules, while the non-polar portion is repelled by water molecules, remaining in the air or oil phase. Consequently, surface-active agents tend to accumulate at the interface (Martin et al., 2006).

Fluid interfaces, particularly those involving water, are prone to contamination by surfactants, whether intentional or unintentional (de Gennes et al., 2004). Figure 2.3 depicts a schematic of a surfactant layer adsorbed at the interface of a water droplet immersed in an oil matrix. As illustrated, the polar head of the surfactant is attracted to the water phase, while the non-polar tail resides within the oil phase. Surfactants aid in stabilizing emulsions by reducing surface tension, forming a protective layer around the droplets, and introducing electrical charges to the interface. Emulsions are mixtures of immiscible liquids where one liquid is dispersed as small droplets within the other. They find wide-ranging industrial applications. For example, many active substances are only soluble in oil (non-polar solvents) but need to be diluted in water to mitigate their toxicity in pure solvent form (de Gennes et al., 2004). Emulsions are thermodynamically unstable due to the stronger cohesive forces between alike molecules compared to the adhesive forces between different molecules. Additionally, as the dispersed phase exists as small droplets, the interfacial area and, consequently, the system's free surface energy are elevated. Therefore, droplets tend to coalesce, merging to form larger droplets, to minimize the system's energy. However, emulsions can be kinetically stabilized through the use of emulsifying agents (surfactants). The three mentioned mechanisms by which surfactants stabilize emulsions operate as follows: First, the attractive forces between the polar heads of the surfactants and the water molecules at the interface counterbalance the inward pulling force exerted by water molecules in the bulk, thereby reducing the system's surface free energy. Second, surfactants can create a "skin" around the droplets, effectively sealing them and preventing close proximity between water droplets, thereby inhibiting coalescence. In the case of the water droplet shown in Fig. 2.3, the surfactant tails prevent it from approaching and merging with another droplet. Third, the presence of surfactants can impart an electrical charge to the droplet's surface, leading to electrostatic repulsion between droplets, thereby further hindering coalescence (Martin et al., 2006).

If the surface tension is uniform along a closed line element, the net force exerted on this element is zero, resulting in a static state. However, if there is a non-zero gradient in surface tension, different parts of the line element will experience varying forces, leading to a non-zero net force that distorts the element and induces flow. The surface tension coefficient σ generally depends on both temperature and the chemical composition of the

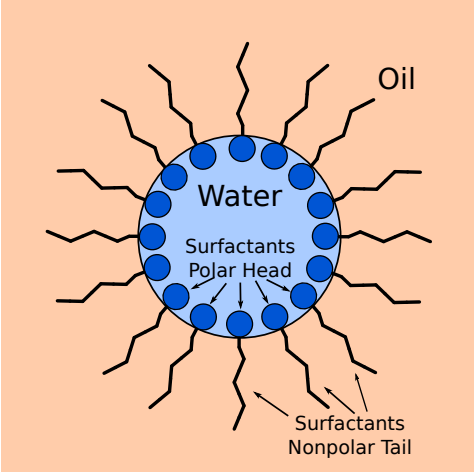

Figure 2.3: Surfactants on a water (drop)/oil (surrounding) interface.

interface. Consequently, a gradient in surfactant concentration gives rise to a gradient in surface tension, which triggers a distinct type of flow known as Marangoni flow (flow driven by surface tension gradients). Hence, surfactants not only influence the balance of normal stresses across an interface (*e.g.*, altering curvature pressure by modifying σ), but they also impact the balance of tangential stresses through the generation of Marangoni stresses. As a result, surfactants impart an effective elasticity to the interface by resisting any divergence or convergence motion of the surface. For example, in a radially divergent surface motion, surfactants are swept away from near the divergent point, leading to a non-zero surfactant concentration gradient. However, the Marangoni stresses drive the flow back toward the divergent point, opposing the surface motion and effectively suppressing it through surface elasticity. The opposite occurs for a radially converging surface motion (Bush, 2013).

For more on interfacial phenomena, the reader should refer to de Gennes et al. (2004), Martin et al. (2006), and Bush (2013).

2.2 Numerical Modeling of Flows with Interfaces

This section introduces numerical techniques to deal with flows with free interfaces based on the "one-fluid" formulation. It begins by presenting the mathematical expressions for the unit normal vector and curvature of an interface. In the sequence, the governing equations for single-phase flows and flows with free interfaces using the one-fluid approach are presented. Then, numerical methods for representing and advecting an interface are reviewed, along with techniques for numerically calculating and incorporating the surface tension force into the momentum equation.

2.2.1 The one-fluid formulation

In the "one-fluid" formulation, a single set of governing equations is written for the entire flow domain, treating the different phases as a single fluid with varying material properties that undergo abrupt changes at the interface. The derivation of the one-fluid equations begins with the governing equations for a single-phase flow, to which an additional singular force is introduced to incorporate the effects of surface tension. However, before discussing this, the interface unit normal vector and curvature are first described.

2.2.1.1 Interface normal and curvature

Consider a domain containing two immiscible fluids, referred to as fluid 1 and fluid 2, separated by an interface. The regions occupied by each fluid can be defined using a function that assumes different values in each fluid. For example, a smooth Level-Set function $\mathcal{L}(\mathbf{x})$ (the Level-Set method for numerically advecting an interface is discussed in Sec. 2.2.3.2) can be used to define the regions occupied by fluids 1 and 2 as the regions where $\mathcal{L} > 0$ and $\mathcal{L} < 0$, respectively, as exemplified in Fig. 2.4. The interface location is described by the contour $\mathcal{L} = 0$. Since the gradient of a scalar function is perpendicular to its level curves, the unit normal vector $\mathbf{n}$ to the interface (considering that the normal points outwards, in the direction in which $\mathcal{L}$ decreases) and the interface curvature κ can be determined as follows:

$$\mathbf{n} = -\frac{\nabla \mathcal{L}}{|\nabla \mathcal{L}|} \tag{2.3}$$

and

$$\kappa = -\nabla \cdot \mathbf{n} = \nabla \cdot \left(\frac{\nabla \mathcal{L}}{|\nabla \mathcal{L}|} \right), \tag{2.4}$$

respectively. These equations are evaluated on the contour $\mathcal{L} = 0$ (a detailed derivation of Eq. 2.4 is presented in Tryggvason et al. (2011).

Fluids 1 and 2 in Fig. 2.4 can also be identified by a marker function defined in the whole domain, such as a Heaviside function $\mathcal{H}(\mathbf{x})$, defined as follows:

$$\mathcal{H} = \begin{cases} 1 & \text{if inside fluid 1,} \\ 0 & \text{if inside fluid 2.} \end{cases} \tag{2.5}$$

The interface is identified at a sharp change in the value of $\mathcal{H}$ when crossing between the two fluids. Thus, a non-zero value of the gradient of $\mathcal{H}$ ($\nabla \mathcal{H} \neq 0$) indicates the presence of the

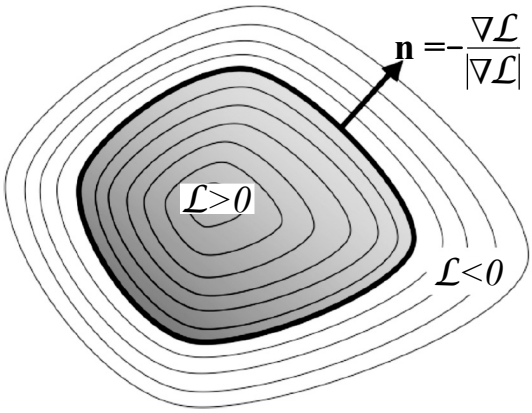

Figure 2.4: An interface described by a Level-Set function, which identifies the interface location at the contour $\mathcal{L} = 0$.
Source: adapted from Tryggvason et al. (2011).

interface. The gradient of $\mathcal{H}$ can be expressed as:

$$\nabla \mathcal{H} = -\delta_S(\mathbf{x})\mathbf{n}, \tag{2.6}$$

where, $\delta_S(\mathbf{x}) = \delta(n)$ is a surface distribution (a one-dimensional δ-function concentrated on the interface, instead of being concentrated at a point as the Dirac δ-function). The presence of $\delta_S(\mathbf{x})$ allows for the transformation of a volume integral into a surface integral through the following relationship:

$$\int_V \delta_S(\mathbf{x}) f(\mathbf{x}) dV = \int_S f(\mathbf{x}) dS, \tag{2.7}$$

where $f(\mathbf{x})$ represents an arbitrary function.

Additionally, the interface location can also be explicitly defined by a height function $y = \mathtt{h}(x)$ (as the graph of a function), with first ($\mathtt{h}_x = d\mathtt{h}/dx$) and second ($\mathtt{h}_{xx} = d^2\mathtt{h}/dx^2$) derivatives. In a two-dimensional domain, the interface is represented by a line, and its location can determined by a functional $f(x, y) = y - \mathtt{h}(x)$ that vanishes on the surface. By using $f(x, y)$ in the definitions of Eq. 2.3 and 2.4, $\mathbf{n} = (n_x, n_y)$, and κ can be written as

$$\mathbf{n} = \frac{1}{\sqrt{1 + \mathtt{h}_x^2}} \left(-\mathtt{h}_x, 1\right), \tag{2.8}$$

and

$$\kappa = \frac{\mathtt{h}_{xx}}{\sqrt[3/2]{1 + \mathtt{h}_x^2}}, \tag{2.9}$$

respectively.

2.2.1.2 Governing equations for incompressible single-phase flows

The governing equations for single-phase flows of an incompressible fluid rely on the principles of mass and momentum conservation, which can be expressed by the following partial differential equations:

$$\nabla \cdot \mathbf{u} = 0, \tag{2.10}$$

$$\rho \left(\frac{\partial \mathbf{u}}{\partial t} + \mathbf{u} \cdot \nabla \mathbf{u} \right) = \mathbf{f} + \nabla \cdot \mathbf{T}. \tag{2.11}$$

Equation 2.10 is the continuity equation and Eq. 2.11 is Cauchy's equation, which is valid for any continuous medium. Equation 2.10 states that for an incompressible flow, the fluid volume is conserved, while Eq. 2.11 states that the total acceleration of a material element is equal to the net flux of stress plus the body force applied to the element. In Eqs. 2.10 and 2.11, $\mathbf{u}$ is the velocity vector field, ρ is the fluid's density, t is time, and $\mathbf{f}$ is the body forces per unit volume acting on the fluid element, which usually is only the gravitational force, $\mathbf{f} = \rho\mathbf{g}$, where $\mathbf{g}$ is the gravity acceleration vector. $\mathbf{T}$ is the stress tensor or total stress tensor, which can be decomposed into a spherical and a deviatoric part. For incompressible pure viscous fluids (*e.g.*, Generalized Newtonian Fluids), it can be written as:

$$\mathbf{T} = -p\mathbf{I} + \boldsymbol{\tau}. \tag{2.12}$$

Here, $-p\mathbf{I}$ is an isotropic tensor which corresponds to the spherical part of the $\mathbf{T}$ and $p = -1/3\,\mathrm{tr}(\mathbf{T})$ is a scalar that represents the fluid's pressure. For a Newtonian fluid at rest, it reduces to the static-fluid pressure and it is the only non-zero part of the stress tensor. For an incompressible fluid in motion, in which the normal components of $\mathbf{T}$ generally depend on the normal direction to the surface of the fluid element, $-p\mathbf{I}$ provides an appropriate generalization of the notion of pressure, as it is an isotropic tensor and its normal components do not depend on the direction of the normal to the surface element (Batchelor, 1967). According to Batchelor (1967), p is not a variable of state used in equilibrium thermodynamics anymore, but rather a mechanical definition of "pressure" that gives a "measure of the local intensity of the squeezing of the fluid". Thus, p represents the mean normal stresses and it is not explicitly dependent on any kinematic quantity (Lai et al., 2009).

The second term on Eq. 2.12, $\boldsymbol{\tau}$, is the extra stress tensor, which corresponds to the deviatoric part of $\mathbf{T}$. The extra stress depends on kinematic quantities (*e.g.*, deformation and rate of deformation) and material properties. It tries to deform the material or to deviate

it from its spherical state. The specific nature of the material is described by constitutive equations, which relate the extra stress tensor to the deformation and/or rate of deformation of the material. For example, in the case of an incompressible Newtonian fluid, the constitutive equation can be written as $\boldsymbol{\tau} = \eta\dot{\boldsymbol{\gamma}}$, where η is the fluid's viscosity and $\dot{\boldsymbol{\gamma}}$ is the strain rate tensor given by $\dot{\boldsymbol{\gamma}} = \nabla\mathbf{u} + \nabla\mathbf{u}^{\mathbf{T}}$. In this case, the diagonal elements of $\boldsymbol{\tau}$ make zero contribution to the mean normal stress since $\mathrm{tr}(\dot{\boldsymbol{\gamma}}) = 0$. Therefore, $\boldsymbol{\tau}$ corresponds to the deviatoric part of $\mathbf{T}$ and captures only the deformation of the fluid element. Differently from pure viscous fluids, the extra stress tensor generally is not deviatoric for fluids with elastic behavior (as discussed in Secs. 2.3.2 and 2.3.3). In this case, $\boldsymbol{\tau}$ has a non-deviatoric part contributing to the mechanical pressure (which is not given by p alone anymore). The spherical part of stress tensor is then written as $[-p + (1/3)\mathrm{tr}(\boldsymbol{\tau})]\mathbf{I}$ and the deviatoric part as $\boldsymbol{\tau} - (1/3)\mathrm{tr}(\boldsymbol{\tau})\mathbf{I}$.

2.2.1.3 Governing equations for incompressible flows with free interfaces

This section discusses the governing equations for flows with free interfaces, starting with the jump condition at the interface. It then introduces the additional singular force required to incorporate the effects of surface tension into the momentum conservation equation.

In flows with free interfaces, it is often assumed that the interfaces have negligible thickness based on the continuum principle. Therefore, the hypothesis of sharp interfaces is commonly used (Tryggvason et al., 2011). To derive the jump conditions at the interface, conservation principles are applied. Starting with the mass conservation principle, the mass fluxes into and out of the interface must be equal. Since the interface has zero thickness, no mass accumulation can occur within it. In the case of incompressible fluids without a change of phase, the normal components of the velocity on each side of the interface, $u_{n1} = \mathbf{u}_1 \cdot \mathbf{n}$ and $u_{n2} = \mathbf{u}_2 \cdot \mathbf{n}$, are equal at the interface. Additionally, under the assumption of a no-slip condition at the interface for fluids with finite viscosity, the tangential components of the velocity for fluid 1 and fluid 2 are also equal. Thus, the interfacial condition for viscous fluids can be expressed as $\mathbf{u}_1 = \mathbf{u}_2$ (Tryggvason et al., 2011).

To account for the effects of surface tension, it is important to assess the stresses acting at the interface. Similar to the stress tensor $\mathbf{T}$, a surface tension tensor $\mathbf{T}_S^\sigma$ can also be defined. As the surface tension can be seen as a surface pressure, $\mathbf{T}_S^\sigma$ can be written as $\mathbf{T}_S^\sigma = \sigma\mathbf{I}_S$ (recalling that $-p\mathbf{I}$ is an isotropic tensor), where $\mathbf{I}_S$ is the surface identity tensor, defined as $\mathbf{I}_S = (\mathbf{I} - \mathbf{nn})$. It is the tangential projection of the three-dimensional identity tensor $\mathbf{I}$ on the surface. Its use is because surface tension acts only on the surface. Hence, the force on the edge of a small surface element can be written as $\mathbf{T}_S^\sigma \cdot \mathbf{q}$, where $\mathbf{q}$ is a unit vector tangent to the surface S and normal to the contour C of the element, as shown in Fig. 2.5.

Applying the surface identity tensor to the gradient operator results in the surface gradient operator $\nabla_S = (\mathbf{I} - \mathbf{nn}) \cdot \nabla$. It can be shown that $\nabla_S \cdot \mathbf{n} = \nabla \cdot \mathbf{n}$ and $\nabla_S \cdot \mathbf{I}_S = \kappa \mathbf{n}$. Detailed derivations of these results can be found in Appendix A of Tryggvason et al. (2011).

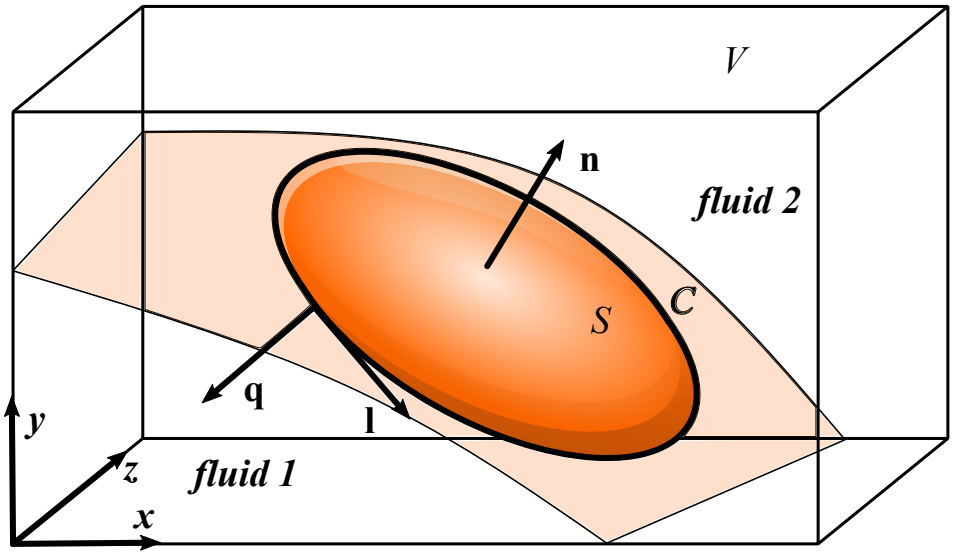

Figure 2.5: A small surface element S bounded by a closed contour C and inside a control volume V. The unit vectors $\mathbf{n}$, $\mathbf{l}$, and $\mathbf{q}$ directions are normal to S, tangent to S and C, and tangent to S and normal to C, respectively.

Now, performing a force balance in integral form on the control volume V involving the surface S in Fig. 2.5, and incorporating a term to account for the surface tension effect results in:

$$\int_V \rho \frac{D\mathbf{u}}{Dt}\, dV = \int_V \mathbf{f}\, dV + \int_S \mathbf{n} \cdot \mathbf{T}\, dS + \int_C \mathbf{T}_S^{\sigma} \cdot \mathbf{q}\, dl. \tag{2.13}$$

The last term on the right-hand side is the surface tension force exerted on perimeter C. It is important to note that if there is no interface present within the control volume, or in other words, excluding the last term on the right-hand side, the force balance expressed by Eq. 2.13 can be used as the starting point to derive Eq. 2.11 (Cauchy's equation for single-phase flows).

In case the thickness of the control volume tends to zero, the boundary of V tends to coincide with S, and Eq. 2.13 reduces to

$$\int_S \mathbf{n} \cdot \mathbf{T}\, dS + \int_C \sigma \mathbf{I}_S \cdot \mathbf{q}\, dl = 0. \tag{2.14}$$

By integrating the stress on each side of the interface separately, a stress jump across the interface can be obtained: $\mathbf{n} \cdot [\mathbf{T}] = \mathbf{n} \cdot \mathbf{T}_2 - \mathbf{n} \cdot \mathbf{T}_1$. The term involving the surface tension

can be rewritten using the Stokes Theorem as

$$\int_C \sigma \mathbf{I}_S \cdot \mathbf{q}\, dl = \int_S \nabla_S \cdot (\sigma \mathbf{I}_S)\, dS = \int_S \sigma \nabla_S \cdot \mathbf{I}_S + \mathbf{I}_S \cdot \nabla_S \sigma\, dS. \tag{2.15}$$

Since the integrand must vanish identically, Eq. 2.14 becomes

$$\mathbf{n} \cdot \mathbf{T}_1 - \mathbf{n} \cdot \mathbf{T}_2 = \sigma \nabla_S \cdot \mathbf{I}_S + \mathbf{I}_S \cdot \nabla_S \sigma, \tag{2.16}$$

which is a stress balance at the interface. This is equivalent to

$$\mathbf{n} \cdot \mathbf{T}_1 - \mathbf{n} \cdot \mathbf{T}_2 = \sigma \kappa \mathbf{n} + \nabla_S \sigma, \tag{2.17}$$

where the right-hand side is the surface force per unit area,

$$\mathbf{f}_\sigma = \sigma \kappa \mathbf{n} + \nabla_S \sigma. \tag{2.18}$$

Taking the dot product between Eq. 2.17 and the unit normal vector to the surface $\mathbf{n}$ results in a normal stress balance equation:

$$\mathbf{n} \cdot \mathbf{T}_1 \cdot \mathbf{n} - \mathbf{n} \cdot \mathbf{T}_2 \cdot \mathbf{n} = \sigma \kappa. \tag{2.19}$$

The term $\nabla_S \sigma \cdot \mathbf{n}$ is zero since $\nabla_S \sigma$ is parallel to the interface and $\mathbf{n}$ is perpendicular to the interface. Equation 2.19 states that a jump in normal stress across the interface is balanced by the curvature pressure. Now, taking the dot product between Eq. 2.17 and any unit tangent vector to the interface (*e.g.*, $\mathbf{q}$) yields a tangential stress balance equation:

$$\mathbf{n} \cdot \mathbf{T}_1 \cdot \mathbf{q} - \mathbf{n} \cdot \mathbf{T}_2 \cdot \mathbf{q} = \nabla_S \sigma \cdot \mathbf{q}. \tag{2.20}$$

The right-hand side represents the Marangoni stresses in the $\mathbf{q}$-direction associated with gradients in σ. The left-hand side includes only the terms of $\mathbf{T}$ associated with velocity gradients (non-diagonal), and thus any gradient of σ must always drive motion.

Rewriting Eq. 2.13 and applying the divergence theorem to the second term on the right-hand side and the Stokes theorem (*e.g.*, Eq. 2.15) and the properties of δ_S (*e.g.*, Eq. 2.7) to the third term on the right-hand, results in:

$$\int_V \rho \frac{D\mathbf{u}}{Dt}\, dV = \int_V \mathbf{f}\, dV + \int_V \nabla \cdot \mathbf{T}\, dV + \int_V \mathbf{f}_\sigma \delta_S\, dV. \tag{2.21}$$

Since V is arbitrary, the localization theorem applies and the integrand must vanish identi-

cally. Then, the "one-fluid" version of the Cauchy's equation can be written:

$$\rho\left(\frac{\partial \mathbf{u}}{\partial t} + \mathbf{u}\cdot\nabla\mathbf{u}\right) = \nabla\cdot\mathbf{T} + \mathbf{f} + \mathbf{f}_\sigma\delta_S. \tag{2.22}$$

The solution of Eq. 2.22 is valid for the whole domain. It is worth noting that the last term on the right-hand side is only non-zero at the interface.

Since the fluids generally have different densities, the density field ρ can be expressed as

$$\rho(\mathbf{x}) = \rho_1\mathcal{H}(\mathbf{x}) + \rho_2(1-\mathcal{H}(\mathbf{x})), \tag{2.23}$$

where ρ_1 and ρ_2 are the densities of fluids 1 and 2, respectively. The density field is updated by the advection of the marker function $\mathcal{H}(\mathbf{x})$ according to

$$\frac{\partial \mathcal{H}}{\partial t} + \mathbf{u}\cdot\nabla\mathcal{H} = 0. \tag{2.24}$$

Finally, for a constant surface tension coefficient, considering the gravitational force as the only body force, and writing the stress tensor as in Eq. 2.12, Eq. 2.22 becomes

$$\rho\left(\frac{\partial \mathbf{u}}{\partial t} + \mathbf{u}\cdot\nabla\mathbf{u}\right) = -\nabla p + \nabla\cdot\boldsymbol{\tau} + \rho\mathbf{g} + \sigma\kappa\mathbf{n}\delta_S. \tag{2.25}$$

2.2.2 Non-dimensional numbers for flows with free interfaces

Dimensional analysis in fluid mechanics is a valuable tool that helps to gain insights into flow behavior before extensive theoretical analyses or experiments are conducted. It also aids in visualizing trends from data that would otherwise be incoherent and disorganized (Fox and McDonald, 1998). This method aims to reduce the number and complexity of parameters that influence a given flow problem by grouping the dimensional variables into a smaller set of dimensionless variables. Generally, the number of reduced variables is equal to the number of distinct dimensions governing the problem (White, 1998). The resulting dimensionless numbers provide information about the relative significance of different forces governing the flow, and they can be used to establish scaling laws. Various dimensionless numbers with different interpretations can be obtained depending on the approach used for dimensional analysis. These numbers can be derived using techniques such as the Buckingham Pi-theorem or by non-dimensionalizing the governing equations through the use of scaling parameters.

Therefore, by scaling the forces per unit volume involved in the force balance in the equation of the momentum conservation (*e.g.*, Eq. 2.25), dimensionless numbers that govern

flows with free interfaces can be obtained. Consider, for example, the case of a bubble rising in a Newtonian liquid. The balance force is composed of inertial, viscous, buoyancy, and surface tension forces. The inertial forces per unit of area (using a stress scale) can be scaled as ρU^2, where ρ is the surrounding fluid density and U is a characteristic velocity, here the bubble rising velocity. The viscous stresses can be scaled as $\eta U/D$, where η is the surrounding fluid viscosity, and D is a characteristic length, which here is the bubble diameter. The buoyancy force per unit of area scales as $|\Delta\rho|gD$, where $|\Delta\rho|$ is the difference between the density of the surrounding and the density of the bubble, and g is the acceleration of gravity. Lastly, the surface tension force per unit of area can be scaled as σ/D, where σ is the surface tension coefficient.

The division of the scaled forces by each other forms dimensionless numbers that give a measure of the relative significance of each force to the flow. For example, the ratio of inertial to viscous forces gives the Reynolds number, Re:

$$Re = \frac{\rho DU}{\eta}, \tag{2.26}$$

while the ratio of inertial to surface tension forces gives the Weber number, We:

$$We = \frac{\rho DU^2}{\sigma}. \tag{2.27}$$

The ratio of the viscous to capillary stresses results in the capillary number, Ca:

$$Ca = \frac{\eta U}{\sigma}, \tag{2.28}$$

and the ratio of viscous stresses of both phases is described by the viscosity ratio, η_r:

$$\eta_r = \frac{\eta_b}{\eta}, \tag{2.29}$$

where η_b is the viscosity of the fluid composing the bubble.

For relatively large bubbles (and drops) in low-viscosity liquids, the dominant force counteracting the buoyancy force is the inertial force. In this scenario, a characteristic velocity can be defined as $U = \sqrt{(|\Delta\rho|/\rho)gD}$. By substituting this velocity definition into Eq. 2.26 and Eq. 2.27, the resulting dimensionless numbers are known as the Archimedes number, Ar, representing the ratio of buoyancy to viscous forces, and the Bond number, Bo, representing the ratio of buoyancy to surface tension force, respectively:

$$Ar = \frac{\sqrt{\rho|\Delta\rho|gD^3}}{\eta}, \tag{2.30}$$

$$Bo = \frac{|\Delta\rho| g D^2}{\sigma}. \tag{2.31}$$

In the case of rising bubbles where $\Delta\rho \to \rho$ (the density of the gas phase of the bubble is negligible), the characteristic velocity becomes $U = \sqrt{gD}$ and the Archimedes number is now called the Galilei number,

$$Ga = \frac{\rho\sqrt{gD^3}}{\eta}. \tag{2.32}$$

For relatively small bubbles in high-viscosity liquids, the dominant force opposing the buoyancy force is the viscous force. Balancing these two forces allows for the definition of a characteristic viscosity defined as $\eta_c = |\Delta\rho| g D^2/U$. Replacing η_c into Eq. 2.26 results in the Froude number, Fr, which expresses the ratio of inertial to buoyancy forces.

$$Fr = \frac{\rho U^2}{|\Delta\rho| g D}. \tag{2.33}$$

2.2.3 Advecting a fluid interface numerically

The numerical solution of interfacial flows presents two primary challenges. The first challenge involves accurately advecting or updating the position of the interface as it moves with the fluids. The second challenge involves calculating and appropriately incorporating the surface tension force into the momentum equation. This section addresses the first challenge, while the next section will focus on the second challenge.

In the one-fluid formulation, a single set of equations is solved on a fixed grid throughout the entire computational domain. The multiphase system is treated as a single fluid with variable properties, and the effects of surface tension are introduced as a force per unit volume. It is important to note that the individual flows in each phase are not solved separately and then coupled together. Instead, a marker function is employed to identify the different fluids within the computational domain. This marker function can be a material property such as density or viscosity. Another example is the Heaviside function $\mathcal{H}$ introduced in Sec. 2.2.1.1, which was used in Eq. 2.23 (Sec. 2.2.1.3) to distinguish the regions in the domain occupied by fluid 1 with density ρ_1 and fluid 2 with density ρ_2. In the current context, a numerical approximation of $\mathcal{H}$, the volume fraction (or color function), c, is employed, and its role is only to identify, or mark, the different fluids. c is defined as the average value of $\mathcal{H}$ in a given grid cell. Thus, for cells that do not contain an interface, $c = 1$ (indicating a filled cell) or 0 (indicating an empty cell), while $0 < c < 1$ represents interfacial cells. As the fluids move, the scalar field c evolves with them. The volume fraction field can be updated by directly advecting it, or by advecting an auxiliary field, which is subsequently used to determine c.

Some of the most widely used methods for addressing this challenge are the Volume-Of-Fluid (VOF), Level-Set (LS), and Front-Tracking (FT). In the VOF method, c is advected directly, whereas the LS and FT methods employ auxiliary fields in the advection process.

2.2.3.1 The Volume-of-Fluid method

The advection equation for the volume fraction c can be expressed by

$$\frac{\partial c}{\partial t} + \nabla \cdot (c\mathbf{u}) = 0. \tag{2.34}$$

Equation 2.34 does not contain a dissipative term, and hence the function c should only be transported by the flow without any diffusion. Therefore, any initial discontinuity present in c is propagated over time ($t > 0$) without introducing additional diffusion or oscillations in the function. Despite its apparent simplicity, the numerical solution of Eq. 2.34 is not straightforward (Fortuna, 2012). Advecting a sharp interface numerically is surprisingly difficult. This section initially addresses the numerical solution of Eq. 2.34 using standard schemes. Subsequently, it introduces the concept of numerical schemes based on the Volume-Of-Fluid (VOF) method.

Figure 2.6 presents a schematic representation of a one-dimensional domain with an interface illustrated by the function $\mathcal{H}$ (red line). The interface is numerically approximated by the function c, which is advected by an incompressible flow of constant velocity u from left to right. The grid cell has a volume of $\Delta x = x_{\mathsf{i}+1/2} - x_{\mathsf{i}-1/2}$, with a unity face area. Both $\mathcal{H}$ and c are equal to 1 in a cell completely filled with fluid 1 (a full cell) and equal to 0 in a cell completely filled with fluid 2 (an empty cell). The interface is located in the cells where $\mathcal{H}$ changes abruptly from 1 to 0 and where $0 < c < 1$. In Eq. 2.34, the quantity $F = c\mathbf{u}$ is the flux of c through the boundaries (faces) of the control volume (grid cell). Thus, Eq. 2.34 states that the net flux of c through the boundaries (faces) of the grid cell i, $x_{\mathsf{i}-1/2}$ and $x_{\mathsf{i}+1/2}$, is equal to the rate of change of c inside the cell.

Using a first-order time-discretisation explicit scheme, Eq. 2.34 can be written in a discrete version as:

$$c_{\mathsf{i}}^{\mathsf{n}+1} = c_{\mathsf{i}}^{\mathsf{n}} + \frac{\underline{\Delta}t}{\underline{\Delta}x}\left(c_{\mathsf{i}-1/2}^{\mathsf{n}} u_{\mathsf{i}-1/2}^{\mathsf{n}} - c_{\mathsf{i}+1/2}^{\mathsf{n}} u_{\mathsf{i}+1/2}^{\mathsf{n}}\right), \tag{2.35}$$

where $\underline{\Delta}t$ is the timestep and n is the current time step. The quantities $F_{\mathsf{i}-1/2}^{\mathsf{n}} = c_{\mathsf{i}-1/2}^{\mathsf{n}} u_{i-1/2}^{n}$ and $F_{\mathsf{i}+1/2}^{\mathsf{n}} = c_{\mathsf{i}+1/2}^{\mathsf{n}} u_{\mathsf{i}+1/2}^{\mathsf{n}}$ are the fluxes of c through the left and right boundaries of cell i, respectively. Since the fluxes leaving one cell equals the flux entering the next cell, this algorithm is discretely conservative. Also, the time step should obey the Courant-Friedrich-Lewy (CFL) condition: $\underline{\Delta}t \leq \underline{\Delta}x/u$. Now, the value of c on the cell faces needs to be

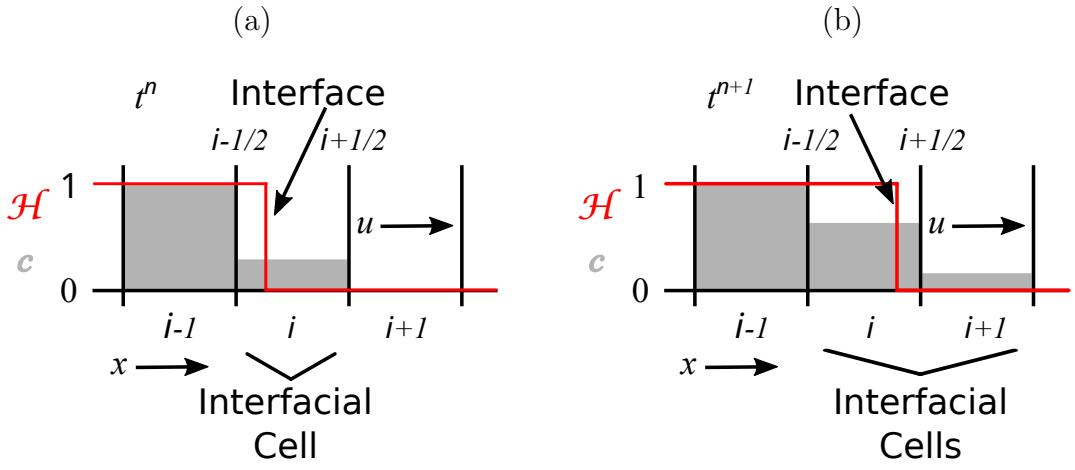

Figure 2.6: One-dimensional advection of an interface represented by the Heaviside function $\mathcal{H}$ (red line) and by the volume fraction c (grey area) at time step (a) n and (b) $\mathsf{n}+1$.

determined to compute the fluxes.

First, if the value of $c_{\mathsf{i}+1/2}$ is taken as the value of c in the center of the left cell, $c_{\mathsf{i}+1/2} = c_{\mathsf{i}}$, one obtains the first-order Upwind advection scheme. Since the flow moves from left to right, the value of c in the cell on the left side is chosen. As shown in Fig. 2.6(b), this choice results in a flux of c from cell i to cell $\mathsf{i}+1$, given by $F_{\mathsf{i}+1/2} = c_{\mathsf{i}}u$, before the actual interface, represented by the jump in $\mathcal{H}$, crosses the boundary between the two cells. As the advection progresses, a small amount of c leaks into cell $\mathsf{i}+2$ at $t^{\mathsf{n}+2}$ and so on. Although the first-order Upwind scheme is highly stable and unconditionally bounded ($0 \leq c \leq 1$), it introduces numerical diffusion, widening the interface thickness as the solution evolves over time (Versteeg and Malalasekera, 2007).

An alternative is to employ a higher-order scheme for advecting the volume fraction. For example, a centered advection scheme sets $c_{\mathsf{i}+1/2} = (c_{\mathsf{i}} + c_{\mathsf{i}+1})/2$, which achieves second-order accuracy. However, this second option produces oscillations with increasing amplitude in the values of c, even though it is a second-order scheme. Additionally, the scheme is not unconditionally bounded.

A third possibility is to use a second-order upwind scheme, where $c_{\mathsf{i}+1/2} = c_{\mathsf{i}} + (c_{\mathsf{i}} - c_{\mathsf{i}-1})/2$. Nevertheless, this scheme still generates oscillations and numerical diffusion, albeit to a lesser extent compared to the second-order centered scheme and the first-order upwind scheme, respectively.

Another higher-order schemes can be developed by using slope-limiter, $\phi(\mathsf{r})$, and write $c_{\mathsf{i}+1/2} = c_{\mathsf{i}} + \phi(\mathsf{r})(c_{\mathsf{i}} - c_{\mathsf{i}-1})/2$, where $\mathsf{r} = (c_{\mathsf{i}} - c_{\mathsf{i}-1})/(c_{\mathsf{i}+1} - c_{\mathsf{i}})$. The function $\phi(\mathsf{r})$ assigns weight to the values of c in the neighboring cells during the computation of $c_{\mathsf{i}+1/2}$. Various choices for $\phi(\mathsf{r})$ exist, often based on empirical considerations. By carefully selecting slope

limiters that satisfy specific conditions, higher-order numerical schemes can be constructed to yield oscillation-free solutions (Sweby, 1984). These schemes possess the desirable property of monotonicity preservation, meaning they do not introduce new undershoots or overshoots in the solution or exacerbate existing ones. Consequently, the total variation of the discrete solution should decrease over time, giving rise to Total Variation Diminishing (TVD) schemes. TVD schemes can also incorporate artificial diffusion components to counteract the tendency for oscillations (Versteeg and Malalasekera, 2007).

Some options for slope limiters are the "minmod" and "van Leer" limiters. The minmod slope limiters are the same ones used in the widely employed second-order Essentially Non-Oscillatory (ENO) scheme for higher dimensions (Tryggvason et al., 2011). On the other hand, the Bell-Collela-Glaz scheme extends the van Leer scheme to multiple dimensions and incorporates second-order time discretization. This scheme is employed in software such as Basilisk and Gerris for the advection of diffusive tracers and in the solution of the momentum equation (Popinet, 2009). Although these slope limiters can significantly reduce numerical diffusion and eliminate oscillations, the sharpness of the interface is compromised (spans over more than one cell), and the solution tends to deteriorate in long-time simulations (Tryggvason et al., 2011).

As evident, advecting c directly is not a trivial task, and standard schemes, even the higher-order TVD schemes, fail to produce satisfactory results due to the way the fluxes of c are calculated. Different from these standard schemes, the Volume-of-Fluid method utilizes the interface's own position (*e.g.*, the interface geometry) to calculate the fluxes of c across cell faces. For example, in Fig. 2.6, the interface position is defined by the discontinuity of $\mathcal{H}$. Suppose $c_{\mathsf{i}} = 0.25$ at t^{n} in Fig. 2.6(a), and hence, the step in $\mathcal{H}$ is located at a distance $\underline{\Delta}x/4$ from the face $x_{\mathsf{i}-1/2}$. This implies that the value of c can be used to determine the interface position, x_{I}, using geometrical considerations. By calculating the advancement of the discontinuity within one time step, it becomes possible to precisely determine the flux of c through cell faces and reevaluate the positions of the $\mathcal{H}$ discontinuity. For example, the inward flux into cell i through the left face ($x_{\mathsf{i}-1/2}$) is clearly equal to u (since $c_{\mathsf{i}-1} = 1$). However, while the step in $\mathcal{H}$ has not reached the right face ($x_{\mathsf{i}+1/2}$), as shown in Fig. 2.6(b), the flux of c through that face is zero. On the other hand, if the distance traveled by the interface within one time step $\underline{\Delta}t$ is greater than $x_{\mathsf{i}+1/2} - x_{\mathtt{I}}$ (or $(1-c_{\mathsf{i}})\underline{\Delta}x$), $F_{\mathsf{i}+1/2} < 0$ (c is leaving the cell). The flux on the right face can be computed as:

$$F_{\mathsf{i}+1/2} = \begin{cases} 0 & \text{if} \quad \underline{\Delta}t \leq (1-c_{\mathsf{i}})\dfrac{\underline{\Delta}x}{u}, \\ (1-c_{\mathsf{i}})\dfrac{\underline{\Delta}x}{\underline{\Delta}t} - u & \text{if} \quad \underline{\Delta}t > (1-c_{\mathsf{i}})\dfrac{\underline{\Delta}x}{u}. \end{cases} \tag{2.36}$$

This formulation utilizes the fact that c is discontinuous and bounded between zero and one. Due to the fluxes of c in and out of grid cells, the Volume-of-Fluid method naturally handles topology changes such as coalescence and breakup. As a matter of fact, the method has to be modified if the desire is to avoid topology changes. For one-dimensional incompressible flows, the scheme in Eq. 2.36 for advecting c is exact. It is conservative and non-diffusive, and the interface thickness is restricted to one cell. However, its extrapolation to higher dimensions is not straightforward (Tryggvason et al., 2011).

One way to use the above scheme in higher dimensions is to perform advection using the flux given by Eq. 2.36 in each direction separately. In two dimensions, the interface is represented by a pair of lines perpendicular to each other and aligned with the coordinate system (x, y), as exhibited in Fig. 2.7(a). The red line is parallel to the x-direction and the green line is parallel to the y-direction. The line parallel to the y direction is reconstructed based on the flux of c in the x-direction, and vice versa. This method is known as the Simple Line Interface Calculation (SLIC) method. Although the scheme is non-diffusive and conservative, it often generates a considerable amount of "flotsam" and "jetsam" (break away of pieces of interfaces in an unphysical way). Additionally, the SLIC method is only first-order accurate in space because it cannot reconstruct an interface at arbitrary angles (Tryggvason et al., 2011).

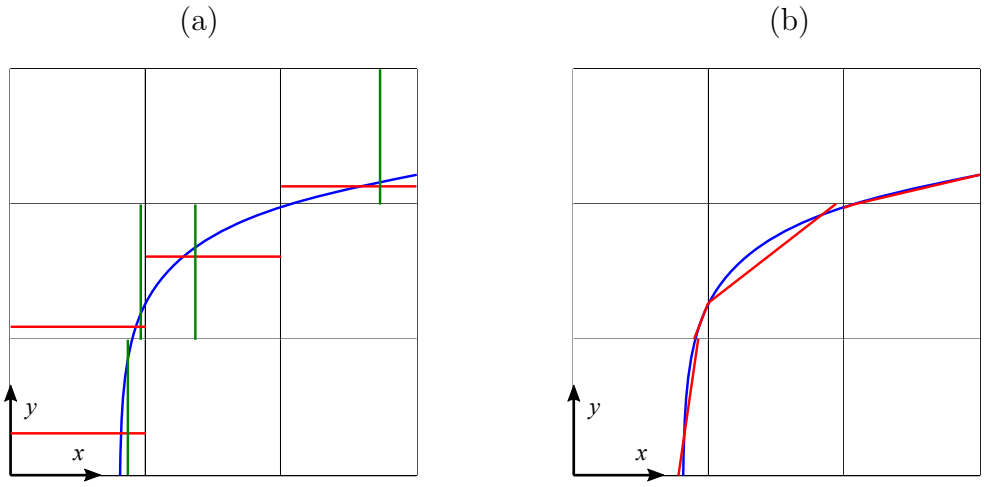

Figure 2.7: Illustration of an interface (blue line) represented using the SLIC method (a) and the PLIC method (b).

By using the value of c in a given cell and its neighboring cells, it is possible to reconstruct and represent an interface by a single straight line at an arbitrary angle (thus achieving second-order accuracy in space) relative to the coordinate system in each cell. This method is known as the Piecewise Linear Interface Calculation (PLIC) method, and it is exemplified

in Fig. 2.7(b), where the interface is approximated by straight red lines. The line segments do not need to be continuous across cell boundaries. As can be observed, the PLIC method provides a better representation of the interface compared to the SLIC method. The line segment can be locally described by the equation:

$$\mathbf{m}_{\mathsf{i},\mathsf{j}} \cdot \mathbf{x} = \alpha_{\mathsf{i},\mathsf{j}}, \tag{2.37}$$

where $\mathbf{m}_{\mathsf{i},\mathsf{i}}$ is a local unit normal vector to the line segment calculated numerically, and $\alpha_{\mathsf{i},\mathsf{i}}$ determines the location of the line segment in the direction of $\mathbf{m}_{\mathsf{i},\mathsf{i}}$. The subscripts i and j correspond to the cell indices in the x and y directions, respectively. The interface location is thus a function of $\mathbf{m}_{\mathsf{i},\mathsf{j}}$ and $\alpha_{\mathsf{i},\mathsf{j}}$. Fig. 2.8 exhibits an interface represented by a straight line in a grid cell with $c_{\mathsf{i},\mathsf{j}} = 0.4$. The line segment is perpendicular to the vector $\mathbf{m}_{\mathsf{i},\mathsf{j}}$. If the volume fraction increases and $\mathbf{m}_{\mathsf{i},\mathsf{j}}$ retains its direction, the line element should slide along the dashed line (in the same direction as $\mathbf{m}_{i,j}$) in order to increase the portion of the cell filled with the marker functions c. If the volume fraction decreases, the line segment should slide in the opposite direction. By using geometrical considerations, the value of $\alpha_{\mathsf{i},\mathsf{j}}$ is adjusted so that the percentage of the volume of the cell filled with the color function is equal to the value of c in the cell. For more details, refer to Tryggvason et al. (2011). The local unit normal vector $\mathbf{m}_{\mathsf{i},\mathsf{j}}$ can be calculated as in Eq. 2.3, but using a numerical discrete gradient operator, ∇_h, and using the volume fraction c instead of $\mathcal{L}$:

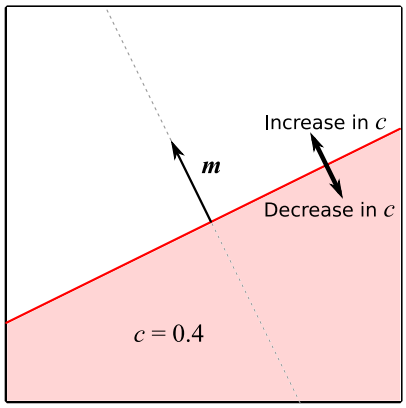

Figure 2.8: Orientation and location of a line segment used in the PLIC method to represent an interface. The line segment is perpendicular to $\mathbf{m}$ and its location is determined by the value of α in order to adjust the value of c in the cell.

$$\mathbf{m}_{\mathsf{i},\mathsf{j}} = -\frac{\nabla_h c_{\mathsf{i},\mathsf{j}}}{|\nabla_h c_{\mathsf{i},\mathsf{j}}|}, \tag{2.38}$$

where a discrete approximation for $\nabla_h c_{\mathsf{i},\mathsf{j}}$ in two dimensions is

$$\nabla_h c_{\mathsf{i},\mathsf{j}} = \frac{1}{2\underline{\Delta}x} \begin{pmatrix} c_{\mathsf{i}+1,\mathsf{j}} - c_{\mathsf{i}-1,\mathsf{ij}} \\ c_{\mathsf{i},\mathsf{j}+1} - c_{\mathsf{i},\mathsf{j}-1} \end{pmatrix}. \tag{2.39}$$

However, due to the discontinuous nature of c, the ∇_h operator is not consistent (does not converge with spatial resolution) as it would when applied to a smooth function like $\mathcal{L}$.

Now, with the interface represented by a line segment (specified by $\mathbf{m}$ and α), the flux of c through the boundaries of a grid cell can be calculated by using geometric considerations, such as the area of triangles. For example, consider a 2D interface being advected by a uniform flow (one-dimensional advection), as shown in Fig. 2.9. The amount of c that flows through face $x_{\mathsf{i}+1/2}$ from cell i to cell $\mathsf{i}+1$ in one time step $\underline{\Delta}t$ is equal to the red area in cell $\mathsf{i}+1$.

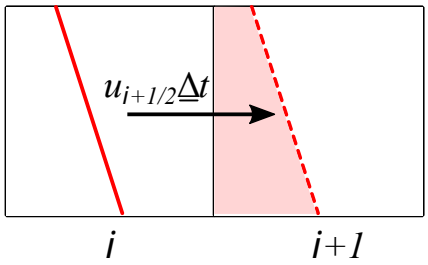

Figure 2.9: Illustration of the flux of c in one-dimensional advection using the PLIC method for interface representation.

For two-dimensional flows, the one-dimensional scheme of Eq. 2.35 can be written as:

$$c_{\mathsf{i},\mathsf{j}}^{\mathsf{n}+1} = c_{\mathsf{i},\mathsf{j}}^{\mathsf{n}} + \frac{\underline{\Delta}t}{\underline{\Delta}x} \left(F_{\mathsf{i}-1/2,\mathsf{j}} - F_{\mathsf{i}+1/2,\mathsf{j}} + F_{\mathsf{i},\mathsf{j}-1/2} - F_{\mathsf{i},\mathsf{j}+1/2} \right). \tag{2.40}$$

The scheme is conservative by construction; however, it will not guarantee that c remains bounded between zero and one since transverse or diagonal fluxes are not computed correctly. To enforce the boundedness of the volume fraction, excess volume fraction can be removed, but this approach leads to a loss of mass conservation. Advanced and more complex schemes have been developed to address this issue. Discussing these schemes is beyond the scope of this literature review. Interested readers are referred to Tryggvason et al. (2011) for further information.

It is evident that the accuracy of VOF methods is closely tied to interface reconstruction, specifically the determination of the interface's normal vector and position. Additionally, an appropriate interface reconstruction is crucial for calculating the interface curvature, which is later used in computing the surface tension term. In VOF methods, these quantities are

directly obtained from the volume fraction.

For smooth functions such as the Level-Set function $\mathcal{L}$ (more details on the Level-Set method in the next section), Eqs. 2.3 and 2.4 can be employed to calculate $\mathbf{n}$ and κ. The discretization can be accomplished using standard finite difference operators, and higher-order numerical schemes can be formulated (Tryggvason et al., 2011). An alternative is to utilize a smoothed or filtered version of the function c, denoted as $\tilde{c}$. However, simple filtering methods do not generally yield satisfactory results; for instance, the estimation of curvature fails to converge with grid resolution. An alternative approach involves approximating the smoothed functions using the Level-Set function $\mathcal{L}$, leading to the development of the CLSVOF (coupled Level-Set VOF) method, which tends to produce favorable outcomes. Nonetheless, this introduces complexity to the method and may result in a loss of accuracy and consistency when transitioning between the methods (Popinet, 2018).

It is worth noting that the geometric parameters of the interface can also be computed using a Height Function (HF), as expressed in Eq. 2.8 and 2.9, for the interface normal and curvature, respectively. The Height Function $\mathtt{h}$ can be directly constructed from the distribution of c and allows for accurate calculations of $\mathbf{n}$ and κ. The first and second derivatives of $\mathtt{h}$, respectively, can be numerically approximated as follows:

$$\mathtt{h_i}_x = \frac{\mathtt{h_{i+1}} - \mathtt{h_{i-1}}}{2\Delta x} + O(\Delta x^2), \tag{2.41}$$

and

$$\mathtt{h_i}_{xx} = \frac{\mathtt{h_{i+1}} - 2\mathtt{h_i} + \mathtt{h_{i-1}}}{\Delta x^2} + O(\Delta x^2). \tag{2.42}$$

These approximations are second-order accurate and can be made higher-order by employing a wider stencil.

For an interfacial cell, the value of $\mathtt{h}$ can be calculated by

$$\mathtt{h_i} = c_{\mathtt{i,j}}\Delta x + y_{\mathtt{i,j}-1/2}, \tag{2.43}$$

which is equivalent to

$$\mathtt{h_i} = \Delta x \sum_j c_{\mathtt{i,j}}. \tag{2.44}$$

In case the interface can not be represented by a single-valued function, the height function can be calculated locally, and the sum in Eq. 2.44 can also be performed in the x-direction, instead of the y-direction:

$$\mathtt{h_j} = \Delta y \sum_i c_{\mathtt{i,j}}. \tag{2.45}$$

This is illustrated in Fig. 2.10, where $\mathtt{h}$ is calculated as $\mathtt{h}_i = 2.5$ for the cell in the top/right

corner of the stencil and as $\mathtt{h}_j = 2.2$ for the cell in the bottom/left corner of the stencil. The choice between x-direction and y-direction is based on the alignment of the interface with the respective direction. For further details on the use of the Height Function (HF) method, please refer to Tryggvason et al. (2011).

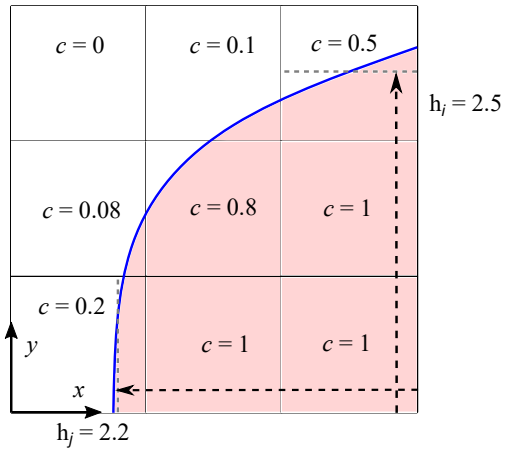

Figure 2.10: Calculation of $\mathtt{h}$ in a cell with a roughly horizontal interface orientation (top/right corner) and in a cell with a roughly vertical interface orientation (bottom/left corner).

2.2.3.2 The Level-Set method

The interface position can also be defined implicitly using a smooth Level-Set function $\mathcal{L}(\mathbf{x}, t)$, which is positive in one fluid and negative in the other. The interface is located where $\mathcal{L}(\mathbf{x}) = 0$, as depicted in Fig. 2.11.

As $\mathcal{L}$ evolves with the fluids, its motion can be described by

$$\frac{\partial \mathcal{L}}{\partial t} + \mathbf{u} \cdot \nabla \mathcal{L} = 0.$$

That is, $\mathcal{L}$ is advected by the flow as an ordinary tracer. Discretization of $\mathcal{L}$ can be performed using standard techniques such as TVD schemes and appropriate data structures. The new position of the interface $x_{\mathtt{I}}^{\mathtt{n}+1}$ is obtained from the location where $\mathcal{L} = 0$ after being advected. Then, c can be determined using an equation of the form (Sussman et al., 1994; Engquist et al., 2005):

$$c = \begin{cases} 1 & \text{if} \quad \mathcal{L} > \alpha_{\mathcal{L}} \underline{\Delta} x; \\ \frac{1}{2}\left[1 + \mathcal{L}/\alpha_{\mathcal{L}}\underline{\Delta}x + \frac{1}{\pi}\sin(\pi\mathcal{L}/\alpha_{\mathcal{L}}\underline{\Delta}x)\right] & \text{if} \quad |\mathcal{L}| \leq \alpha_{\mathcal{L}}\underline{\Delta}x; \\ 0 & \text{if} \quad \mathcal{L} < -\alpha_{\mathcal{L}}\underline{\Delta}x. \end{cases} \tag{2.46}$$

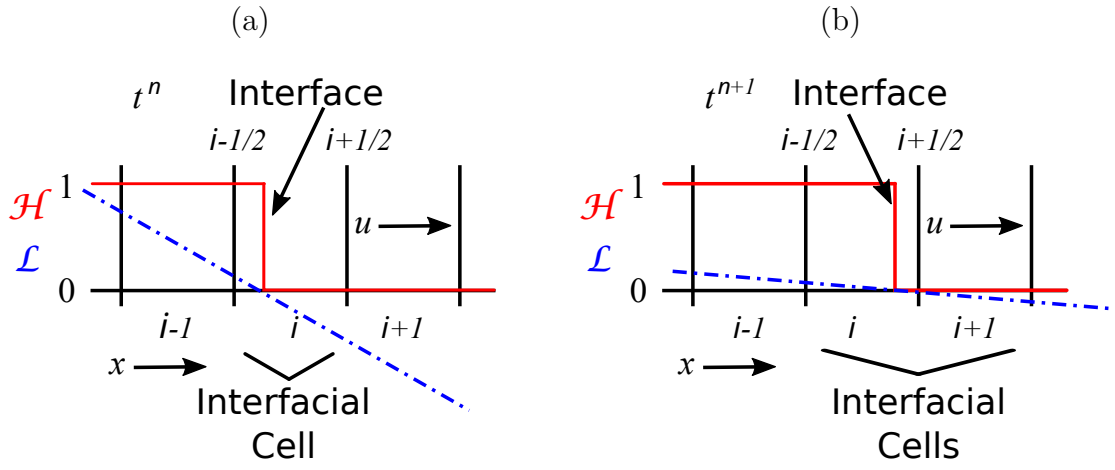

Figure 2.11: One-dimensional advection of an interface represented by the Heaviside function $\mathcal{H}$ (red line) and by a Level-Set function $\mathcal{L}$ (blue dashed dotted line) at time step (a) n and (b) $\mathsf{n}+1$.

Here, $\alpha_{\mathcal{L}}$ is an empirical coefficient, typically set to three. In the case of using Eq. 2.46, c is smoothed across the interface, which has a thickness of $2\alpha_{\mathcal{L}}\underline{\Delta}x$.

The Level-Set model naturally handles topology changes, allowing for accurate representation of complex interface dynamics. It is important to note that throughout the simulation, $\mathcal{L}$ does not necessarily need to be a distance function, but it must be equal to zero at the interface. Choosing $\mathcal{L}$ to be a smooth function enables more accurate advection compared to the volume fraction c when using the standard schemes discussed in Section 2.2.3.1. Furthermore, since the interface is located where $\mathcal{L}=0$, the numerical diffusion during the advection process does not affect the sharpness of the interface. However, as the simulation progresses the gradient of $\mathcal{L}$ in the interface region can become smaller, as exemplified in Fig. 2.11 (b), leading to imprecise determination of the interface position $x_{\mathtt{I}}$. In other words, although the interface is sharp, its locations may be inaccurate, resulting in a violation of the mass conservation principle and incorrect estimations of the interface curvature (Popinet, 2018). To mitigate this issue, re-initializing $\mathcal{L}$ can be performed, but it comes at the cost of increased complexity for the method.

2.2.3.3 The Front-Tracking method

In the Front-Tracking method, the interface is treated as a collection of material particles that are transported by the flow with velocity $dx_{\mathtt{I}}(t)/dt = u$, where $x_{\mathtt{I}}(t)$ is the interface position. This approach utilizes a Lagrangian representation of the interface. The volume

fraction field can be constructed using the interface position as follows:

$$c_{\mathrm{i}} = \begin{cases} 1 & \text{if} \quad x_{\mathrm{i}+1/2} \leq x_{\mathtt{I}}; \\ \frac{x_{\mathtt{I}} - x_{\mathrm{i}-1/2}}{x_{\mathrm{i}+1/2} - x_{\mathrm{i}-1/2}} & \text{if} \quad x_{\mathrm{i}-1/2} \leq x_{\mathtt{I}} \leq x_{\mathrm{i}+1/2}; \\ 0 & \text{if} \quad x_{\mathrm{i}-1/2} \geq x_{\mathtt{I}}. \end{cases} \tag{2.47}$$

This formulation can be extended to higher dimensions by employing a finite number of material particles on the interface. The position of each particle is updated according to $d\mathbf{x}_{\mathtt{I}}^{k}/dt = \mathbf{u}$, which can be discretized and solved with high accuracy. After updating the position of all k particles, the volume fraction field can be reconstructed. Figure 2.12 illustrates an interface defined by connected points that separate two fluids in a two-dimensional domain.

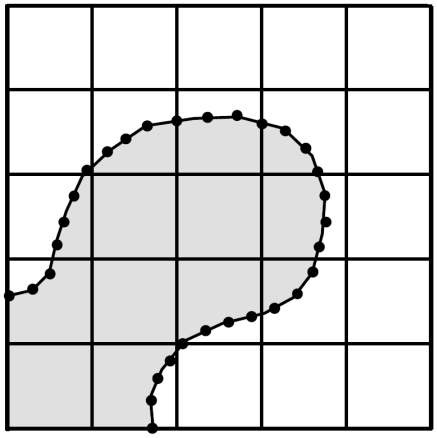

Figure 2.12: An interface represented by connected points (Front-tracking method) separating two fluids.
Source: Tryggvason et al. (2011)

Front-Tracking methods also have some drawbacks. As the interface position evolves, the distribution of particles along the interface may become uneven, potentially compromising the resolution of the interface in certain regions. To address this issue, periodic redistribution of particles along the interface is necessary, which adds complexity to the method implementation. Additionally, changes in topology such as breakup and coalescence do not occur naturally in the Front-Tracking method and require further modifications, increasing the overall complexity of the approach.

2.2.4 Calculating the surface tension force

Besides advecting an interface, it is also important to calculate and include surface tension as a force per unit volume in the momentum equation. In the continuous version of the momentum equation, Eq. 2.25, this was accomplished by the last term on its right-hand side:

$$\mathbf{f}_\sigma = \sigma\kappa\mathbf{n}\delta_S. \tag{2.48}$$

Integrating Eq. 2.48 over the control volume and using the properties of δ_S results in:

$$\sigma \int_V \kappa\mathbf{n}\delta_S \, dV = \sigma \int_S \kappa\mathbf{n} \, dS. \tag{2.49}$$

In a two-dimensional domain, the surface becomes a line, and the Frenet–Serret formulae,

$$\kappa\mathbf{n} = \frac{d\mathbf{q}}{dl}, \tag{2.50}$$

where $\mathbf{q}$ is a vector tangent to the interface and dl is an increment in the arc length, can be used to rewrite Eq. 2.49 as:

$$\sigma \int_C \kappa\mathbf{n} \, dl = \sigma \int_C d\mathbf{q}. \tag{2.51}$$

The integral on the right-hand side of Eq. 2.51 becomes:

$$\sigma \int_A^B d\mathbf{q} = \sigma(\mathbf{q}_B - \mathbf{q}_A). \tag{2.52}$$

Here, A and B are two points on the faces $x_{\mathrm{i}+1/2,\mathrm{j}}$ and $x_{\mathrm{i}-1/2,\mathrm{j}}$, respectively, of a grid cell, as shown in Fig. 2.13. Thus, Eq. 2.52 states that the geometry of the endpoints can be used to determine the net force resulting from the curvature pressure.

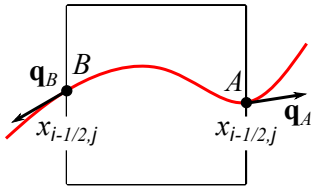

Figure 2.13: Surface tension representation as a tangential force to an interface, which is represented by a line in 2D.

This formulation is momentum-conserving since the surface tension force acting on the border of the neighboring cell has an equal magnitude but opposite sign. For a closed contour, the net force due to surface tension is zero. This formulation can easily be extended

for non-constant surface tension by specifying the values of σ at points A and B. It can also render good results when used in conjunction with the Front-Tracking and Level-Set methods. However, its effectiveness is limited when used with the Volume-of-Fluid (VOF) method. This is because the piecewise-linear representation of the interface in VOF is discontinuous, resulting in interface tangents with different directions between neighboring cells, and thus the surface tension force does not cancel out.

In the case of working with the Volume-of-Fluid method, Eq. 2.49 can be rewritten using the definition of Eq. 2.6, and then be approximated in a discrete form as:

$$\sigma \int_V \kappa \mathbf{n} \delta_S \, dV = -\sigma \int_V \kappa \nabla c \, dV \approx -\sigma \underline{\Delta} x^2 \kappa_{\mathtt{i}} \nabla_h c_{\mathtt{i}} \tag{2.53}$$

This formulation is known as the Continuum-Surface-Force (CSF) method, first proposed by Brackbill et al. (1992). The discrete versions of the interface curvature, $\kappa_{\mathtt{i}}$, can be computed from $c_{\mathtt{i}}$ using a discrete version of Eq. 2.4 (the divergence of $\mathbf{n}$) or Eq. 2.9 (the HF function). However, it is important to note that this formulation is no longer momentum-conserving, and the approximation of the gradient of c by $\nabla_h c_{\mathtt{i}}$ (Eq. 2.39) does not present good convergence properties with spatial resolution.

It is important for discrete numerical methods to be well-balanced, meaning that they accurately reproduce specific equilibrium results of the continuous equations. Take, for example, the case of an equilibrium droplet, which is static and spherical. In this scenario, the stress equations (Eq. 2.25) reduces to:

$$\nabla p = \sigma \kappa \mathbf{n} \delta_S \tag{2.54}$$

The pressure jump across the interface, $[p_{\mathtt{I}}]$, is precisely balanced by the curvature pressure $\sigma\kappa$, where both σ and κ are constant. However, the discretization of Eq. 2.54 with a second-order accuracy scheme can be written as

$$\nabla_{h,\mathtt{p}} p_{\mathtt{i}} + O_{\mathtt{p}}(\Delta x^2) = -\sigma \kappa \nabla_{h,\sigma} c_{\mathtt{i}} + O_\sigma(\Delta x^2). \tag{2.55}$$

However, the equilibrium solution of Eq. 2.54 is not recovered in this case. This discrepancy arises because the discretization of each side of the equation employs different numerical schemes. For example, the gradient of pressure is calculated at the cell faces (mid-points), while the gradient of volume fraction is computed at the cell centers (Popinet, 2018). Consequently, the truncation errors $O_{\mathtt{p}}(\Delta x^2)$ and $O_\sigma(\Delta x^2)$ do not cancel out as they behave differently. This issue persists even when a discrete version of the formulation in Eq. 2.52 is used for the surface tension term. As a consequence, Eq. 2.55 is not well-balanced and an

equilibrium solution is not achieved. This leads to the emergence of spurious currents, where the velocity field is purely numerical. For low values of the Capillary number (high surface tension force and low viscous dissipation), the spurious currents can be strong enough to cause the breakup of the drop. Figure 2.14 illustrates a velocity field developed solely due to numerical effects around a spherical drop.

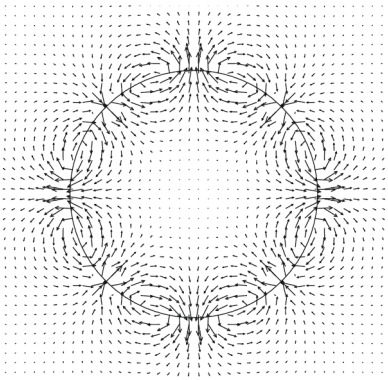

Figure 2.14: Spurious currents in a static spherical droplet.
Source.: Popinet (2009).

To achieve a well-balanced model, it is necessary to discretize both the pressure and volume fraction gradients using the same discrete operator, denoted as ∇_h. Furthermore, aspects such as curvature estimation, time integration, and projection methods, among others, also influence the method's ability to reach an equilibrium solution. In practical situations, the curvature κ is estimated based on the interface geometry, as discussed in previous sections. The accuracy of the method heavily relies on the correct estimation of interface curvature. The use of the discrete gradient operator ∇_h (Eq. 2.39) does not yield a consistent method for computing $\mathbf{n}$ and κ, even when applied to the smoothed version of the volume fraction $\tilde{c}$. Although the use of ∇_h with the Level-Set function $\mathcal{L}$ provides a consistent method for calculating $\mathbf{n}$ and κ, the curvature is determined within a local contour rather than precisely on the interface ($\mathcal{L} = 0$). Consequently, in the case of a spherical drop, this results in a non-constant curvature, leading to spurious currents even in a well-balanced method. On the other hand, the Height Function approach naturally defines curvatures on the interface and exhibits good convergence properties with a higher order of accuracy. It is conceptually straightforward and less sensitive to the precise distribution of volume fractions within a column. The Height Function can be utilized for both interface reconstruction and the calculation of the surface tension force (Popinet, 2018). The well-balanced Continuum-Surface-Force and Height Function curvature estimation methods implemented in the software Basilisk and Gerris have demonstrated always converge towards the equilibrium solution described by Eq. 2.54 (Popinet, 2009).

2.3 Modeling of Non-Newtonian Materials

Materials exhibiting non-Newtonian behaviors, such as plasticity and elasticity, are widespread in various applications. Examples include crude oil, drilling mud, greases, biological fluids, shampoos, skin care creams, toothpaste, chocolate, mayonnaise, ketchup, yogurts, polymeric solutions, emulsions, paints, inks, adhesives, cement, natural muds, volcanic lava, gels, and various slurries. Understanding the individual rheological characteristics of these materials can be challenging, and it becomes even more complex when multiple behaviors are combined. Consequently, it is common practice to simplify the modeling by neglecting less significant rheological behaviors and employing ideal constitutive models, such as inelastic viscoplastic fluids or viscoelastic fluids. However, relying on such simplifications can lead to inaccurate flow predictions. This section aims to introduce the modeling of non-Newtonian behaviors. To facilitate comprehension, this review begins with simpler inelastic viscoplastic models and gradually progresses to more complex viscoelastic and elasto-viscoplastic models. Additionally, the constitutive models are presented in the form of equations along with their corresponding 1-D mechanical analogs.

2.3.1 Inelastic viscoplastic models

Viscoplastic materials exhibit a yield stress, τ_y. According to Bingham (1922), who first introduced the concept of viscoplastic materials, these materials undergo deformation and display a "liquid-like behavior" when subjected to stress levels above τ_y. Conversely, they remain undeformed or exhibit a "solid-like behavior" when the stress level is below τ_y. Viscoplastic materials commonly are modeled as Generalized Newtonian Fluids, and as such, their viscosity depends on the strain rate, while disregarding elastic effects (Barnes et al., 1989; Bird et al., 1987a). The viscosity, η, of the Bingham model may be written as:

$$\eta = \begin{cases} \dfrac{\tau_y}{|\dot{\boldsymbol{\gamma}}|} + \mu_p & \text{if} \quad |\boldsymbol{\tau}_d| \geq \tau_y, \\ \infty & \text{if} \quad |\boldsymbol{\tau}_d| < \tau_y, \end{cases} \tag{2.56}$$

Here, μ_p is the plastic viscosity, $|\dot{\boldsymbol{\gamma}}|$ is the magnitude of the strain rate tensor, $\dot{\boldsymbol{\gamma}} = \nabla\mathbf{u} + \nabla\mathbf{u}^{\mathbf{T}}$, and $|\boldsymbol{\tau}_d|$ is the magnitude of the deviatoric part of the extra stress tensor, $\boldsymbol{\tau}_d = \boldsymbol{\tau} - 1/3\,\mathrm{tr}(\boldsymbol{\tau})\mathbf{I}$. The magnitude of the tensors is given by the Frobenius norm, $|\mathbf{A}| = \sqrt{1/2\,\mathbf{A} : \mathbf{A}}$, where $\mathbf{A}$ is a generic tensor. Recall from Eq. 2.12 that $\boldsymbol{\tau} = \mathbf{T} + p\mathbf{I}$. It should be noted that in Eq. 2.56, the von Mises criterion is employed to determine the transition from solid-like to liquid-like behavior. A mechanical analog of the Bingham model is exhibited in Fig. 2.15, where the

solid-like and liquid-like contributions are combined in parallel. The yield stress term is represented by a friction element, while the plastic viscosity is represented by a dashpot.

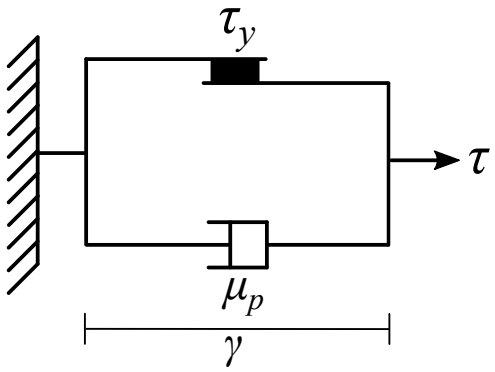

Figure 2.15: Mechanical analog of the Bingham model.

Before proceeding, it is important to discuss the rationale behind considering only the deviatoric part of the extra stress tensor in the von Mises criterion. Since the yield stress involves the collapse or breaking of the material's microstructure, which is associated with material deformation rather than rigid body motion, the von Mises criterion focuses solely on the deviatoric part $\boldsymbol{\tau}_d$ and excludes the spherical part of the tensor $\mathbf{T}$ (Souza Mendes and Thompson, 2012; Moschopoulos et al., 2021). For Newtonian fluids and Generalized Newtonian Fluids, the extra stress tensor is equivalent to the deviatoric part of $\mathbf{T}$ ($\boldsymbol{\tau} = \boldsymbol{\tau}_d = \mathbf{T}_d$), as its trace is zero. Therefore, $\boldsymbol{\tau}_d$ could be replaced by $\boldsymbol{\tau}$ in Eq. 2.56. As it will be discussed in Sec. 2.3.2, this is not the case for viscoelastic materials, in which normal stresses associated with the material elasticity arise in the extra stress tensor, making $\boldsymbol{\tau} \neq \boldsymbol{\tau}_d$.

If the Newtonian contribution of the plastic viscosity, μ_p, is replaced with a non-Newtonian function of the strain rate; for example, a power-law dependence with the strain rate, the Herschel–Bulkley model is obtained. The Herschel–Bulkley model is one of the most representative and used models of its kind (Mendes and Thompson, 2012). It is mathematically expressed as:

$$\begin{cases} \eta = \dfrac{\tau_y}{|\dot{\gamma}|} + K|\dot{\gamma}|^{\mathtt{n}-1} & \text{if} \quad |\boldsymbol{\tau}_d| \geq \tau_y, \\ \eta = \infty & \text{if} \quad |\boldsymbol{\tau}_d| < \tau_y, \end{cases} \tag{2.57}$$

where K is the consistency index, and $\mathtt{n}$ is the power-law index. The mechanical analog of the Herschel–Bulkley model is similar to that of the Bingham model, but the plastic viscosity,

μ_p, is replaced by a term of the form $K\dot{\gamma}^{\mathtt{n}-\mathtt{1}}$.

Both models have the following shortcomings. First, the stress distribution in the unyielded region is unspecified. Any solution that satisfies the von Mises criterion and the mass and momentum conservation principles is acceptable. This issue may be addressed by employing elasto-viscoplastic models, which will be discussed in Sec. 2.3.3. Second, below the yield stress the material has an infinity viscosity, and the derivative of the viscosity function is not continuous. These may be addressed by employing regularized viscosity functions, or by using the augmented Lagrangian method (ALM).

There is a large number of regularization functions, and a well-known example applied to the Bingham model is (Frigaard and Nouar, 2005; Mitsoulis and Tsamopoulos, 2017)

$$\eta = \frac{\tau_y}{|\dot{\boldsymbol{\gamma}}| + \epsilon} + \mu_p. \tag{2.58}$$

Here, ϵ is a regularization parameter that assumes small values. Using a regularized approach results in a large, but not infinity viscosity below the yield stress, and in a continuous derivative of the viscosity function. The magnitude of the regularization parameter depends on the particular flow field (Dimakopoulos et al., 2013). As $\epsilon \to 0$, the regularized viscosity function approaches the original model; however, it may produce numerical instabilities. Therefore, convergence tests for the regularization parameters are usually necessary (Frigaard and Nouar, 2005). For more details on viscosity regularization, the interested reader may refer to Frigaard and Nouar (2005) and Mitsoulis and Tsamopoulos (2017).

The augmented Lagrangian method, based on the theory of variational inequalities, involves more complex mathematical formulations compared to the regularization method (Glowinski, 1983). Although the computational cost is higher, this method allows for the solution of the original Bingham model (as well as other models with discontinuous viscosity derivatives). Solutions obtained using the augmented Lagrangian method can serve as benchmark references for evaluating and comparing results obtained through regularized methods (Mitsoulis and Tsamopoulos, 2017).

It is important to note that the existence of a yield stress is a matter of debate in the literature, and the Bingham model is considered an idealized representation of real material (Mendes and Thompson, 2013). Furthermore, an infinite viscosity below the yield stress, implying complete rigidity of the material, does not align with the behavior of real yield-stress materials (Mitsoulis and Tsamopoulos, 2017). While Generalized Newtonian Fluid models may provide satisfactory results for steady-state shear flows, they may fail to accurately predict unsteady-state and extensional flows, even at low levels of elasticity (Bird et al., 1987a).

This limitation becomes evident when studying bubble rising in real yield-stress materials, as discussed in more detail in Section 2.4. Therefore, the development of constitutive formulations based on the underlying physics is desirable for accurately predicting the flow behavior of real materials.

2.3.1.1 Non-dimensional numbers for flows of viscoplastic materials

The determination of dimensionless numbers that characterize a given flow is not always evident, especially for non-Newtonian fluids. The Buckingham-Pi theorem is a procedure for deducing dimensionless groups for a certain flow. Although the theorem provides a possible set of dimensionless groups that describe the problem from a mathematical point of view, not all the dimensionless numbers are equivalent to describing the problem from a physical point of view.

Thompson and Soares (2016) recommend, whenever possible, to regard the flow of Newtonian fluids as the limiting scenario for the flow of non-Newtonian fluids. Therefore, it is essential to understand how dimensionless numbers that appear for the flow of Newtonian fluids should be treated for non-Newtonian cases. Dimensionless numbers are intended to express the relative importance of different physical quantities. In the presence of non-Newtonian effects, special care should be taken on how to express the viscous effects to maintain consistent interpretations of dimensionless numbers. For instance, dimensionless numbers such as the Reynolds number, capillary number, and viscosity ratio indicate the relative importance of viscous effects to inertia, interfacial tension, and viscous effects of a second fluid, respectively. They all can be defined in the flow of Newtonian fluids. For example, the general definition of the Reynolds number for the flow of a fluid in a pipe is (Reynolds, 1883; Thompson and Soares, 2016)

$$Re = \frac{8\rho U^2}{\tau_w}, \tag{2.59}$$

where ρ is the fluid density, U is the mean velocity, and τ_w is the shear stress at the wall for laminar flows. From the velocity profile, the shear stress at the wall can be calculated as $\tau_w = \eta 8U/D_p$, where η is the viscosity of the Newtonian fluid and D_p is the pipe diameter. Hence, the Reynolds number may be rewritten as

$$Re = \frac{\rho D_p U}{\eta}. \tag{2.60}$$

The ratio of inertial to viscous forces is evident in Eq. 2.59, but it is not so clear in Eq. 2.60. As a consequence, it is common to encounter in the literature definitions of the Reynolds

number for the flow of Bingham materials of the form $Re = \rho D_p U/\mu_p$. The definition of Eq. 2.59 uses the stress at the wall, regardless of the material. It is clear from Eq. 2.56 that μ_p is not the fluid's viscosity, especially at the wall, which may lead to misinterpretations of the problem physics. For instance, using the definition of viscosity, $\eta = |\boldsymbol{\tau}|/|\dot{\boldsymbol{\gamma}}|$, it is possible to see that τ_y also contributes to the viscosity. Hence, if μ_p is low compared to $\tau_y/|\dot{\boldsymbol{\gamma}}|$, this poor formulation of the Reynolds number may indicate that inertial forces are dominant over the viscous forces, while the opposite may be true. Instead, the value of τ_w for the flow of a Bingham fluid in a pipe should be used in the definition of Eq. 2.59:

$$\tau_w = -\left(\frac{\tau_y}{-\dot{\gamma}_w} + \mu_p\right)\dot{\gamma}_w, \tag{2.61}$$

where

$$\dot{\gamma}_w = \frac{\frac{8U}{D_p}\left(\xi_p - 1\right)}{1 - \frac{1}{4}\xi_p + \frac{1}{3}\xi_p}. \tag{2.62}$$

Here, $\dot{\gamma}_w$ is the shear rate on the pipe wall, and $\xi_p = R_p/R$ is the ratio of the radius of the unyielded region in the center of the pipe to the pipe radius. As the magnitude of the strain rate is positive, as well as the viscosity, $-\dot{\gamma}_w$ is used in the term between brackets in Eq. 2.61, since $\dot{\gamma}_w = du/dr < 0$.

For the flow of viscoplastic materials, it is natural to ask, what is the importance of the yield stress? In other words, is the material more "liquid-like" or more "solid-like"? A commonly used dimensionless number to express this is the Bingham number, which for a Bingham material may be defined as:

$$Bi = \frac{\tau_y}{\mu_p \dot{\gamma}_c}. \tag{2.63}$$

Here, $\dot{\gamma}_c$ is a characteristic strain rate of the flow. Bi may vary from zero to infinity. Another dimensionless number that expresses the degree of plasticity of the fluid is the plastic number, defined as (Thompson and Soares, 2016):

$$Pl = \frac{\tau_y}{\tau_y + \mu_p \dot{\gamma}_c}. \tag{2.64}$$

The plastic number, denoted as Pl, provides a measure of the significance of the yield stress within the total stress of a viscoplastic material. By using the plastic number, it is possible to alter the relative importance of the yield stress while keeping the total characteristic stress unchanged. Unlike the Bingham number, the plastic number is constrained within the range of 0 to 1. A plastic number close to zero indicates a dominant "liquid-like" behavior of the

material, while a plastic number close to 1 suggests a dominant "solid-like" nature. Hence, the plastic number offers a more straightforward assessment of material plasticity compared to the Bingham number. Moreover, by defining the characteristic stress as $\tau_c = (\tau_y/|\dot{\gamma}_c| + \mu_p)\dot{\gamma}_c$ (for the case of a Bingham material), the Reynolds number in the form of Eq. 2.59 and the plastic number naturally emerge. If changes in the yield stress τ_y are accompanied by corresponding adjustments in $\mu_p\dot{\gamma}_c$, such that the characteristic stress τ_c remains constant, the Reynolds number remains invariant while the plastic number changes. In this scenario, variations in the flow arising from modifications in τ_y and $\mu_p\dot{\gamma}_c$ (with τ_c held constant) result from alterations in the level of plasticity rather than changes in the relative magnitude of viscous and inertial forces. This allows for a fairer comparison with the Newtonian counterpart exhibiting the same ratio of inertial to viscous forces.

2.3.2 Viscoelastic models

The second class of materials, the viscoelastic materials, has a hybrid nature and combines viscosity and elasticity (Barnes et al., 1989). Although difficult to prove unequivocally, it could be assumed that viscous and elastic properties coexist in all real materials. The response of the material depends on the timescale of the experiment and on the natural time of the material. If the experiment timescale is slower than the material's natural time, the sample appears to be viscous, otherwise it appears to be elastic. For intermediate timescales, a mixed, or a viscoelastic response is observed (Barnes et al., 1989). Further discussion on the timescales can be found in Sec. 2.3.2.1, which discusses dimensionless numbers for viscoelastic materials.

Experiments have shown that when submitted to a stress load some materials respond with an instantaneous deformation, as Hookean solids, but followed by continuous small deformations. Upon the removal of the load, a portion of the deformation quickly recovers, while another portion recovers over an extended period, and some may remain deformed. This behavior is known as viscoelasticity (Macosko, 1994; Barnes et al., 1989). In the case of small deformations, viscoelastic materials often exhibit a linear relationship between stress and strain. In this regime, material properties such as elastic modulus and viscosity remain constant. However, for larger strain magnitudes, a nonlinear viscoelastic regime is observed and the material properties may vary (Barnes et al., 1989; Macosko, 1994; Bird et al., 1987a).

Maxwell proposed one of the earliest viscoelastic models over a century ago (Maxwell, 1867, *apud* Bird et al., 1987a). The mechanical analog of the model is depicted in Figure 2.16. It consists of a spring with an elastic modulus G and a dashpot with viscosity η connected in series. Notably, the stress applied to both mechanical elements is identical, but each element undergoes a different strain. γ_e represents the elastic strain of the spring, while γ_v represents

the viscous strain of the dashpot. The overall material experiences a total strain $\gamma = \gamma_e + \gamma_v$. In case the material is submitted to a stress load, the spring stretches up to a certain point, as expected from a Hookean solid, while the viscous element continues to deform, as would be expected from a Newtonian fluid. If the stress load is removed, the strain γ_e is recovered, while the strain γ_v is not recovered. Thus, the Maxwell model is considered a representation of a viscoelastic fluid. Furthermore, it should be noted that the elasticity of the material increases with a decrease in G, and vice versa. As G increases, the spring deformation reduces for a given applied load. In the limiting case where $G \to \infty$, the Maxwell model reduces to a Newtonian fluid.

The total strain rate of the material, $\dot{\gamma}$, can be expressed as the sum of the elastic and viscous strain rates, $\dot{\gamma} = \dot{\gamma}_e + \dot{\gamma}_v$. Assuming the elastic strain rate follows that of a Hookean solid ($\dot{\gamma}_e = (1/G)\partial\tau/\partial t$), and the viscous strain rate follows that of a Newtonian fluid ($\dot{\gamma}_v = \tau/\eta$), the stress can be described by the following equation:

$$\tau + \lambda \frac{\partial \tau}{\partial t} = \eta \dot{\gamma}. \tag{2.65}$$

Here, $\lambda = \eta/G$ is the material relaxation time. If the material is subjected to a steep increase in strain, the stress in the material suddenly increases and then gradually diminishes. The value of λ controls the rate at which the stress relaxes. This formulation represents the simplest expression for the stress for a fluid with both viscous and elastic responses. Equation 2.65 is a first-order linear partial differential equation for τ as a function of time. By rewriting Eq. 2.65 in an integral form, it is possible to verify that the stress at the current time depends not only on the current strain rate but also on the strain rates from past times. However, the importance of past strain rates in determining the current stress diminishes as time progresses. This indicates that viscoelastic materials, here modeled by the simple Maxwell formulation, have "memory" (or "fading memory") since the material response depends on

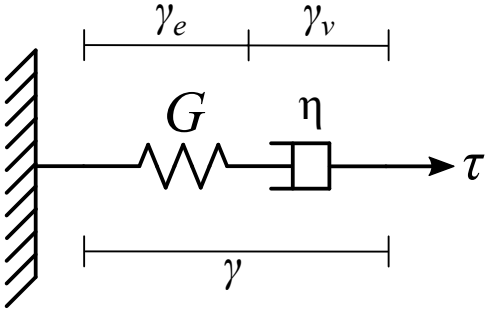

Figure 2.16: Mechanical analog of the viscoelastic Maxwell model.

the flow history (Bird et al., 1987a).

Another simple viscoelastic model is the Kelvin-Voigt model. Here, the spring and the dashpot are arranged in parallel, instead of being arranged in series as in the Maxwell model, as schematized in Fig. 2.17. Both mechanical elements are subjected to the same strain but have different stress loads. In case a stress load is applied, both the spring and the dashpot deform up to a certain point (due to the parallel arrangement), preventing the dashpot from further deformation as in the Maxwell model. At the moment the load is removed, all the deformation is recovered. Thus, the Kelvin-Voigt model is considered to represent a viscoelastic solid. Due to the presence of the viscous element, a Kelvin-Voigt material does not achieve its final deformation instantaneously, as a purely elastic material would when subjected to a step stress load. Additionally, unlike the Maxwell model, the elasticity of the Kelvin–Voigt material increases with an increase in G, and vice versa. For example, in the limit as $G \to 0$, the Kelvin-Voigt model reduces to a Newtonian fluid.

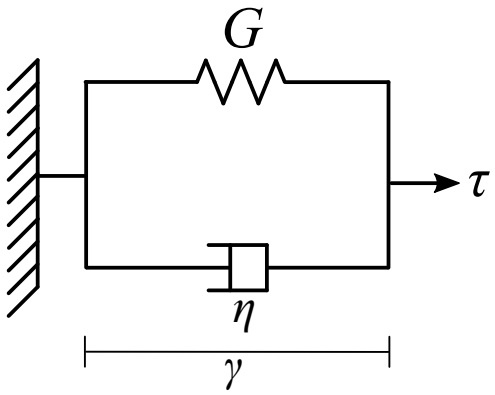

Figure 2.17: Mechanical analog of the viscoelastic Kelvin–Voigt model.

The total stress can be expressed as $\tau = \tau_e + \tau_v$, where τ_e represents the elastic stress, and τ_v represents the viscous stress. Consequently, the stress can be written as follows:

$$\tau = G\gamma + \eta\dot{\gamma}. \tag{2.66}$$

For a Kelvin–Voigt material, the ratio η/G is referred to as the retardation time, which determines the rate at which strain grows for a given stress load.

Another linear viscoelastic model is the Jeffreys model, which combines characteristics of both the Maxwell and Kelvin-Voigt models. Its mechanical analog is illustrated in Fig. 2.18, where a spring is connected in series with a dashpot (similar to the Maxwell model), and in parallel with another dashpot (similar to the Kelvin-Voigt model). A stress equation for the

Jeffreys model can be written as

$$\tau + \lambda \frac{\partial \tau}{\partial t} = \eta \left(\dot{\gamma} + \theta \ddot{\gamma} \right). \tag{2.67}$$

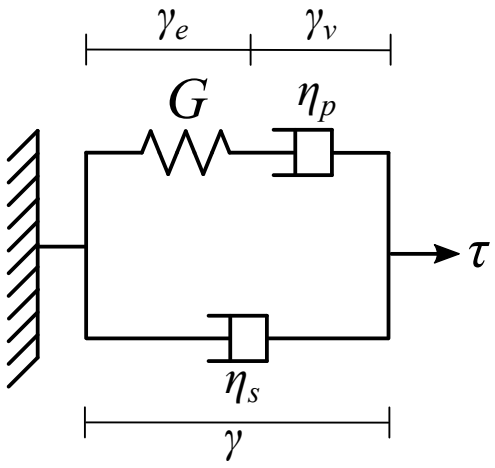

Figure 2.18: Mechanical analog of the Jeffreys model.

Here, $\lambda = \eta_p/G$ is the relaxation time of the material and $\theta = \eta_s \eta_p / G\eta$ is the retardation time of the material. The total viscosity of the material is denoted as $\eta = \eta_s + \eta_p$. Equation 2.67 was originally proposed for the study of wave propagation in the Earth's mantle (Jeffreys, 1929; Bird et al., 1987a). It was also derived by Fröhlich and Sack (1946) for dilute suspensions of solid elastic spheres in a viscous liquid, and by Oldroyd (1953) for a dilute emulsion composed of incompressible viscous liquids (apud Barnes et al. 1989). In Fig. 2.18, the viscosities η_p and η_s represent the polymer and solvent viscosities, respectively. The Jeffreys model is also frequently used as a basis for the development of quasi-linear and non-linear models viscoelastic models (Bird et al., 1987a); for example, the Oldroyd-B model (Oldroyd, 1950).

Viscoelastic fluids typically exhibit normal stress differences in shear flows, rendering the flow of viscoelastic fluids fascinating. Linear viscoelastic models are not capable of predicting them and more advanced models applicable to larger deformations are desirable in order to gain qualitative insights into the flow of viscoelastic fluids (Bird et al., 1987a)

Considering a fluid in a simple shear flow between two parallel plates with area A and a small gap of width `L`, the components of the velocity vector are $u_x = \dot{\gamma} y$ and $u_y = u_z = 0$, as shown in Fig. 2.19. The upper plate motion is driven by the force `F`, and it is moving with a constant velocity U, while the lower plate is stationary.

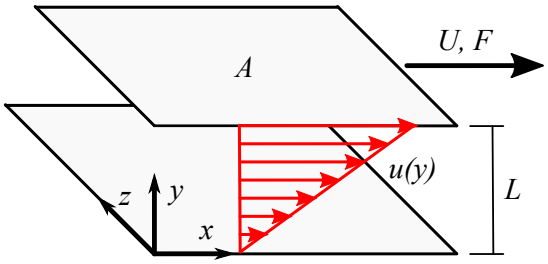

Figure 2.19: Shear flow of fluid between two parallel plates with area A and a small gap $\mathtt{L}$ between them. The upper plate velocity is U and the lower plate is stationary.

If the fluid is Newtonian, the stress distribution may be expressed as:

$$\tau_{xy} = \eta\dot{\gamma},\ \tau_{xz} = \tau_{yz} = 0,\ \tau_{xx} - \tau_{yy} = 0,\ \tau_{yy} - \tau_{zz} = 0. \tag{2.68}$$

The diagonal elements of the stress tensor which correspond to the normal stresses aligned with the coordinate system, are equal to zero, $\tau_{xx} = \tau_{yy} = \tau_{zz} = 0$. On the other hand, the non-diagonal elements, known as shear stresses, are zero except for the component $\tau_{xy} = \eta\dot{\gamma}$, where η denotes the fluid's viscosity and $\dot{\gamma} = U/\mathtt{L}$ represents the strain rate. Due to the effects of the isotropic pressure in incompressible fluids, it is usual to work with normal stress differences rather than the individual stresses. Hence, the differences between the normal stresses for a Newtonian fluid in a simple shear flow are zero.

For a viscoelastic fluid, normal stresses arise due to the elastic nature of the material, and the stress distribution may be written as:

$$\tau_{xy} = \eta(\dot{\gamma})\dot{\gamma},\ \tau_{xz} = \tau_{yz} = 0,\ \tau_{xx} - \tau_{yy} = N_1(\dot{\gamma}),\ \tau_{yy} - \tau_{zz} = N_2(\dot{\gamma}) \tag{2.69}$$

where, N_1 and N_2 are the first and second normal stress differences, respectively.

Polymeric fluids consist of an important class of viscoelastic materials and exhibit a wide range of rheological phenomena, which is attributed to their long-chain molecules. Viscoelasticity arises from intramolecular forces that depend on the orientation of chemical bonds in the polymer chains. Elastic effects emerge when the molecules are deformed and the orientation of the chemical bonds change. Elastic recovery occurs when the molecules return to the state of minimum energy (chemical bonds orientation) (Barnes et al., 1989). The normal stress differences may be explained by the fact that in shear flow (Fig. 2.19) the polymer molecules, which tend to have a spherical shape at rest, are stretched in the direction of the streamlines, as illustrated in Fig. 2.20. Consequently, the microstructure of the material becomes anisotropic (Barnes et al., 1989). As the molecules are stretched, they behave like

small springs, or "rubber balls", exerting a greater restoring force in the direction of the streamlines. Therefore, $\tau_{xx} \geq \tau_{yy}$ and $N_1 \geq 0$. Some authors argue that τ_{xx} is negative due to the tendency of polymer molecules to snap back. Consequently, N_1 becomes negative because the magnitude of τ_{xx} exceeds that of τ_{yy}, rather than the latter being greater than the former (Bird et al., 1987a,b). In terms of magnitude, N_1 is significantly larger than N_2, or $|N_2| \lesssim 0.1|N_1|$ (Barnes et al., 1989).

The normal stress differences due to molecule stretching result in intriguing and captivating phenomena such as the famous rod climbing and others. The rod-climbing phenomenon, also known as the Weissenberg effect, is produced when a rotating rod is inserted into a vessel containing an elastic fluid. In a Newtonian fluid, the centrifugal force (inertial effects) would cause the fluid to move towards the periphery, resulting in a higher fluid level at the outer region and a lower level near the rod. However, in an elastic fluid, the macromolecules act like a hoop that pulls the fluid towards the rod. As a result, the fluid level increases near the rod and decreases at the periphery, as illustrated in Fig. 2.21. This phenomenon is directly influenced by the normal stress τ_{xx}.

Normal stress differences in viscoelastic fluids also give rise to interesting secondary flows. Primary flows are associated with viscous properties of the fluid, while secondary flows usually are associated with inertial and elastic effects, which often exhibit contrasting behaviors, although this is not a universal rule (Bird et al., 1987a). One example of a secondary flow is observed in a tank driven by a rotating lid. In a Newtonian fluid, a secondary rotating flow occurs where the liquid moves away from the rotating disk at the periphery, close to the tank walls, due to the centrifugal force, and then approaches the disk at its center. However, for a polymer fluid, the rotation happens in the opposite direction due to elastic effects, resembling a rod climbing experiment without a rod. Reverse secondary flow can even be

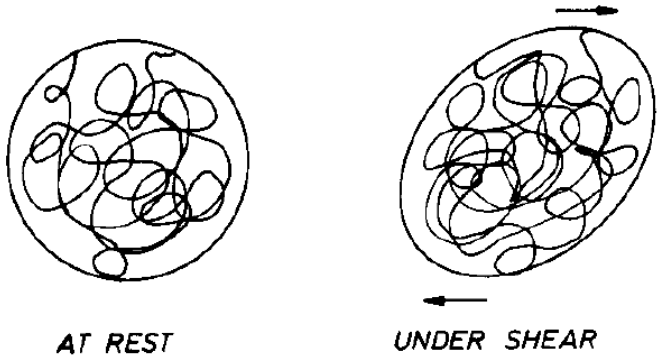

Figure 2.20: Scheme of a molecular envelope before and during shear deformation. Source.: Barnes et al. (1989).

Figure 2.21: Rod climbing effect of a viscoelastic fluid.
Source.: Barnes et al. (1989)

observed in cases of low polymer concentrations, where normal stresses may not be detectable using standard techniques.

The flow of polymer fluids through expansions and contraction also demonstrate the influence of normal stress differences. In the flow through an expansion (exit), the diameter of a jet of a Newtonian fluid increases slightly, whereas for a polymer fluid, the stretched polymer molecules recoil back, resulting in a significant increase in the jet diameter, as illustrated in Fig. 2.22. In a contraction at very low Reynolds number (Fig. 2.23), a circulating dead zone emerges near the exit in the flow of a viscoelastic fluid, while the streamlines tend to be straight for a Newtonian fluid. In case of a flow of real yield stress fluids (elasto-viscoplastic) through an expansion followed by a contraction, the flow configuration pattern exhibits an asymmetry, as illustrated in Fig. 2.24. The figure displays the trajectory of injected particles in a Carbopol solution flowing through an expansion/contraction configuration obtained by Mendes et al. (2007). The diameter of the yielded region near the expansion is larger than that near the contraction. Numerical simulations performed by dos Santos et al. (2014) demonstrated that the flow of inelastic viscoplastic fluids is symmetric at low Reynolds numbers and asymmetric at high Reynolds numbers. However, the observed asymmetry is the inverse of that observed when the fluid exhibits elasticity (*i.e.*, the diameter near the contraction is larger than the diameter near the expansion). This inverse asymmetry is attributed to inertial effects.

Another intriguing phenomenon exhibited by polymer fluids is the formation of stable films, as observed in experimental setups like the tubeless siphon experiment (Bird et al., 1987a). Moreover, viscoelasticity plays a substantial role in the dynamics of bubble and drop rise and coalescence, which are reviewed in Sec. 2.4 and 2.5, respectively.

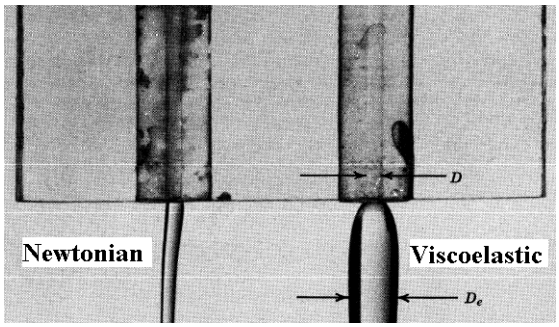

Figure 2.22: Flow of a Newtonian (left) and a viscoelastic fluid (right) exiting a capillary tube.
Source.: adapted from Bird et al. (1987a)

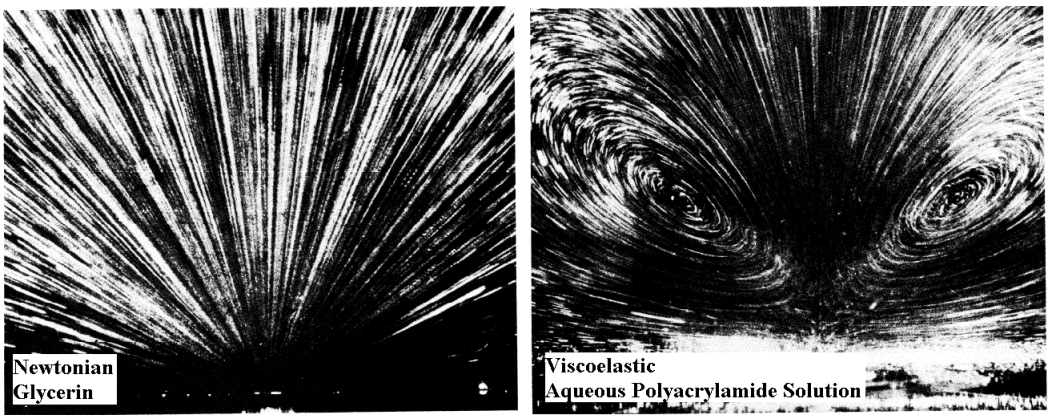

Figure 2.23: Flow of glycerin (left) and 1.67 % aqueous polyacrylamide solution (right) entering a contraction.
Source.: adapted from Bird et al. (1987a)

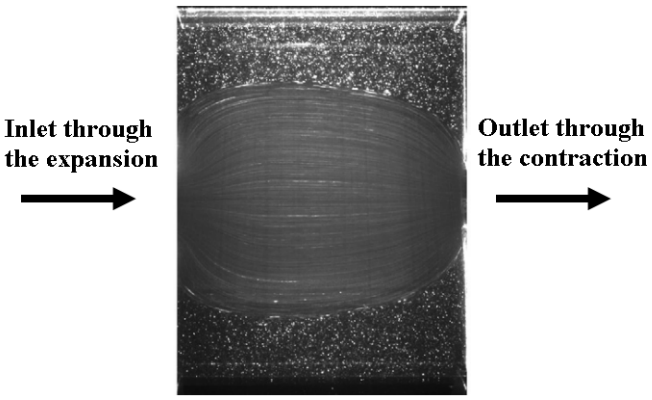

Figure 2.24: Particles path in a flow of Carbopol® solution through an expansion/contraction (left to right).
Source.: adapted from Mendes et al. (2007)

Regarding the construction of constitutive equations (equations that relate stress and deformation variables) of viscoelastic materials, there are two main alternatives: the molecular approach and the continuum approach. In the former, the material molecules are represented by a physical model. For example, a molecule can be represented by a set of spheres (beads) connected by springs. The elastic effects are introduced by the deformation of the springs, while viscous effects may be calculated from the frictional drag between the beads and the surrounding fluids (solvent) using the Stokes' equation (Barnes et al., 1989). Then, the governing principles (*e.g.*, momentum and mass conservation principles) are employed to relate the average stress and strain and to formulate constitutive equations. This approach tends to be more specific and relevant to the material in question since the material underlying microstructure is taken into account. For more about molecular theory, the reader may refer to Bird et al. (1987b) and Phan-Thien and Mai-Duy (2013). In the continuum approach, no microstructure is featured and equations are written in a form that ensures invariance under a change of frames. In this approach, the constitutive equation generally has some undetermined functions which may be tuned by experiments (Phan-Thien and Mai-Duy, 2013).

Oldroyd (1950) laid down principles based on continuum-mechanics concepts for the admissibility of constitutive equations. According to these principles, rheological equations of state must:

1. Be independent of the frame of reference. Hence, one should use a tensorial formulations;

2. Be independent of absolute motion in space (*e.g.*, superimposed rigid body motion);

3. Depend only on the previous history of that same material element and not on the neighboring elements (except for the arbitrary small neighborhood used to calculate the strain).

The stress tensor is objective, meaning it is frame-indifferent. However, its material derivative does not possess the same property, which violates the second principle (Lai et al., 2009). Simply replacing the partial time derivative of the stress tensor in linear viscoelastic models with the material derivative does not satisfy the second principle. To address this issue, Oldroyd (1950) introduced a convected coordinate system that is embedded in the material and deforms continuously with it. In this new coordinate system, a fluid particle maintains the same coordinates at all times, and the derivative of the stress tensor becomes objective. By working in a tensorial-consistent form within the convected coordinate system, the fundamental principles 1 to 3 are satisfied.

Admissible constitutive equations can be built by replacing the partial time derivative in the linear elastic models, which are valid only for small displacement gradients, with other derivatives which are objective. These derivatives can be obtained by transforming the material derivative in the convected coordinate system to the fixed "laboratory" coordinate system. There are various choices of convected derivatives; for example, the Oldroyd upper convected derivative, Oldroyd lower convected derivative, and Jaumann Derivative (Bird et al., 1987a; Lai et al., 2009). Nevertheless, the continuum approach lays down admissible, or permissible, conditions regarding frame invariance, but not regarding the choice of the convected derivative, which turns out to be arbitrary. This creates arguments in favor of the molecular approach, although it also contains arbitrariness regarding the representation of the molecule. Interestingly, molecular dynamics may also lead to models with frame-indifferent time derivatives (Macosko, 1994). Of the convected derivatives mentioned above, the upper convected derivative can be justified (obtained) by the molecular theory and has a better response for most materials than the other derivatives. It is worth noting that the continuum approach formulations may also make use of a thermodynamical framework that leads to rational models, which allows for the study of a wide class of material responses. The thermodynamical framework is based on the way the material stores and dissipates energy, which must obey the second law of thermodynamics, for example. This results in specific convected derivatives depending on the material being modeled (Rajagopal and Srinivasa, 2000).

In case the partial time derivatives of the linear Maxwell (Eq. 2.65) and Jeffreys (Eq. 2.67) models are replaced with the upper convected time derivative, one obtains the Upper Convected Maxwell (UCM) model and the Upper Convected Jeffreys models, respectively. The latter is also known as the Oldroyd-B model (Oldroyd, 1950). The upper convected derivative of a generic tensor $\mathbf{A}$ is represented by the symbol $^{\triangledown}$ over the tensor. It is defined as:

$$\overset{\triangledown}{\mathbf{A}} = \frac{\partial \mathbf{A}}{\partial t} + \mathbf{u} \cdot \nabla \mathbf{A} - (\nabla \mathbf{u})^{\mathbf{T}} \cdot \mathbf{A} - \mathbf{A} \cdot (\nabla \mathbf{u}). \tag{2.70}$$

The term $\partial \mathbf{A}/\partial t$ quantifies the variation of the tensor at a point in space, $\mathbf{u} \cdot \nabla \mathbf{A}$ quantifies the changes in the tensor when a particle fluid moves from one point to another and $-(\nabla \mathbf{u})^T \cdot \mathbf{A} - \mathbf{A} \cdot (\nabla \mathbf{u})$ quantifies the deformation suffered by the tensor and arises from the transformation of the convective coordinate system that moves with the particles to the "laboratory" coordinate system. With the definition of the upper connected derivative, stresses are produced only when material elements are deformed and mere rotation of the element does not produce stress. This time derivative is defined in a manner such that they are independent of superposed rigid rotations. Thus, the stress equation for the Upper Convected

Maxwell model may be written as:

$$\boldsymbol{\tau} + \lambda \overset{\nabla}{\boldsymbol{\tau}} = \eta \dot{\boldsymbol{\gamma}}. \tag{2.71}$$

The model is capable of predicting normal stress differences. It is worth noting that the strain rate tensor is objective.

Similarly, the stress equation for the Upper Convected Jeffreys model, or Oldroyd-B model, may be given by

$$\boldsymbol{\tau} + \lambda \overset{\nabla}{\boldsymbol{\tau}} = \eta \left(\dot{\boldsymbol{\gamma}} + \theta \overset{\nabla}{\dot{\boldsymbol{\gamma}}} \right). \tag{2.72}$$

The total stress, $\boldsymbol{\tau}$, in the Oldroyd-B model is the sum of the stress associated with the polymer, $\boldsymbol{\tau}_p$, and the stress associated with the solvent, $\boldsymbol{\tau}_s$. The latter is modeled as a Newtonian fluid, while the former is modeled as an Upper Convected Maxwell model (Eq. 2.71). Hence, the total stress can also be represented in the following form

$$\boldsymbol{\tau} = \boldsymbol{\tau}_p + \boldsymbol{\tau}_s, \tag{2.73}$$

$$\boldsymbol{\tau}_s = \eta_s \dot{\boldsymbol{\gamma}}, \tag{2.74}$$

$$\boldsymbol{\tau}_p + \lambda \overset{\nabla}{\boldsymbol{\tau}}_p = \eta_p \dot{\boldsymbol{\gamma}}. \tag{2.75}$$

For more on viscoelastic fluids, the reader may refer to: Bird et al. (1987a,b); Barnes et al. (1989); Macosko (1994) and Phan-Thien and Mai-Duy (2013).

2.3.2.1 Non-dimensional numbers for flows of viscoelastic materials

As introduced at the beginning of Sec. 2.3.2, real materials may present viscous (liquid-like) or elastic (solid-like) behaviors. The relative importance of elastic and viscous effects depends on the stress and the duration of application of the stress relative to the material characteristic time. A material with a short relaxation time subjected to an experiment with a long observation time will behave more like a fluid. On the other hand, if the observation time is short and/or the material relaxation time is long, the material will behave more like a solid. The material response when undergoing a deformation over some time can be characterized by the Deborah number, which was proposed by Reiner (1964) and defined as the ratio of a characteristic time of the material t_m, to the time of observation, t_o (Bird et al., 1987a; Barnes et al., 1989; Dealy, 2010; Poole, 2012),

$$De = \frac{t_m}{t_o}. \tag{2.76}$$

The characteristic time or natural time of the material depends on the molecular motion and can be chosen as the largest time constant (the relaxation time) of the slowest molecular motions. However, since obtaining this value directly is challenging, a constant in the constitutive equation, often represented by λ, is commonly used as an approximation for t_m (Bird et al., 1987a). The observation time typically corresponds to the duration of the experiment (Poole, 2012). If $De \to 0$, the material tends to behave like a liquid, while $De \to \infty$ indicates solid-like behavior. A practical example is the behavior of lubricating oils passing through gears which may have a solid-like behavior since t_o may be about the same order of magnitude as t_m (Barnes et al., 1989).

For slowly changing or essentially steady flows, t_o is infinite, and thus, $De = 0$. This implies that no change in behavior is observed regardless of the observation time (Dealy, 2010; Metzner et al., 1966). Hence, the definition provided in Eq. 2.76 may be insufficient to fully describe viscoelastic effects (Poole, 2012). In response to this limitation, Metzner et al. (1966) proposed a more rigorous definition by modifying the original definition of De. The new definition incorporates a "time scale of the process", such as the reciprocal of a characteristic strain rate ($1/\dot{\gamma}_c$), or the "fluid residence time", rather than the observation time.

Another important dimensionless number to describe the relative significance of elastic to viscous forces is the Weissenberg number, Wi. It was proposed by White (1964) when the author used dimensional analysis to non-dimensionalize the momentum equation for the flow of a viscoelastic fluid and write:

$$Wi = \lambda \frac{U}{\mathtt{L}}. \tag{2.77}$$

Here, U and $\mathtt{L}$ are a characteristic velocity and a characteristic length of the flow, respectively. According to White (1964), Wi can be interpreted as a measure of the recoverable strain (). Alternatively, Wi can be defined as the ratio of the first normal stress difference (elastic forces) to the shear stress (viscous forces) in a steady simple shear flow (Barnes et al., 1989),

$$Wi = \frac{\tau_{xx} - \tau_{yy}}{\tau_{xy}}. \tag{2.78}$$

For viscoelastic materials in steady-state simple shear flow, Thompson and Oishi (2021) demonstrate that the Weissenberg number can be expressed as:

$$Wi = \lambda \dot{\gamma}_c, \tag{2.79}$$

which corresponds to the definition in Eq. 2.77. Here, $\dot{\gamma}_c$ is a characteristic strain rate of the

flow (*e.g.*, $\dot{\gamma}_c = U/\mathtt{L}$). Therefore, the Weissenberg number incorporates a characteristic rate of deformation rather than an observation time, as in the Deborah number.

To illustrate the concepts of De and Wi, consider two examples, the flow in a lid cavity and the oscillatory test with imposed deformation. In the case of the lid-driven cavity flow, the the observation time may be taken as the time for one turnover, which can be approximated by $t_r = U/\mathtt{L}$, where U represents the lid velocity and $\mathtt{L}$ is the lid length. The characteristic strain rate can be approximated by $\dot{\gamma}_c = 1/t_c = H/U$, where H denotes the cavity height. In the scenario of a square cavity, where $\mathtt{L} = H$, the definitions of De and Wi coincide. For the case of the oscillatory test, consider the imposition of a deformation $\gamma = \gamma_a \mathrm{sin}\omega t$, where γ_a is the amplitude of the deformation, ω is frequency, and t is time. The deformation rate is given by $\dot{\gamma} = \dot{\gamma}_a \mathrm{cos}\omega t$, where $\dot{\gamma}_a = \omega\gamma_a$, the the amplitude of the deformation rate. Here, the Deborah number may be defined as $De = \lambda\omega$, and represents the ratio of the material's characteristic time to the period during which changes in the material's deformation occur ($\dot{\gamma}$ is a function of t). The Weissenberg number may be defined as $Wi = \lambda\dot{\gamma}_a$, in which the characteristic time of the experiment expresses the intensity of the deformation.

Similar to the Reynolds number, which is used to categorize flows into laminar and turbulent regimes, the Weissenberg number can be used to classify flows based on the presence or absence of significant elastic effects. For example, in the flow of a polymeric solution through a contraction, as illustrated in Fig. 2.23, the flow may exhibit straight streamlines resembling a Newtonian fluid for sufficiently small values of Wi. This occurs when the flow rate is small enough that $Wi \to 0$, as $\dot{\gamma}_c \to 0$, even if λ is finite. As the flow rate increases, $\dot{\gamma}_c$ also increases, and above a critical Weissenberg number, a flow pattern with a circulating dead zone (characteristic of elastic effects) may be observed (Bird et al., 1987a).

Additionally, in the case of polymeric solutions, it is important to evaluate the relative significance of the solvent viscosity to the total viscosity. This can be expressed by the viscosity ratio β, which is defined as:

$$\beta = \frac{\eta_s}{\eta_s + \eta_p}. \tag{2.80}$$

2.3.3 Elasto-viscoplastic models

In their work, Mendes and Thompson (2012) conducted a critical review of the modeling of elasto-viscoplastic thixotropic (EVPT) materials and classified them into two types: Type I and Type II, based on the fundamental principles underlying the models. Numerous thixotropic constitutive equations have been proposed in the literature, typically built upon a limited number of elasto-viscoplastic models. Type I models are primarily based on the Bingham model, where the solid contribution below the yield stress takes the form of a

Hookean solid. These models begin with a viscoplastic stress equation (e.g., Eq. 2.56), to which elasticity is subsequently added. In contrast, Type II models are based on a viscoelastic stress equation, with plasticity introduced later through a viscosity function that diverges at low deformation rates. The Maxwell model (Eq. 2.65) is commonly used as the foundation for these models.

One of the most intuitive Type I models is the one proposed by Oldroyd (1947) where the behavior of a Bingham material below the yield stress takes the form of a Hookean solid. Hence, Eq. 2.56 can be reformulated for stress as

$$\boldsymbol{\tau}_d = \begin{cases} \tau_y + \mu_p \dot{\boldsymbol{\gamma}} & \text{if} \quad |\boldsymbol{\tau}_d| \geq \tau_y, \\ G\boldsymbol{\gamma} & \text{if} \quad |\boldsymbol{\tau}_d| < \tau_y. \end{cases} \tag{2.81}$$

Following the concept introduced by Oldroyd (1947), many Type I models take the form (Mendes and Thompson, 2012):

$$\boldsymbol{\tau} = G\boldsymbol{\gamma}_e + \mu_p \dot{\boldsymbol{\gamma}}, \tag{2.82}$$

where an equation for the elastic strain may be written as (inspired in the elasto-viscoplastic thixotropic model of Mujumdar et al. (2002)):

$$\begin{cases} \boldsymbol{\gamma}_e = \boldsymbol{\gamma} & \text{if} \quad |\boldsymbol{\tau}_d| \geq \tau_y, \\ |\boldsymbol{\gamma}_e| = \tau_y / G & \text{if} \quad |\boldsymbol{\tau}_d| < \tau_y. \end{cases} \tag{2.83}$$

It is worthy noting that the elastic strain is limited by $|\boldsymbol{\gamma}_e| \leq \tau_y/G$. As result, constructing a direct mechanical analog of Eq. 2.82 is not straightforward since $\gamma \geq \gamma_e$ in general. Replacing the friction element of the Bingham model (acting in parallel to the viscous element) with a spring in the mechanical analog results in a viscoelastic solid represented by the Kelvin-Voigt model. For the case of viscoelastic fluids, the coupling between the components of a mechanical analog representing Eq. 2.82 is not clear. Furthermore, the model does not reduces to its inelastic counterpart, since as $G \to 0$, $\tau_y \to 0$.

For models of Type II, which are based on viscoelastic models, the counterpart of the Bingham model is the Maxwell model (Eq.2.65). However, instead of being a constant, η now becomes a function of the viscous strain rate, $\dot{\gamma}_v$, and diverges as $\dot{\gamma}_v \to 0$. In case of adding a solvent viscosity, one ends up with the Jeffreys model where η_s is still a Newtonian contribution. In a three-dimensional formulation, the time derivative can be replaced with an upper convected derivative, and an EVP model based on the Oldroyd-B-like model is obtained. It is important to note that for EVP models (excluding thixotropy), the elastic

modulus G typically remains constant. However, the relaxation of the material is no longer constant, as it becomes a function of $\eta_p(\dot{\gamma}_v)$. Mendes and Thompson (2012) advocates some advantages of Type II over Type I models: i) Type II models can be clearly described using a mechanical analog, ii) they do not require an evolution equation for γ_e, and iii) they can be reduced to simpler formulations, such as Newtonian, inelastic viscoplastic, and pure viscoelastic materials.

The "tricky" aspect of Type II models lies in obtaining the magnitude of the viscous strain rate (not the total strain rate) in order to calculate the diverging viscosity η_p. This can be achieved by expressing the strain rate as a function of the stress. Consider a Type II model based on the Oldroyd-B model with a mechanical analog shown in Fig. 2.25, where the polymeric viscosity η_p is modeled as an inelastic viscoplastic fluid. The deviatoric part of the polymeric contribution to the extra stress tensor, $\boldsymbol{\tau}_{pd}$, is a function of the viscous strain rate, $\dot{\boldsymbol{\gamma}}_v$. Hence, the magnitude of $\boldsymbol{\tau}_{pd}$ may be written as $|\boldsymbol{\tau}_{pd}| = f(|\dot{\boldsymbol{\gamma}}_v|)$, where f is a function that involves an equation for the viscosity η_p; for instance, $f = \eta_p(|\dot{\boldsymbol{\gamma}}_v|)|\dot{\boldsymbol{\gamma}}_v|$. By utilizing the known polymeric stress $\boldsymbol{\tau}_p$ (obtained by solving Eq. 2.75), an equation for $|\dot{\boldsymbol{\gamma}}_v|$ can be obtained as a function of $|\boldsymbol{\tau}_{pd}|$, or $|\dot{\boldsymbol{\gamma}}_v| = f^{-1}(|\boldsymbol{\tau}_{pd}|)$.

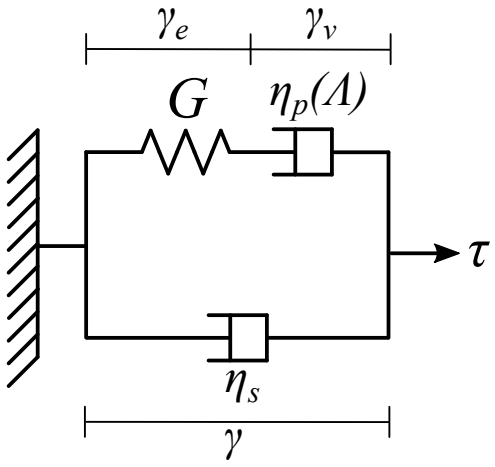

Figure 2.25: Mechanical analog of the Mendes (2011) model.

In their study, Frey et al. (2015) utilized the elasto-viscoplastic thixotropic (EVPT) model developed by Mendes (2011), reduced to its elasto-viscoplastic (EVP) formulation, to investigate a series of benchmark problems. These included flow scenarios such as lid cavity flow, flow through an expansion followed by a contraction, flow over a flat plate, channel entry flow, and flow around a cylinder confined between parallel plates. The authors observed significant alterations in the flow pattern, as well as changes in the shape and size of the yielded region when considering the elasticity of the material. Consequently, they recommended the

inclusion of elasticity when modeling complex flows involving yield stress materials. Oishi et al. (2020) also employed the EVP model of Mendes (2011) to investigate the effect of gravity on the collision of elasto-viscoplastic drops on a vertical plane. The authors found a rich variety of outputs and classified collisions as sticking, sliding, bouncing, detaching, and slithering.

In the EVP formulation of the Mendes (2011) model, $|\dot{\boldsymbol{\gamma}}_v|$ is found by an iterative method until $f(|\dot{\boldsymbol{\gamma}}_v|) \in (|\boldsymbol{\tau}_{pd}| - \mathcal{E}, |\boldsymbol{\tau}_{pd}| + \mathcal{E})$, where $\mathcal{E}$ is an error margin. In their work, Frey et al. (2015) employed

$$|\boldsymbol{\tau}| = \left(\left[1 - \exp\left(-\frac{\eta_o |\dot{\boldsymbol{\gamma}}_v|}{\tau_y} \right) \right] \left[\frac{\tau_y}{|\dot{\boldsymbol{\gamma}}_v|} + K |\dot{\boldsymbol{\gamma}}_v|^{n-1} \right] \right) |\dot{\boldsymbol{\gamma}}_v|. \tag{2.84}$$

The term inside the brackets is the polymeric viscosity η_p. Equation 2.84 can be viewed as a regularized version of the Herschel-Bulkley model. The first term in brackets serves as a regularization term, where η_o is very large but finite. It should be noted that Equation 2.84 remains bounded as $|\dot{\boldsymbol{\gamma}}_v| \to 0$ (since $\eta \to \eta_o + \eta_s$) and as $|\dot{\boldsymbol{\gamma}}_v| \to \infty$ (since $\eta \to \eta_s$). This is in contrast to the original Herschel-Bulkley model, where the viscosity approaches infinity as $|\dot{\boldsymbol{\gamma}}_v| \to 0$ and approaches zero as $|\dot{\boldsymbol{\gamma}}_v| \to \infty$, which is physically unrealistic. In a time-dependent numerical simulation, $\eta_p(|\dot{\boldsymbol{\gamma}}_v|)$ is calculated after finding $|\dot{\boldsymbol{\gamma}}_v|$ which satisfies $f(|\dot{\boldsymbol{\gamma}}_v|) \in (|\boldsymbol{\tau}_{pd}| - \mathcal{E}, |\boldsymbol{\tau}_{pd}| + \mathcal{E})$, and then used in the next time step to calculate $|\boldsymbol{\tau}_p|$.

Saramito (2007) proposed an EVP model where $|\dot{\boldsymbol{\gamma}}_v|$ is explicitly written as a function of $|\boldsymbol{\tau}_{pd}|$ using the Bingham model and combining it with a viscoelastic model. In addition to adhering the constitutive rules proposed by Oldroyd, as discussed in Sec. 2.3.2, this model also satisfies the second law of thermodynamic and predicts continuous stresses upon yielding. As result, the viscosity η_p is written as a function of $|\boldsymbol{\tau}_{pd}|$ instead of $|\dot{\boldsymbol{\gamma}}_v|$. By writing $\eta_p(|\dot{\boldsymbol{\gamma}}_v|)$ as an Bingham material (Eq. 2.56), multiplying by $|\dot{\boldsymbol{\gamma}}_v|$, and rearranging, an equation for the magnitude of the viscous strain rate tensor can be written:

$$|\dot{\boldsymbol{\gamma}}_v| = \begin{cases} \dfrac{|\boldsymbol{\tau}_{pd}| - \tau_y}{\mu_p} & \text{if} \quad |\boldsymbol{\tau}_{pd}| \geq \tau_y, \\ 0 & \text{if} \quad |\boldsymbol{\tau}_{pd}| < \tau_y. \end{cases} \tag{2.85}$$

This is equivalent to

$$|\dot{\boldsymbol{\gamma}}_v| = \max\left(\frac{|\boldsymbol{\tau}_{pd}| - \tau_y}{\mu_p}, 0 \right). \tag{2.86}$$

Replacing Eq. 2.86 in Eq. 2.56 results in

$$\eta_p = \begin{cases} \dfrac{\mu_p|\boldsymbol{\tau}_{pd}|}{|\boldsymbol{\tau}_{pd}| - \tau_y} & \text{if} \quad |\boldsymbol{\tau}_{pd}| \geq \tau_y, \\ \infty & \text{if} \quad |\boldsymbol{\tau}_{pd}| < \tau_y. \end{cases} \tag{2.87}$$

Now, using this formulation of the Bingham model to express the viscosity in the polymeric stress equation of the Oldroyd-B model (Eq. 2.75) results in:

$$\frac{1}{\eta_p}\boldsymbol{\tau}_p + \frac{1}{G}\overset{\nabla}{\boldsymbol{\tau}}_p = \dot{\boldsymbol{\gamma}}. \tag{2.88}$$

$$\max\left(\frac{|\boldsymbol{\tau}_{pd}| - \tau_y}{|\boldsymbol{\tau}_{pd}|}, 0\right)\boldsymbol{\tau}_p + \frac{\mu_p}{G}\overset{\nabla}{\boldsymbol{\tau}}_p = \mu_p\dot{\boldsymbol{\gamma}}. \tag{2.89}$$

It is important to note that the relaxation time is given by $\lambda = \eta_p/G$, not μ_p/G. Therefore, λ is no longer a constant. In EVP materials, λ is a function of η_p, which in turn depends on $|\dot{\boldsymbol{\gamma}}_v|$ and τ_y. For the specific case of the Saramito (2007) model, the relaxation time is expressed as $\lambda = (\tau_y/|\dot{\boldsymbol{\gamma}}_v| + \mu_p)/G$. This indicates that there is an interplay between plastic and elastic effects in EVP materials (Oishi et al., 2019).

The momentum conservation principle can be mathematically expressed for an interfacial flow involving an elasto-viscoplastic Saramito (2007) material as

$$\rho\left(\frac{\partial \mathbf{u}}{\partial t} + \mathbf{u}\cdot\nabla\mathbf{u}\right) = -\nabla p + \nabla\cdot(\boldsymbol{\tau}_s + \boldsymbol{\tau}_p) + \rho\mathbf{g} + \sigma\kappa\mathbf{n}\delta_S. \tag{2.90}$$

Here, $\boldsymbol{\tau}_s$ is given by E. 2.74 and $\boldsymbol{\tau}_p$ is given by Eq. 2.89. Recall that $-p\mathbf{I}$ is an isotropic tensor which contributes to the spherical part of the total stress tensor $\mathbf{T}$. It is not related to any kinematic quantity of the flow and does not have a constitutive equation. While $\boldsymbol{\tau}_s = \boldsymbol{\tau}_{ds}$, $\boldsymbol{\tau}_p \neq \boldsymbol{\tau}_{dp}$ due to the elastic nature of the material. Therefore, $\boldsymbol{\tau}_p$ contains a non-deviatoric part, which is different from $-p\mathbf{I}$ and can be expressed by a constitutive equation. A mechanical analog of Saramito (2007) model is exhibited in Fig. 2.26, where the mechanical analog of the Bingham model represents η_p.

In a time-depended numerical simulation, $|\boldsymbol{\tau}_p|$ is obtained from Eq. 2.89 in the current time step. Then, the value of η_p calculated from Eq. 2.87 is plugged back into Eq. 2.89 to calculate the stress in the next time step.

Later, Saramito (2009) proposed another model that combined the Maxwell model with

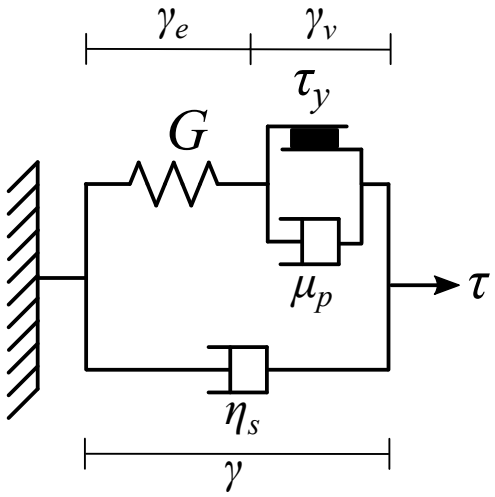

Figure 2.26: Mechanical analog of the Saramito (2007) model.

the Herschel-Bulkley model:

$$\eta_p = \begin{cases} \left(\dfrac{K|\boldsymbol{\tau}_{pd}|^{\mathtt{n}}}{|\boldsymbol{\tau}_{pd}| - \tau_y}\right)^{1/\mathtt{n}} & \text{if} \quad |\boldsymbol{\tau}_{ps}| \geq \tau_y, \\ \infty & \text{if} \quad |\boldsymbol{\tau}_{pd}| < \tau_y, \end{cases} \tag{2.91}$$

$$\max\left(\frac{|\boldsymbol{\tau}_{pd}| - \tau_y}{K|\boldsymbol{\tau}_{pd}|^{\mathtt{n}}}, 0\right)^{1/\mathtt{n}} \boldsymbol{\tau}_p + \frac{1}{G}\overset{\nabla}{\boldsymbol{\tau}}_p = \dot{\boldsymbol{\gamma}}. \tag{2.92}$$

The mechanical analog of this model is similar to the one shown in Fig. 2.26, except that μ_p is replaced by a term of the form $K\dot{\gamma}_v^{n-1}$.

The Saramito models have been used in a number of numerical simulations of flows involving EVP materials. For instance, Izbassarov and Tammisola (2020) studied the dynamics of EVP droplets immersed in a plane shear flow of a Newtonian fluid in 3D. The authors assessed the effects of the Bingham number, the Capillary number, the Weissenberg number, and the ratio of solvent and total drop viscosity on the drop deformation. Syrakos et al. (2020) applied the Saramito (2009) model to investigate the flow of an EVP material in a lid-driven cavity. Fraggedakis et al. (2016b) showed that these models can be solved coupled to the mass and momentum conservation equations without causing numerical difficulties or needing special numerical treatment. Fraggedakis et al. (2016a) were the first to simulate the settling of a single particle in an EVP material and predict the loss of fore-aft symmetry and the appearance of the "negative wake" behind it. Additionally, Moschopoulos et al. (2021) successfully predicted the inverted teardrop shape observed experimentally when using the

Saramito (2009) model to simulate rising bubbles. Such features are not predicted when using simple inelastic viscoplastic models and are further discussed in Sec. 2.4.2.

To conclude this section, it is important to mention that the elasto-viscoplastic models present here can reduce to simpler material formulations by adjusting G and τ_y. Table 2.1 presents the values of G and τ_y for the different model formulations.

Formulation	G	τ_y
Newtonian	$0,\ \infty$	0
Viscoelastic fluid	$]0, \infty[$	0
Viscoelastic solid	$]0, \infty[$	∞
Inelastic viscoplastic	∞	$]0, \infty[$
Elasto-viscoplastic	$]0, \infty[$	$]0, \infty[$

Table 2.1: Elasto-viscoplastic models formulation reduction based on the values G and τ_y.

2.4 The Drop Rise Phenomenon

This section presents a review of the drop rise phenomenon. It commences with an overview of drop rise in Newtonian fluids and subsequently delves into the literature on drop rise in non-Newtonian materials focused on the plastic and elastic behaviors.

2.4.1 Drop rise general concepts

The dynamics of rising drops in Newtonian fluids have been extensively discussed in the literature, with studies focusing on various aspects such as terminal velocity and shape of the drops (Clift et al., 1978; Bhaga and Weber, 1981; Wegener et al., 2010; Tripathi et al., 2014, 2015a; Cano-Lozano et al., 2016a; Sharaf et al., 2017; Charin et al., 2019). Drop rise is driven by the buoyancy force, which is proportional to drop volume and density difference between the fluids. As the boundary between the fluids is a free interface, the drop can deform in response to the action of external forces and surface tension. The velocity and shape of the rising drop play a crucial role in processes such as mixing, separation, and heat and mass transfer between the phases. These phenomena have significant applications in industries such as oil, liquid-liquid extraction, and vapor power systems (Saien and Jafari, 2019).

To better understand the dynamics of drop rise, it is helpful to consider the settling of a spherical solid particle in a quiescent Newtonian fluid within the Stokes regime. The

buoyancy force acting on the sphere can be determined using the equation:

$$\mathtt{F}_B = |\Delta\rho| g \pi \frac{D^3}{6}, \tag{2.93}$$

where $|\Delta\rho|$ is the density difference between the solid sphere and the surrounding fluid, g is the acceleration due to gravity, and D is the diameter of the sphere. At a steady state, $\mathtt{F}_B$ is balanced by the drag force, $\mathtt{F}_D$, which is given by

$$\mathtt{F}_D = \frac{1}{2} C_D \rho A u_t^2, \tag{2.94}$$

where ρ is the surrounding fluid density, $A = \pi D^2/4$ is the cross-sectional area of the drop, u_t is the sphere terminal velocity, and C_D is the drag coefficient. In the Stokes regime ($Re \ll 1$) the drag is predominantly friction drag, and C_D is given by

$$C_D = \frac{24}{Re} = \frac{24}{\frac{\rho D u_t}{\eta}}. \tag{2.95}$$

Here, η is the surrounding fluid viscosity. The drop terminal velocity, u_t, can be calculated by substituting Eq. 2.95 into Eq. 2.94, and then, equating it to Eq. 2.93:

$$u_{ST} = \frac{|\Delta\rho| g D^2}{18\eta}. \tag{2.96}$$

This is the Stokes terminal velocity of a solid sphere. Some inferences about the rise of drops can be already made based on Eq. 2.96. Firstly, the terminal velocity scales with the diameter squared, meaning that an increase in particle diameter, such as through coalescence, accelerates the phase separation process. Additionally, since the flow is driven by the buoyancy force, the velocity scales with the density difference. Moreover, the terminal velocity is inversely proportional to the viscosity of the surrounding fluid, suggesting that the rheological properties of the medium influence the dynamics of the rising process.

Now, consider the case of a fluid particle rising in a quiescent and clean liquid. The tangential stresses on both sides of the interface are equal, as seen in the tangential stress jump condition across the interface given by Eq. 2.20 with a constant σ. Unlike a solid sphere, the shearing at the drop surface transfer momentum to the drop interior, generating an internal circulating flow. Figure 2.27 illustrates the pattern of streamlines obtained from theoretical analysis (left) and experimental observations of a drop of glycerine falling through castor oil (right).

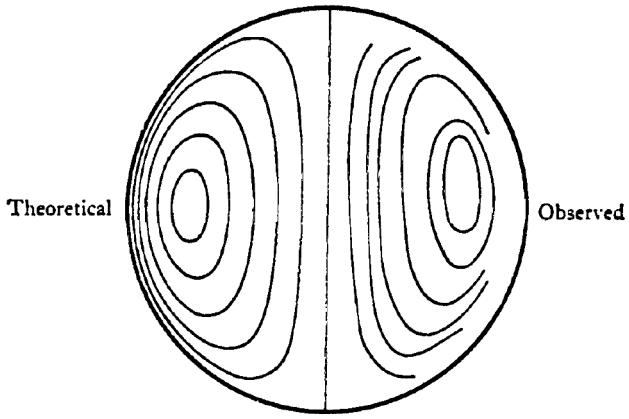

Figure 2.27: Streamlines of the circulating flow inside a droplet. The left side corresponds to a theoretical solution and the right side corresponds to a pattern observed experimentally for a drop of glycerine falling through castor oil.
Source: Batchelor (1967).

Hadamard (1911) and Rybczynski et al. (1911) (apud Clift et al. (1978)) extended the analytical solution for the Stokes terminal velocity of a solid sphere to the case of a rising drop in creeping flow, where surface tension and/or viscous forces dominate over inertia. The velocity of the rising drop in this regime, denoted as u_{HR}, can be expressed as:

$$u_{HR} = u_{ST} \left(\frac{\eta_{\mathsf{s}} + \eta_{\mathsf{d}}}{\frac{2}{3}\eta_{\mathsf{s}} + \eta_{\mathsf{d}}} \right). \tag{2.97}$$

Here, η_{s} is the surrounding fluid viscosity, and η_{d} is the drop viscosity. The drop shape is considered to be spherical. Equation 2.97 states that the terminal velocity decreases with an increase in the viscosity internal phase (*e.g.*, liquid drops rise slower than gas bubbles).

In practical situations, the interface between the drop and the surrounding fluid can easily become contaminated by surfactants. The adsorbed surface-active agents are swept to the back of the drop by the shear stress on the interface. As discussed in Sec 2.1, this creates a surfactant concentration gradient, and consequently, Marangoni stresses. As a result, the interface becomes immobilized in the tangential direction, preventing or reducing the occurrence of internal circulation within the drop (Maldonado et al., 2013; Pawliszak et al., 2019; Zawala et al., 2020). This effect is more pronounced for small drops (Clift et al., 1978; Kulkarni and Joshi, 2005). Figure 2.28(a) illustrates a schematic of a water droplet falling through oil in a clean system (without contaminants), along with the streamlines pattern associated with the internal circulating flow. In contrast, Fig. 2.28(b) depicts a schematic of a water droplet with a surfactant-contaminated interface. Despite falling through oil, no internal circulation occurs within the droplet due to the presence of surfactants on the inter-

face. As a consequence, the terminal velocity of drops and bubbles observed experimentally falls between u_{ST} and u_{HR} as a result of interface contamination.

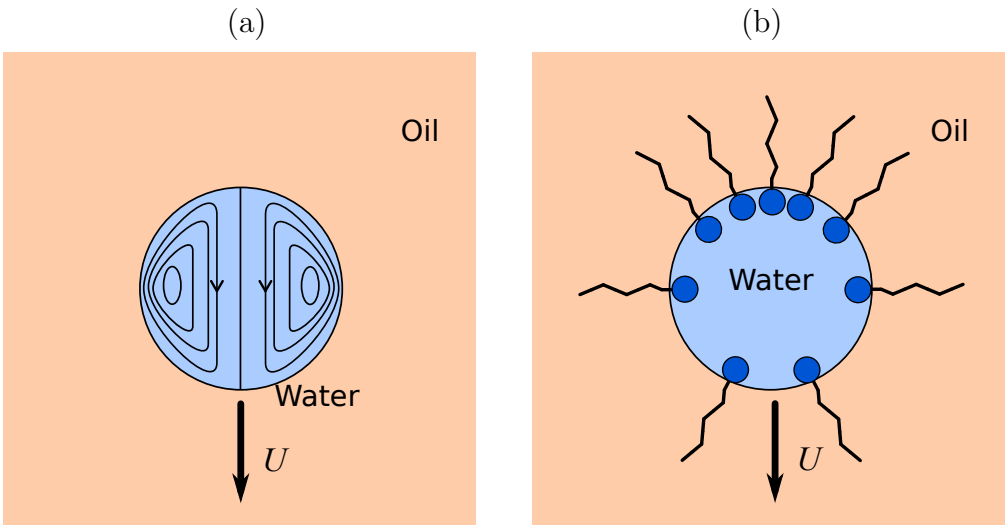

Figure 2.28: A water droplet falling in oil in (a) a clean system with internal circulation and in (b) a contaminated system with no internal circulation.

Increasing the drop diameter increases the relative significance of inertial forces compared to surface tension force and viscous forces. Consequently, the drop undergoes deformation from its initial spherical shape. The map presented in Fig. 2.29, originally introduced by Clift et al. (1978), illustrates the different shape regimes of rising bubbles and drops as a function of the Bond number ($Bo = |\Delta\rho| g D^2/\sigma$) and Reynolds number ($Re = \rho D u_t/\eta$). In this map, the drop diameter and terminal velocity are used as the characteristic length and velocity, respectively. It is important to note that, in most cases, the presence of surfactants in the multiphase system renders the internal phase viscosity less influential in determining the shape regimes depicted in the map.

The lines on the map of Fig. 2.29 represent constant Morton numbers, Mo. The Morton number depends on the properties of the fluids only and here is defined as

$$Mo = \frac{g\eta^4\Delta\rho}{\rho^2\sigma^3}. \tag{2.98}$$

Thus, in case of increasing the drop diameter in an experimental analysis using the same fluid system, the drop shape regime follows a line of constant Morton number.

For example, considering an air bubble rising in water with a Morton number of approximately 2.52×10^{-11} (or $\log Mo \approx -10.6$), small drops exhibit a spherical shape under creeping flow conditions characterized by low Reynolds and Bond numbers. As the drop diameter increases, both Re and Bo increase, leading to a higher rising velocity. Inertial forces,

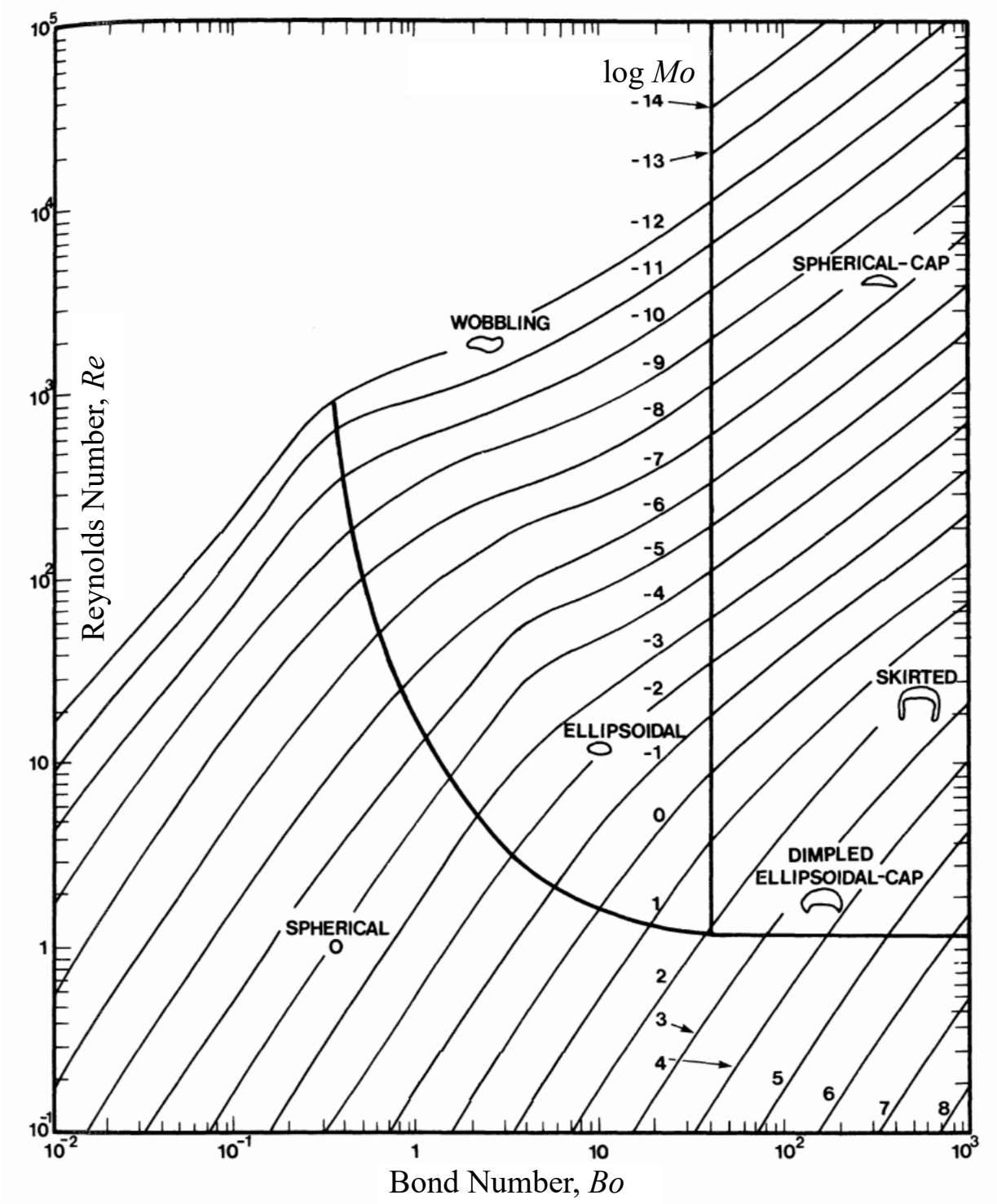

Figure 2.29: Drops and bubbles shape regime map.
Source: adapted from Clift et al. (1978).

which scale with ρu_t^2, increase faster than viscous forces, which scale with $\eta u_t/D$. Additionally, larger drop diameters are more deformable due to reduced surface tension effects, which scale with σ/D. Consequently, the higher hydrodynamic pressure on the front of the drop induces a departure from its spherical shape, resulting in an oblate ellipsoid with an aspect ratio, D_{AR}, less than unity ($D_{AR} = D_H/D_W < 1$, where D_W is the drop width and D_H is the drop height). Further increasing the drop diameter leads to the wobbling regime characterized by periodic oscillations and unsteady rising motion (Cano-Lozano et al., 2016a). For even larger diameters, Clift et al. (1978), Tripathi et al. (2015a), and Sharaf et al. (2017) observed that the drop acquires a spherical-cap shape, akin to a segment cut from a sphere, with fore-and-aft asymmetry and the potential development of a "skirt". Breakup regimes of drops have been predicted for much larger diameters by Tripathi et al. (2015a) and Sharaf et al. (2017).

The velocity of a rising drop and its shape are intricately linked. Figure 2.30 illustrates two curves depicting the terminal velocity, u_t, of air bubbles in water as a function of the bubble equivalent diameter, D. Experimental data points are also included and represented by symbols. The lower curve corresponds to a system contaminated with added surfactants, while the upper curve represents a "clean" system consisting of distilled water. At small diameters,

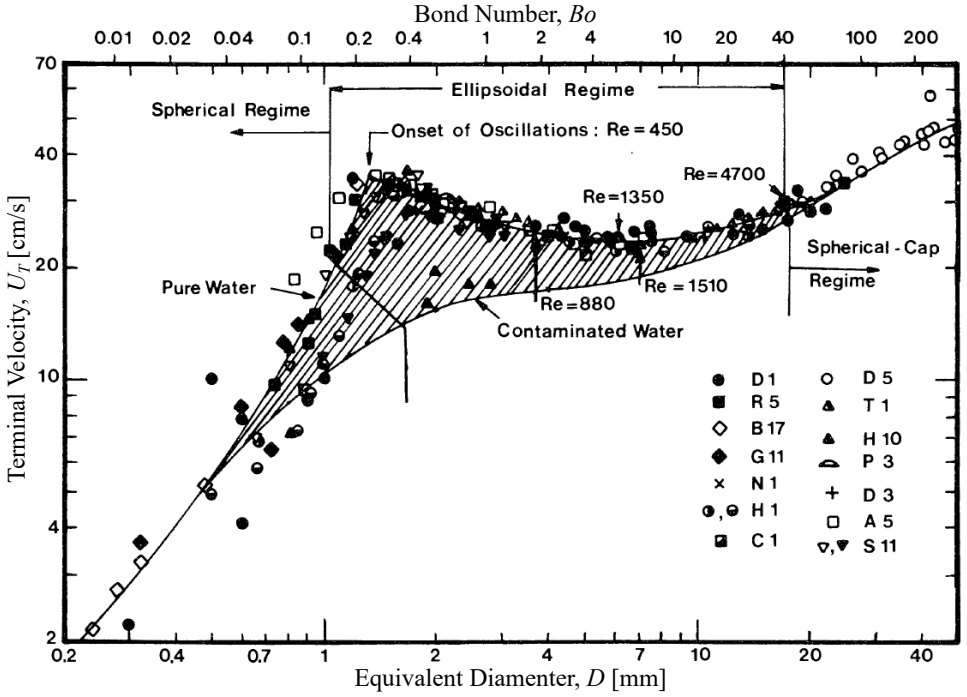

Figure 2.30: Terminal velocity of air bubbles in water. Symbols are experimental data, and the lines approximations for distilled water ("clean" system) and contaminated water. Source: adapted from Clift et al. (1978).

the bubbles exhibit a spherical shape, and the two curves converge. This convergence can be attributed to the fact that even trace amounts of contaminants (including those present in distilled water) can immobilize the interface of small bubbles. The surface tension coefficient between air and water is approximately $\sigma = 72.4, \mathrm{mN/m}$, and minor changes on the order of 0.1mN/m in the value of σ can induce a transition from a mobile to an immobile interface (Liu et al., 2019). According to Yaminsky et al. (2010), the presence of surfactants is not required for interface contamination in water. Since water is never a single-component liquid, ions inevitably present due to the water's self-dissociation can contribute to local variations in surface tension. It is widely acknowledged that air/water and oil/water interfaces are negatively charged due to the adsorption of hydroxyl ions, OH^-, which are formed through the reaction of excited oxygen atoms with water. Pawliszak et al. (2019) conducted an experimental study using high-purity water to investigate bubble rise velocities in the range of 50 to 1500 μm using a microfluidic chip. The authors found three distinct flow regimes, dependent on bubble size, which were associated with variations in the mobility of the bubble interface. For bubbles with diameters smaller than 200 μm, the rise velocity matched that predicted by the Stokes formula, Eq. 2.96. For bubbles larger than 800 μm, the rise velocity aligned with theoretical predictions for mobile interfaces. For intermediate-sized bubbles, the rise velocity gradually transitioned from that predicted for immobile interfaces to velocities characteristic of mobile interfaces as the diameter increased. Prior to reaching the terminal steady-state velocity, the bubbles attained a maximum velocity. The subsequent velocity decrease was attributed to the gradual adsorption of surfactants at the water/air interface, resulting in the immobilization of the interface and a reduction in bubble velocity. This demonstrated that the hydrodynamic boundary conditions experienced at the rising bubble surface depend on the bubble size. Even in ultra-pure water, the interfacial mobility of bubbles with diameters less than 400 μm was affected by traces of surface-active contaminants present in the system. This behavior can be attributed to the larger surface-to-volume ratio of smaller bubbles, making even trace amounts of impurities adsorbed at the water/air interface significantly impact the hydrodynamic boundary conditions of the fluid interface. The curves in Fig. 2.30 also converge for large bubbles, which assume a spherical-cap shape, where surface tension effects are less significant. In the intermediate diameter range, the bubbles exhibit an ellipsoidal shape with higher variability in terminal velocity. Inertia tends to flatten the bubble, increasing the cross-sectional area normal to the flow direction ($A = \pi D_W^2/4$) and subsequently raising the drag force. Thus, the bubble velocity curve may exhibit a maximum within the ellipsoidal region. Notably, in the clean system curve, a distinct change in the relationship between rise velocity and diameter is observed at the onset of oscillations. The unstable path of wobbling bubbles can manifest in various three-dimensional patterns, such

as zigzagging and spiraling (Cano-Lozano et al., 2016a). The cause of path instability remains a subject of debate in the literature, with Cano-Lozano et al. (2016b) suggesting that instability occurs when the amount of vorticity produced at the surface surpasses a critical value. As a portion of the energy of oscillating bubbles is expended in generating horizontal motion, their rising velocity decreases.

2.4.2 Drop rise in non-Newtonian fluids

In the context of drop rise in complex materials, the shape and velocity of the drop deviate from those observed in Newtonian fluids, resulting in significant implications for the handling of multiphase systems (Dimakopoulos et al., 2013; Premlata et al., 2017). This section provides a review of the literature on the effects of the surrounding phase plasticity and elasticity on drop rise dynamics.

The review begins by examining the influence of yield stress on drop rise dynamics. In the case where the surrounding fluid exhibits viscoplastic behavior, drops may become entrapped if the buoyancy force is insufficient to overcome the yield stress of the surrounding material (Dubash and Frigaard, 2004). The concept of the yield-stress parameter, Y_g, was introduced by Beris et al. (1985) for the fall of solid spheres in viscoplastic materials. It represents the ratio of the yield strength to the external buoyancy force acting on the sphere:

$$Y_g = \frac{3}{2}\frac{\tau_y}{R\Delta\rho g}. \tag{2.99}$$

The critical value of Y_{gc} for entrapment of solid spheres was calculated by Beris et al. (1985) to be 0.143. If $Y_g < Y_{gc}$, the particle moves; otherwise it is trapped by the yield stress. This threshold was later verified by the experimental data of Tabuteau et al. (2007). Numerous studies have been devoted to determining Y_{gc} in the case of fluid particles (Dubash and Frigaard, 2004, 2007; Sikorski et al., 2009; Tsamopoulos et al., 2008; Dimakopoulos et al., 2013; Lopez et al., 2018; Pourzahedi et al., 2022). Dubash and Frigaard (2004) theoretically estimated the entrapment condition of bubbles using variational principles. In cases where surface tension dominates over the yield stress ($\tau_y \ll \sigma/R$), the entrapment bubble assumes a spherical shape, and the authors estimated $Y_{gc} = 0.866$. Conversely, if surface tension effects are unimportant (for large bubbles), the value of Y_{gc} depends on the bubble shape, which can be non-unique due to the yield stress. Subsequently, Dubash and Frigaard (2007) experimentally demonstrated that the previously determined critical yield stress parameters for spherical bubbles overestimated the level of plasticity required for entrapment. The authors utilized a Carbopol solution as a model for the viscoplastic material, and the bubbles obtained exhibited an inverted teardrop shape with a cusp-like tail.

Tsamopoulos et al. (2008) conduct a numerical study investigating the rise of bubbles in a viscoplastic fluid under axisymmetric and steady-state conditions. The Papanastasiou model (PM) (Papanastasiou, 1987), a regularized version of the Bingham model, was employed to simulate the behavior of the viscoplastic material. The study focused on calculating the bubble shape and rise velocity, as well as the shape of the yield surface, for a wide range of dimensionless governing numbers, namely the Bingham ($Bi = \tau_y/\rho g R$), Bond ($Bo = \rho g R^2/\sigma$), and Archimedes ($Ar = \rho^2 g R^3/\mu_p^2$) numbers. Figure 2.31 illustrates the shape of bubbles and yielded surfaces obtained by the authors as a function of the Bi, Bo, and Ar. The results demonstrate that as the level of plasticity (indicated by the Bingham number) increases, bubbles tend to adopt a prolate shape ($D_{AR} > 1$) to facilitate penetration through the viscoplastic material. Additionally, regions of unyielded material can be observed inside the yield envelope, particularly near the bubble equator and below it. As the Bingham number increases further, these unyielded regions and the surrounding yield envelope tend to merge, resulting in the entrapment of the bubble. The study reports that the critical entrapment limit, denoted as Y_{gc}, ranges from 0.214 to 0.321 and varies monotonically with the Bond number. For a spherical bubble, the calculated value of Y_{gc} is 0.214, which is 3/2 times higher than the critical value for a solid sphere. This finding is in direct correspondence with the 3/2 higher terminal velocity of a bubble over that of a sphere under the same buoyancy force in Stokes flow.

Dimakopoulos et al. (2013) conducted a comparative analysis of the earlier findings by Tsamopoulos et al. (2008) using the Augmented Lagrangian Method to obtain steady-state solutions. They observed that the entrapment condition proposed by Tsamopoulos et al. (2008) provided a reliable estimate when the viscosity regularization parameter had sufficiently large values. Additionally, Dimakopoulos et al. (2013) investigated bubble rise in Herschel-Bulkley and Bingham fluids, and their results indicated that the entrapment condition was unaffected by the consistency and power-law indices of the fluid, consistent with the observations of Dubash and Frigaard (2007). The values of Y_{gc} obtained in their study ranged from 0.194 to 0.217.

In a numerical study by Potapov et al. (2006), the rise of single and paired drops falling in a tube filled with a viscoplastic fluid was investigated using a regularized viscosity function. The drops descended within a yielded material envelope. Unlike drops falling in Newtonian fluids, where the streamlines are open and nearly straight, the streamlines in the surrounding viscoplastic fluid were closed, restricted to the yield envelope. The authors observed that the size of the yielded region increased with decreasing Bingham number. For two drops falling in line, the size of the yielded region expanded significantly, eventually resulting in coalescence. These findings are consistent with the numerical results of Singh and Denn

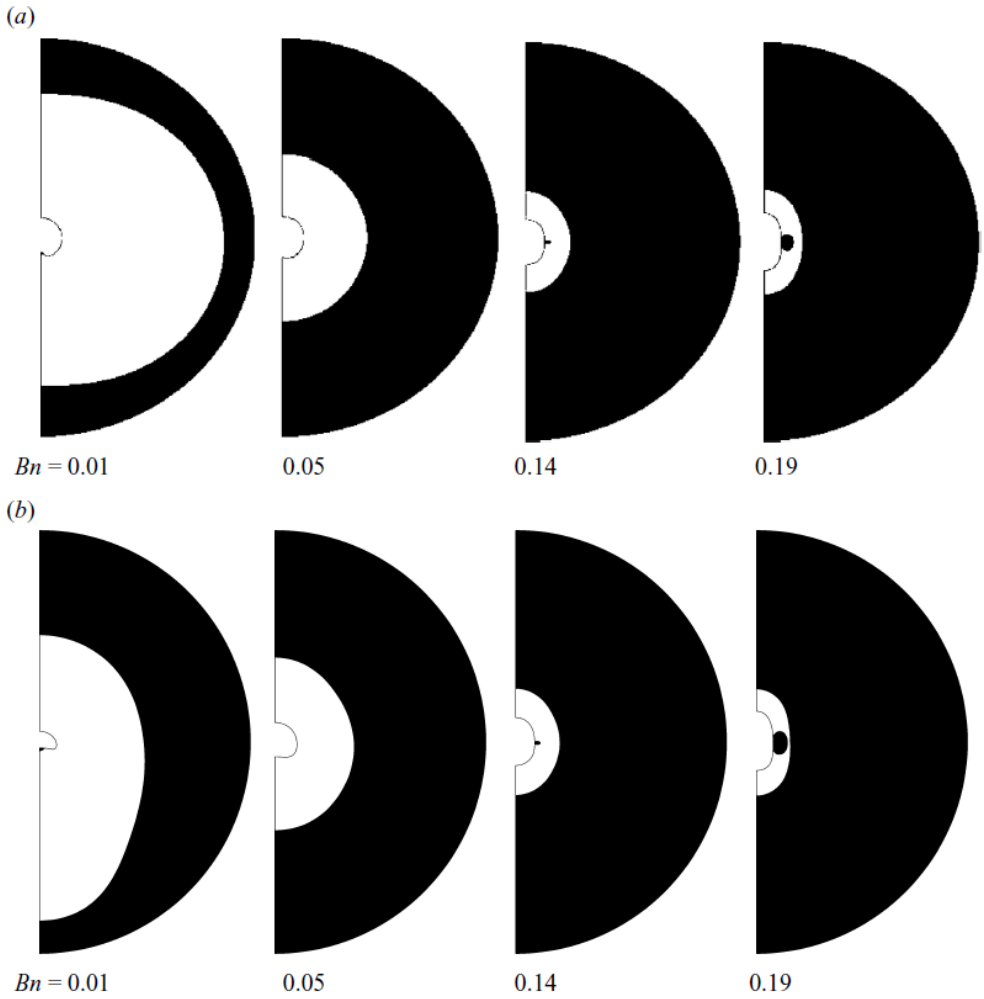

Figure 2.31: Bubble shape and yield surface shape dependence on the Bingham number ($Bi = \tau_y/\rho g R$). The yielded region is depicted in white and the unyielded region in black. (a) $Ar(= \rho^2 g R^3/\mu_p^2) = 1$ and $Bo(= \rho g R^2/\sigma) = 50$ and (b) $Ar = 50$ and $Bo = 10$.
Souce: Tsamopoulos et al. (2008).

(2008), who employed the Level-Set method to study the buoyancy-driven motion of bubbles and drops in Bingham materials, as well as the experimental observations of Lavrenteva et al. (2009), who investigated the fall of viscous drops in a tube filled with a Carbopol solution. The authors of the former study assumed a creeping flow condition and verified that multiple bubbles could move under the conditions in which a single bubble would be entrapped. Lavrenteva et al. (2009) noticed that the trailing drop exhibited a higher velocity than the leading drop, eventually resulting in coalescence. Coalescence sometimes led to the fragmentation of the larger drop, leaving behind a small and elongated fragment. The study also observed that small drops were permanently entrapped, while large drops underwent unsteady motion until eventual breakup. Intermediate-sized drops reached a steady state

after a relatively long transient period. Tripathi et al. (2015b) conducted transient numerical simulations employing the volume of fluid method and a regularized viscosity function. Their findings revealed that under conditions of high yield stress and weak surface tension, the rise of bubbles exhibited transient or oscillating behavior.

Sikorski et al. (2009) conducted a study on the rise of bubbles in Carbopol solutions. They observed that the bubbles exhibited an inverted teardrop shape with a rounded head and a cusp-like tail, rather than being spheroidal. The shape of the bubbles varied depending on their size, with smaller bubbles appearing longer and more slender compared to larger bubbles. This suggests that the influence of yield stress is significant for small bubbles, as surface tension effects alone were insufficient to maintain the spherical shape. For larger bubbles, inertial effects became more pronounced, resulting in a slightly more pronounced head and a more concave tail profile. In their study, Sikorski et al. (2009) proposed an alternative length scale for calculating the yield stress parameter. Instead of using the equivalent radius of a spherical bubble, they utilized the radius of the maximum cross-sectional plane normal to the flow, denoted as R_{max}. The yield stress parameter, Y_g, representing the ratio between the resistive force exerted by the yield stress and the buoyancy force, was defined as:

$$Y_g = \frac{3}{2}\frac{\tau_y}{R\Delta\rho g}\frac{R_{max}^2}{R^2}. \tag{2.100}$$

The denominator of the equation reflects the buoyancy force using the equivalent radius of a spherical bubble, while the numerator accounts for the resistance offered by the yield stress using the maximum radius, R_{max}. This parameter differs from the previously defined Y_g in Eq. 2.99 by a factor of $(R_{max}/R)^2$. Based on their experimental results, Sikorski et al. (2009) estimated the critical parameter Y_{gc} to be 0.50 ± 0.04.

Elastic effects manifest in intriguing phenomena observed during the rise of drops and bubbles, including distinctive features such as teardrop shapes, negative wakes, and velocity jump discontinuity (Bothe et al., 2022). Figure 2.32 depicts a bubble ascending in a viscoelastic fluid, exhibiting a remarkable teardrop shape characterized by a cusp-formed tail. For bubbles with volumes below a critical value, their shape are either a prolate or an oblate shape depending on the Reynolds number (Liu et al., 1995), suggesting that the ratio of inertial to elastic forces plays a pivotal role in determining bubble shape. For small inertia regimes, the prolate shape is caused by additional tension that elongates the bubble by the presence of elastic forces, rather than steady shear flow. As the size of the bubble increases, they may acquire the teardrop shape, as depicted in Fig. 2.32. In this scenario, smaller bubbles undergo vertical elongation, and larger bubbles adopt a flattened shape. However, in both cases, a cusped tail is observed (Kemiha et al., 2006). In Fig 2.32, the tail of the

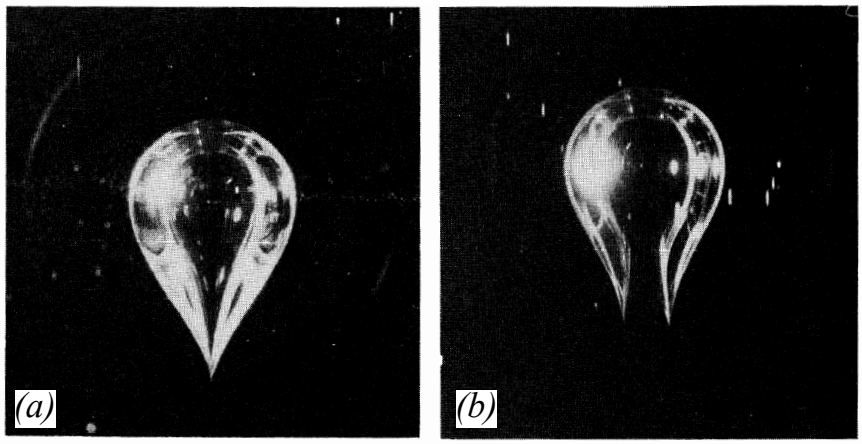

Figure 2.32: Bubble with a teardrop shape (with a cusped tail) rising in a polyacrylamide solution. (a) Front view and (b) side view. The end of the bubble tail is not symmetric but has a knife-edge shape, which forms an air sheet.
Source: Bird et al. (1987a).

bubble assumes an asymmetrical knife-edge-like form, creating a thin sheet of air. Notably, a cusp is observable from the viewpoint shown in Fig. 2.32(a), while a broader trailing edge is evident from the perspective in Fig. 2.32(b). Pillapakkam et al. (2007) conducted 3D direct numerical simulations (DNS) using the Oldroyd-B constitutive equation to study the transient and steady-state motion of bubbles rising in a viscoelastic fluid. Their findings revealed that bubbles below the critical volume adopt a prolate shape, while larger bubbles exhibit cusp-like trailing ends, consistent with experimental results by Liu et al. (1995). Fraggedakis et al. (2016c) performed axisymmetric numerical simulations, obtaining quasi-steady state solutions and investigating the jump discontinuity phenomenon. Their study encountered challenges in modeling bubbles beyond the critical regime, as experimental observations reported deviation from axisymmetry, which was also observed in the 3D numerical simulations by Pillapakkam et al. (2007). During the ascent of a bubble through a polymer fluid, polymer molecules undergo biaxial extension in the upstream region and experience uniaxial extension upon reaching the rear pole, leading to significant stretching aligned with the streamlines (Fraggedakis et al., 2016c; Bothe et al., 2022). Yuan et al. (2020) indicated that the stretching of polymers in the trailing edge region of the bubble causes an outward pull on the interface, resulting in a tapered trailing end. In scenarios where bubbles possess relatively low surface tension, the stretching of polymers can induce bubble breakup due to strong extensional flow, giving rise to satellite tails. In an experimental study of drops in a viscoelastic medium, Ortiz et al. (2016) confirmed that when the drop diameter exceeds a critical value, the drop tail breaks and releases small fragments, as depicted in Fig. 2.33.

In the case of viscoelastic fluids, the flow behavior around bubbles deviates from that

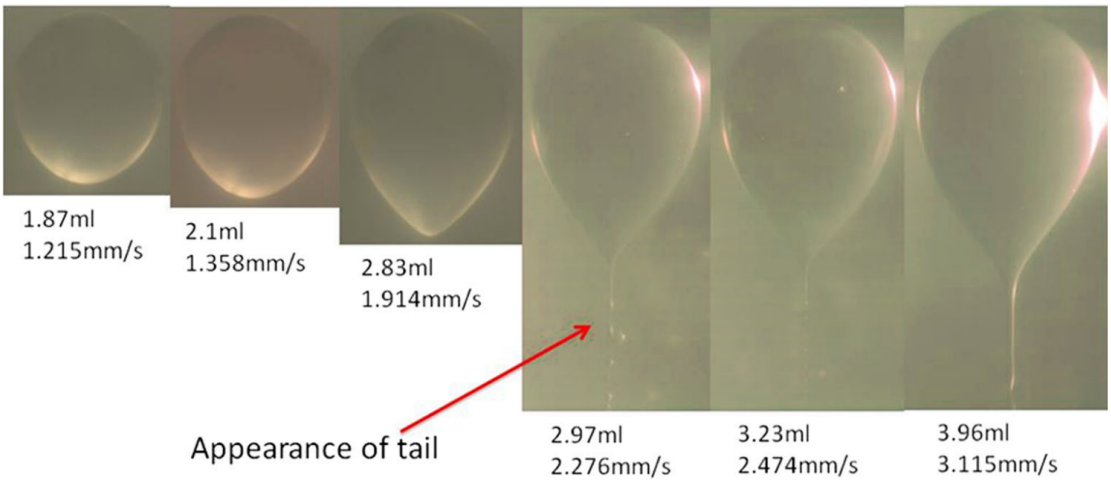

Figure 2.33: Oil drop of silicone oil rising in Polyox 0.5 % aqueous solution at different volumes and velocities.
Source: Ortiz et al. (2016).

observed in Newtonian fluids when the bubble volume exceeds a certain threshold, which may not necessarily correspond to the critical volume for cusped-tail formation (Fraggedakis et al., 2016c; Bothe et al., 2022). In the results presented by Pillapakkam et al. (2007), for a bubble with a diameter smaller than the critical volume, the wake structure closely resembles that of a bubble rising in a Newtonian fluid. Above this critical level, the flow field surrounding a bubble can be classified into three distinct zones, as depicted in Fig. 2.34: zone 1 exhibits an upward flow in front of the bubble, resembling Newtonian fluid behavior; zone 2 encompasses a hollow cone of upward flow surrounding, and zone 3, which comprises a downward flow in the central wake, commonly referred to as negative wake. Kemiha et al. (2006) employed Particle Image Velocimetry (PIV) to investigate the flow field around bubbles and glass spheres in polyacrylamide solutions. They found that the same flow pattern was observed for both bubbles and glass spheres, indicating that the physical mechanism underlying the negative wake is attributed to the viscoelastic nature of the fluid rather than particle deformation.

As the bubble volume surpasses another critical threshold, a sudden discontinuity in their rise velocity can be observed (Pilz and Brenn, 2007; Fraggedakis et al., 2016c; Bothe et al., 2022). The pioneering work by Astarita and Apuzzo (1965) first reported this phenomenon. The velocity change can reach up to an order of magnitude (Bothe et al., 2022). Some authors have associated this jump discontinuity with the appearance of a teardrop shape and the negative wake (Astarita and Apuzzo, 1965; Bird et al., 1987a; Bothe et al., 2022). However, subsequent studies confirmed that the presence of a cusp or teardrop shape alone is insufficient to explain the jump discontinuity (Pilz and Brenn, 2007; Fraggedakis et al.,

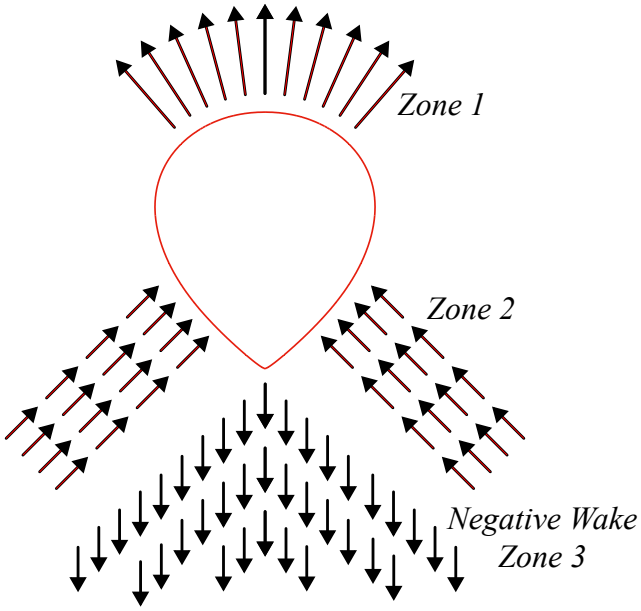

Figure 2.34: The overall flow pattern characterized by the negative wake surrounding a bubble immersed in a viscoelastic fluid.

2016c; Bothe et al., 2022). Bothe et al. (2022) conducted detailed numerical simulations of the transient rise of single bubbles in three dimensions. They attributed the jump discontinuity to the release of elastic energy stored in polymer molecules in the region below the bubble's equator. The energy was stored by the polymer molecules during the biaxial stretch in the upper stream region. Experimental velocity measurements in the liquid field surrounding the bubble supported the conclusion that the ratio of the Lagrangian transport time scale of polymer molecules along the bubble contour to the relaxation time scale of the polymer molecules determines whether the bubble motion is subcritical or supercritical. These findings illustrate that the ascent of drops and bubbles in viscoelastic materials is a dynamic and highly nonlinear process. The numerical results of Fraggedakis et al. (2016c) suggest that the change in the flow field after the jump velocity should be distinguished from the negative wake and teardrop shape formation. This is consistent with the numerical findings of Yuan et al. (2020), who also emphasized that there is no direct correlation between bubble deformation and the generation of the negative wake. In the subcritical regime, Fraggedakis et al. (2016c) observed a slight increase in bubble velocity with an increasing Deborah number, defined as $De = \lambda \rho g R/\eta$. Yuan et al. (2020) also noted a velocity increase with increasing Weissenberg number, defined as $Wi = \lambda\sqrt{g/R}$, which they attributed to the partial activation of polymer viscosity in a dynamic flow. Specifically, the Oldroyd-B fluid initially (starting from a relaxed state) exhibits effectively lower viscosity at higher Wi values when its overall viscosity matches that of a Newtonian fluid. This is caused by the delay in

stress build-up due to the elasticity of the material.

Depending on the flow parameters such as Reynolds number (Re), Bond number (Bo), and Weissenberg number (Wi), various rising dynamics can be observed. Furthermore, drops and bubbles ascending in viscoelastic liquids can exhibit pulsating rising velocities under conditions of high elasticity (Pillapakkam et al., 2007). Later, Yuan et al. (2021) constructed a map similar to the one presented by Clift et al. (1978) (see Fig. 2.29) using three-dimensional numerical simulations of bubbles rising in viscoelastic fluids modeled by the Phan-Thien and Tanner model (Thien and Tanner, 1977). In their map, the Reynolds number ($Re = \rho D u_t/\eta$) was replaced by the Galilei number ($Ga = \rho g^{1/2} R^{3/2}/\eta$), which was obtained by substituting the terminal velocity u_t by the characteristic velocity $U = \sqrt{gR}$. The transition from prolate ellipsoidal to teardrop shape, along with the associated velocity jump, occurred at low Ga values (< 1) and low $Bo = \rho g R^2/\sigma$ values (< 1). At higher Galilei numbers (approximately 10), while maintaining the same Bond number, bubbles became oblate due to inertial effects and exhibited shape changes over time (pulsation). For intermediate values of Ga and $Bo \sim 10$, smaller bubbles experienced tail break-up, whereas larger bubbles formed a skirt at their rear.

Understanding and modeling the flow dynamics of elasto-viscoplastic materials presents significant challenges due to their diverse non-Newtonian behaviors. In some cases, the elastic effects exhibited by real viscoplastic materials are considered relatively small and often neglected to simplify the modeling process. Instead, inelastic viscoplastic models, such as the Bingham model, are commonly employed (discussed in Section 2.3.1). This approach is frequently adopted for Carbopol, a solution widely used to mimic ideal viscoplastic behavior. Carbopol possesses favorable properties such as low cost, ease of preparation, transparency, and minimal elastic behavior at low shear rates (Balmforth et al., 2014; Pourzahedi et al., 2021). However, certain experimental observations made with Carbopol cannot be adequately predicted, even qualitatively, by inelastic models (Dubash and Frigaard, 2007; Lopez et al., 2018; Pourzahedi et al., 2021). One notable example is the distinct teardrop shape typically observed for bubbles rising in viscoelastic fluids (Bird et al., 1987a; Fraggedakis et al., 2016c; Yuan et al., 2020). Such a shape is not observed in inelastic fluids (Dubash and Frigaard, 2007), rendering numerical simulations based on inelastic viscoplastic models incapable of reproducing this behavior, even at a qualitative level (Dimakopoulos et al., 2013). Pourzahedi et al. (2021) demonstrated that the geometrical differences in bubble shape between experiments and numerical simulations arise from the elastic nature of the fluid, which is absent in simple rheological models used in simulations. The authors employed a multi-layered experimental design to eliminate any possible influence from the injection process. The pointed tail, caused by the fluid's rheology, remained observable. Elasticity can also contribute to dis-

crepancies in estimating bubble entrapment conditions between numerical and experimental studies (Lopez et al., 2018; Moschopoulos et al., 2021). Experimental observations of elastic effects during bubble ascent can be qualitatively reproduced through numerical models that incorporate both elastic and plastic effects. Moschopoulos et al. (2021) utilized the elasto-viscoplastic constitutive model proposed by Saramito (2009) and successfully predicted the teardrop shape of bubbles rising in elasto-viscoplastic media. The authors also observed the formation of a negative wake in the trailing edge of the bubble, even under creeping flow conditions. The entrapment condition for the bubbles analyzed was $Y_{gc} \approx 0.24$ (using Eq. 2.99), slightly higher than that predicted by Tsamopoulos et al. (2008) and Dimakopoulos et al. (2013) for spherical bubbles in the inelastic viscoplastic formulation. The authors attributed the increase in Y_{gc} to the incorporation of normal stresses in the von Mises criterion, facilitating the material yielding. Holenberg et al. (2011) experimentally studied the fall of Newtonian drops in a low concentration Carbopol aqueous solution in creeping flow conditions. The authors employed PIV (Particle Image Velocimetry) and PTV (Particle Tracking Velocimetry) to determine the yielded surface and to visualize the flow inside the yielded region, respectively. Even though no cusped tail was observed, probably due to the low level of elasticity since the Carbopol concentration was low, the authors were able to detect a negative wake behind the drop.

Fluid characterization and memory effects presents various challenges in experiential works. In case of studying Carbopol solutions, changing the Carbopol concentration alters multiple properties simultaneously, making it difficult to vary parameters independently. For example, the commonly used Herschel-Bulkley constitutive model for fitting the flow curve of Carbopol solutions requires consideration of three rheological parameters, which cannot be varied independently (Dubash and Frigaard, 2007). Additionally, separating the contributions of plastic, elastic, and other non-Newtonian behaviors is not straightforward. In experimental setups, the drop diameter is often the only other parameter that can be modified. Consequently, even the Reynolds and Bond numbers are not varied independently.

Care must also be taken to minimize issues related to repeatability and fluid relaxation time. Dubash and Frigaard (2007) observed that after the release of an initial bubble, subsequent bubbles of the same volume exhibited significantly higher rise velocities and substantially different shapes if the fluid in the column was not adequately mixed. Furthermore, if the first bubble followed a winding and tortuous path, the subsequent bubbles would follow the same path, suggesting the creation of a preferential path. To address this, thorough mixing or complete replacement of the fluid is necessary after each bubble passage to minimize the shear history and improve result consistency and repeatability. Preferential paths are attributed to internal stresses that can persist for long periods, even years, without relaxation.

Carbopol solutions may contain undissolved polymeric particles, and the rise of a bubble can alter the particle distribution, leading to inhomogeneity. Regions with higher particle concentration exhibit higher viscosity and yield stress (Lopez et al., 2018). Mougin et al. (2012) investigated the influence of internal stresses on bubble dynamics in Carbopol solutions. Figure 2.35 illustrates a sequence of bubbles injected by the authors, which followed a preferential and tortuous path along regions of lower stress resistance. The radial expansion of the bubbles is restricted, causing elongation. Occasionally, the slender bubbles break and leave behind small fragments. PIV analysis confirmed that at a distance approximately equal to one bubble diameter from the bubble surface, the fluid experiences elastic strain that does not alter the particle distribution once the bubble has passed.

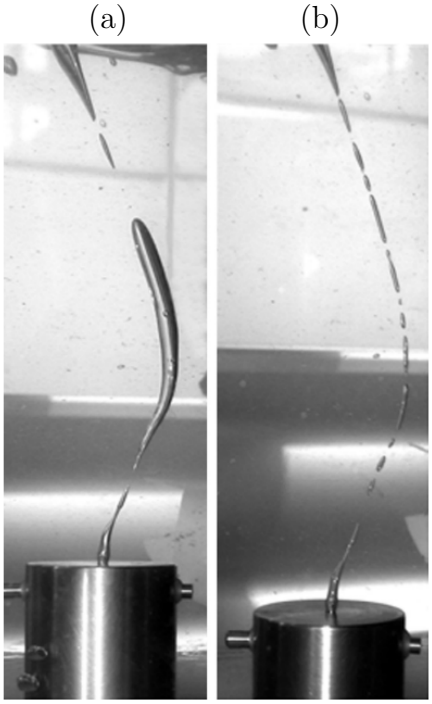

Figure 2.35: (a) Bubble rising in a Carbopol solution and leaving (b) a trail of entrapped small bubbles.
Source: Mougin et al. (2012).

Lopez et al. (2018) conducted an experimental study on the rise of single bubbles in a quiescent elasto-viscoplastic materials, specifically an aqueous solution of Carbopol 980 NF polymer. Their investigation focused on bubble dynamics and shape under low and intermediate Reynolds number regimes, considering the influence of yield stress, inertia, buoyancy, and elasticity. However, due to the dependence of these factors on bubble size, isolating their individual effects proved challenging. The authors also observed the presence of teardrop-shaped bubbles in their experiments. The entrapment condition, given by Y_{gc}, was

estimated to be approximately 0.13 using the alternative definition given in Eq. 2.100, and it varied between 0.15 and 0.45 when using the original definition in Eq. 2.99. These values differ significantly from those reported by Sikorski et al. (2009). The competition between inertia and elasticity was well-described by the ratio of Reynolds number to Deborah number, defined as $Re = \rho u_t R/\eta_c$ and $De = (\eta_c/G)(u_t/R)$, respectively, where the η_c is a characteristic viscosity given by $\eta_c = \tau_y/(u_t/R) + K(u_t/R)^{n-1}$. For low ratios of Re/De, slender/cusped bubble shapes were observed, while high values of the ratio resulted in oblate-shaped bubbles.

2.5 The Drop Coalescence Phenomenon

This section reviews the drop coalescence phenomenon in both Newtonian and non-Newtonian mediums. Similar to the previous section, it initiates with an overview of the general concepts of coalescence in Newtonian fluids and concludes with a review of drop coalescence in non-Newtonian materials.

2.5.1 Drop coalescence general concepts

Owing to the excess surface free energy, two drops, or a drop and its phase bulk, may coalesce when in close proximity. Coalescence, along with breakup, governs the drop size distribution in dispersed systems, and thus, it is a key factor in the dynamics of heat, mass, and momentum exchange in multiphase systems (Liao and Lucas, 2010). The process of coalescence can be categorized into binary coalescence, which occurs between two drops, and interfacial coalescence, which transpires between a drop and its phase bulk. Irrespective of the type, it may be divided into four sequential steps that span a wide range of length and time scales: i) collision, ii) film drainage, iii) film rupture, and iv) merging (Goel and Ramachandran, 2017; Liao and Lucas, 2010; Mohamed-Kassim and Longmire, 2003; Chesters, 1991). Figure 2.36 depicts the various stages of coalescence between a drop and its bulk phase. The collision phase arises from the action of external forces that bring the fluid bodies together. In the context of binary coalescence, it can take place due to motion induced by turbulence and velocity gradients of the surrounding phase, and different rise velocities of drops of different sizes (Liao and Lucas, 2010). Conversely, interfacial coalescence is primarily driven by buoyancy, thereby emphasizing the significance of drop rising dynamics (Fig. 2.36(a)) in the coalescence process. During the collision step (Fig. 2.36(b)), a portion of the surrounding fluid becomes trapped, forming a thin liquid film that needs to be drained out for the completion of the coalescence process. The drop velocity and shape during the collision step dictate the film's initial shape and size, consequently influencing the unfolding

of the film drainage process (Chan et al., 2011). The thinning process (Fig. 2.36(c)) continues until the film thickness reaches a critical rupture threshold, at which point non-hydrodynamic short-range intermolecular forces destabilize and rupture the film (Fig. 2.36(d)). The length and time scales involved are of the order of nanometres and milliseconds, respectively. After film rupture, a bridge is formed, and the bulk fluids of the internal phase merge due to surface tension effects (Fig. 2.36(e)) (Weheliye et al., 2017).

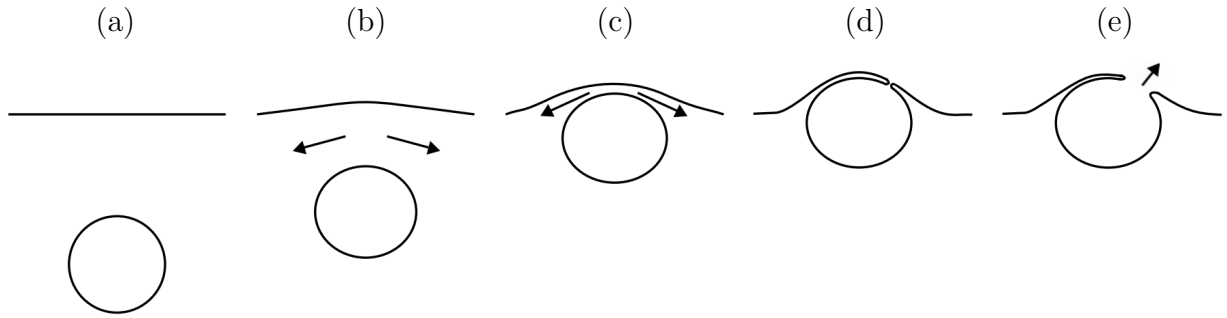

Figure 2.36: Interfacial coalescence process: (a) drop rise, (b) drop impact on a liquid-liquid interface and trapping of a film of the surrounding phase, (c) drainage of the trapped film, (d) rupture of the film, and (e) merging of the fluids.
Source: adapted from Aarts and Lekkerkerker (2008).

Modeling the temporal evolution of the drop size distribution is of paramount importance in the analysis of dispersed system flows. However, due to the wide range of temporal and spatial scales associated with the coalescence phenomenon, it becomes highly challenging to fully resolve all the relevant scales in numerical simulations using current state-of-the-art computing capabilities. Resolving each step of the coalescence process, spanning from drop impact at the centimeter scale to film rupture at the nanometer scale, would necessitate an excessively large number of grid points (approximately 10^7 in each direction), leading to prohibitively high computational costs (Tryggvason et al., 2011). Even without explicitly resolving the intricate flow within the film, simulating each drop within a dispersed system (drop swarm) incurs significant computational expenses. Consequently, numerical simulations of dispersed systems commonly employ the Population Balance Equation approach, where the phases are treated as interpenetrating, and the drops are categorized into size classes. Each size class represents a range of drop sizes and accounts for a certain percentage of the total mass of the dispersed phase. In the event of coalescence or breakup, the mass distribution within each size class changes (Deoclecio et al., 2020).

The PBE approach relies on the utilization of kernels or models to estimate coalescence and breakup rates, thereby enabling the prediction of the temporal evolution of the droplet size distribution. Coalescence is considered more complex than breakup because it involves

the interaction between the continuous phase and two fluid particles, whereas breakup only involves the continuous phase and one fluid particle (Chesters, 1991). Coalescence models used with the PBE formulation generally are composed of two terms, one for the collision frequency between fluid particles, and one for the collision efficiency. The former depends on the mechanism that brings the drops together (*e.g.*, turbulence and buoyancy), while the latter accounts for the outcome of the collision, recognizing that not all collisions lead to coalescence. For binary coalescence, most of the models for the collision efficiency component are based on the film drainage theory. This theory posits that during a collision, part of the kinetic energy of the drop is dissipated by viscous effects, and part is converted (stored) to surface free energy (interface deformation), which subsequently attempts to restore the fluid particle to a spherical shape. Consequently, a collision between two drops may result in rebound (no coalescence) if the time required for film drainage to reach the critical rupture thickness exceeds the contact time between the drops (Liao and Lucas, 2010). A comprehensive review of coalescence kernels can be found in Liao and Lucas (2010).

The lubrication theory is commonly employed to simplify the mass and momentum equations when analytically resolving the drainage of a thin liquid film (Ozan et al., 2021). This theory is applicable to gentle collisions, where the deformation of the drop interface is small, $h \ll s \ll D$ (h is the film thickness, s is the film length, and D is the drop diameter). The lubrication theory often incorporates simplifications such as imposing initial and boundary conditions, neglecting the collision dynamics, and disregarding inertial terms in the momentum conservation equation (Stokes flow) (Chesters, 1991; Abid and Chesters, 1994; Chan et al., 2011; Goel and Ramachandran, 2017). As a result, models derived from the theory typically include adjustable parameters (Liao and Lucas, 2010). A thorough review of drainage models, focusing on low Reynolds numbers where inertial effects are negligible in hydrodynamic interactions, is provided by Chan et al. (2011). In contrast to the lubrication theory, direct numerical simulations of the full conservation equations offer valuable insights into the dynamics of film drainage and can facilitate the development of novel coalescence models. However, the use of numerical simulations for investigating film drainage remains limited, with only a few attempts reported in the literature (Vakarelski et al., 2022; Albadawi et al., 2014).

The coalescence process is similar for both binary and interfacial collisions, and in certain cases, theoretical solutions can be unified through the concept of equivalent radius (Chesters, 1991; Oldenziel et al., 2012). For gentle collisions, the theoretical solutions for film drainage between two drops of the same size, two drops of different sizes, or between a drop and an interface can be the same via the equivalent radius principle. The equivalent radius, denoted

as R_{eq}, is determined by the following expression:

$$R_{eq} = \frac{2}{\dfrac{1}{R_{\mathtt{d1}}} + \dfrac{1}{R_{\mathtt{d2}}}} \tag{2.101}$$

where $R_{\mathtt{d1}}$ is the radius of the first drop and $R_{\mathtt{d2}}$ is the radius of the second drop. In case of interfacial coalescence, $R_{\mathtt{d2}} = \infty$, and thus $R_{eq} = 2\,R_{\mathtt{d1}}$. Hence, for interfacial coalescence, the collision can be viewed as a binary collision between a drop of finite size and a drop of infinite size. The main difference between binary and interfacial collisions is that in the former, buoyancy keeps pushing the interfaces together and the drop may rebound on the interface more than once. However, unless film rupture is impeded by short-range forces, the merging of the fluid bodies will eventually take place. In this context, the film drainage process governs the time required for coalescence to occur, rather than determining whether coalescence will occur. Besides the extrapolation of results derived from the study of interfacial coalescence to binary coalescence, even if only qualitative, the former is also an important phenomenon in its own right. For example, the conversion of the dispersed phase in a gravitational separator into a continuous phase depends on interfacial coalescence.

At the moment the film thickness approaches the critical rupture thickness, short-range intermolecular forces become relevant to the flow dynamics. The magnitude of these forces depends on the film thickness h, and are either attractive or repulsive in nature. For example, the van der Waals forces (introduced in Sec. 2.1) between two identical phases are attractive. Hence, at the moment the film reaches a thickness where these forces become important, the van der Waals forces assist in bringing the two interfaces together in a non-hydrodynamics drainage, which accelerates the drainage process by increasing the pressure in the film. This additional pressure is known as disjoining pressure Π, and for the van der Waals forces, it is negative and can be expressed as:

$$\Pi_{vdW} = \frac{-A_H}{6\pi h^3}. \tag{2.102}$$

Here, A_H is the Hamaker constant which is actually a function of h. It depends on the dielectric properties of the materials involved and typically has a value on the order of $10^{-20} J$. For pure fluids, considering only the van der Waals forces, Chesters (1991) proposed the following equation for the critical film rupture thickness

$$h_{\mathtt{c}} = \left(\frac{A_H R_{eq}}{8\pi\sigma}\right). \tag{2.103}$$

Alternatively, other surface forces, such as the Electrical Double Layer (EDL), act in a repulsive manner, aiming to keep the film interfaces separated. As discussed in Sec. 2.1, an

electrostatic repulsive force repeals the interfaces away when the interfaces become electrically charged. The dispersed phase may become charged by the adsorption of ionic species present in the solution. Suppose that these ions are cations, and the interface becomes positively charged. As a result, a layer of anions (negatively charged) will be formed around the positively adsorbed cations, while non-adsorbed cations will be repealed. This anion layer is tightly bound to the surface. As one moves away from the interface, a second layer composed predominantly of anions not bond to the interface is formed. Moving further away from the interface, the distribution of ions is uniform and electric neutrality is obtained (Martin et al., 2006). Therefore, as expected, the presence of surfactants tends to strengthen the repulsive forces and stabilize the film. In this case, the disjoining pressure Π_{EDL} is positive. If the resultant disjoining pressure $\Pi = \Pi_{EDL} + \Pi_{vdW}$ is positive, the film stabilizes, and after some drainage time, it acquires a nearly parallel and flat shape. Conversely, if the attractive forces outweigh the repulsive forces, the film becomes destabilized and eventually ruptures (Chan et al., 2011; Yaminsky et al., 2010).

For a negative disjoining pressure, the film drainage step controls the outcome of the collision. For a binary impact, the outcome can be rebound or coalescence, while for an interfacial collision, film drainage controls the coalescence time (Chesters, 1991; Kamp et al., 2017; Henschke et al., 2002). Therefore, understanding the dynamics of film drainage is crucial for improving mixing and separation processes. Due to the action of the external forces, a radial pressure gradient arises within the squeezed film, that acts against viscous forces, to drain out the surrounding phase. The fluid-fluid interfaces then deform in response to this pressure gradient. The shape change of the film, which is influenced by the density, viscosity, surface tension coefficient, and mobility of the interface, in turn affects the drainage process.

The flow in the film is strongly influenced by the mobility of the interface, which directly impacts the boundary conditions and the dynamics of drainage. The interface mobility may be classified as mobile, immobile, and partially mobile (Oldenziel et al., 2012). Figure 2.37 showcases the velocity profiles developed in the film based on the interface mobility. In contaminant-free systems with low viscosity ratios ($\eta_r = \eta_{\mathsf{d}}/\eta_{\mathsf{s}} \ll 1$, where η_{d} is the viscosity of the drop and η_{s} is the viscosity of the surrounding fluid), the interface is considered mobile (Fig. 2.37(a)). In this case, the flow in the film can be approximated as a fluid being squeezed between two parallel disks with a free slip boundary condition, resulting in a uniform velocity profile $u(h)$ (plug flow). Consequently, the pressure gradient along the film is weak. Conversely, in contaminated and/or high viscosity ratio systems ($\eta_r = \eta_{\mathsf{d}}/\eta_{\mathsf{s}} \gg 1$), the interface tends to be immobile (Fig. 2.37(b)). Here, the flow in the film resembles a fluid being squeezed between two disks with a no-slip boundary condition, leading to a Poiseuille

flow velocity profile. In this scenario, the pressure gradient along the film is strong. For intermediate viscosity ratio values, the interface is partially mobile, and the flow in the film can be considered as a combination of Poiseuille flow and plug flow, as depicted in Fig. 2.37(c). The pressure gradient in this case is moderate.

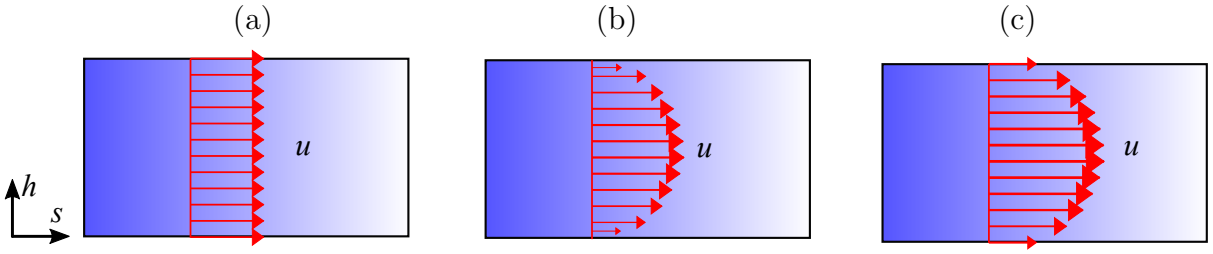

Figure 2.37: Example of the velocity profile in the film for different interface mobilities: (a) mobile interface with a plug flow, (b) immobile interface with a Poiseuille flow, and (c) partially immobile interface with a superposition of a Poiseuille flow and a plug flow. The coordinate s is along fluids interface and the coordinate h is along the film thickness.

The deformability of the film is closely linked to the mobility of the interface. In the case of mobile interfaces, where the pressure gradient ∇p along the film is weak, the film tends to have its minimum thickness h_{min} at the center (the film is spherical: the film thickness increases monotonically from the center to the periphery). However, for immobile interfaces with a strong pressure gradient ∇p along the film, the interface forms a dimple, resulting in the minimum film thickness occurring at the film periphery (Chi and Leal, 1989; Oldenziel et al., 2012; Liu et al., 2019). Figures 2.38(a) and (b) depict the collision of two bubbles with a solid wall under free slip and no-slip boundary conditions, respectively. In Fig. 2.38(a), the minimum film thickness is observed at the film center ($r = 0$), while in Fig. 2.38(b), the film forms a dimple and the minimum film thickness occurs at the film periphery. Due to the nearly constant pressure inside the drop/bubble, which is approximately equal to the Laplace pressure ($\approx \sigma/D$), the film assumes a concave shape in the center (higher pressure within the film than within the drop) and a convex shape at the periphery (lower pressure within the film than within the drop) in Fig.2.38(b). The presence of the dimple creates an obstruction to the flow in the film periphery, making the drainage process more challenging.

Aarts and Lekkerkerker (2008) studied the interfacial coalescence of bubbles and liquid drops with a liquid-liquid interface and with a fluid-gas interface, respectively. The authors observed that film rupture tends to occur at center of the film for bubbles, while for drops, it occurs on one side of the film. Liquid drops initially exhibit a symmetric film shape, but instabilities in the system often lead to asymmetry (Oldenziel et al., 2012; Burrill and Woods, 1973). This loss of symmetry accelerates the drainage process as the constriction on one side of the film widens, facilitating drainage. The exact cause of this loss of symmetry

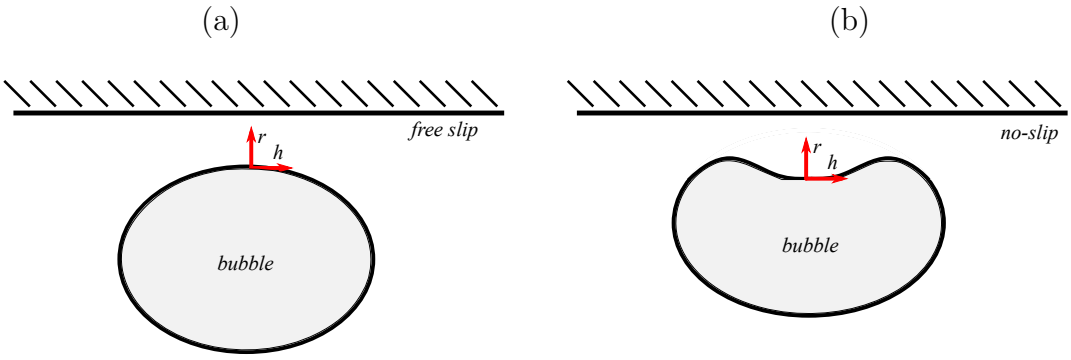

Figure 2.38: Bubble deformation when impacting on a solid wall with (a) free slip boundary condition and (b) no-slip boundary condition. In (a) the film thickness $h(r)$ minimum occurs at the film center, while in (b) the minimum occurs at the film periphery.

is still unclear (Liu et al., 2018). It may be induced by a surfactant concentration gradient that generates a Marangoni flow (Burrill and Woods, 1973; Shi et al., 2021), or it may result from a small disturbance in the experiment that disrupts the system's unstable configuration (Oldenziel et al., 2012). The system's unstable configuration arises from the density difference between the phases. For instance, in the coalescence of an air bubble at an air/water interface, the water trapped above the bubble is heavier than the air below, leading to an unstable configuration where any disturbance can cause preferential drainage from one side of the film.

Increasing interface mobility tends to enhance the drainage rate due to reduced viscous resistance and the more spherical film shape. Vakarelski et al. (2019) experimentally found that bubbles with mobile interfaces exhibit stronger bouncing but faster coalescence compared to bubbles with immobile interfaces. This behavior was attributed to lower viscous dissipation in mobile interfaces. Bubbles with contaminated interfaces may experience coalescence times three orders of magnitude longer than those of clean bubbles (Liu et al., 2019).

In addition to the film drainage theory, another approach is the critical approximation velocity theory. Models based on this theory rely on experimental data indicating that coalescence between two bubbles occurs when the approach velocity is below a threshold, otherwise resulting in rebound (Ribeiro and Mewes, 2006). Ribeiro and Mewes (2007) experimentally verified that the critical velocity for coalescence decreases with increasing bubble diameter, which aligns with the film drainage theory. For interfacial coalescence, increasing bubble diameter leads to higher impact velocity and greater deformability (reduced Laplace pressure). Consequently, the impact of a larger bubble forms a larger film, potentially with a substantial dimple, compared to the impact of a smaller bubble. In this case, the buoyancy force pressing the bubble against the interface and draining the film is distributed over a larger area, resulting in a reduction in the average pressure within the film responsible for

film drainage. Zawala and Malysa (2011) studied the collision of bubbles at a water/air interface with different impact velocities, achieved by varying bubble diameter and rising distance. The authors found that coalescence time increased with bubble velocity and was related to the size of the liquid film formed. Depending on the impact velocity, bubbles could bounce several times on the interface before coalescing, prior to the film reaching the critical film rupture thickness. Kočárková et al. (2013) conducted experimental investigations on drainage time as a function of the Bond number ($Bo = \rho g D^2/\sigma$). They observed that the thinning rate decreased as the Bond number increased. This behavior was attributed to the interplay between the increase in film area associated with an increase in buoyancy force (higher impact velocity) and the decrease in surface tension force, which allowed for a greater deformation of the fluid interfaces.

2.5.2 Drop coalescence in non-Newtonian fluids

Drop coalescence in non-Newtonian materials, particularly those exhibiting plastic and elastic behaviors, has been relatively understudied compared to its Newtonian counterpart, despite the significance of such materials in various industries, including petroleum, medicines, cosmetics, and food. Dispersed systems like oil-in-water emulsions are thermodynamically unstable due to the surface free energy minimization. However, they can be made kinetically stable by the use of surfactants to modify the interface properties and create a barrier against coalescence, or by the use of stabilizers dissolved in the continuous phase to alter its rheological characteristics (Nomena et al., 2018). Most studies have focused on Newtonian fluids, with strategies for stabilizing (or destabilizing) dispersed systems primarily centered around interfacial properties, which can be modified by surfactant addition or removal (Goel and Ramachandran, 2017; Zawala et al., 2020). However, non-Newtonian behaviors can significantly influence film drainage dynamics and impact the stability of dispersed systems. Thus, understanding the various mechanisms of film stabilization is crucial for selecting appropriate emulsion-breaking strategies (Tchoukov et al., 2014). Additionally, as discussed in Sec. 2.4.2, non-Newtonian behaviors of the surrounding medium can alter the rise dynamics of drops, consequently affecting the drop impact conditions that govern film formation.

In the case of a yield stress material as the surrounding medium, the drainage process can be arrested if the stress within the film becomes lower than the yield stress (Goel and Ramachandran, 2017). Theoretical investigations by Hartland and Jeelani (1986) examined the drainage of dimpled films made of power-law and Bingham fluids. The author considered the drop shape to be spherical outside the film region and calculated the time-dependent thickness of the film at its center and edge of the dimple. Hartland and Jeelani (1987)

further studied the radial and linear drainage of non-Newtonian fluids in horizontal and inclined planar films. The film materials were modeled using as a Power-law and Bingham Generalized Newtonian Fluids. For Bingham fluids, the author's results suggested that the drainage process would cease when the stress at the film wall (fluid-fluid interface) equaled the yield stress. However, these studies made ad-hoc assumptions regarding the drop impact conditions and film shape, leading to inaccurate predictions of the level of plasticity required to inhibit coalescence (Goel and Ramachandran, 2017). To overcome these limitations, Goel and Ramachandran (2017) employed scaling analysis and the lubrication theory to model the drainage dynamics of Bingham fluid films. Their results demonstrated that the drainage process could halt for dimpled films with thicknesses greater than the threshold at which intermolecular forces aid in film drainage. Nonetheless, the results indicated that the film could not freeze entirely due to the bulk yield stress when the film shape was spherical (minimum thickness at the film center).

The stabilization of water-in-oil emulsions by asphaltenes was investigated by Czarnecki et al. (2013). Asphaltenes lack the well-defined amphiphilic structure characteristic of surfactants, and it was hypothesized that asphaltene molecules aggregate and form a network structure within the film, endowing it with a yield stress, thereby impeding film drainage at thicknesses around 50-100 nm. Subsequently, Tchoukov et al. (2014) examined the drainage of thin water-in-oil emulsion films containing asphaltenes, bitumen (heavy oils), and maltenes (deasphalted heavy oils). The results supported the hypothesis proposed by Czarnecki et al. (2013), indicating that asphaltenes stabilize the film by forming a 3D network and altering the film's rheological properties. While they may also induce changes in interfacial properties on a smaller scale, films stabilized by asphaltenes exhibited significant thicknesses that exceeded the size of an asphaltene molecule or their nanoaggregate clusters. Notably, experimental studies investigating the drainage of thin non-Newtonian films are limited due to the technical challenges associated with measuring the film's viscosity, which can exhibit temporal and spatial dependencies (Chatzigiannakis et al., 2021). For instance, the rheological properties of bitumen films can differ considerably from the bulk rheological properties, with the former potentially exhibiting a yield stress (attributed to the 3D aggregates of asphaltenes) and higher viscosity (Goel et al., 2018).

Another application of practical significance lies in the fabrication of hydrogels, which find wide utilization in the clinical field for purposes such as tissue regeneration, drug delivery, and wound healing. The liquid-liquid phase separation (LLPS) technique is employed to produce hydrogel microstructures. LLPS is also valuable in the extraction and purification of materials like DNA, proteins, and metals. Emulsions created through this technique can be stabilized without the use of surfactants by modifying the rheological properties of the

film phase. This property alteration, known as gelation, provides a straightforward approach to introduce a yield stress to the dispersing phase, rendering it more resistant to drainage and impeding coalescence. Moreover, the introduced yield stress can facilitate the formation of non-spherical drops. Various additives such as whey protein microgels, bacterial cellulose, and cellulose microfibrils have been employed to achieve this effect (Garcia and Kiick, 2019), resembling the stabilization mechanism exhibited by asphaltenes.

In their numerical study, Sanjay et al. (2021) examined the phenomenon of bubble bursting at a fluid-fluid interface in Bingham materials. The authors focused on modeling the final stage of the coalescence process, specifically the merging of the fluid bodies following film rupture. Their findings revealed that the resulting free surface adopts a non-flat equilibrium shape, which is influenced by the interplay between the yield stress of the surrounding material and the surface tension. Additionally, they demonstrated that the yield stress acts to dampen capillary waves and decelerate the flow during the merging phase.

In scenarios where the surrounding material exhibits elasticity, the stability of a film can be influenced by elastic normal stresses and the thickening extensional viscosity. As discussed in Section 2.3.2, even polymeric solutions with low concentrations can exhibit non-linear viscoelastic effects. Moreover, polymers can affect coalescence through their electrostatic effects on the surface. For instance, the use of polyacrylamide in polymer flooding has proven highly effective in enhancing oil production in mature oilfields. However, it has the unintended consequence of stabilizing the produced emulsions, thereby making harder subsequent oil and water separation processes in surface systems. The injected polymer ultimately degrades and alters the physical and chemical properties of the produced emulsion, resulting in the formation of significantly tighter emulsions and higher viscosities of produced water. Therefore, it is essential to understand and distinguish the influence of each mechanism to effectively manage the dispersed system (Zheng et al., 2011; Wang et al., 2020).

The drain and rupture of polymer solutions were investigated using a dynamic thin film balance by Chatzigiannakis and Vermant (2021). The authors observed a significant increase in film resistance to deformability and coalescence time due to the presence of polymeric molecules. Phenomena like cyclic dimple formation and dimple recoil were also documented. Similarly, Acharya and Ulbrecht (1978) demonstrated that the elasticity of polymer solutions tends to prolong both the collision and coalescence times of gas bubbles and liquid drops. In a separate study, Chandran Suja et al. (2020) experimentally investigated the thin film drainage dynamics preceding the coalescence of bubbles at flat wormlike micelles (WLM) solution-air interfaces. The authors also observed phenomena such as dimple recoil and film ripping, which can hinder coalescence. The self-assembly of surfactant molecules can result in the formation of wormlike micelles exhibiting viscoelastic properties, thereby influenc-

ing bubble coalescence. WLMs find relevance in diverse applications, including cosmetic products, drag reduction, and hydraulic fracturing. Films with WLM initially possessed a thickness approximately one order of magnitude greater than those stabilized by pure surfactants. Moreover, drainage in the former was three to four orders of magnitude slower than in the latter, and the film's lifetime was approximately inversely proportional to the maximum elastic modulus.

Mitrias et al. (2019) utilized numerical simulations to investigate the influence of viscoelasticity on the drainage time of binary head-on collisions. The authors' findings reveal a different trend from previous experimental results, as the drainage time decreases with an increase in the Weissenberg number. This observation aligns with the numerical results reported by Yue et al. (2005). The authors argue that in the initial stage of the approach, drops move faster than in the Newtonian case since elastic stresses are still negligible. Subsequently, elastic stresses accumulate during the collision (second stage), but they decay again as the drops come into close proximity and the thin film is drained out. Furthermore, the authors note that the effect of the Weissenberg number is more pronounced at higher values of the Capillary number.

The addition of a polymer-like molecule to a solvent leads to an increase in material viscosity, resulting in an inherent increase in coalescence time. In case of assessing the effects of incorporating elasticity into the continuous phase, it is essential to compare it to the Newtonian counterpart with an equivalent viscosity level. While this comparison is challenging in experimental approaches, it can be achieved straightforwardly in numerical simulations.

As demonstrated in this review, the phenomena of drop rise and coalescence in materials exhibiting plastic and elastic behaviors encompass complex subjects involving interfacial phenomena, film drainage, and non-Newtonian behaviors, rendering their study challenging. Despite recent efforts within the academic community, there is still room for improvement in processes involving drop dynamics in complex materials.

Chapter 3

Formulation of the Physical Problem

The problems of drop rise and interfacial coalescence initiation in Newtonian, inelastic viscoplastic, viscoelastic, and finally, elasto-viscoplastic materials are investigated using direct numerical axisymmetric simulations. This chapter introduces the physical problem studied, beginning with the computational domain along with the boundary and initial conditions used in the simulations. In the sequence, the governing equations, including the employed constitutive models, are presented. The chapter ends with the governing dimensionless numbers used to conduct the study.

3.1 Computational Domain

Figure 3.1(a) shows a representative diagram of the computational domain, a square of height $H = 25\,D$, where D is the diameter of the initially spherical drop. The axisymmetric simulations are performed in a cylindrical coordinate system (r, z), where the axis of symmetry lies along the z-axis (the right boundary) and the origin lies at the crossing of the fluid-fluid interface rest position with the axis of symmetry. The rising distance, $z_{\mathtt{r}}$, corresponds to the distance between the initial drop position, $z_{\mathtt{o}}$, and the interface rest position at $z = 0$. The value of $z_{\mathtt{r}}$ is enough to ensure that the drop achieves its terminal velocity before interacting with the upper interface, and it is adjusted based on the governing parameters (discussed at the end of the chapter) to minimize computational time. The upper fluid layer has a depth of $z_i = 5\,D$. The drop and top layer interface (Fluid 2) are composed of the same Newtonian fluid, and the surrounding material (Fluid 1) may be Newtonian, inelastic viscoplastic, viscoelastic, or elasto-viscoplastic. In the beginning, both fluids are at rest and the initially spherical drop rises due to gravity, which acts on the negative z-direction. Free-slip boundary condition with no mass penetration (symmetry boundary condition) is applied for the velocity field at the bottom, left, and top boundaries. The Neumann boundary con-

dition for the pressure field is applied at these boundaries. The size of the computational domain, H, and top layer interface depth, z_i, are sufficiently large to mitigate boundary effects. Preliminary results indicate that doubling, H, and reducing the fluid layer depth, z_i, by half altered the drop's terminal velocity, u_t, and computational drainage time, Δt (defined subsequently), in less than 1 % and 0.15 %, respectively, which are considered negligible.

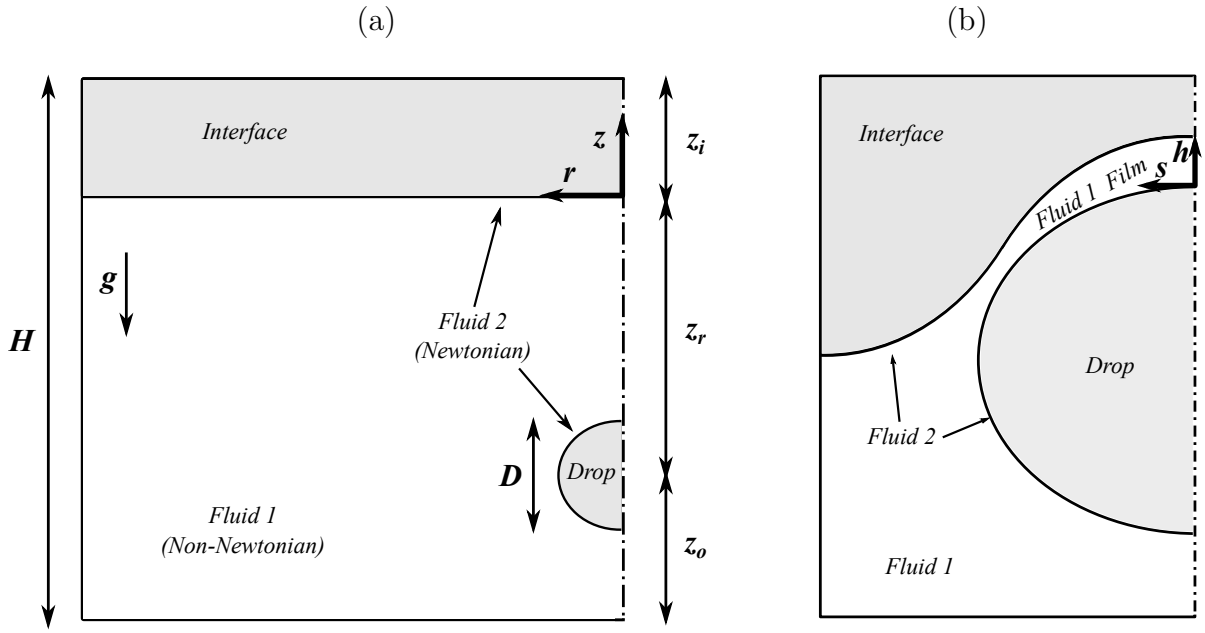

Figure 3.1: (a) A representative diagram of the computational domain. (b) A scheme representing the drop impact on the top layer interface and trapping a thin film of the surrounding material.

Figure 3.1(b) depicts a schematic representation of a drop impacting on the top layer interface and subsequently entrapping and draining a thin film comprised of the surrounding material (Fluid 1). The evolution of the film shape over time is examined in a non-orthogonal coordinate system (s, h) with a mobile origin positioned at the front tip of the drop. The coordinate s follows the drop surface, and the coordinate h extends in the direction of the closest point on the upper fluid-fluid surface (the top layer interface) from the point $(s, 0)$ on the lower fluid-fluid surface (the drop). Consequently, the h-direction may not necessarily align with the normal direction to the drop surface.

Due to challenges associated with identifying the onset of asymmetric instability in film drainage and the computational cost involved in conducting comprehensive parametric numerical studies in three dimensions (or even two dimensions) that encompass the length and time scales relevant to the film rupture step, the investigation of coalescence dynamics primarily focuses on the initial symmetric stage of film drainage. The influence of the external

phase rheological properties on the coalescence time of the drop, which corresponds to the time needed for the film to rupture, is inferred based on the computational drainage time, denoted as Δt. This computational drainage time is defined as the elapsed time from when the minimum thickness of the film decreases from $h_{min} = 0.1\,D$ to $0.01\,D$ (note that the film rupture is generally less than $0.01\,D$).

3.2 Governing Equations

In the studied problem, both fluids are considered incompressible and the one-fluid formulation is used to describe the multiphase flow. The governing equations are given by the continuity equation (Eq. 2.10), Cauchy's equation (Eq. 2.90), and volume fraction advection equation (Eq. 2.34) repeated here for the sake of clarity:

$$\nabla \cdot \mathbf{u} = 0, \tag{2.10}$$

$$\rho \left(\frac{\partial \mathbf{u}}{\partial t} + \mathbf{u} \cdot \nabla \mathbf{u} \right) = -\nabla p + \nabla \cdot \boldsymbol{\tau} + \rho \mathbf{g} + \sigma \kappa \mathbf{n} \delta_S, \tag{2.90}$$

$$\frac{\partial c}{\partial t} + \nabla \cdot (c\mathbf{u}) = 0. \tag{2.34}$$

Here, $\mathbf{u}(u_r, u_z)$ is the velocity field, where u_r and u_z are the velocity components in the radial (r) and axial (z) directions, respectively; p is the pressure field; $\mathbf{g} = -g\mathbf{e_z}$, where g is the acceleration due to gravity and $\mathbf{e_z}$ is the unit vector in the z-direction; t is time; σ is the surface tension coefficient, κ is the mean curvature of the interface, δ_s is a delta function which is zero everywhere except at the interface and $\mathbf{n}$ is the unit normal vector to the interface; ρ is the density field; $\boldsymbol{\tau}$ is the extra stress tensor; c is the volume fraction field, which is used to mark the different fluids and to allocate material properties within the fluids' domain.

The elasto-viscoplastic surrounding material is modeled using the Saramito (2007) model. It is commonly observed in elasto-viscoplastic materials that the contribution of solvent viscosity is significantly lower compared to the polymeric contribution (Lopez et al., 2018; Pourzahedi et al., 2021; Moschopoulos et al., 2021). To simplify the analysis, the influence of the solvent contribution is disregarded. The EVP model employed is based on the Upper Convected Maxwell model, with the mechanical analog depicted in Fig. 3.2. Thus, $\boldsymbol{\tau}$ is given by Eq. 3.1,

$$\boldsymbol{\tau} + \lambda \overset{\nabla}{\boldsymbol{\tau}} = \eta \dot{\boldsymbol{\gamma}}, \tag{3.1}$$

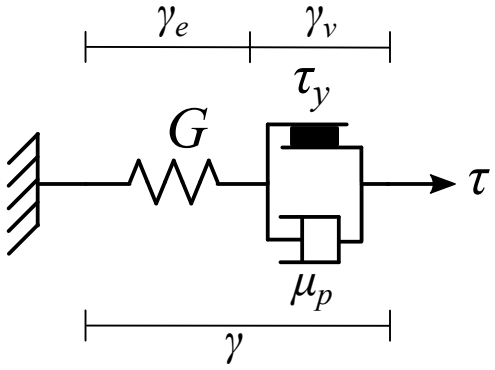

Figure 3.2: Mechanical analog of EVP model employed.

where, λ is the relaxation time of the material, defined as the ratio of the material's viscosity, η, to the elastic modulus, G, expressed as $\lambda = \eta/G$. A bi-viscosity regularized version of the viscosity η based on the Bingham model (Eqs. 2.87) is used:

$$\eta = \begin{cases} \dfrac{\mu_p |\boldsymbol{\tau}_d|}{|\boldsymbol{\tau}_d| - \tau_y + \mu_p \epsilon} & \text{if} \quad |\boldsymbol{\tau}_d| \geq \tau_y, \\ \dfrac{\tau_y}{\epsilon} & \text{if} \quad |\boldsymbol{\tau}_d| < \tau_y. \end{cases} \tag{3.2}$$

Here, μ_p is the plastic viscosity; τ_y is the yield stress; $|\boldsymbol{\tau}_d|$ is the magnitude of the deviatoric part of the extra stress tensor; ϵ is the regularization parameter, written as $\epsilon = \tau_y/(N\eta_c)$. Thus, for $|\boldsymbol{\tau}_d| < \tau_y$, $\eta = N\eta_c$ (Frigaard and Nouar, 2005; Allouche et al., 2000; Balmforth et al., 2014). The characteristic viscosity η_c is defined in the next section, and N is a dimensionless regularization parameter whose value is large. The yielded and unyielded regions are separated based on the von Mises criterion and are identified by the regions where $|\boldsymbol{\tau}_d| \geq \tau_y$ and $|\boldsymbol{\tau}_d| < \tau_y$, respectively. In a time-dependent numerical simulation, $|\boldsymbol{\tau}_d|$ is obtained from Eq. 3.1 in the current time step. Then, the value of η is calculated from Eq. 3.2 and plugged back into Eq. 3.1 to calculate the polymeric stress in the next time step.

In the case of inelastic formulations, the relaxation time λ is equal to zero, and instead of a differential equation for the stress, an algebraic expression is employed: $\boldsymbol{\tau} = \eta\dot{\boldsymbol{\gamma}}$. As $\boldsymbol{\gamma}_v$ is equivalent to $\boldsymbol{\gamma}$ in this scenario, the viscosity can be expressed as the following regularized version of the Bingham model:

$$\eta = \frac{\tau_y}{|\dot{\boldsymbol{\gamma}}| + \epsilon} + \mu_p. \tag{2.58}$$

The material property fields are written as a function of the smoothed volume fraction

field, $\tilde{c}$, which is equal to 0 in Fluid 1 and equal to 1 in Fluid 2. For instance,

$$\xi = \xi_1(1 - \tilde{c}) + \xi_2\tilde{c}. \tag{3.3}$$

Here, ξ is a generic property of the material and the subscripts 1 and 2 stand for Fluid 1 and 2, respectively. $\tilde{c}$ is the smoothed volume fraction field obtained by averaging the eight neighboring cells. The form of Eq. 3.3 indicates a linear jump in the value of the material property across the interface. In the simulations, the arithmetic (linear) mean for ρ and G are employed. However, as discussed in more detail in Chapter 4, the specific form of the viscosity, η, jump depends on the formulation used for the surrounding material.

3.3 Non-dimensional Governing Parameters

The following scaling is used to non-dimensionalize the governing equations and boundary conditions:

$$\begin{aligned}&(\bar{r}, \bar{z}) = (r/D, z/D),\ (\bar{s}, \bar{h}) = (s/D, h/D),\ \bar{\mathbf{u}} = \mathbf{u}/U,\ \bar{t} = t/t_c,\ \bar{p} = p/\rho_1 U^2,\\ &\bar{\dot{\boldsymbol{\gamma}}} = \dot{\boldsymbol{\gamma}}/\dot{\gamma}_c,\ \bar{\rho} = \rho/\rho_1,\ \bar{\eta} = \eta/\eta_c,\ \bar{\boldsymbol{\tau}} = \boldsymbol{\tau}/\tau_c,\ \bar{\lambda} = \lambda/\lambda_c.\end{aligned} \tag{3.4}$$

The characteristic time, t_c, is defined as $t_c = D/U$ and the characteristic strain rate, $\dot{\gamma}_c$, is defined as $\dot{\gamma}_c = 1/t_c = U/D$. The characteristic viscosity is defined as $\eta_c = \tau_y/\dot{\gamma}_c + \mu_p$. It should be emphasized that the definition of the characteristic viscosities includes the contribution of the yield stress, as recommended by Thompson and Soares (2016). The characteristic relaxation time, λ_c, is defined as $\lambda_c = \eta_c/G$, which also includes a contribution from τ_y. The characteristic stress is defined based on the buoyancy force, $\tau_c = |\Delta|\rho g D$. The characteristic velocity, U, is defined by balancing the buoyancy, $\tau_b = |\Delta\rho|gD$, and viscous, $\tau_v = \tau_y + \mu_p U/D$, stresses ($\tau_c = \tau_b = \tau_v$) as

$$U = \begin{cases} \dfrac{|\Delta\rho|gD^2 - \tau_y D}{\mu_p} & \text{if} \quad |\Delta\rho|gD \geq \tau_y, \\ 0 & \text{if} \quad |\Delta\rho|gD < \tau_y. \end{cases} \tag{3.5}$$

Note that U includes a contribution from the yield stress. Equation 3.5 expresses that in case $|\Delta\rho|gD < \tau_y$ the characteristic velocity is zero, meaning that the drop is entrapped.

The following dimensionless parameters, which describe the problem of interest, are obtained using the above scaling analyses:

$$Fr = \frac{\rho_1 U^2}{|\Delta\rho| g D} = \frac{\rho_1 U^2}{\eta_c \dot{\gamma}_c},$$
$$Bo = \frac{|\Delta\rho| g D^2}{\sigma},$$
$$Pl = \frac{\tau_y}{\eta_c \dot{\gamma}_c} = \frac{\tau_y}{|\Delta\rho| g D},$$
$$Wi_c = \lambda_c \dot{\gamma}_c = \frac{|\Delta\rho| g D}{G},$$
$$\eta_r = \frac{\eta_2}{\eta_c},$$
$$\rho_r = \frac{\rho_2}{\rho_1}.$$

The Froude number, Fr, represents the relative importance of inertial to buoyancy forces. Since the buoyancy force scales with viscous forces Fr also represents the ratio of inertial to viscous forces. It is noteworthy that the characteristic velocity can also be expressed as $U = \sqrt{Fr|\Delta\rho|gD/\rho_1}$. The Bond number, Bo, represents the relative importance of the buoyancy force to capillary forces. The plastic number, Pl, indicates the plastic nature of the material and its value ranges from 0 to 1. $Pl = 0$ signifies that the yield stress is zero (Newtonian fluid) or the material is completely yielded ($\mu_p \dot{\gamma}_c \to \infty$). In contrast, $Pl = 1$ indicates that the fluid is completely plastic ($\tau_y \to \infty$) and/or remains undeformed ($\dot{\gamma}_c = 0$). Here, $Pl = Y_g/3$, where Y_g is the yield stress parameters, first defined by Beris et al. (1985). The characteristic Weissenberg number, Wi_c, provides an indication of the relative significance of elastic forces in comparison to viscous forces. Specifically, the interplay between these two forces is expressed by the Weissenberg number, $Wi = \eta(|\dot{\boldsymbol{\gamma}}|)\dot{\gamma}_c/G$, which depends on the magnitude of the strain rate (a kinematic quantity), as discussed shortly. Conversely, Wi_c solely relies on the parameter $\dot{\gamma}_c$. Hence, Wi takes the same form as Wi_c when η is calculated with $\dot{\gamma}_c$ instead of $|\dot{\boldsymbol{\gamma}}|$. Consequently, in the case of viscoelastic materials, Wi_c is equal to Wi, while for inelastic materials, Wi_c is zero. Because the viscosity of Fluid 1 is not constant, the viscosity ratio η_r is defined as the viscosity of Fluid 2, η_2, over the total characteristic viscosity, η_c. Unless otherwise specified, the density ratio ρ_r is held constant with a value of 0.1 throughout the analysis. It is noteworthy that the buoyant stress, τ_b, remains constant across all studied drops (unless explicitly stated). Furthermore, as discussed in Sec. 3.2, the EVP model is based on the Upper Convected Maxwell model, so β (the solvent to total viscosity ratio) is equal to zero (unless explicitly stated). Setting $\beta = 0$ simplifies the dimensional analysis because despite being defined in the polymeric branch of the EVP model, Pl and Wi indicate the plastic and elastic nature of the material as a whole.

The non-dimensionalization of the momentum equations using the above scaling results in (see Appendix A)

$$\bar{\rho}\left(\frac{\partial \bar{\mathbf{u}}}{\partial \bar{t}} + \bar{\mathbf{u}} \cdot \nabla \bar{\mathbf{u}}\right) = -\nabla \bar{p} + \frac{1}{Fr}\nabla \cdot \bar{\boldsymbol{\tau}} + \frac{1}{FrBo}\bar{\kappa}\mathbf{n}\delta_s - \frac{1}{Fr}\frac{1}{1-\rho_r}\bar{\rho}\mathbf{e_z}. \tag{3.6}$$

The dimensionless form of the stress equation yields:

$$\bar{\boldsymbol{\tau}} + Wi\, \overset{\triangledown}{\bar{\boldsymbol{\tau}}} = \bar{\eta}\bar{\dot{\boldsymbol{\gamma}}}. \tag{3.7}$$

Here, the Weissenberg number is defined as $Wi = \bar{\eta} Wi_c$. The plastic number is hidden inside $\bar{\eta}$, expressed as

$$\bar{\eta} = 1 + Pl\frac{(1 - |\bar{\dot{\boldsymbol{\gamma}}}|)}{|\bar{\dot{\boldsymbol{\gamma}}}|}. \tag{3.8}$$

It is important to emphasize again that the relative importance of elastic and viscous forces is expressed by Wi, which is affected by the plastic nature of the material through $\bar{\eta}(Pl)$ (Oishi et al., 2019).

Table 3.1 exhibits the values of the dimensionless numbers used in the investigation to evaluate the dynamics of drop rise and initiation of interfacial coalescence. The parameter range is chosen to be sufficiently broad to enable an examination of their influence on flow dynamics while avoiding excessively distinct drop shapes (such as a purely spherical cap shape) or extensive drop fragmentation across all studied material formulations.

Non-dimensional numbers	**Values**			
Fr	200	2000		
Bo	2	20		
Pl	0.00	0.02	0.04	0.06
Wi_c	0	2	4	6
η_r	0.1	10.0		
ρ_r	0.1			
β	0.0			

Table 3.1: Value of the dimensionless governing numbers used in the simulations for the rise and interfacial coalescence initiation of drops.

Chapter 4

Numerical Methodology

This chapter introduces the numerical tool utilized for conducting the numerical simulations, namely the software Basilisk, and the author's specific implementations. The chapter also presents validation tests performed to check the solver accuracy, as well as grid and regularization parameter dependency.

4.1 Numerical Tool

The numerical simulations are performed using the open-source software Basilisk, which was developed for the solution of partial differential equations on adaptive Cartesian meshes. The software's incompressible Navier–Stokes solver allows for variable density and viscosity fields and is second-order accurate in time and space. A second-order projection method is used for the temporal discretization, while the viscous terms are discretized using a second-order implicit scheme. The robust Bell-Colella-Glaz (Bell et al., 1989) second-order unsplit upwind scheme is used for the velocity advection, which is stable for CFL numbers ($CFL = u\underline{\Delta}t/\underline{\Delta}x$) smaller than one (Popinet, 2003, 2009).

The Basilisk solver has been demonstrated to give accurate and efficient solutions for surface-tension-driven flows (Popinet, 2009). The Basilisk website (http://basilisk.fr/) provides numerous test cases for reference. Interfacial flows are modeled using a sharp interface (one grid cell in thickness) geometrical Volume-of-Fluid (VOF) interface representation method, in conjunction with a balanced-force (BF) continuum-surface-force (CSF) formulation for surface-tension and a height-function (HF) curvature estimation. The implemented HF demonstrates second-order accuracy and consistency even at low interface resolutions. The method is shown to recover exact equilibrium for the case of a stationary droplet, irrespective of viscosity and spatial resolution (Popinet, 2009). In simulations employing the Volume-of-Fluid method, the software automatically adjusts the time step to

satisfy the Courant-Friedrichs-Lewy condition of $CFL < 0.5$. Moreover, the maximum time step is also constrained by the oscillation period T_σ of the smallest capillary wave, given by $\mathsf{T}_\sigma = \sqrt{\rho_\mathsf{m} \underline{\Delta} x_{min}^3 / (\pi\sigma)}$, where $\rho_\mathsf{m} = (\rho_1 + \rho_2)/2$ represents the average density, and $\underline{\Delta} x_{min}$ corresponds to the size of the smallest grid element. For more details on Volume-of-Fluid and surface-tension implementations, see Popinet (2009).

Basilisk also incorporates adaptive mesh refinement. The grid cells have a square shape (cubic in 3D) and are organized in a tree structure. The quadtree discretization method proves to be very flexible and allows accurate and efficient tracking of flow features (Popinet, 2003). Figure 4.1 presents an example of the quadtree discretization and its corresponding tree representation. The standard domain has a square shape (generic domains can be construed using embedded boundaries), which consists of the root cell (the base of the tree). The cell size is determined according to its level in the tree, being the root cell the level zero. Every time a cell is divided into a group of four children cells, a level is added. Cells without children are referred to as leaf cells. The number of cells per dimension is given by 2^n, where n is the level of refinement. For instance, if all cells in Fig. 4.1 were leaf cells of level 4 (the whole 2D domain), each direction would contain 16 cells, and the whole domain would contain $16^2 = 256$ cells. The adaptative grid scheme allows for the refinement along the interfaces and in regions of interest; for example, with high velocity or vorticity gradients. In the case of capillary breakup of a three-dimensional liquid jet, the method yielded a fifty-fold reduction in the number of cells compared to a scenario with a constant mesh resolution along the interface (Popinet, 2009). Figure 4.2 presents an example of an adapted mesh in the context of a rising bubble flow. For a more comprehensive understanding of the quad/octree spatial discretization, refer to Popinet (2003).

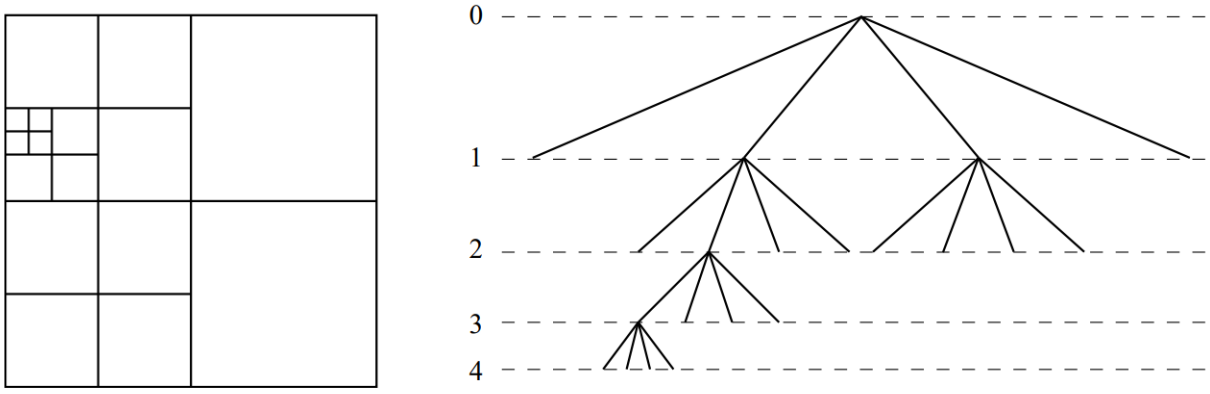

Figure 4.1: Scheme of a quadtree discretization and corresponding tree representation. Source: Popinet (2003).

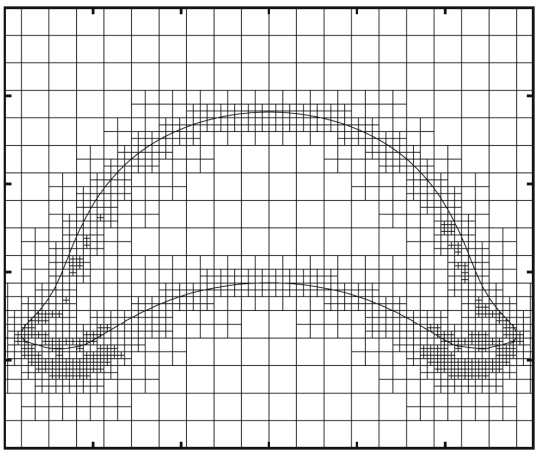

Figure 4.2: Illustration of mesh adaptation in a simulation of a rising bubble flow. Source: Popinet (2009).

The software also includes a viscoelastic solver of the Upper Convected Maxwell model. The viscoelastic solver can be employed together with the Navier–Stokes solver, resulting in Oldroyd-B model. In this configuration, the viscoelastic solver addresses the polymeric branch, and the input parameters are the polymeric viscosity, η_p, and relaxation time, λ. The Navier-Stokes solver handles the solvent branch, with the solvent viscosity, η_s, as the input parameter. The Basilisk viscoelastic solver utilizes the log-conformation method to mitigate numerical instabilities that may arise at high Weissenberg numbers. It has been proposed for studying multiphase flows of viscoelastic materials and has been efficiently used to study the splashing of weakly viscoelastic drops on a solid surface, among other two-phase flows (López-Herrera et al., 2019).

4.1.1 Additional implementations

This section presents the implementations of the elasto-viscoplastic Saramito model and the film region identification method made by the author.

4.1.1.1 The Saramito model

The (Saramito, 2007, 2009) models were implemented by making the polymeric viscosity and relaxation time passed to the viscoelastic solver as a function of the polymeric stress, instead of being constants as in the Oldroyd-B model. By setting the solvent viscosity to zero (in the Navier-Stokes solver), the model of the mechanical analog of Fig. 3.2 is obtained. The material's viscosity η (*i.e.*, η_p in the viscoelastic solver) is then calculated according to Eq. 3.2. Therefore, the value of the viscosity in the next time step is determined based on the calculated intensity of the deviatoric part of the extra stress tensor, $|\boldsymbol{\tau}_d|$, in the current

time step. The input for the relaxation time is given by $\lambda = \lambda_c(\eta(|\boldsymbol{\tau}_d|)/\eta_c)$, so that G remains constant. Given that $\eta(|\boldsymbol{\tau}_d|)$ depends on the stress, special care must be taken for the viscosity jump across the interface, an issue discussed in more detail in Sec. 4.2.4.

4.1.1.2 Film region identification method

In order to achieve appropriate mesh refinement and extract crucial data from the thin-film region, a film structure identification method based on the work of Chirco et al. (2022) was implemented. This method involves the utilization of a scalar field, denoted as $\mathsf{F}_{i\mathtt{d}}$, which takes on a value of 1 within the film region and 0 outside of it. The Basilisk algorithm to refine the adaptable mesh is "tricked" to always refine the mesh to the maximum level of refinement (L_{max}) in the film region. The film region is defined as the region within Fluid 1 located at a distance d up to three times the current minimum film thickness ($3 \times h_{min}(t)$) from both the interfaces of the drop and of the top layer, and above $z = 0$. More specifically, if a point P_1 in Fluid 1 is located at $z > 0$ and at a distance $d = P_1 - P_i < 3 \times h_{min}(t)$ from both the interfaces (where P_i is the position of the interfaces), then P_1 is considered to be inside the film and the value of 1 is assigned to $\mathsf{F}_{i\mathtt{d}}$. Otherwise, if P_1 is outside the film, $\mathsf{F}_{i\mathtt{d}} = 0$. To facilitate the identification of which interface the distance d is being calculated from the drop and the top layer are marked by two different volume fraction fields, $c_{\mathtt{d}}$ and c_i, respectively. Therefore, for P_1 to be classified as inside the film, both $d_{\mathtt{d}} = P_1 - P_{i-\mathtt{d}}$ and $d_i = P_1 - P_{i-i}$ must be less than $3 \times h_{min}(t)$. Using two volume fraction fields also helps prevent the merging of the drop with the top layer interface due to the nature of the VOF model. Adding these two volume fractions together results in the volume fraction $c = c_{\mathtt{d}} + c_i$ used in the mapping of the fluids' properties in Eq. 3.3.

During the rise of the drop, the maximum level of mesh refinement remains constant. However, following the impact of the drop on the top layer interface, the maximum level of refinement is increased to ensure a minimum number of cells in the thinnest part of the film. The objective is to achieve sufficient spatial resolution within the film region to accurately capture the film's shape and solve for the field variables (*e.g.*, velocity, stress, and yielded/unyielded regions) within the film while using a coarser grid during the rise stage. The maximum level of refinement after the drop impact is a function of the film's minimum thickness $h_{min}(t)$ and the minimum number of cells in the film, $\mathcal{C}$. The relationship is described by Eq. 4.1, where only the floor integer part[1] is taken to determine the values of L_{max},

$$L_{max} = \lfloor \frac{\log\left(\frac{\mathcal{C}H}{h_{min}}\right)}{\log 2} \rfloor. \tag{4.1}$$

[1]The part of a real number that precedes the decimal point; for example, $\lfloor 3.1415 \rfloor = 3$.

Here, H is the size of the square numerical domain. Figures 4.3(a) and (b) illustrate the film region during the impact of a drop with the fluid-fluid interface in the dimensionless coordinate systems $(\bar{r}, \bar{z})$ and $(\bar{s}, \bar{h})$, respectively. The mesh cells within the film region are marked with black crosses. In Fig 4.3(b), the region below the lower and horizontal red line corresponds to the interior of the drop, while the region above the upper and curved red line corresponds to the fluid above the fluid-fluid interface.

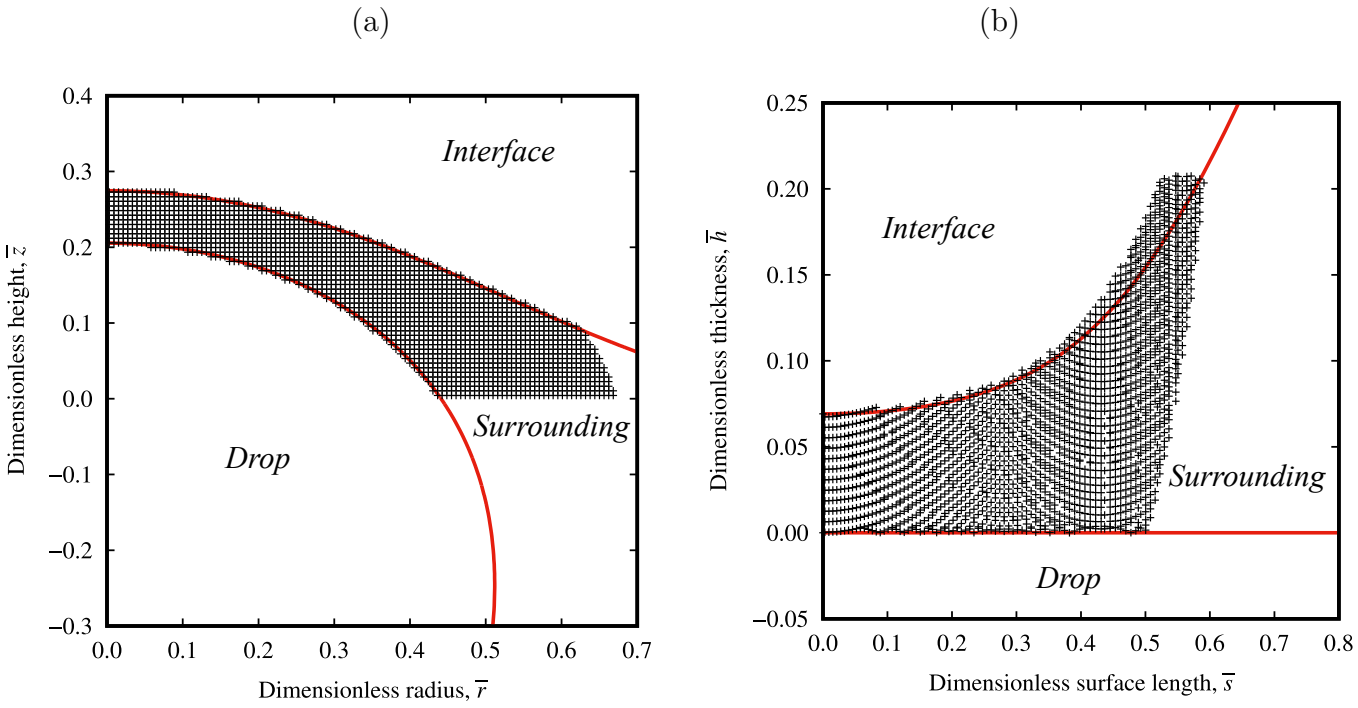

Figure 4.3: Film region identified by black crosses during the impact of a drop with the top layer interface in the dimensionless coordinate systems (a) $(\bar{r}, \bar{z})$ and (b) $(\bar{s}, \bar{h})$.

4.2 Code Validation

The validation tests conducted to assess the accuracy of the solver and its dependency on the grid and regularization parameter are organized into two main categories: drop rise phenomenon and coalescence phenomenon. The first set of tests focuses on the drop rise phenomenon and examines the solver's performance and dependencies in the four different material formulations studied: i) Newtonian, ii) inelastic viscoplastic, iii) viscoelastic, and iv) elasto-viscoplastic materials. These tests evaluate the solver accuracy and grid and regularization parameter dependencies, as well as the implementation of the elasto-viscoplastic (EVP) model for the drop rise phenomenon. The second set of tests addresses the drop

interfacial collision and draining film shape of the coalescence phenomenon. This portion of the validation tests investigate the grid requirements and the numerical method's ability to replicate the dynamics of drop collision and film drainage initiation. The results obtained with the code are compared against experimental and numerical results from the literature. Table 4.1 provides a summary of the validation tests, categorizing them based on the specific problem addressed, the comparison criterion employed, the authors of the respective works, and the type of study conducted. Additionally, the viscosity jump associated with each formulation of the surrounding material is discussed and presented in conjunction with the validation tests.

Resolved problem	Comparison	Reference	Work type
Rising phenomenon			
Drop rise in Newtonian materials	Bubble shape and drop terminal velocity	Bhaga and Weber (1981) and Wegener et al. (2010)	Experimental
Drop rise in inelastic viscoplastic materials	Yield surface and bubble shape	Dimakopoulos et al. (2013)	Numerical
Drop rise in viscoelastic materials	Bubble shape	Pilz and Brenn (2007)	Experimental
Drop rise in elasto-viscoplastic materials	Bubble shape	Lopez et al. (2018)	Experimental
Coalescence phenomenon			
Drop collision on a fluid-fluid interface	Interfaces' shape and position	Mohamed-Kassim and Longmire (2003)	Experimental
Drop collision on a liquid-solid interface	Film shape evolution and bubble position	Vakarelski et al. (2022)	Experimental

Table 4.1: Validation tests conducted to check the accuracy of the solver and its dependency on the grid and regularization parameter.

4.2.1 Drop rise in Newtonian materials

In this section, the experimental results of Bhaga and Weber (1981) and Wegener et al. (2010) on bubble shape and drop terminal velocity, respectively, in Newtonian media are numerically reproduced.

Prior to conducting the comparison, a grid dependency test is performed. Figure 4.4 presents the variation of the dimensionless velocity, $\bar{u}$, of a bubble versus dimensionless time, $\bar{t}$, for different levels of maximum refinement. The dimensionless parameters are $Fr = 232$, $Bo = 243$, $\rho_r = 0.01$, and $\eta_r = 0.01$. The simulations employ the harmonic mean of viscosity

to account for the viscosity jump across the interface, as described by Eq. 4.2:

$$\eta = \frac{1}{\dfrac{\tilde{c}-1}{\eta_1} + \dfrac{\tilde{c}}{\eta_2}}. \tag{4.2}$$

Here, $\tilde{c}$ is the smoothed version of the volume fraction field c, and η_1 and η_2 are the viscosities of the Newtonian fluids. A comparison with an arithmetic mean of viscosity is presented in the next section. The minimum level of refinement is set to 6, based on previous tests indicating that the solution remains unaffected by this minimum refinement level. The mesh is refined as a function of the volume fraction and velocity fields. No significant variation in $\bar{u}$ is observed for $L_{max} = 12$ and 13. Given the higher computational cost associated with $L_{max} = 13$, the simulations are carried out using $L_{max} = 12$, corresponding to a cell size of approximately $6.10 \times 10^{-3}\, D$.

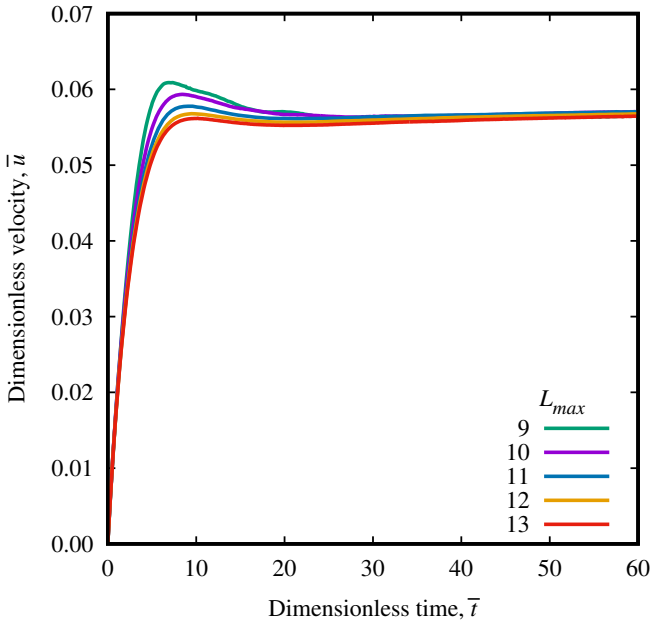

Figure 4.4: Bubble dimensionless rise velocity, $\bar{u}$, versus dimensionless time, $\bar{t}$, for different mesh maximum refinement levels, L_{max}. The dimensionless parameters are $Fr = 232$, $Bo = 243$, $\rho_r = 0.01$, and $\eta_r = 0.01$.

Figures 4.5(a), (b), and (c) present the experimental observations of three bubbles rising in aqueous sugar solutions obtained by Bhaga and Weber (1981). These experimental results are reproduced numerically with the software Basilisk with $L_{max} = 12$ in Figs. 4.5(d), (e), and (f). Note that the conditions for the grid dependency test in Fig. 4.4 corresponds to

the bubble of Fig. 4.5(d). The numerical results agree reasonably well with the experimental bubble rising results.

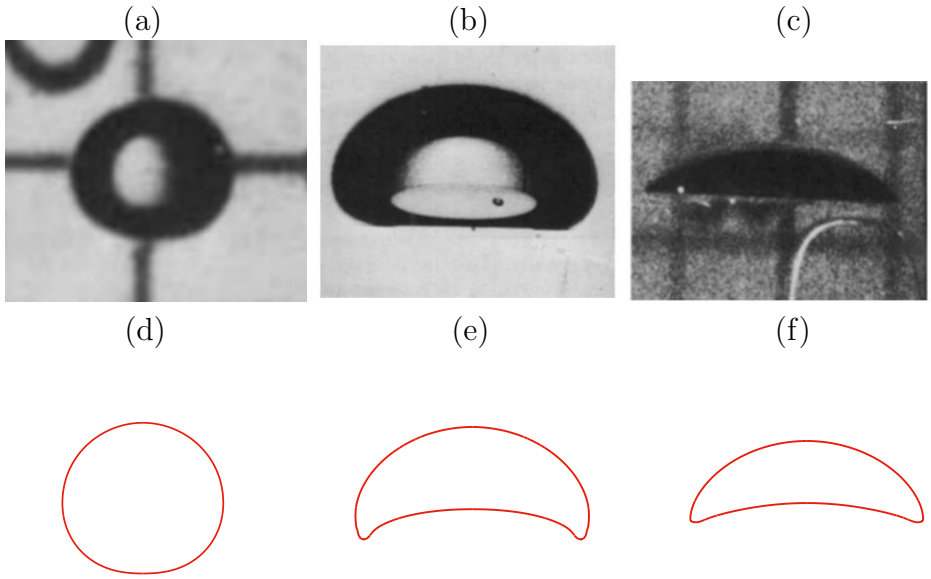

Figure 4.5: Bubbles shape at steady-state rise. Experimental results of Bhaga and Weber (1981) (a,b,c) and numerical results with the software Basilisk (d,e,f). The dimensionless parameters are $Fr = 2.8$, $Bo = 17.7$ (a,d), $Fr = 232$, $Bo = 243$ (b,e), and $Fr = 18,108$, $Bo = 115$ (c,f). The density and viscosity ratios are $\rho = 0.01$ and $\eta_r = 0.01$, respectively

Figure 4.6 provides a comparison between the dimensionless terminal velocity of toluene drops rising in water as a function of the drop diameter obtained experimentally by Wegener et al. (2010) and the corresponding numerical results. The observed decrease in terminal velocity after reaching a maximum value is attributed to alterations in the drop shape, which becomes more oblate (larger width). The maximum level of refinement is the level of 12 and a good agreement between the numerical and experimental results is observed. It is noteworthy that the characteristic velocity U exhibits a more rapid growth with Fr compared to the dimensional velocity u. Therefore, an increase in u would correspondingly lead to a reduction in the dimensionless velocity $\bar{u} = u/U$. In order to ensure that u and $\bar{u}$ behave similarly in the plot, the dependency of U on Fr is removed by multiplying $\bar{u}$ by $Fr^{1/2}$.

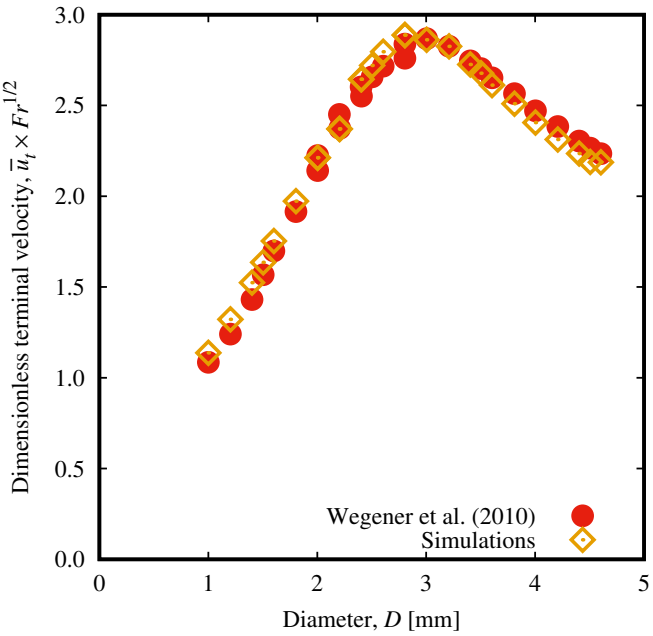

Figure 4.6: Comparison of the dimensionless terminal velocity, $\bar{u}_t$ ($\times Fr^{1/2}$), with drop diameter, D, obtained with the software Basilisk and in the experimental results of Wegener et al. (2010). Both the drop and the surroundings are Newtonian fluids.

4.2.2 Drop rise in inelastic viscoplastic materials

The numerical result of Dimakopoulos et al. (2013) of a bubble rising in a Bingham material using the Augmented Lagrangian method is reproduced with the Basilisk software. The dimensionless numbers are $Fr = 38025$, $Bo = 200$, and $Pl = 0.025$. The viscosity and density ratios are equal to zero in Dimakopoulos et al. (2013) (the viscosity and density of the gas phase in the bubble were neglected by the authors), but both are equal to 0.01 in the present simulations. The viscosity of the Bingham model is calculated using the algebraic expression of Eq. 2.58. The viscoplastic model of Basilisk has been successfully used for complex flows by different researchers (Lagrée et al., 2011; Deka et al., 2019, 2020).

Before reproducing the results of Dimakopoulos et al. (2013), a grid and regularization parameter dependency test is conducted for the same physical conditions used by the authors. Figures 4.7(a) and (b) exhibit the bubble dimensionless rising velocity, $\bar{u}$, with dimensionless time, $\bar{t}$, for different values of L_{max} and N, respectively. In these simulations, the minimum level of refinement is set to 6, and the mesh is refined based on the volume fraction field, velocity field, and yield surface. L_{max} is equal to 10, 11, 12, and 13 and N is equal to 10^5 in Fig. 4.7(a). The harmonic mean for the viscosity is used, except for the black dashed line, where an arithmetic linear mean is employed. The results with the harmonic and

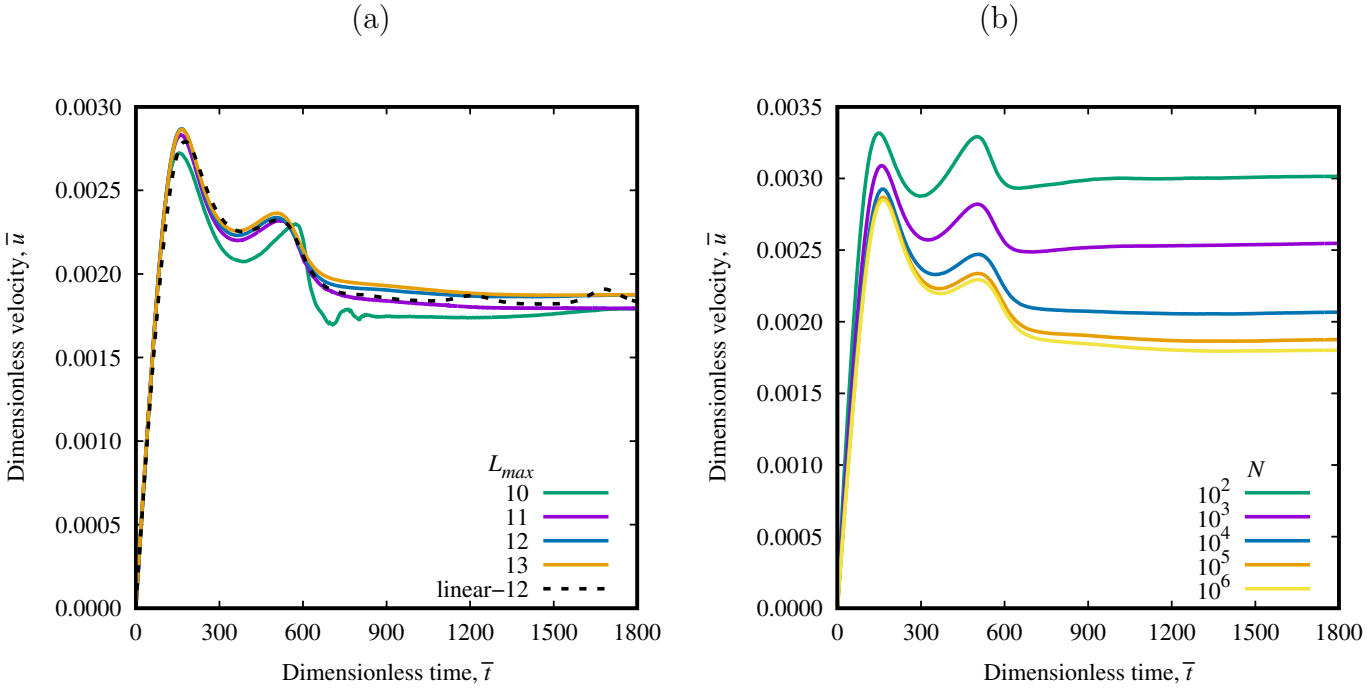

Figure 4.7: Dimensionless rise velocity, $\bar{u}$, with dimensionless time, $\bar{t}$, for (a) different mesh maximum refinement levels, L_{max}, and (b) dimensionless regularization parameters, N. The minimum refinement level in all cases is 6, while L_{max} is (a) changed from 10 to 13 in (a) and equal to 12 in (b). $N = 10^5$ in (a) and changed from 10^2 to 10^6 in (b). The dashed line in (a) shows the result using a linear mean for the viscosity jump. The dimensionless parameters are $Fr = 38025$, $Bo = 200$, $Pl = 0.025$, $\eta_r = 0.01$, and $\rho_r = 0.01$.

arithmetic mean do not agree much. The latter results in velocity oscillations at later times, while the bubble for the former reaches a steady-state rise. Moreover, the bubble simulated with the arithmetic mean develops a skirt in its back, in disagreement with the results of Dimakopoulos et al. (2013) (as further demonstrated in the subsequent analysis). Although the velocity profile does not change much when changing the maximum level of refinement from 12 to 13, the computational cost increases significantly. In Fig. 4.7(b), different values of N are considered: $10^2, 10^3, 10^4$, 10^5, and 10^6, all with $L_{\max} = 12$. The result with $N = 10^5$ does not change much from the result with $N = 10^6$, but the latter presents a higher computational time. Furthermore, it is observed that the shape of the yield surface starts to fluctuate for $N = 10^6$, whereas for $N = 10^5$, the yield surface shape remains stable. Hence, a maximum refinement level of 12 and a dimensionless regularization parameter of 10^5, with the harmonic mean for the viscosity, are selected to simulate the bubble rise in inelastic viscoplastic materials. Figure 4.8 compares the obtained result (right) with the numerical solution of Dimakopoulos et al. (2013) (left). The agreement regarding the bubble shape,

yielded surface envelope, and yielded surface beneath the bubble is reasonable.

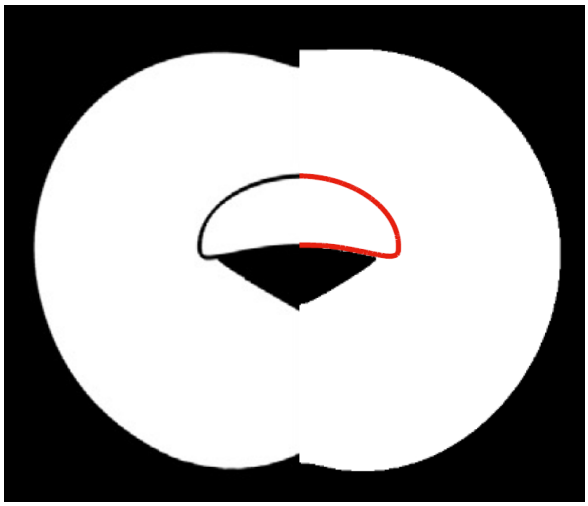

Figure 4.8: Steady-state solution of Dimakopoulos et al. (2013) using the ALM (left half) is compared with the numerical results obtained with the software Basilisk (right). The simulations are performed using $N = 10^5$, $L_{max} = 12$, $Fr = 38025$, $Bo = 200$, $Pl = 0.025$, $\eta_r = 0.01$, and $\rho_r = 0.01$.

4.2.3 Drop rise in viscoelastic materials

This section replicates the experimental results of Pilz and Brenn (2007) for the shape of bubbles rising in viscoelastic materials (aqueous Praestol 2500 (PAM) solutions). Before diving into it, the viscosity jump across the interfaces and the solution dependency on the grid are checked.

In the simulations conducted in this study, the solvent to total viscosity, β, is set to zero and the surrounding medium (Fluid 1) is modeled as an UCM material (polymeric branch). However, utilizing the polymeric branch (reduced to the Newtonian formulation with $\lambda = 0$) to model Fluid 2 (the drop and top layer) has been shown to result in numerical instability and simulation breakdown. Therefore, in practice, the adopted numerical methodology consists of using the polymeric branch for Fluid 1 (with the viscoelastic solver), and the solvent branch for Fluid 2 (with the Navier-Stokes solver). From a physical perspective, the studied problem remains unaltered, and the mechanical analog presented in Fig. 3.2 remains valid. Nonetheless, this procedure results in setting the numerical variable used to allocate the "solvent" viscosity of Fluid 1 (surroundings), η_{s1}, and the "polymeric" viscosity of Fluid 2 (drop and top layer), η_{p2}, to zero. This leads to a division by zero when using the harmonic mean for viscosity calculation. Consequently, an arithmetic mean for viscosity is employed in the case of elastic materials. A preliminary test was conducted to investigate the impact of

setting a very small value for η_{s1} of Fluid 1 (much smaller than of Fluid 2) with a harmonic mean for viscosity. This approach did not yield any significant differences compared to the case where the arithmetic mean was used and η_{s1} was set to zero in Fluid 1. Notably, the solution obtained using the arithmetic mean for the numerical variables η_s and η_p, representing viscosity, resulted in a drop rise velocity with time that closely matched the observations obtained using only the solvent branch (Navier-Stokes solver) and the harmonic mean, as depicted in Fig. 4.9. The dimensionless numbers are $Wi_c = 0$, $Fr = 200$, $\eta_r = 0.1$, $\rho_r = 0.1$, and $Bo = 2$ and 20, and the maximum and minimum levels of refinement are $L_{max} = 12$ and $L_{min} = 6$, respectively. In the figure, the dashed lines correspond to the solutions employing both solvers and the arithmetic mean while the solid lines correspond to the solutions employing the Navier-Stokes solver only and the harmonic mean. In the implementation of the solvers, η_s is defined on grid cell faces while η_p is defined on the center of the grid cells. The agreement observed in Fig. 4.9 may be attributed to the distinct numerical schemes used to represent η_s and η_p, despite employing different means for viscosity calculation. The results of Fig. 4.9 demonstrate that the viscoelastic model reduces nicely to its Newtonian counterpart as $Wi_c = \lambda = 0.0$.

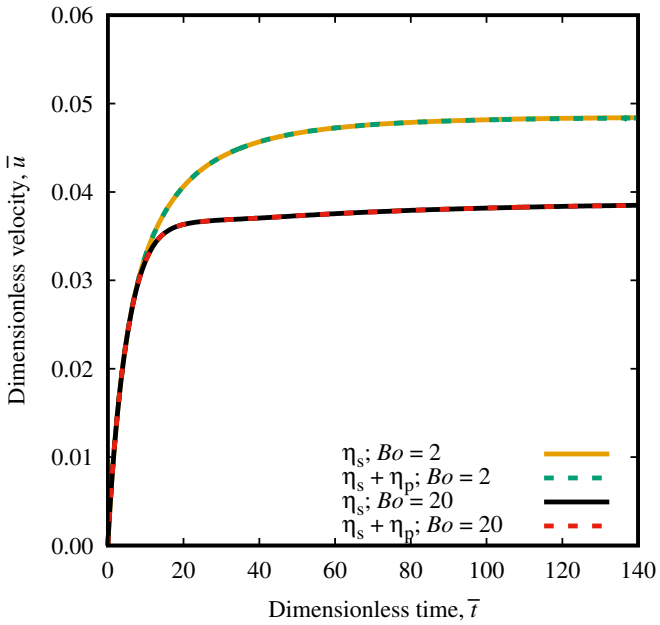

Figure 4.9: Drop dimensionless rise velocity, $\bar{u}$ versus dimensionless time, $\bar{t}$, for $Pl = 0.00$, $Wi_c = 0$, $Fr = 200$, $\eta_r = 0.1$, $\rho_r = 0.1$, and $Bo = 2$ and 20. The continuous lines represent the solution with Navier-Stokes solver only, and the dashed lines represent the solution with both Navier-Stokes and viscoelastic solvers. The maximum and minimum levels of refinement are $L_{max} = 12$ and $L_{min} = 6$, respectively.

For the dependency of the solution on the grid resolution, Fig. 4.10 depicts the dimensionless rise velocity, $\bar{u}$, versus dimensionless time, $\bar{t}$, for $Wi_c = 4$, $Fr = 200$, $Bo = 20$, and $\eta_r = 0.1$ and different values of L_{max}. Interestingly, the drop velocity for the levels of refinement overlap. To keep consistency with previous results, the maximum level of 12 is selected.

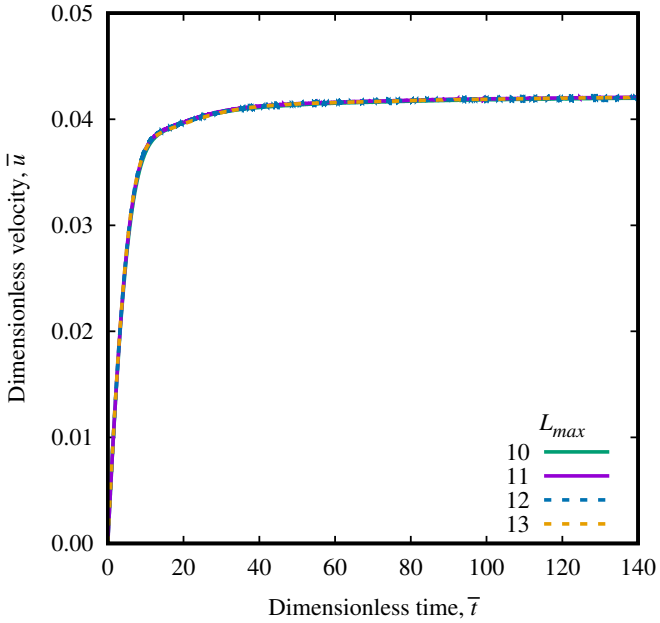

Figure 4.10: Dimensionless rise velocity, $\bar{u}$, with dimensionless time, $\bar{t}$, for different mesh maximum refinement levels, $L_{max} = 10, 11, 12$, and 13. The minimum refinement level in all cases is 6. The dimensionless parameters are $Fr = 200$, $Bo = 20$, $Wi_c = 4$, $\eta_r = 0.1$, $\rho_r = 0.1$, and $\beta = 0.00$. The viscosity jump across the interface is linear.

Figures 4.11(a), (c), and (e) present the bubble shape observed in the experimental analysis by Pilz and Brenn (2007). The corresponding numerical simulations are depicted in Fig. 4.11(b), (d), and (f), respectively. In the experimental study, the surrounding materials are composed of aqueous Praestol 2500 (PAM) solutions with 0.8 (Fig. 4.11(a)) and 0.3 (Figs. 4.11(c) and (e)) $wt.\%$, with bubble volume of 45.8 mm^3 (Fig. 4.11(a)), 19.0 mm^3 (Fig. 4.11(c)), and 11.1 mm^3 (Fig. 4.11(e)). The agreement regarding the bubble shape is reasonably good.

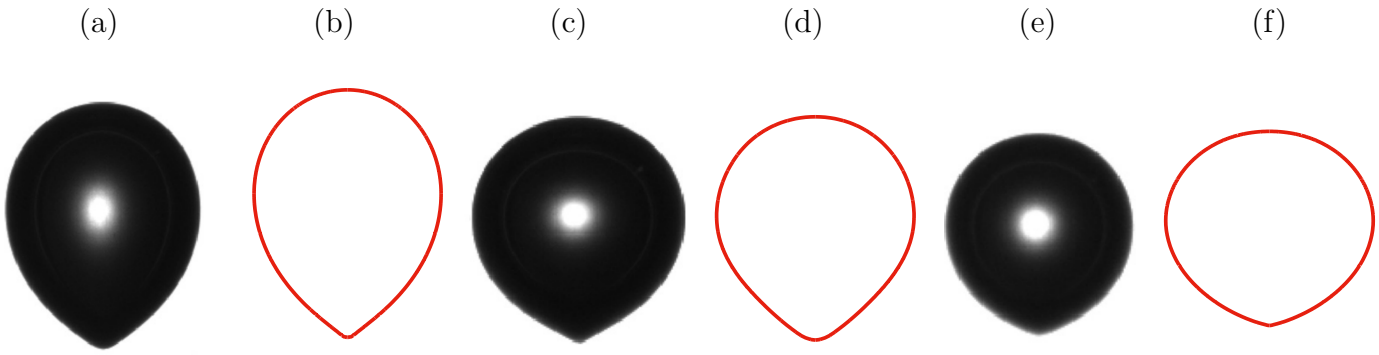

Figure 4.11: Bubble rising in elasto-viscoplastic materials experimental results of Pilz and Brenn (2007) (a,c,e) and numerical simulations (b,d,f). The dimensionless parameters are (a,b) $Fr = 0.375$, $Bo = 2.558$, and $Wi_c = 5.969$, (c,d) $Fr = 38.126$, $Bo = 1.467$, and $Wi_c = 36.128$, and (e,f) $Fr = 22.274$, $Bo = 1.025$, and $Wi_c = 30.202$ For the numerical results, (b,d,f) $\eta_r = 0.01$, $\rho_r = 0.01$, and $\beta = 0.01$.

4.2.4 Drop rise in elasto-viscoplastic materials

This section presents a validation test for the elasto-viscoplastic implemented model, where the experimental results of Lopez et al. (2018) of bubbles rising in elasto-viscoplastic materials (Carbopol solutions) are reproduced using the Saramito model. The section begins by discussing the viscosity jump in elasto-viscoplastic materials. To ensure the accuracy and reliability of the numerical simulations, preliminary tests are conducted to check the dependency of the solution on the grid and regularization parameter, as well as the range of applicability of the EVP model.

In the EVP model, the viscosity and relaxation time are dependent on the stress. As the fluid interface undergoes advection, the cells located at the interface gradually become filled or emptied with elasto-viscoplastic material. For example, when a cell initially contains the Newtonian phase and starts to be filled with elasto-viscoplastic material, the stress within the cell is relatively low. Consequently, the calculated viscosity, $\eta((|\boldsymbol{\tau}_d|)$ becomes high. This leads to significant fluctuations in viscosity across the interface, regardless of using the harmonic or arithmetic mean. To address this issue, a workaround is implemented wherein the viscosity for interfacial cells is determined by averaging the viscosities of four neighboring cells. Specifically, only non-interfacial neighboring cells are considered in this averaging process. This approach helps to mitigate the strong viscosity fluctuations that would otherwise occur across the interface and break the simulation. Finally, after obtaining the viscosity field, η is multiplied by the smoothed volume fraction field $\tilde{c}$, to improve the calculation.

A grid and regularization parameter dependency test is now conducted to assess the sensitivity of the elasto-viscoplastic model. Figures 4.12(a) and (b) present the results for the

dimensionless velocity, $\bar{u}$, as a function of dimensionless time, $\bar{t}$, with respect to the mesh maximum refinement level and regularization parameter, respectively. The dimensionless parameters considered for these tests are $Fr = 200$, $Bo = 20$, $Pl = 0.04$, $Wi_c = 3$, $\eta_r = 0.1$, and $\rho_1 = 0.1$. As evident in Fig. 4.12(a), the results for $L_{max} = 12$ and 13 are close. However, the computational cost associated with $L_{max} = 13$ is considerably higher. Therefore, considering both the computational efficiency and the negligible difference in results, $L_{max} = 12$ is deemed appropriate for simulating the rise of drops in elastic materials. Figure 4.12(b) shows that there is not much change in $\bar{u}$ for $N = 10^5$ and 10^6. Since the computational cost of the latter is higher, $N = 10^5$ is selected for the simulations, consistent with the choice made for the inelastic viscoplastic case.

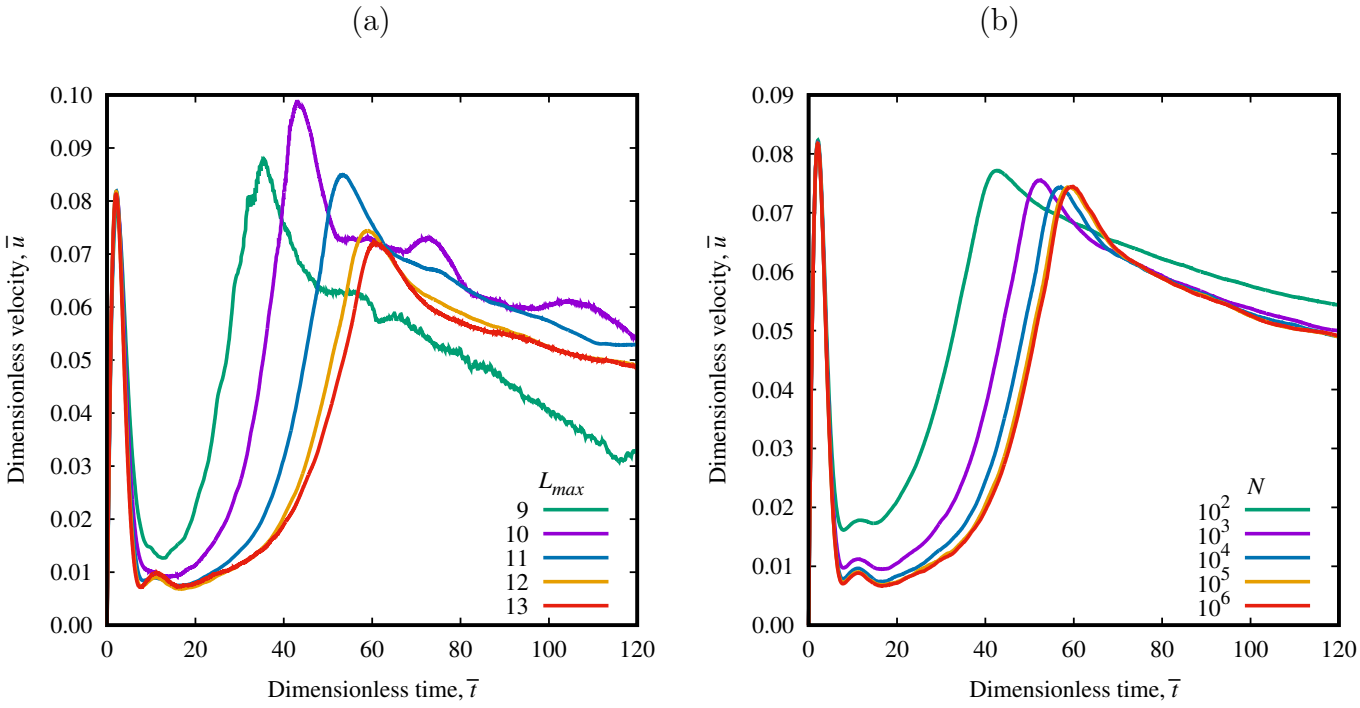

Figure 4.12: Drop dimensionless rise velocity, $\bar{u}$, with dimensionless time, $\bar{t}$, for (a) different mesh maximum refinement levels, $L_{max} = 9$ to 13 (b) and dimensionless regularization parameters, $N = 10^2$ to 10^6. The minimum refinement level in all cases is 6, while L_{max} is (a) changed from 9 to 13 in (a) and equal to 12 in (b). $N = 10^5$ in (a) and changed from 10^2 to 10^6 in (b). The dimensionless parameters are $Fr = 200$, $Bo = 20$, $Pl = 0.04$, $Wi_c = 3$, $\eta_r = 0.1$, and $\rho_r = 0.1$.

In contrast to the Upper Convected Maxwell model, whose numerical implementation reduces to the simpler Newtonian formulation (as demonstrated in Fig. 4.9), reducing the EVP Saramito model to the simpler inelastic viscoplastic Bingham formulation ($Wi_c \to 0$) gives rise to numerical instabilities. Figure 4.13(a) presents the drop dimensionless terminal

velocity, $\bar{u}_t$, as a function of Wi_c for $Pl = 0.04$, $Fr = 200$, $Bo = 20$, $\eta_r = 0.1$, $\rho_r = 0.1$, and two values of the solvent to the total viscosity ratio, $\beta = 0.00$ and 0.01. The terminal velocity obtained with the inelastic Bingham model is represented by the black dashed line. For $Wi_c \gtrapprox 1.5$, the deviation between the two solutions is virtually negligible. For $Wi_c \lessapprox 1.5$, the solution with $\beta = 0.01$ tends towards the inelastic solution while the solution with $\beta = 0.00$ tends to a non-negligible higher terminal velocity. Figure 4.13(b) shows the dimensionless computational drainage time for the same parameters and demonstrates a similar behavior for $\Delta\bar{t}$. Moreover, the solutions for $Wi_c \lessapprox 1.5$ and $\beta = 0.00$ presented strong fluctuations in the stress field, while for $\beta = 0.01$ the spatial variation of the stress was smooth. Decreasing the time step and smallest grid element size did not yield any improvement. The cause of these instabilities is not clear but could be attributed to two aspects of the model: the dampening of stress fluctuations by viscosity and/or the addition of one more non-linear term to the constitutive equation.

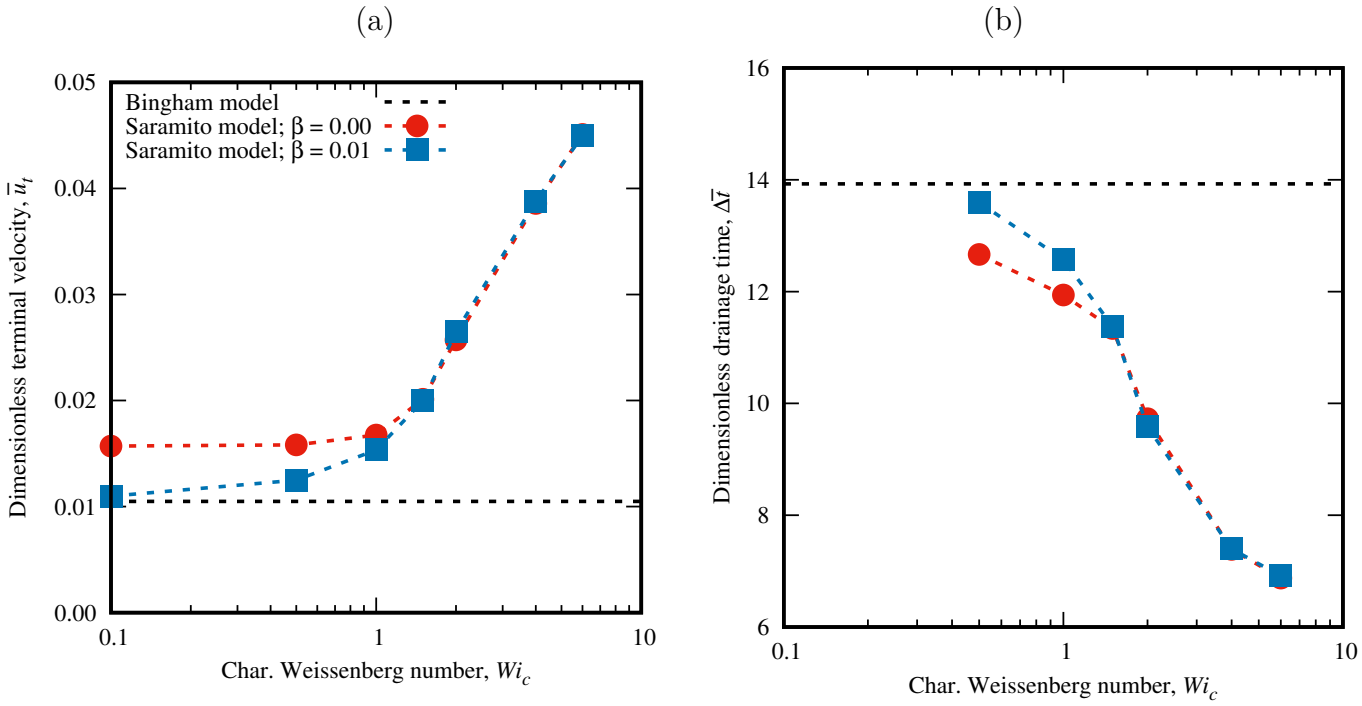

Figure 4.13: (a) Drop dimensionless rise velocity $\bar{u}$ and (b) the dimensionless computational drainage time, $\Delta\bar{t}$, as a function of Wi_c for $\beta = 0.00$ (red line with circles) and 0.01 (blue line with squares). The other dimensionless parameters are $Pl = 0.04$, $Fr = 200$, $Bo = 20$, $\eta_r = 0.1$, and $\rho_r = 0.1$. The inelastic viscoplastic solution (Bingham model) is represented by the black dashed lines.

To illustrate the influence of the solvent viscosity, Fig. 4.14 displays the development of the magnitude of the dimensionless stress, $|\bar{\boldsymbol{\tau}}| = |\boldsymbol{\tau}|/(\eta\dot{\boldsymbol{\gamma}}_{shear})$, of Oldroyd-B materials

with $\beta = 0.00$ and 0.01 in a Couette flow. The initial velocity is zero everywhere, and at $\bar{t} = 0$ the upper plate starts to move with a velocity, U. The distance between the plates is H. The stress is measured at the middle of the domain at the height $0.5\,H$, where the shear rate remains zero for a small period of time. The characteristic Weissenberg number, defined as $Wi_c = \lambda\dot{\gamma}_{shear}$, is equal to 1, where $\dot{\gamma}_{shear} = U/H$ is the shear stress at steady state. For the UCM model, $\beta = 0.00$ (red line), the solution oscillates significantly, and at later times (not shown) diverges. By introducing a small solvent viscosity (blue line for $\beta = 0.01$), the small oscillations disappear. In the case of employing the EVP Saramito model with $\beta = 0.00$, the simulation broke down after the first peak oscillation. The smoothing of oscillations in the stress in transient viscoelastic flows by using a relatively small solvent viscosity, $\beta \sim 0.01 - 0.001$, which has a negligible effect on the main flow, has been demonstrated by different researchers (Keiller, 1992; Xue et al., 2004; Duarte et al., 2008). It is worthy noting that $|\bar{\boldsymbol{\tau}}|$ reaches a higher peak value for $\beta = 0.00$ than for $\beta = 0.01$. The higher terminal velocity reached by the drops and the fluctuations in the yielded region for small values of Wi_c may be explained by the peak oscillations of the stress, which facilitates the yielding of the surrounding material.

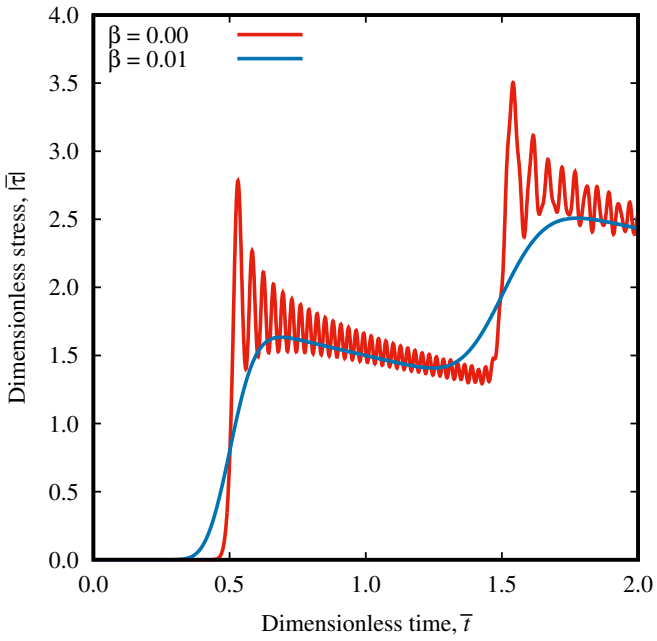

Figure 4.14: Magnitude of the dimensionless stress, $|\bar{\boldsymbol{\tau}}|$, with dimensionless time, $\bar{t}$, for $\beta = 0.00$ (red line) and 0.01 (blue line) and $Wi_c = 1$.

In the case of the EVP formulation, the situation may be aggravated by an additional non-linearity introduced when writing the viscosity as a function of the stress (*i.e.*, the first

term of Eq. 2.89, $\boldsymbol{\tau}/\eta(\boldsymbol{\tau_d})$). This may lead to a numerical instability phenomenon. The development of the stress also depends on the elastic modulus G. One possible consequence is that for high values of G (small Wi_c), changes in the stress for a given elastic deformation increase, causing large variations in $\overset{\nabla}{\boldsymbol{\tau}}$, which in turn affect $\eta(\boldsymbol{\tau})$, and in the sequence affect $\boldsymbol{\tau}$. Nevertheless, according to Fig. 4.13, the results for $\beta = 0.00$ and 0.01 are comparable for $Wi_c \gtrapprox 1.5$. The Sarmito model reduces to the inelastic formulation, but for small values of Wi_c it is advised to add a small solvent viscosity.

Figures 4.15(a) and (c) present the experimental results of Lopez et al. (2018) for two bubbles rising in an aqueous solution of Carbopol and Figs. 4.15(b) and (d) display the corresponding numerical simulations. The flow curve of the Carbopol solutions used by Lopez et al. (2018) is better described by the Herschel-Bulkley model rather than the Bingham model and the power-law index n is determined to be 0.4251, and the Herschel-Bulkley version of the Saramito model (Eq. 2.92) is employed for the numerical solution. In the numerical simulations presented in Fig. 4.15, the following parameters are used: $\beta = 0$, $\rho_r = 0.01$, $\eta_r = 0.01$, $L_{max} = 12$, and $N = 10^4$. It was observed that using $N = 10^5$ for the specific case of the bubbles investigated by Lopez et al. (2018) led to the formation of bubbles with slender tails (thread-like), ultimately resulting in the breakdown of the simulations. The choice of the regularization parameter depends on the characteristics of the flow under consideration (Frigaard and Nouar, 2005). Given that the Froude and Bond numbers in the study conducted by Lopez et al. (2018) are significantly larger than those examined in this present study (see Table 3.1), a value of $N = 10^5$ appears to be overly stringent for this particular case. Furthermore, the results from Fig. 4.12(b) show that the difference

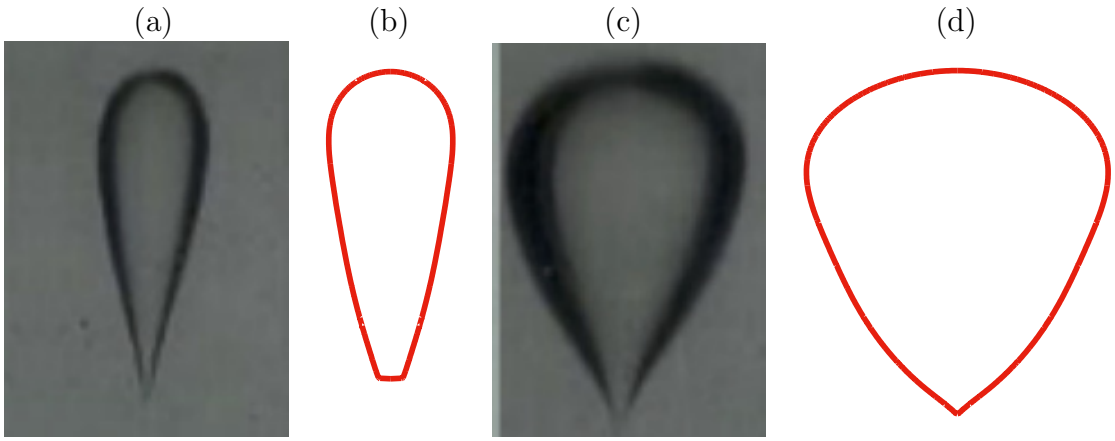

Figure 4.15: Bubble rising in elasto-viscoplastic materials experimental results of Lopez et al. (2018) (a,c) and numerical simulations (b,d). The dimensionless parameters are (a,b) $Fr = 22,098$, $Bo = 88.5$, $Pl = 0.1130$, and $Wi_c = 1.544$ and (c,d) $Fr = 562,712$, $Bo = 254$, $Pl = 0.0668$, and $Wi_c = 2.611$. For the numerical results, (b,d) $\beta = 0$ $\rho_r = 0.01$, $\eta_r = 0.001$.

in rise velocity for $N = 10^4$ and 10^5 is relatively small. Therefore, setting $N = 10^4$ in Figs. 4.15(b) and (d) should not result in a significant error for the overall drop shape. It is evident that the experimental results of Lopez et al. (2018) are reasonably well reproduced, and the implemented Saramito model is able to predict the inverted teardrop shape. It is worth noting that the tail of the bubble in Fig. 4.15(b) appears to be cut, without a sharp point, although its overall shape is similar to that seen in the photograph of Fig. 4.15(a). Importantly, the tail of bubbles rising in elastic materials, which adopt a teardrop shape, may not necessarily be conical but can have an asymmetric shape, resembling a knife's edge (Bird et al., 1987a; Fraggedakis et al., 2016c). The observed shape of the tail (conical or knife's edge) may depend on the viewing angle. Hence, the cut tail of the bubble in Fig. 4.15(b) may not be a purely numerical effect since it may also be observed experimentally.

4.2.5 Drop impact on a fluid-fluid interface: drop collision dynamics

To investigate the collision stage of the coalescence phenomenon, the experimental result of Mohamed-Kassim and Longmire (2003) of a Newtonian drop falling in a Newtonian matrix and impacting on a fluid-fluid interface is reproduced. Since the drop is heavier than the surroundings, it falls instead of rising. Hence, the direction of the gravity vector is inverted (in the positive z-direction). Here, the film region does not receive any special treatment, and the mesh is refined only as a function of the volume fraction and velocity fields. The objective of this test is to evaluate the grid requirements for accurately capturing the outer flow dynamics during drop collision, without explicitly resolving the inner flow within the film region. Figure 4.16 (a) shows the dimensionless position, $\bar{z}$, of the point at the interface located at $\bar{r} = 0$ and initially at $\bar{z} = 0$ (see the yellow square in the insert of Fig. 4.16 (b)) with dimensionless time during the drop impact for different mesh maximum refinement levels ($L_{max} = 10$, 11, 12, 13, and 14). Here, $\bar{t} = 0.0$ denotes the time at which the drop front reaches the interface rest position $\bar{z} = 0.0$. As can be seen in the figure, the interface position does not vary much for the different values of L_{max} until the first part of the drop rebound ($\bar{t} \lessapprox 200$) takes place. Subsequently, for the later stage of the drop rebound ($\bar{t} \gtrapprox 400$), the solution does not vary much when changing the maximum level of refinement from 13 to 14. Therefore, a level of at least 13 is required to reproduce the collision dynamics in the latter part of the impact. Figure 4.16(b) compares the dimensionless positions of the top layer interface (yellow squares), drop front (red crosses), and drop back (blue circles), all at $\bar{r} = 0$, obtained experimentally by Mohamed-Kassim and Longmire (2003) and the numerical results with $L_{max} = 13$ (lines). Furthermore, Fig. 4.17 compares snapshots of

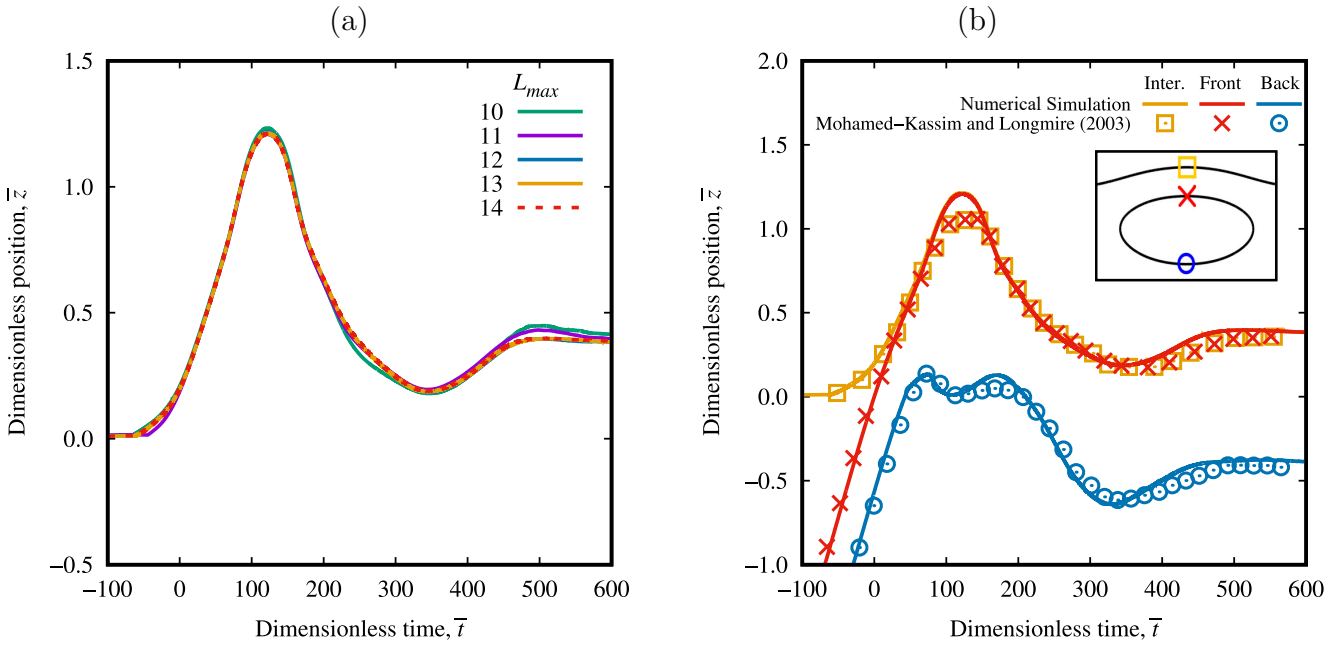

Figure 4.16: (a) Change of the interface dimensionless position, $\bar{z}$, due to drop impact versus dimensionless time, $\bar{t}$, for $L_{max} = 10$, 11, 12, 13, and 14. (b) Experimental results of Mohamed-Kassim and Longmire (2003) (symbols) and the present simulations (lines) for the drop back (blue) and front (red), and interface (yellow) positions with dimensionless time for $L_{max} = 13$. The dimensionless parameters are $Fr = 5044$, $Bo = 6.40$, $Pl = 0.00$, $\eta_r = 0.33$ and $\rho_r = 1.189$

the drop and interface shape of the experimental result of Mohamed-Kassim and Longmire (2003) (first and third columns) and the numerical simulation (second and fourth columns) at different moments (drop impact, local maximum aspect ratio, maximum interface deflection and minimum aspect ratio, maximum aspect ratio, maximum interface rebound, and rest position). Overall, there is reasonable agreement between the experimental and numerical outcomes presented in both Figures 4.16(b) and 4.17.

4.2.6 Drop impact on a liquid-solid interface: film shape evolution

Although $L_{max} = 13$ is enough to model the interfaces' positions during the collision step, a higher level of refinement is required to resolve the inner flow in the film as the drop approaches the interface and the thickness of the film decreases. Employing a constant $L_{\max}$ throughout the simulation, as done thus far, from the initial stages until the film thickness reaches a minimum value of $h = 0.01D$, proves to be computationally intensive. In the present validation tests, during the drop rising stage, $L_{\max}$ is set to 12. However, it is subsequently increased according to Eq. 4.1 following the drop collision. In this section, the experimental results of Vakarelski et al. (2022) of an air bubble impacting a solid interface (a glass plate)

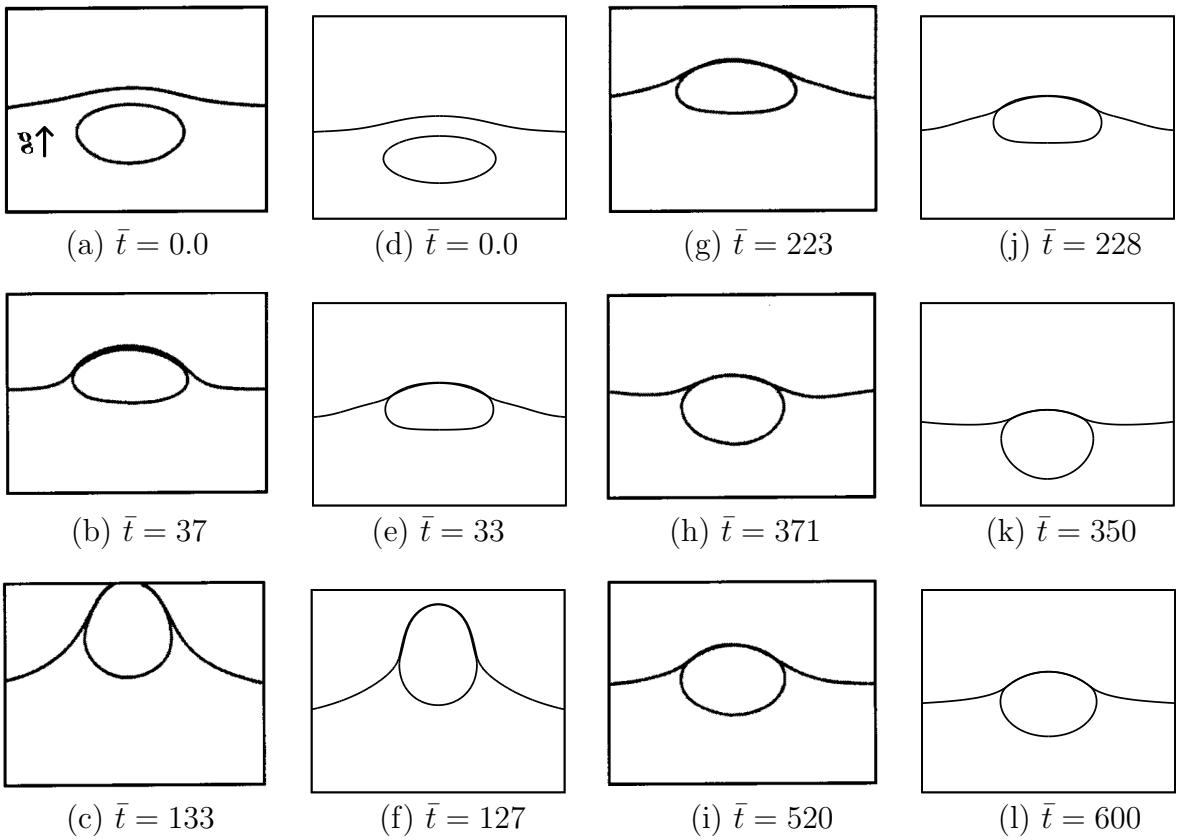

Figure 4.17: Snapshots of the drop and interface at different times. The first and third columns exhibit the experimental of Mohamed-Kassim and Longmire (2003), and the second and fourth columns exhibit the numerical simulations. The dimensionless parameters are $Fr = 5044$, $Bo = 6.40$, $Pl = 0.00$, $\eta_r = 0.33$ and $\rho_r = 1.189$, and $L_{max} = 13$. Drop impact time (a and d), local maximum aspect ratio (b and e), maximum interface deflection and minimum aspect ratio (c and f), maximum aspect ratio (g and j), maximum interface rebound (h and k), and rest position (i and l). *Obs.*: the gravity vector points upwards.

are numerically reproduced. The authors obtained the bubble center of mass position with time and the shape of the draining film with a high-speed interferometry technique. As in the previous sections, a grid dependency test is conducted *a priori* to assess the value of the constant $\mathcal{C}$ in Eq. 4.1. The simulations presented here employed the film identification method implemented and introduced in Sec. 4.1.1. The mesh is adapted as a function of the volume fraction field, velocity field, and the film region.

Figure 4.18(a) shows the dimensionless minimum film thickness, $\bar{h}_{min} = h_{min}/D$, with dimensionless time, $\bar{t}$, for a drop impacting on a liquid-liquid interface for $\mathcal{C} = 5$, 10, and 15. The surrounding is Newtonian and the dimensionless parameters are $Fr = 200$, $Bo = 20$, $\eta_r = 1.0$, and $\rho_r = 0.1$. Figure 4.18(b) exhibits the dimensionless film thickness shape ($\bar{h} = h/D$) as a function of the dimensionless surface length, $\bar{s} = s/D$, at the moment

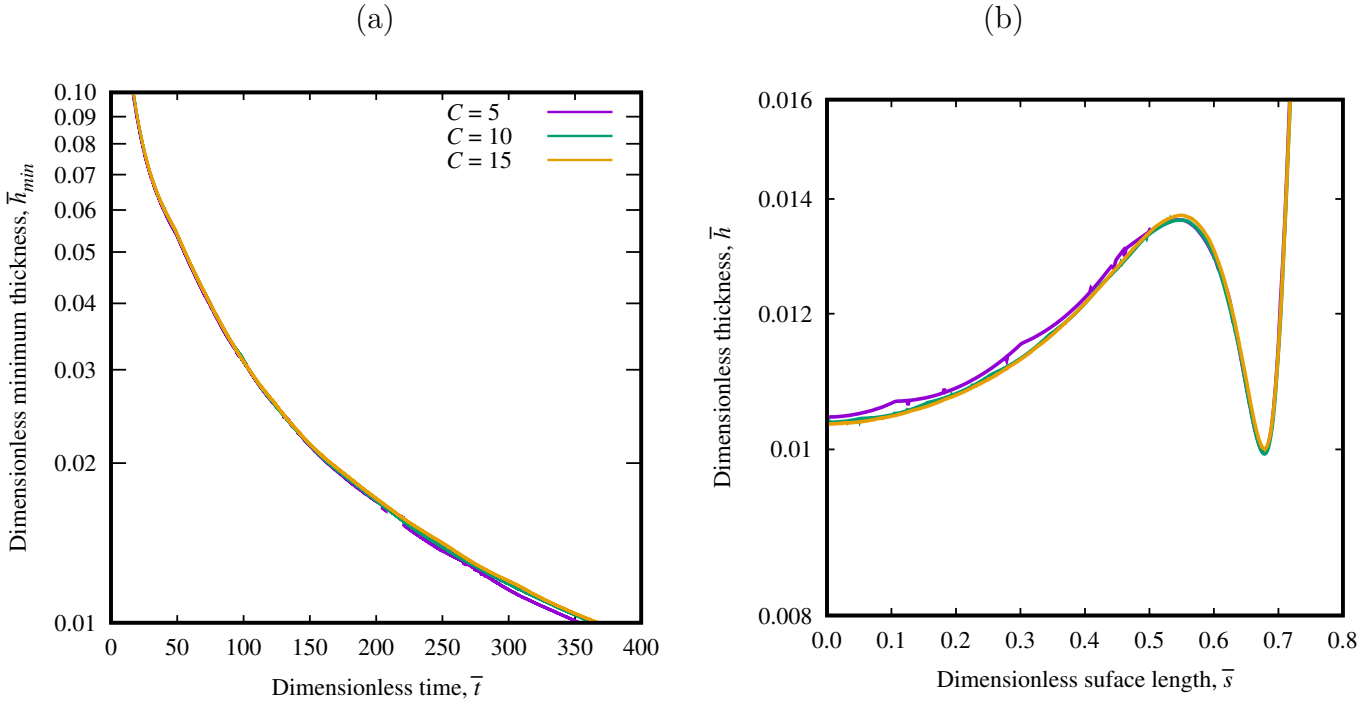

Figure 4.18: (a) Dimensionless minimum film thickness, $\bar{h}_{min}$, versus dimensionless time, $\bar{t}$, and (b) dimensionless film thickness, $\bar{h}$, versus dimensionless surface length, $\bar{s}$, for $\mathcal{C} = 5$, 10 and 15 at the moment $\bar{h}_{min} = 0.01$. Results for $Fr = 200$, $Bo = 20$, $Pl = 0.00$, $\eta_r = 1.0$, and $\rho_r = 0.1$.

$\bar{h}_{min} = 0.01$. The results reveal that $\mathcal{C} = 5$ (where $L_{max}(h_{min} = 0.01) = 13$) does not accurately represent the interface. The film shape demonstrates minimal change when $\mathcal{C}$ is varied from 10 to 15, corresponding to $L_{max} = 14$ and 15, respectively. Nonetheless, the computational time increases significantly. In this case, the interface has a wimpled shape (Chan et al., 2011), with two minimums, one at the film center and one at the film periphery. The shape of the drop and top layer interface are displayed in Fig. 4.19 in the $(\bar{r}, \bar{z})$ coordinate system. Therefore, $\mathcal{C} = 10$ is chosen to numerically produce the film shape $(\bar{h} \times \bar{r}_b)$ and bubble's center of mass position $\bar{z}_{cm}$ of the experimental results of Vakarelski et al. (2022). The corresponding results are shown in Figs. 4.20(a) and (b), respectively, where the open circles are the experimental results and the solid lines are the numerical results. The values of the dimensionless governing numbers are $Fr = 5184$, $Bo = 0.089$, $\eta_r = 0.0181$, and $\rho_r = 0.0012$. There is good agreement between the experimental and numerical results.

In summary, the validation tests demonstrated that the solvers and implementations made by the author are capable of satisfactorily resolving the problems of drop rise and interfacial coalescence initiation in elasto-viscoplastic materials, as well as reduced formulations. The grid and regularization parameter dependency tests have yielded optimal values of $N = 10^5$,

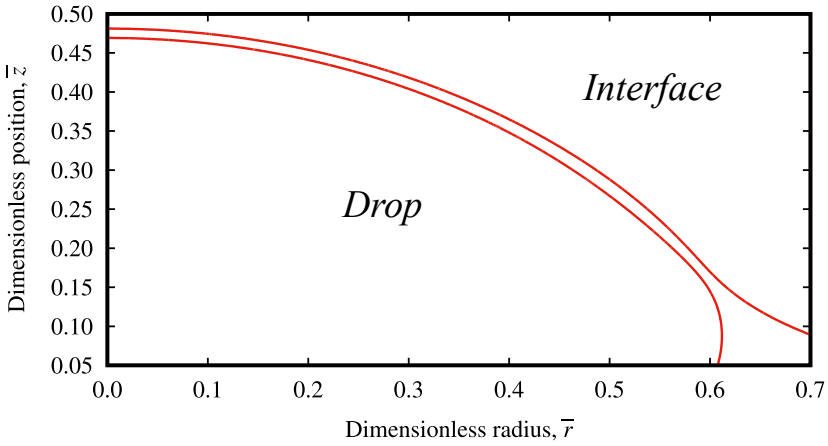

Figure 4.19: Drop collision on the top layer interface and the entrapped film in the $(\bar{r}, \bar{z})$ coordinate system with $\mathcal{C} = 10$ at the moment $\bar{h}_{min} = 0.01$. Results for $Fr = 200$, $Bo = 20$, $Pl = 0.00$, $\eta_r = 1.0$, and $\rho_r = 0.1$.

(a) (b)

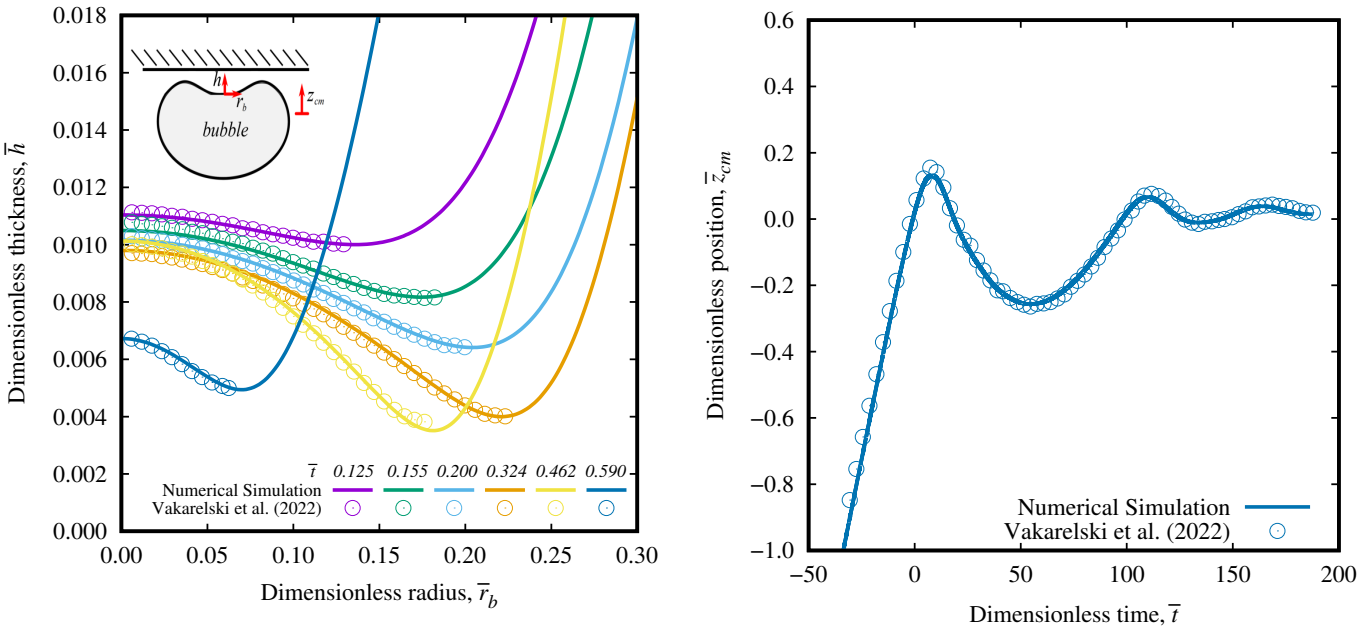

Figure 4.20: (a) Dimensionless film thickness, $\bar{h}$, with dimensionless film radius, $\bar{r}_b$, at different times for an air bubble impacting on a solid surface. Open circles are the experimental results of Vakarelski et al. (2022) and the solid lines are the present numerical simulations. (b) Bubble center of mass dimensionless position, $\bar{z}_{cm}$, with dimensionless time, $\bar{t}$, experimental (open circles) and numerical (solid lines) results. $\mathcal{C} = 10$ and the dimensionless parameters are $Fr = 5184$, $Bo = 0.089$, $\eta_r = 0.0181$ and $\rho_r = 0.0012$.

$L_{max} = 12$ for the rising part, and L_{max} increasing gradually from 12 up to 14 as a function of h_{min} following the drop impact. Thus, the film's minimum number of cells, $\mathcal{C}$, is equal to 10. Prior to proceeding to the subsequent chapter, which encompasses the presentation and discussion of the obtained results, it is important to reiterate the significance of acknowledging the computational limitations associated with conducting extensive simulations for $\bar{h}_{min} < 0.01$. Given the substantial computational expense involved in such cases, the practical approach adopted consists in focusing on the initial stage of the coalescence process and measuring the computational drainage time, Δt, as the duration in which $\bar{h}_{min}$ decreases from 0.1 to 0.01. Furthermore, it is worth mentioning that the simulations were performed on distinct computational platforms featuring processors operating at different clock speeds, specifically 1.80 GHz and 2.40 GHz. The simulations were executed using parallel processing, utilizing 1 to 12 processors. The computational time required for the simulations varied depending on the input dimensionless parameters and complexity of each simulation, ranging from approximately 1 to 20 days.

Chapter 5

Results

This chapter presents and discusses the results of drop entrapment condition, rise, and subsequent interfacial collision, and film drainage initiation. It begins with the condition for drop entrapment in viscoplastic materials (Sec. 5.1), which impedes the rise and collision to happen. Subsequently, the problems of drop rise and interfacial coalescence initiation are addressed in Sec. 5.2 and 5.3, respectively. The ascent and collision of droplets are examined progressively in different surroundings, namely Newtonian, inelastic viscoplastic, viscoelastic, and elasto-viscoplastic. Remarks on drop entrapment in elasto-viscoplastic materials are presented in Sec. 5.2.4.1, following a discussion on the phenomenon of drop rise in EVP materials. Furthermore, the impact of rheological parameters on coalescence is evaluated based on the computational drainage time Δt.

5.1 Drop entrapment in inelastic viscoplastic materials

In investigating the rise dynamics of drops in yield stress materials, the first thing to be assessed is, perhaps, whether a drop will rise in the first place. Drops may permanently be entrapped in inelastic viscoplastic materials if the buoyancy force is not enough to overcome the yield stress of the surrounding material. This section investigates the entrapment condition of spherical and non-spherical drops in inelastic viscoplastic materials.

5.1.1 Bubble entrapment criterion

In the present analyses, the surrounding viscoplastic material is mimicked by the regularized version of the Bingham model of Eq. 2.58. Since the model allows for creeping flow in unyielded regions the criterion of zero velocity as the condition for entrapment is not applicable. Therefore, the criterion used to determine drop mobility is the formation of

a complete envelope of yielded material around the drop, otherwise the drop is considered entrapped. This is similar to the criterion proposed by Tsamopoulos et al. (2008) who considered that a bubble is arrested when the external yield surface merges with the unyielded material around the bubble equator. Figure 5.1 shows the yield surface around four drops with different plastic numbers. Recall that the Yield-stress parameter, Y_g, for spherical drops is defined according to Eq. 2.99 (or three times the plastic number), repeated for the sake of clarity,

$$Y_g = \frac{3}{2}\frac{\tau_y}{R\Delta\rho g}. \tag{2.99}$$

The simulations are run for just enough time to observe, or not, the appearance of a stable yield envelope. As can be seen in Fig. 5.1(a), for the smallest value of the plastic number, $Pl = 0.040$, the yield envelope spans far away from the drop surface. With an increase in the level of plasticity (Fig. 5.1(b)), $Pl = 0.064$, the size of the yield envelope decreases and some unyielded material appears on the drop equator, but the drop is still mobile. With a further increase in Pl to 0.066 (Fig. 5.1(c)), the size of the yield envelope around the drop reduces and the size of the unyielded region on the drop equator increases; nevertheless, the drop is still mobile. Slightly increasing the plastic number yet again ($Pl = 0.068$) results in the vanishing of the yield envelope and the drop entrapment (Fig. 5.1(d)).

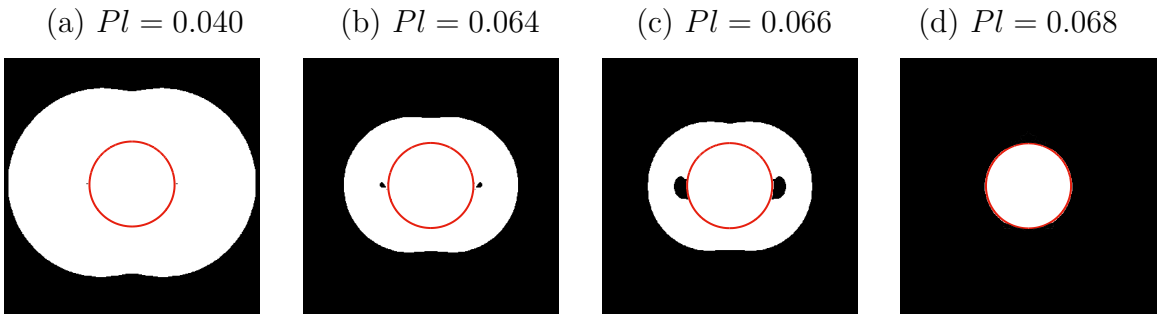

Figure 5.1: The yielded (white) and unyielded (black) regions around drops with different values of Pl. The drop interface is shown in red color. The other dimensionless parameters are $Fr = 2000, Bo = 2$, $\eta_r = 1.0$, $\rho_r = 0.1$.

For the condition in Fig. 5.1, the critical plastic number for entrapment, Pl_c, is between 0.066 and 0.068 (or Y_{gc} between 0.198 and 0.204). Pl_c is determined using a method similar to the root-finding Bisection method. The plastic number is varied in discrete intervals until the difference between the minimum value of Pl for which the drop is static and the maximum value of Pl for which the drop is mobile is less the 5%. Pl_c is taken as the average of these two values, and it has an error margin of about $\pm 2.5\%$. Therefore, the critical plastic number and critical Yield-stress parameter for the drops in Fig. 5.1 are taken to be 0.067 and 0.201, respectively.

5.1.2 Entrapment condition of spherical drops

This section discusses the entrapment condition of initially spherical drops and assesses the effects of Fr, Bo, η_r, and ρ_r. Figure 5.2 exhibits Y_{gc} as a function of the Froude number (red circles) for $Bo = 2$, $\eta_r = 0.1$, and $\rho_r = 0.1$. For this value of the Bond number, the drops simulated in Fig. 5.2 have a negligible deviation from the spherical shape. The figure also presents other results from the literature (horizontal dashed lines). The present results agree with those of Dimakopoulos et al. (2013) and Tsamopoulos et al. (2008) who calculated $Y_{gc} = 0.196$ and 0.210, respectively. The authors' results are for $Bo \ll 1$, and the drops are expected to have a spherical shape. Dubash and Frigaard (2004) theoretically calculated $Y_{gc} = 0.87$, and Sikorski et al. (2009) and Lopez et al. (2018) experimentally obtained $Y_{gc} = 0.50$ and 0.13, respectively, which deviate from the above numerical results. In the experimental works, the drops are non-spherical, and the Yield-stress parameter is

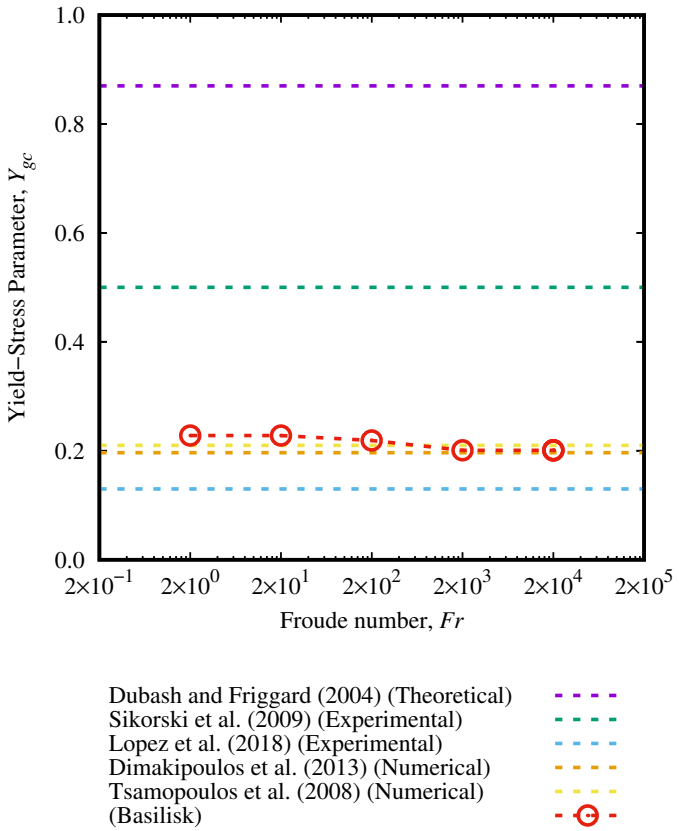

Figure 5.2: Yield-stress parameter, Y_{gc}, as a function of the Froude number, Fr, for $Bo = 2$, $\eta_r = 0.1$, and $\rho_r = 0.1$. Several values of Y_{gc} reported in different literature are also plotted for comparison.

calculated using Eq. 2.100, restated herein for ease of comprehension,

$$Y_g = \frac{3}{2}\frac{\tau_y}{R\Delta\rho g}\frac{R_{max}^2}{R^2}. \tag{2.100}$$

The discrepancy between the two experimental investigations may be attributed to challenges in the experimental characterization of the rheological properties of the surrounding materials and different levels of elasticity. Real yield stress materials also have elastic behavior, which is not accounted for in the simpler inelastic model employed in numerical studies. In fact, the bubbles in the experimental studies exhibited an inverted teardrop shape, which is characteristic of elastic materials (Pourzahedi et al., 2021). Furthermore, the divergence could be ascribed to the difficulties in estimating the entrapment condition experimentally due to the extra buoyancy force required to detach the bubble from the nozzle. Nonetheless, the data obtained from the present computations, as well as from the literature, suggest that Y_{gc} remains largely unaffected by variations in the Froude number for spherical bubbles. The average value of Y_{gc} is 0.209 with a maximum deviation of approximately 4% observed across a four-order-of-magnitude range in Fr.

Figure 5.3 presents Y_{gc} as a function of the Bond number. The other dimensionless numbers are $Fr = 2000$, $\eta_r = 0.1$, and $\rho_r = 0.1$. The figure also showcases the results of Dimakopoulos et al. (2013) and Tsamopoulos et al. (2008). The average value of Y_{gc} is 0.205, with a maximum deviation of about 2% for a five-order of magnitude variation in Bo. These results suggest that Y_{gc} barely depends on Bo for initially spherical drops. The larger deviation in Y_{gc} reported by Tsamopoulos et al. (2008) can be attributed to the alteration in droplet shape. The authors obtained steady-state solutions for the rising of bubbles in a Bingham fluid using the Papanastasiou model (Papanastasiou, 1987). As the yield stress of the surrounding medium varied, both the bubble shape and the yield surface shape underwent progressive transformations. Consequently, since the bubbles do not retain a spherical shape for higher values of Bo, the calculated value of Y_{gc} increases with the Bond number.

Figure 5.4 exhibits the values of Y_{gc} as a function of the viscosity ratio, η_r, and of the density ratio, ρ_r, with fixed values of $Fr = 2000$ and $Bo = 2$. Notably, Y_{gc} remains nearly constant ($Y_{gc} \approx 0.20$) for $\eta_r \lessapprox 10$ and across all values of ρ_r. However, as η_r increases (for $\eta_r \gtrapprox 10$), Y_{gc} diminishes and converges towards the entrapment condition of solid spheres as documented in (Beris et al., 1985), $Y_{gc} = 0.143$ (represented by the red dashed line). This decline in Y_{gc} is a result of the changes in the interfacial stress at the surface of the drop, as it becomes more rigid with a higher viscosity ratio.

In summary, in the case of spherical droplets with $\eta_r \lessapprox 10$, the critical Yield-stress parameter depends on the competition between the resistive force exerted by the yield stress

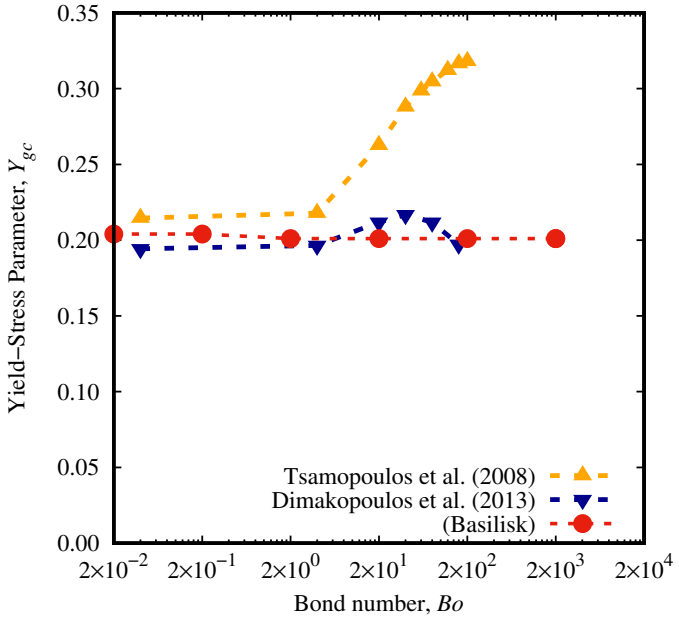

Figure 5.3: Yield-stress parameter, Y_{gc}, as a function of the Bond number, Bo, for $Fr = 2000$, $\eta_r = 0.1$, and $\rho_r = 0.1$ (red circles). The results of Dimakopoulos et al. (2013) (blue inverted triangles) and Tsamopoulos et al. (2008) (yellow triangles) are also presented.

and the buoyancy force, and it is found to be approximately constant, specifically $Y_{gc} = 0.20 \pm 0.02$.

5.1.3 Entrapment condition of non-spherical drops

In this section, the case of non-spherical drops is considered. The drops have an ellipsoid shape and the area where the yield stress acts upon them undergoes changes. This, in turn, affects the level of plasticity required for drop entrapment. Since the drops are no longer spherical, surface tension effects come into play aiding in the yielding of the surrounding material. There are, in this case, two possibilities. Firstly, if surface tension effects are weak, there will be no deformation of the drop because of the limited impact of surface tension. Secondly, if the surface tension force is sufficiently strong, it strives to bring the drop to a spherical shape. Therefore, unlike initially spherical shape drops, Y_{gc} is found to exhibit a dependence on Bo for non-spherical drops.

Figure 5.5 presents the critical Yield-stress parameter defined according to Eq. 2.99 ($Y_{gc} = 3Pl_c$) and Eq. 2.100 ($Y_{gc} = 3Pl_c(R_{max}/R)^2$) for drops with different aspect ratios, defined as the drop height over the drop width, $D_{AR} = D_H/D_W$. The Bond number is set to 200 (low surface tension regime) and the drop shape is virtually unchanged by surface tension

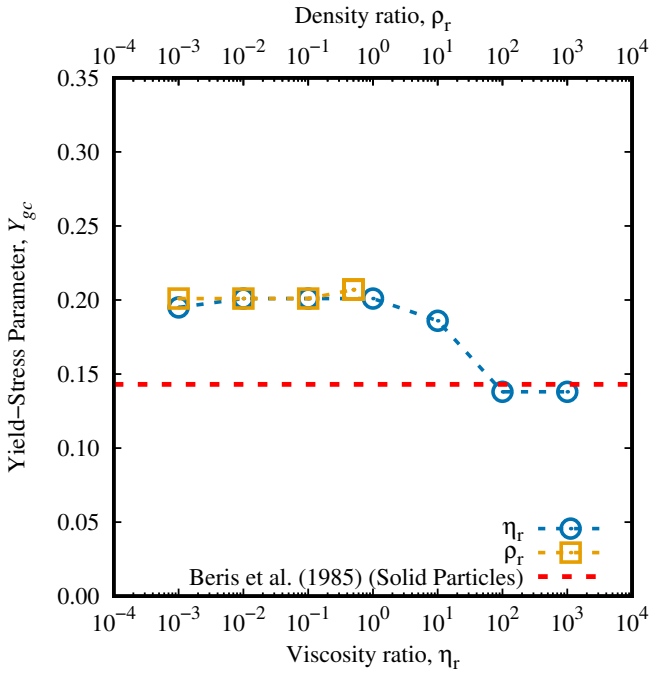

Figure 5.4: Yield-stress parameter, Y_{gc}, as a function of the viscosity ratio, $\eta_r = \eta_2/\eta_1 = \eta_d/\eta_s$ (blue circles), and density ratio, $\rho_r = \rho_2/\rho_1 = \rho_d/\rho_s$ (yellow squares). The dimensionless parameters are $Fr = 2000$ $Bo = 2$, $\eta_r = 0.1$ (yellow squares), and $\rho_r = 0.1$ (blue circles). The result of Beris et al. (1985) for solid particles is represented by the red dashed line.

effects. The classification of the surface tension regimes according to the Bond number as low, intermediate, and high, are discussed later on in the section. As depicted in the figure, Y_{gc} increases significantly and linearly with the aspect ratio using the definition of Eq. 2.99, but it is approximately constant, and approximately equal to 0.20, using the definition of Eq. 2.100, which is the same value obtained for spherical drops. Some earlier literature (Dubash and Frigaard, 2004, 2007; Tsamopoulos et al., 2008; Dimakopoulos et al., 2013) have used Eq. 2.99 since it is easier to relate to the Bingham and plastic numbers when the deformation rate is expressed as a function of the buoyancy force. However, the definition of Eq. 2.100 seems to be more appropriate since the stress exerted by the drop to yield the surrounding viscoplastic material depends on the area perpendicular to the direction of the buoyancy force. In their work, Lopez et al. (2018) estimated Y_{gc} varying between 0.15 and 0.45 when using the definition of Eq. 2.99, but to be approximately 0.13 when using the definition of Eq. 2.100. These results indicate that for low surface tension regimes, the plasticity required to hold a non-spherical bubble is a function of the net buoyancy force as well as the bubble shape.

Figures 5.6(a) and (b) depict the shape evolution of the yield surface around two drops characterized by initial aspect ratios of $D_{AR} = 2.0$ (prolate-shaped) and $D_{AR} = 0.5$ (oblate-

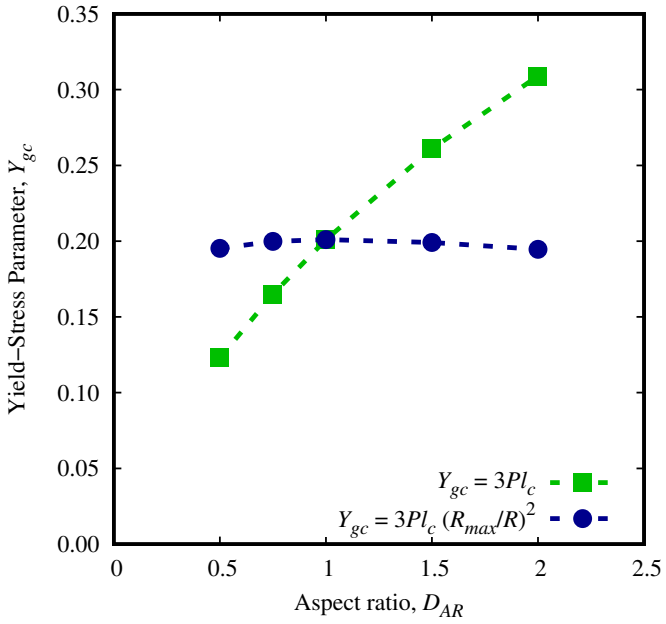

Figure 5.5: The variation of, Y_{gc}, as a function of the initial aspect ratio of the drop, D_{AR}, calculated using Eq. 2.99 (blue line with circles) and Eq. 2.100 (green line with squares). The dimensionless parameters are $Fr = 2000$, $Bo = 200$, $\eta_r = 0.1$, and $\rho_r = 0.1$.

shaped), respectively, in a high surface tension regime, $Bo = 2$. The other dimensionless numbers are $Pl = 0.070$, $Fr = 2000$, $\eta_r = 0.1$, and $\rho_r = 0.1$. As can be observed, both drops acquire a nearly spherical shape ($D_{AR} \to 1$) at $\bar{t} = 85.0$, attributable to the forces exerted by surface tension. In the case of Fig. 5.6(a), surface tension diminishes the drop aspect ratio, which increases the drop cross-sectional area normal to the direction of gravity (where the yield stress resists the drop motion). On the other hand, the oblate drop in Fig. 5.6(b) has its aspect ratio increased, which facilitates the drop motion. As shown in the image, the yield envelope spans farther from the drops' surface at $\bar{t} = 8.5$ than at $\bar{t} = 85.0$. This happens because at $\bar{t} = 8.5$ the drop shape is more distorted from the spherical shape than the drop at $\bar{t} = 85.0$. Consequently, the force exerted by surface tension is stronger at the former than at the latter time. The drops in Fig. 5.6 are close to the entrapment condition at $\bar{t} = 85.0$ and have a shape close to a sphere. In fact, $Pl = 0.070$ is slightly above Pl_c for initially spherical drops ($Pl_c = 0.067$), and an increase in Pl to 0.072 would result in their entrapment. For $Pl = 0.072$, the drops initially exhibit motion but eventually become entrapped as they approach a spherical shape. In this scenario, surface tension may render a drop temporally mobile.

Figure 5.7(a) illustrates the values of $Y_{gc} = 3Pl_c$ (definition of Eq. 2.99) as a function of the Bond number for different initial aspect ratios. For initially prolate drops (red circles)

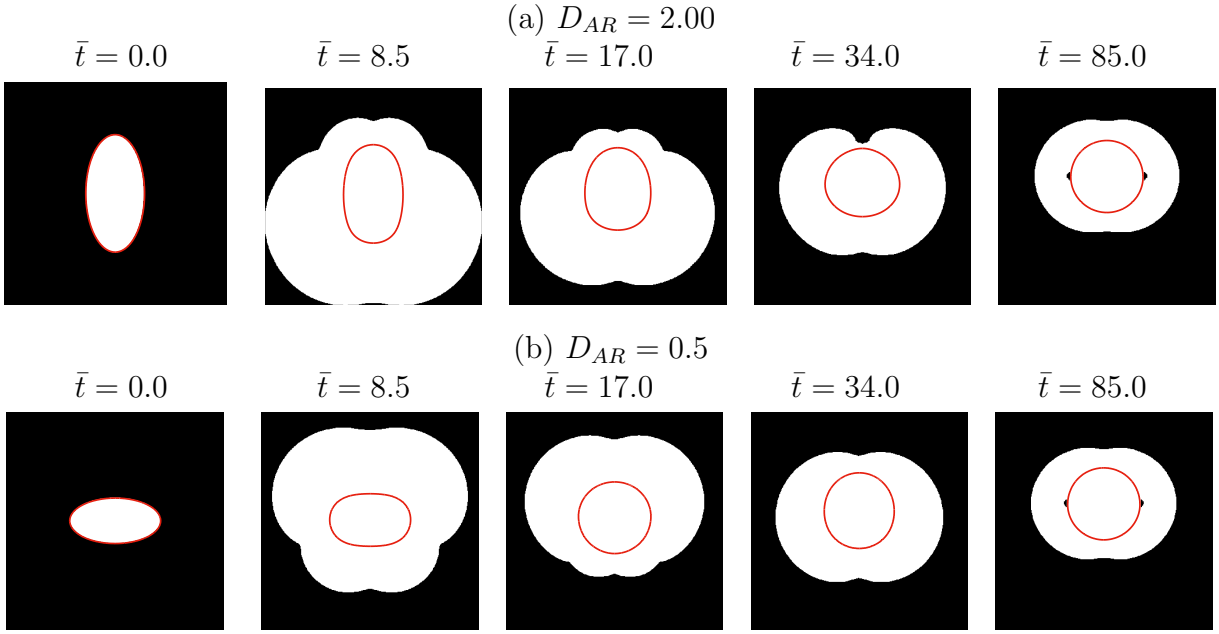

Figure 5.6: Snapshots of the drop interface (red line) and yielded (white)/unyielded (black) regions at different times for non-spherical drops. Initial aspect ratios of D_{AR} 2.0 (a) and 0.5 (b) for, $Pl = 0.070$, $Fr = 2000$, $Bo = 2$, $\eta_r = 0.1$, and $\rho_r = 0.1$.

a decrease in Bo tends to decrease the level of plasticity required for drop entrapment. Conversely, for initially oblate drops (yellow triangles and blue inverted triangles), an increase in the Bond number leads to an elevated level of plasticity necessary for entrapment. This is explained by the change in D_{AR} with Bo, as shown in Fig. 5.7(b), which showcases the drop dimensionless radius R_{max}/D at the entrapment moment. The high surface tension regime refers to a scenario wherein the surface tension force causes the drop to approach a spherical configuration, while the low surface tension regime corresponds to a situation where the drops remain unaffected by the surface tension force and maintain their original shape. The intermediate regime can be characterized as a condition in which the surface tension force initially deforms the drop and enables its ascent, but fails to bring it to a nearly spherical shape. In this particular case, the critical value Pl_{c} lies between the values associated with the low and high surface tension regimes. As seen in Figure 5.7(a), Y_{gc} is approximately constant and equal to that of initially spherical drops for $Bo \lessapprox 6$ (high surface tension regime), regardless of the drop being initially prolate or oblate. For $D_{AR} = 0.50$ and 2.00, Y_{gc} varies with the Bond number for $6 \gtrapprox Bo \lessapprox 60$ (intermediate surface tension regime) and is approximately constant for $Bo \gtrapprox 60$ Y_{gc} (low surface tension regime). For $D_{AR} = 0.75$, the boundary between the intermediate and low surface tension regimes is given by $Bo \approx 20$. Since in this case, the drop's initial shape is closer to the spherical shape, a lower value of Bo is required to set the drop into motion.

Figure 5.8 exhibits the values of $Y_{gc} = 3Pl_c(R_{max}^2/R^2)$ (definition of Eq. 2.100) as a function of Bo. It can be observed that the entrapment condition of $Y_{gc} = 0.20 \pm 0.02$ is also verified for non-spherical temporally mobile drops in case of using the definition of Eq. 2.100 (R_{max} is taken at the moment the drop becomes entrapped, as depicted in Fig. 5.7(b)). The limits ± 0.02 are represented by the black dashed lines.

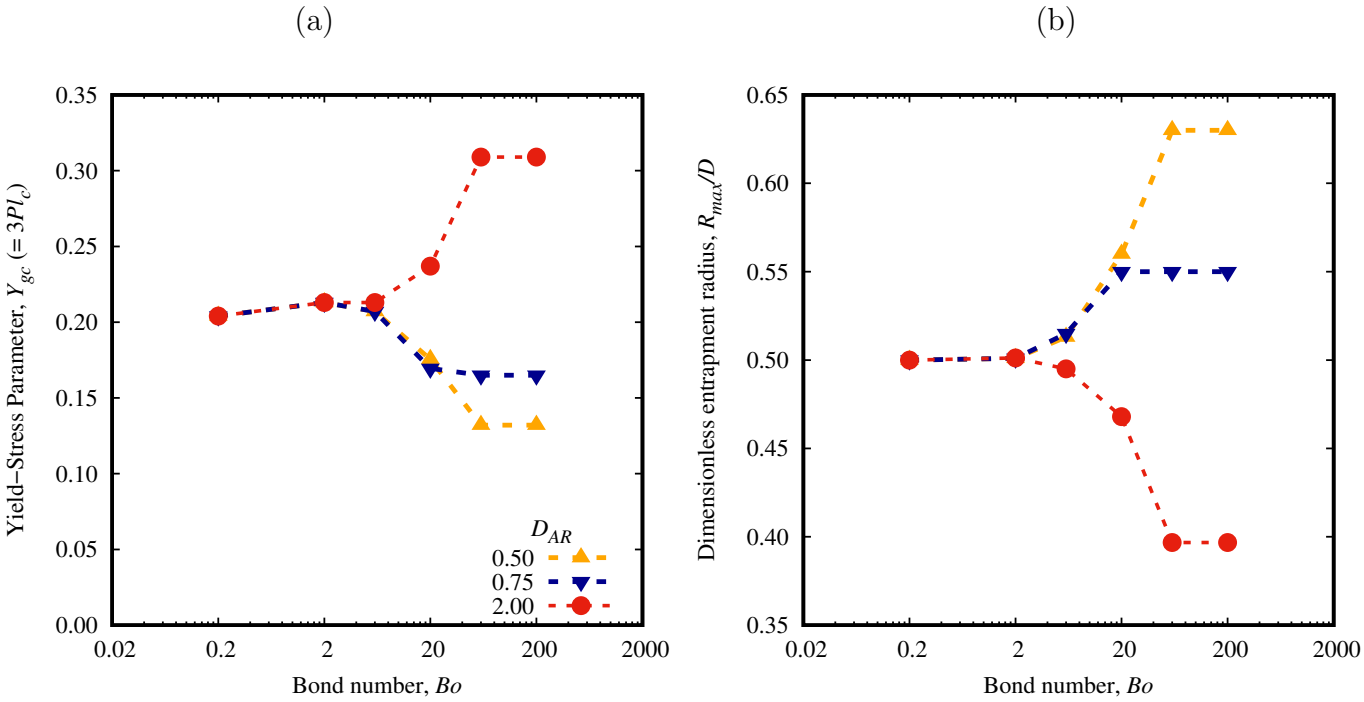

Figure 5.7: (a) The variation of critical Yield-stress parameter, $Y_{gc} = 3Pl_c$, according to Eq. 2.99 and (b) drop dimensionless entrapment radius, R_{max}/D for non-spherical drops as a function of the Bond number Bo. The other dimensionless parameters are $Fr = 2000$, $\eta_r = 0.1$, and $\rho_r = 0.1$.

Elasticity introduces new fascinating and complex phenomena to drop dynamics, affecting the drop entrapment condition; for instance, elastic effects enable material deformation even in the unyielded state (Lopez et al., 2018; Moschopoulos et al., 2021). A discussion on the impact of elasticity on Y_{gc} is presented in Section 5.2.4.1, after examining the rising dynamics of drops in EVP materials.

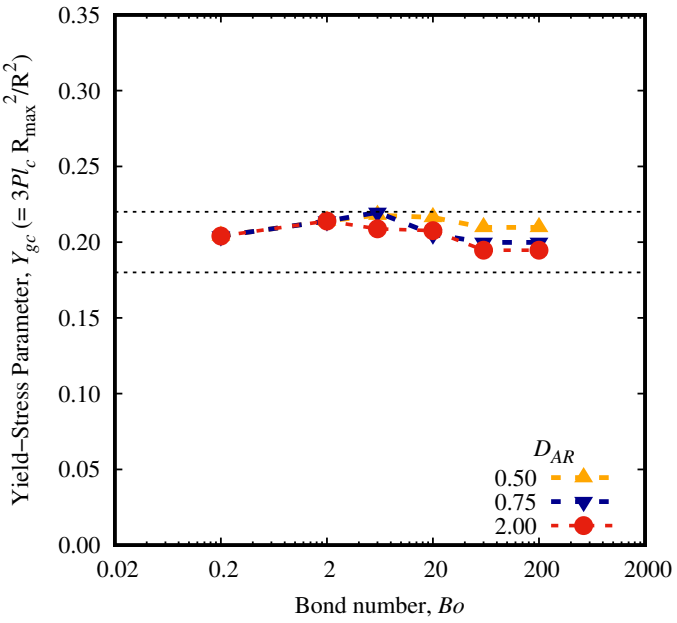

Figure 5.8: The variation of the critical Yield-stress parameter, $Y_{gc} = 3Pl_c(R_{max}^2/R^2)$, according to Eq. 2.100 for non-spherical drops as a function of the Bond number Bo. The other dimensionless parameters are $Fr = 2000$, $\eta_r = 0.1$, and $\rho_r = 0.1$. The limits of $Y_{gc} = 0.20 \pm 0.02$ are represented by the black dashed lines.

5.2 Drop Rise

The drop velocity and shape during the rise stage are important parameters that significantly impact the coalescence process. The interfacial collision of a drop of larger width and higher impact velocity results in a more substantial increase in width during the collision phase. This subsequently generates a draining film with an extended length which tends to decelerate the film drainage process (Zawala and Malysa, 2011; Kočárková et al., 2013). The interdependence between drop velocity and shape characterizes the intricate phenomenon of drop ascent, and these result from the diverse effects of interplaying forces. The drop deformation depends on the balance between the surface tension force, which tends to preserve the drop's spherical shape, and the distorting forces (*e.g.*, inertial, viscous, plastic, and elastic forces), which compete to deform the drop in distinct ways. This section commences discussing drop rising in Newtonian materials in Sec. 5.2.1, focusing on the effects of Fr, η_r, and Bo. Subsequently, the effects of Pl (for inelastic viscoplastic materials) and Wi (for viscoelastic materials) are investigated in Secs. 5.2.2 and 5.2.3, respectively, highlighting the deviations from the Newtonian scenario. Lastly, drop rising in elasto-viscoplastic materials is examined in Sec. 5.2.4 with a particular emphasis on the interaction between plastic and

elastic effects. All the aforementioned dimensionless parameters, except for Bo, exclusively involve the ratio of distorting forces. The Bond number incorporates the shape-persevering surface tension force and provides an indication of the drop deformability (the ease with which the distorting forces deform the drop). Therefore, its influence on drop velocity and shape depends on the dominating distorting force.

5.2.1 Drop rise in Newtonian materials

This section discusses the drop rise dynamics in Newtonian surroundings by assessing the effects of Fr, η_r, and Bo on the drop terminal velocity and shape. Figure 5.9 illustrates the dimensionless terminal velocity of the drops, $\bar{u}_t = u_t/U$ (solid bars), and their dimensionless terminal width, $\bar{D}_{tW} = D_{tW}/D$ (hatched bars), for Newtonian surroundings and different combinations of the dimensionless parameters. The drop width gives a measure of the drop deformation. $\bar{u}_t$ is multiplied by $Fr^{1/2}$ to remove the dependency of U on Fr. The set of dimensionless numbers $Fr = 200$, $\eta_r = 0.1$, and $Bo = 2$ (purple bars) is used in this study as the base scenario. This combination of Fr, η_r, and Bo is used as the base scenario for the other formulations of the surrounding material as well. In order to assess the effects of each parameter on the dynamics of drop rise, Fr, η_r, and Bo are varied individually. To facilitate the discussion, Fig. 5.10 displays the shape of the drop at steady-state rise for the sets of dimensionless parameters shown in Fig. 5.9.

It can be observed that an increase in the Froude number from 200 (purple bars) to 2000 (yellow bars) results in a higher terminal velocity. This increase is attributed to the fact that in the dimensional analyses (Sec. 3.3), viscous forces scale with the buoyant force, thus leading to a rise in the ratio of inertial forces to viscous forces when Fr is increased. Consequently, both the drop terminal velocity and width increase. The widening of the drop occurs due to the higher dynamic pressure in front of the drop, which tends to distort it to an oblate shape ($\bar{D}_{tW} > 1$). The influence of Fr on the drop shape can be observed by comparing Figs. 5.10(a) and (b) for $\eta_r = 0.1$, $Bo = 2$, and $Fr = 200$ and 2000, respectively. On the other hand, an increase in viscosity ratio (the ratio of the drop viscosity, η_2, to the surrounding viscosity, η_1) enhances viscous dissipation, thereby exerting an opposite effect of that of the Froude number. Figure 5.11 shows the magnitude of dimensionless strain rate, $|\bar{\dot{\gamma}}|$, and velocity vectors fields for two different viscosity ratios: $\eta_r = 0.1$ (left) and $\eta_r = 10$ (right). In the case of the lower viscosity ratio, the strain rate (magnitude) is relatively small along the equator of the drop. Conversely, for the higher viscosity ratio case, the opposite is observed, with $|\bar{\dot{\gamma}}|$ attaining its maximum value along the drop equator. Moreover, the internal circulation within the drop is much greater for the $\eta_r = 0.1$ compared to $\eta_r = 10$. These findings suggest that although the interface of the drop for $\eta_r = 0.1$ does not exhibit

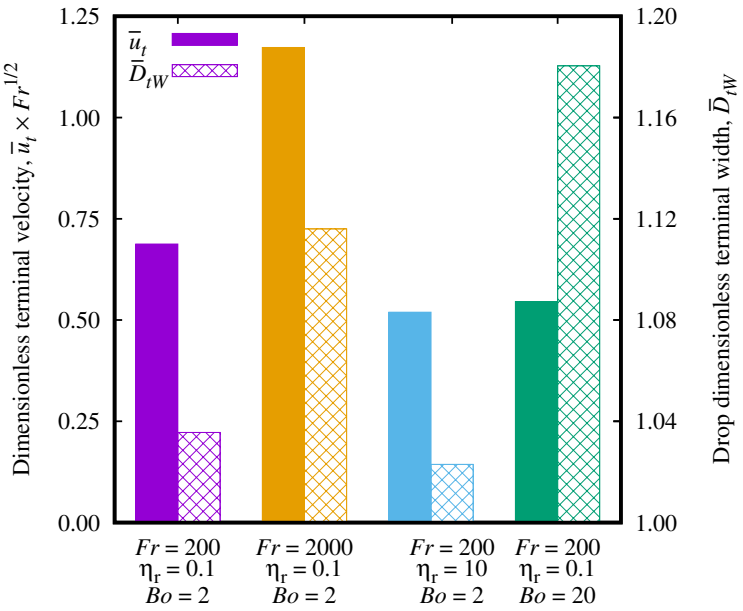

Figure 5.9: Drop dimensionless terminal velocity, $\bar{u}_t$ ($\times Fr^{1/2}$) (solid bars), and (b) drop dimensionless terminal width, $\bar{D}_{tW}$ (hatched bars), in Newtonian surroundings for different sets of Fr, η_r, and Bo.

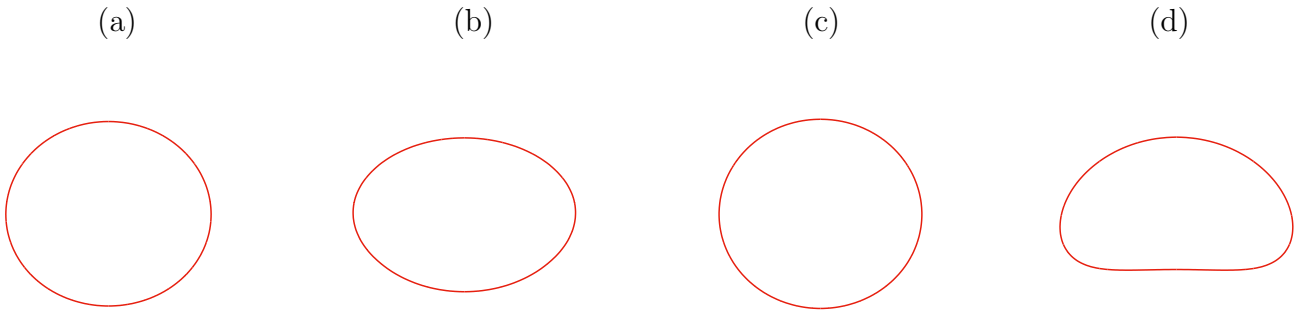

Figure 5.10: Drop shape at steady-state rise in Newtonian materials ($Pl = 0$ and $Wi = 0$) for (a) $Fr = 200$, $\eta_r = 0.1$, and $Bo = 2$, (b) $Fr = 2000$, $\eta_r = 0.1$ and $Bo = 2$, (c) $Fr = 200$, $\eta_r = 10$, and $Bo = 2$, and (d) $Fr = 200$, $\eta_r = 0.1$, and $Bo = 20$.

full mobility (tangentially), it approaches a behavior akin to that of a bubble. In contrast, the drop for $\eta_r = 10$ tends towards resembling a solid sphere, despite its interface not being entirely immobile. An augmented η_r reduces the drop terminal velocity and terminal width, as indicated by the blue bars for $\eta_r = 10$ (compared to the purple bars) in Fig. 5.9. The drop shape for $\eta_r = 10$ (Fig 5.10(c)) exhibits a slightly less oblate shape than that for $\eta_r = 0.1$ (Fig 5.10(a)) and $\bar{D}_{tW} = D_{tW}/D$ slightly deviate from unity.

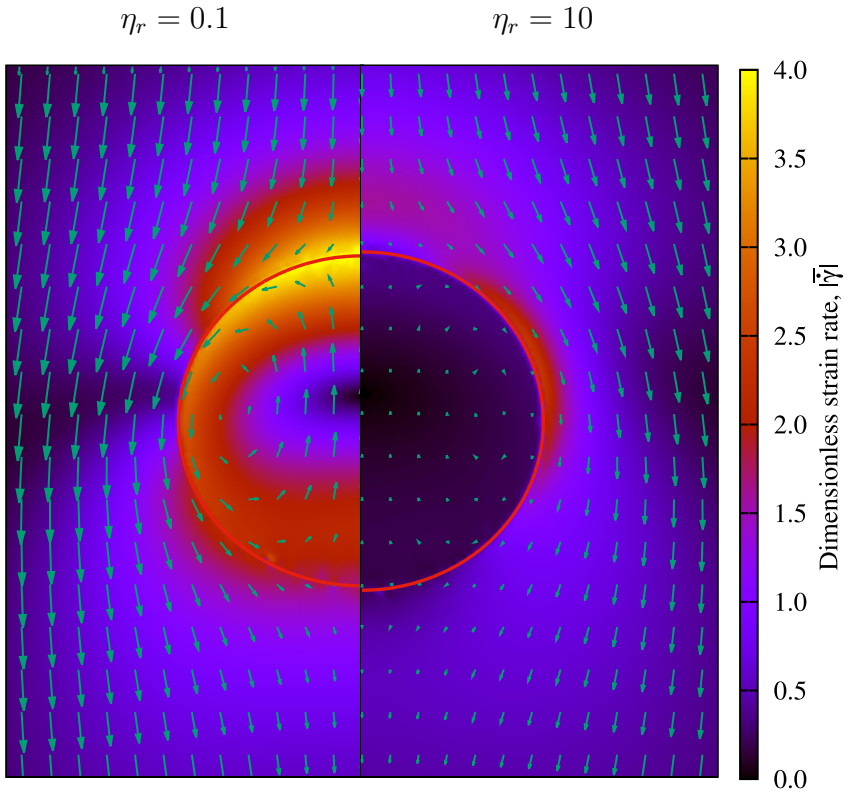

Figure 5.11: Dimensionless strain rate, $|\bar{\dot{\gamma}}|$, and velocity vectors fields for $\eta_r = 0.1$ (left) and $\eta_r = 10$ (right). The other dimensionless parameters are $Fr = 200$, and $Bo = 2$. The u_z component of the velocity vector is subtracted by the drop's center of mass velocity.

Lastly, an increase in Bo tends to enhance the deformation caused by the dominating distorting force, while a reduction in Bo approximates the drop's shape towards that of a sphere. In the case of Newtonian surroundings, where plastic and elastic effects are absent, and inertial effects dominate, drops tend to acquire an oblate shape with an increase in Bo (an increase in $\bar{D}_{tW}$). This can be seen by comparing the purple and green hatched bars in Fig. 5.9 for $Fr = 200$, $\eta_r = 0.1$, and $Bo = 2$ and 20, respectively, as well as by comparing Figs. 5.10(a) and (d). Since the drop's width increases with Bo, the drop's velocity decreases due to its larger cross-sectional area, as depicted by the purple and green solid bars in Fig. 5.9.

5.2.2 Drop rise in inelastic viscoplastic materials

In addition to drop entrapment, plasticity exerts an influence on the rise dynamics of mobile drops. This section is concerned with drop rise in the presence of an inelastic surrounding material exhibiting a yield stress. Specifically, the external phase is modeled by the inelastic Bingham model. In addition to exploring the influence of Pl, the effects of the dimensionless parameters analyzed in the Newtonian analyses are also examined within the

context of plastic surroundings.

Figures 5.12(a) and (b) present drop dimensionless terminal velocity, $\bar{u}_t$ (multiplied by $Fr^{1/2}$), and drop dimensionless terminal width, $\bar{D}_{tW}$, respectively, as a function of Pl. The same combinations of Fr, η_r, and Bo as in Fig. 5.9 for a Newtonian surrounding are employed. The purple line with squares for $Fr = 200$, $\eta_r = 0.1$, and $Bo = 2$ is taken as the base scenario. Considering the influence of the plastic number, Fig. 5.12 reveals that an increase in Pl leads to a reduction in both $\bar{u}_t$ and $\bar{D}_{tW}$. Drops rising in a viscoplastic material are involved by an envelope of yielded material, as demonstrated in Sec. 5.1. The size of the yielded envelope diminishes with an increase in plasticity (Tsamopoulos et al., 2008), restricting the movement of the drop. It is worth noting that $Pl = 0.06$ yields $Y_g = 0.18$, in proximity to the drop entrapment condition discussed in Sec. 5.1, particularly for $\eta_r = 10$. The yield stress exhibits a dual nature, being both plastic and viscous (Thompson and Soares, 2016), and a change in Pl solely affects the contribution of the yield stress to the total viscous stress (*e.g.*, $\tau_v = \tau_y + \mu_p \dot{\gamma}_c$), without altering the total viscous stress itself. Consequently, for a fixed Fr, the reduction in velocity and movement restriction primarily arise from plastic effects rather than an increase in viscous effects. In addition to the reduction in drop velocity associated with Pl, which diminishes the dynamic pressure ahead of the drop and, consequently, its

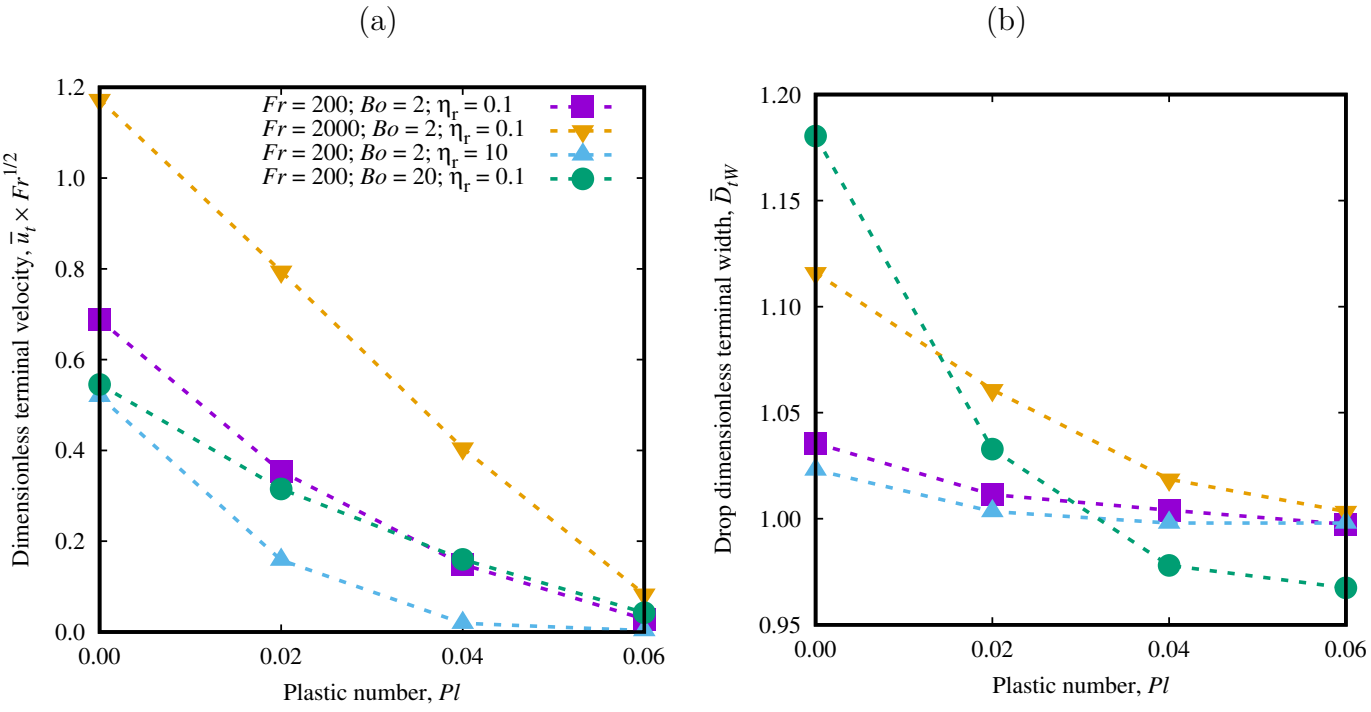

Figure 5.12: (a) Drop dimensionless terminal velocity, $\bar{u}_t$ ($\times Fr^{1/2}$), and (b) drop dimensionless terminal width, $\bar{D}_{tW}$, versus the plastic number, Pl, for different values of Fr, η_r, and Bo.

width, plastic effects counteract the surface tension force, leading to the formation of prolate drops ($\bar{D}_{tW} < 1$). The prolate shape can be attributed to the viscosity field of the surrounding shear-thinning Bingham material. Here, shear-thinning is not related to a power-law index smaller than one (as in the Herschel-Bulkley model), but to the fact that the viscosity of the Bingham model is given by $\eta = \mu_p + \tau_y/|\dot{\gamma}|$, and an increase in $|\dot{\gamma}|$ results in a decrease in η. Figure 5.13 presents the regions of yielded and unyielded material (white and black, respectively) (left) and the viscosity field of the surrounding Bingham material (right) for $Pl = 0.06$, $Fr = 200$, $Bo = 20$, and $\eta_r = 0.1$. The viscosity of the Bingham material is lower at the drop poles compared to the drop equator. This viscosity distribution results in a prolate-shaped drop and facilitates penetration of the drop through the region of lower viscosity. These findings align with the numerical results of Tsamopoulos et al. (2008), who simulated the steady-state rise of bubbles in viscoplastic materials using the Papanastasiou model (*i.e.*, a regularized version of the Bingham model). The authors observed that the strain rate near the equator of the bubble was significantly lower than the strain rate near the poles, leading to elongation of the bubble in the direction of the poles.

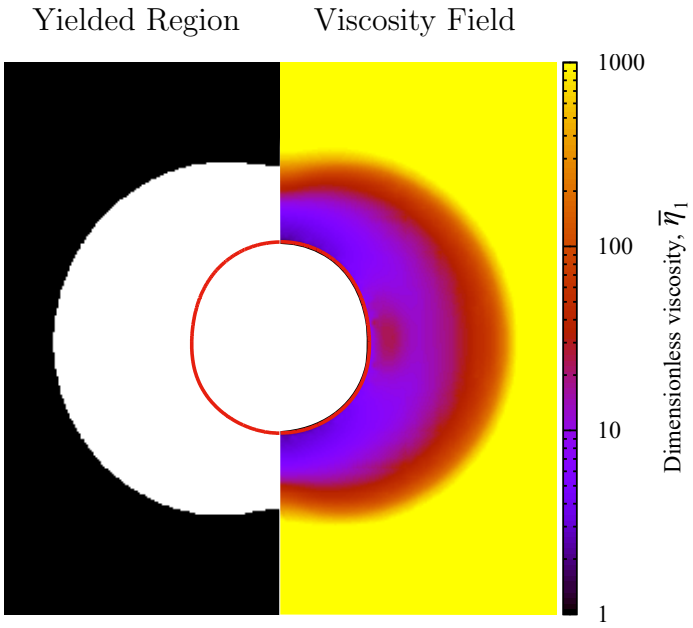

Figure 5.13: Yielded/unyielded (white/black) regions (left) and dimensionless viscosity field, $\bar{\eta}_1$ (right), for a drop at steady-state rise, Pl =0.06, $Fr = 200$, $Bo = 20$, and $\eta_r = 0.1$.

The effects of the Froude number and the viscosity ratio for viscoplastic materials are consistent with those observed in Newtonian materials. Specifically, an increase in Fr and a decrease in η_r diminish viscous effects, leading to an increase in drop velocity and width. However, Bo has the opposite effect as that for Newtonian materials. The drop shape tends to become more prolate with an increase in Pl. This is depicted in Figure 5.14, which shows

the steady-state drop shapes for $Bo = 20$ and different values of Pl. At low plastic numbers ($Pl \leq 0.02$), inertia is the main effect balancing buoyancy, and as shown in Fig. 5.12, drops exhibit an oblate shape and $\bar{D}_{tW}$ increases with an increase in Bo. However, the difference in the drop width for $Bo = 2$ and 20 decreases when changing Pl from 0.00 to 0.02. This can be observed by comparing the purple and green curves in Fig. 5.12(b) for $Pl \leq 0.02$. For high plastic numbers ($Pl \geq 0.04$), plastic effects become dominant, resulting in a more prolate drop shape with increasing Bo (a decrease in $\bar{D}_{tW}$). This behavior is illustrated by the purple and green curves in Figure 5.12(b). Consequently, due to the reduction in width, the drop velocity for the higher Bond number surpasses that of the lower Bond number, as evidenced by the comparison of the purple and green curves in Figure 5.12(a) for $Pl \geq 0.04$.

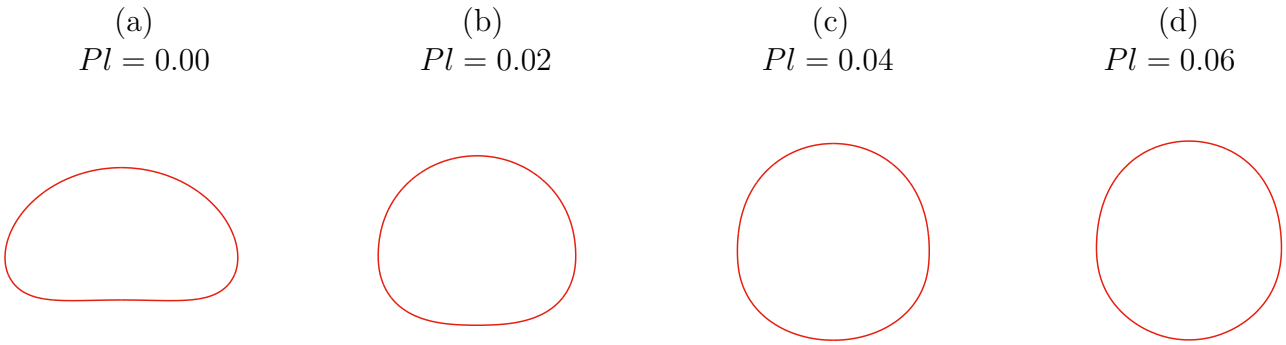

Figure 5.14: Drop shape at steady-state rise for $Fr = 200$, $\eta_r = 0.1$, $Bo = 20$, and (a) $Pl = 0.00$, (b) $Pl = 0.02$, (c) $Pl = 0.04$, and (d) $Pl = 0.06$.

5.2.3 Drop rise in viscoelastic materials

Nonlinear elastic effects have a significant impact on the rise dynamics of drops; for example, the remarkable teardrop shape and negative wake. This section discusses the drop rise phenomenon in viscoelastic surroundings, without plastic effects. The viscoelastic behavior of the external phase is modeled using the Upper Convected Maxwell model (Eq. 2.71). The effects of Wi_c, along with its interplay with Fr, Bo, and η_r, are discussed. Here, the Weissenberg number has the same form as the characteristic Weissenberg number, $Wi = Wi_c$, and the material's relaxation time equals the characteristic relaxation time, $\lambda = \lambda_c$. It is important to mention in advance that the drops under consideration reside within the subcritical regime, and elastic effects are found to be mild. Additionally, the negative wake phenomenon is not observed for any combination of the dimensionless parameters.

Figures 5.15(a) and (b) depict drop dimensionless terminal velocity (multiplied by $Fr^{1/2}$), $\bar{u}_t$, and drop dimensionless terminal width, $\bar{D}_{tW}$, respectively, as a function of Wi_c. The re-

maining dimensionless parameters correspond to those employed in Fig. 5.9. For the reference scenario with $Fr = 200$, $Bo = 2$, and $\eta_r = 0.1$ (purple lines with squares), an increase in Wi_c results in a marginal rise in the terminal velocity of the drop. This observation aligns with the numerical results of Fraggedakis et al. (2016c) and Yuan et al. (2020) for bubbles in the subcritical regime. The observed trend could be attributed to the reduction in drop width caused by elastic effects (Pillapakkam et al., 2007), as seen in Fig. 5.15(b), and the partial activation of the material's viscosity (Yuan et al., 2020).

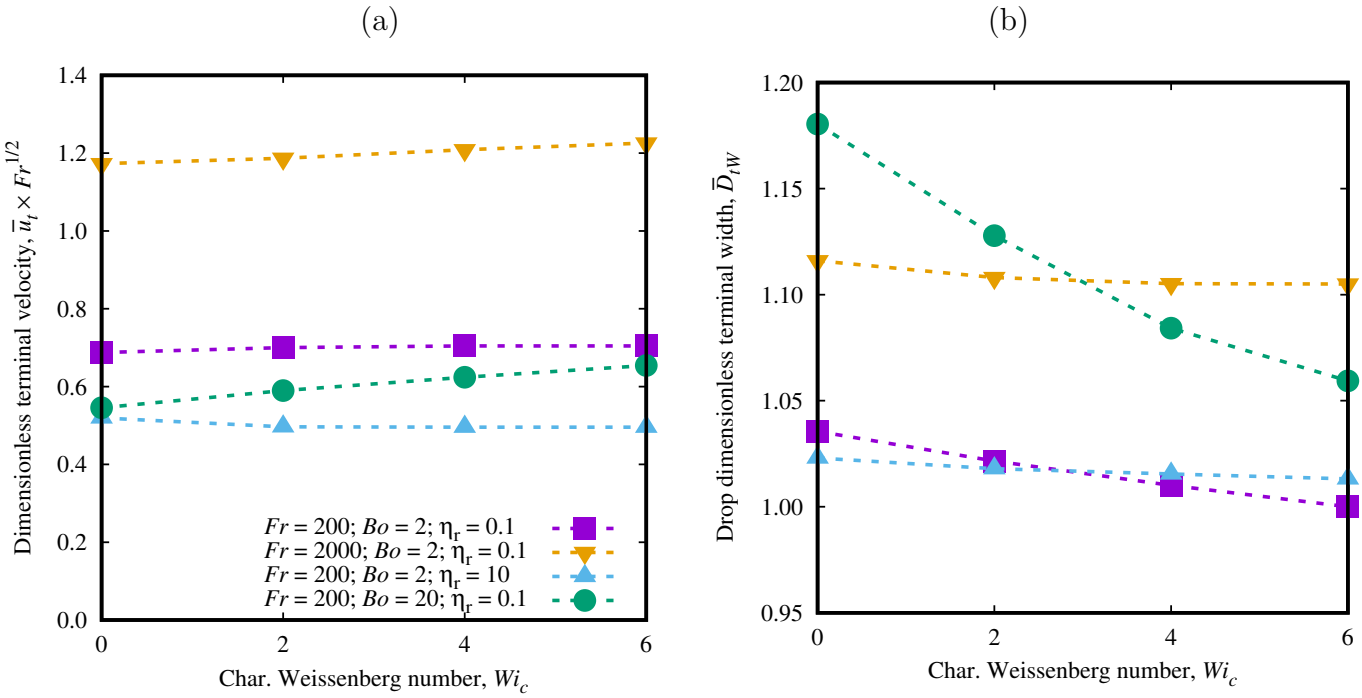

Figure 5.15: (a) Drop dimensionless terminal velocity, $\bar{u}_t$ ($\times Fr^{1/2}$), and (b) drop dimensionless terminal width, $\bar{D}_{tW}$, versus the characteristic Weissenberg number, Wi_c, for different values of Fr, η_r, and Bo.

To begin with, Figs. 5.16 and 5.17 showcase the τ_{rr} and τ_{zz} components (cylindrical coordinate system) of the extra stress tensor, $\boldsymbol{\tau}$, in the surrounding for the base scenario and different values of Wi_c. The value of τ_{rr} around the drop increases with Wi_c, which squeezes the drop, reducing its width. In addition to that, τ_{zz} tends to substantially increase in the lower pole of the drop, exerting a pulling force on the drop surface and contributing to an increase in the drop's aspect ratio (width decrease). Therefore, the molecules of the viscoelastic surrounding experience a biaxial elongational flow around the upper pole of the bubble and a uniaxial elongational flow around the downstream end (Bothe et al., 2022). In the numerical investigations conducted by Pillapakkam et al. (2007) and Fraggedakis et al. (2016c), which investigated the rise of bubbles in a viscoelastic matrix at low Reynolds num-

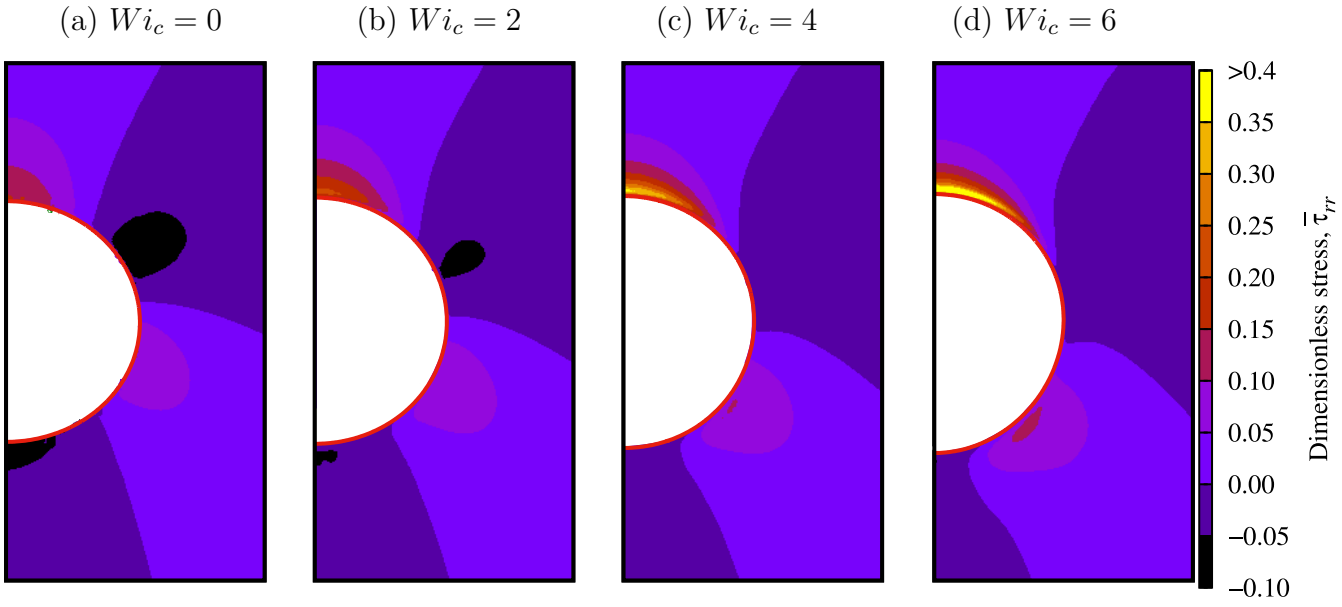

Figure 5.16: The dimensionless extra stress component $\bar{\tau}_{rr}$ for $Wi_c = 0$ (a), 2 (b), 4 (c), and 6 (d) and $Fr = 200$, $Bo = 2$, and $\eta_r = 0.1$.

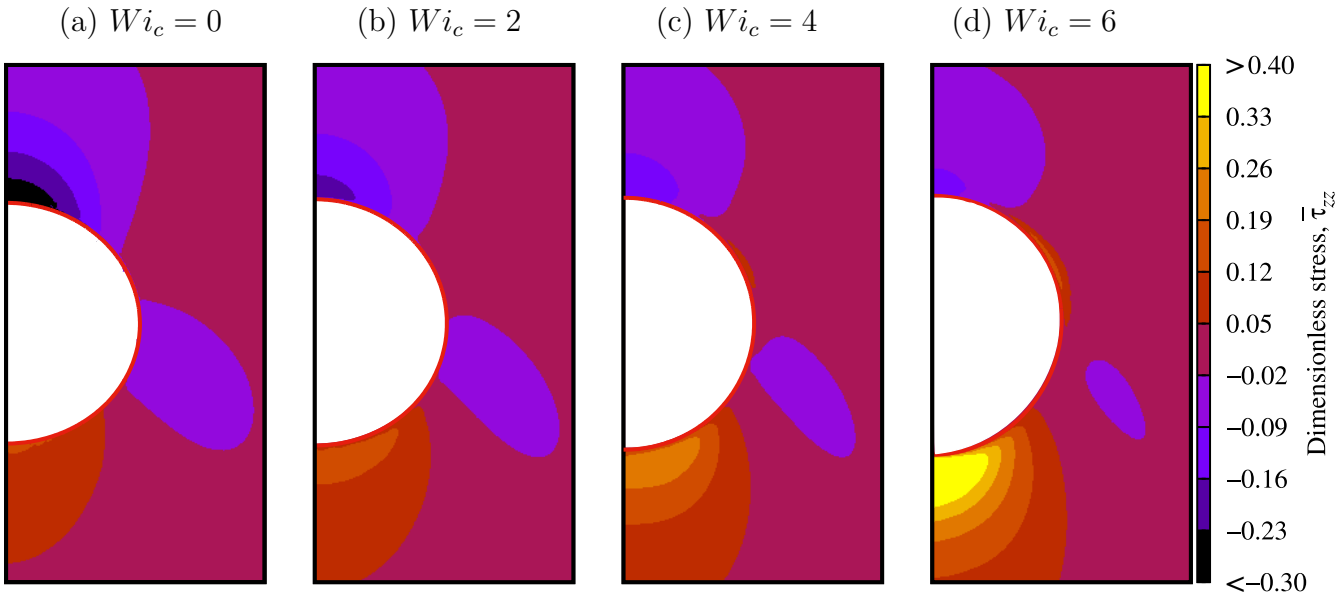

Figure 5.17: The dimensionless extra stress component $\bar{\tau}_{zz}$ for $Wi_c = 0$ (a), 2 (b), 4 (c), and 6 (d) and $Fr = 200$, $Bo = 2$, and $\eta_r = 0.1$.

ber regime, prolate-shaped bubbles were predicted in the subcritical regime. The reduction in drop width was attributed to the emergence of elastic extensional stresses aligned with the outflow direction (in the z-direction) near the trailing edge of the bubble. The drops in Fig. 5.15 are oblate-shaped since inertial effects are not negligible. Nevertheless, a decrease in $\bar{D}_{tW}$ with an increase in elasticity is also observed.

The velocity increase with Wi_c could also be attributed to the partial activation of viscosity of the viscoelastic medium, as suggested by Yuan et al. (2020). In the Upper Convected Maxwell model, an increase in $Wi_c = \lambda_c\dot{\gamma}_c = \eta_c\dot{\gamma}_c/G$ leads to a reduction in the elastic modulus G. Recall that in the dimensional analysis buoyant and viscous stresses balance each other, $|\Delta\rho|gD = \eta_c\dot{\gamma}_c$, and that the buoyant stress is the same for all drops studied. Hence, an increase in Wi_c enhances the significance of elastic effects, indicating that the build-up of elastic stresses takes longer. To exemplify the development of elastic stresses, consider an UCM material submitted to a Couette flow with an imposed constant shear strain rate, $\dot{\gamma}_{shear}$ (developed velocity field at $\bar{t} = 0$). Figure 5.18 shows the magnitude of the dimensionless extra stress tensor, $|\bar{\boldsymbol{\tau}}| = |\boldsymbol{\tau}|/(\eta\dot{\gamma}_{shear})$, with dimensionless time, $\bar{t} = t\dot{\gamma}_{shear}$ for different values of Wi_c. For $Wi_c = 0$ (Newtonian fluid), $|\bar{\boldsymbol{\tau}}| = 1$ while for $Wi_c > 0$, $|\bar{\boldsymbol{\tau}}|$ departs from zero. The development of elastic stresses for higher values of Wi_c is initially slower, but the magnitude of the developed stress at later times is larger. For instance, at $\bar{t} = 0.5$ the measured magnitude of the stress decreases with Wi_c, and the viscosity of the material is partially activated *i.e.*, $\eta > |\boldsymbol{\tau}|/|\dot{\boldsymbol{\gamma}}|$. On the other hand, at $\bar{t} = 5$ the magnitude of $|\bar{\boldsymbol{\tau}}|$ increases with an increase in Wi_c and the viscosity of the material is "overly" activated *i.e.*, $\eta < |\boldsymbol{\tau}|/|\dot{\boldsymbol{\gamma}}|$. For small strains, the elastic response of the material is more substantial,

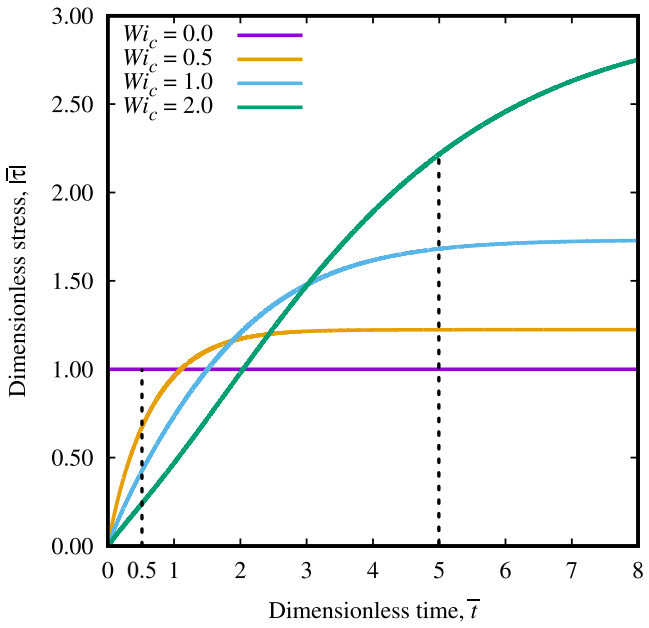

Figure 5.18: Magnitude of the dimensionless extra stress, $|\bar{\boldsymbol{\tau}}|$, as a function of the dimensionless time, $\bar{t}$, in a Couette flow with an imposed shear strain rate, $\dot{\gamma}_{shear}$, for different values of the characteristic Weissenberg number, Wi_c.

and for large strain rates, the viscous response of the material is more substantial. In other words, at early times of the imposed load on a stress-free material, $\dot{\gamma}_e$ is large compared to $\dot{\gamma}_v$. At later times, as elastic stresses develop, the ratio $\dot{\gamma}_e/\dot{\gamma}_v$ decreases.

During its rising, the drop continually encounters new stress-free (relaxed) material, and the attainment of a steady-state rise only means that the drop velocity and shape do not change over time. As G decreases, the initial value of the ratio $\dot{\gamma}_e/\dot{\gamma}_v$ in a relaxed fluid element (when the material starts to be deformed) tends to increase, partially activating the material viscosity (Yuan et al., 2020). One notable outcome of this is an intensified initial acceleration of the drop departing from rest in response to an increase in the Weissenberg number, as evidenced in Fig. 5.19(a). The plot illustrates the temporal evolution of the center of mass velocity of drops for varying Wi_c values and for $Bo = 0.2$. In this high surface tension regime, the drops' shape remains largely unaffected by elastic and inertial effects, thereby maintaining their spherical shape. Thus, the influence of drop width on its rise velocity is mitigated. For the larger values of Wi_c (6 to 18), the rise velocity exhibits an overshoot phenomenon caused by the delayed accumulation of elastic stresses. Due to the larger initial acceleration, the drop reaches a higher velocity, and when elastic stresses grow (which also

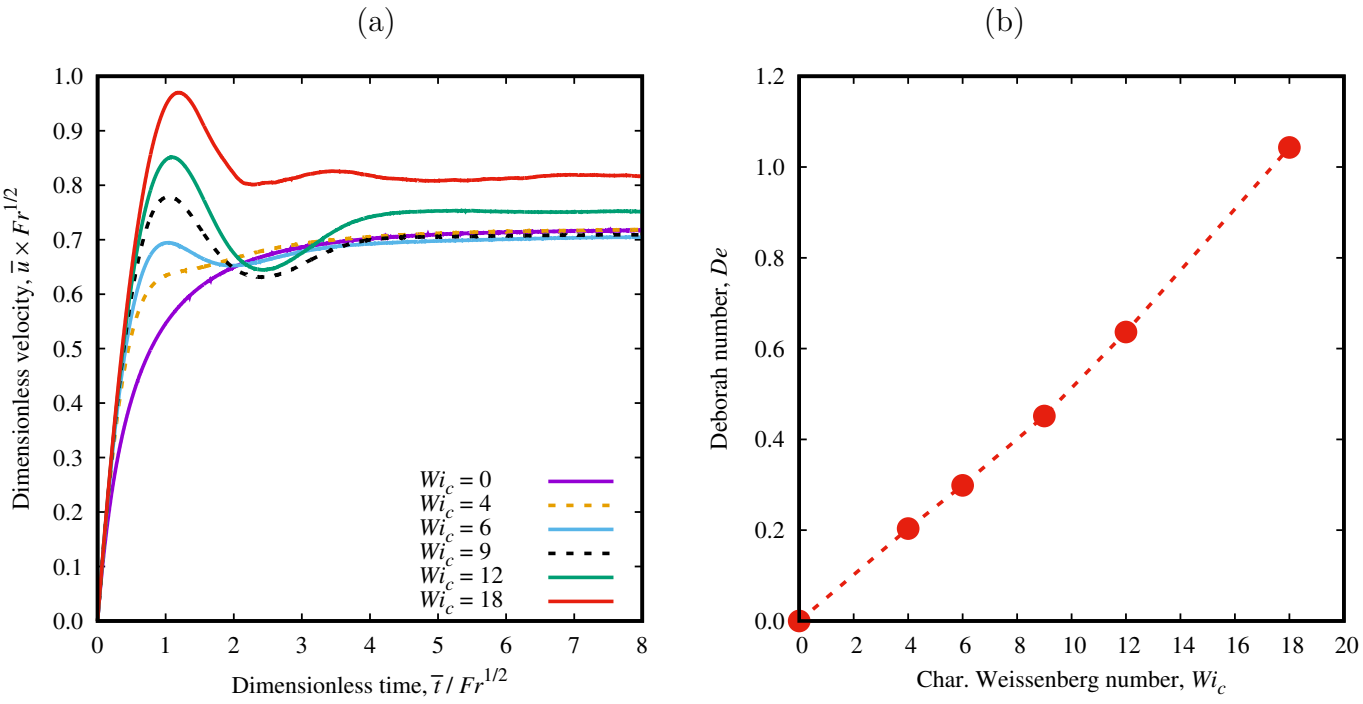

Figure 5.19: (a) Drop dimensionless velocity, $\bar{u}$ ($\times Fr^{1/2}$), versus dimensionless time, $\bar{t}$ ($/Fr^{1/2}$), for different values of Wi_c. (b) The Deborah number, De, as a function of the characteristic Weissenberg number, Wi_c. The other dimensionless parameters are $Fr = 200$, $\eta_r = 0.1$, $Bo = 0.2$. $\bar{t} = 0$ corresponds to the time the drops depart from rest.

depend on the strain rate), they eventually decelerate the drop, creating a local maximum velocity (Pillapakkam et al., 2007; Yuan et al., 2020, 2021). Figure 5.19(a) reveals that the drop's terminal velocity remains nearly unchanged when varying Wi_c from 0 to 4, and slightly decreases for $Wi_c = 6$. Then, it increases slightly for $Wi_c = 9$ (still less than for $Wi_c = 0$) and more substantially for $Wi_c = 12$ and 18. The behavior of the drop velocity may be explained by the partial or over activation of the viscosity. The viscosity activation may be quantified by Deborah number, defined as the ratio of the relaxation time of the material to the drop characteristic rising time, $De = \lambda/t_{ct}$, where t_{ct} is defined upon the drop terminal velocity, $t_{ct} = D/u_t$. Figure 5.19(b) displays the Deborah number for the drops in Fig. 5.19(a). The slope of the line is $De/Wi = \bar{u}$. For small values of De ($\lesssim 9$), elastic stresses have time to grow and stabilize (*e.g*, $\dot{\gamma}_e \to 0$) and the material viscosity may be overly activated. Since $\bar{u}$ is approximately constant with Wi_c, a linear relation between De and Wi is observed. For high values of De, $\dot{\gamma}_e/\dot{\gamma}_v$ tends to be large and the viscosity of the material is partially activated. Figure 5.19 indicates that the transition appears to occur at $De \sim 0.5$. Drop rise in viscoelastic materials is an intricate and dynamic process and the elastic response may depend not only on the relaxation time of the material, but also on drop characteristic rising time, t_{ct} (Bothe et al., 2022), which involves a complex interaction between inertial, viscous, and surface tension effects. Therefore, within the investigated parameter range for the rise and coalescence phenomena ($Wi_c = 0$ to 6), the observed increase in drop velocity in Fig. 5.15(a) is primarily attributed to the reduction in the drop width.

The influence of the Froude number is similar to that observed for Newtonian and inelastic viscoplastic surroundings. An increase in Fr (yellow line with inverted triangles in Fig. 5.15) increases both the drop terminal velocity and width. This behavior arises from the heightened importance of inertial effects relative to viscous and elastic effects.

Similar to previous observations, an increase in Bo facilitates the drop deformation by the dominating distorting force. Consequently, as illustrated in Fig. 5.15(b), the drop width reduction with increasing Wi_c is more pronounced for $Bo = 20$ (green line with circles) than for $Bo = 2$. As a result, the drop velocity increase with Wi_c is also more substantial (see Fig. 5.15(a)). The distinctive teardrop shape, characterized by a cusp-shaped tail is not observed for any drop in Fig. 5.15. Extra simulations reveal that this shape is observed for $Wi_c = 7$ and $Bo = 20$, while for $Wi_c = 7$ and $Bo = 2$ it is not. Figure 5.20 showcases the drop shape at steady-state rise for $Fr = 200$, $\eta_r = 0.1$, $Bo = 20$, and $Wi_c = 0$, 2, 4, 6, and 7. The transition to the teardrop shape exhibits a relatively sharp delineation and occurs between $Wi_c = 6$ and 7. The tail of the drop in Fig. 5.20(e) forms a tread, where the pinch off of small satellite drops eventually occurs. This has also been experimentally observed by Ortiz et al. (2016) and numerically reproduced by Yuan et al. (2020) and Yuan et al.

(2021). This phenomenon occurs when the surface tension force is insufficient to counteract the pulling exerted on the drop surface by elastic stresses.

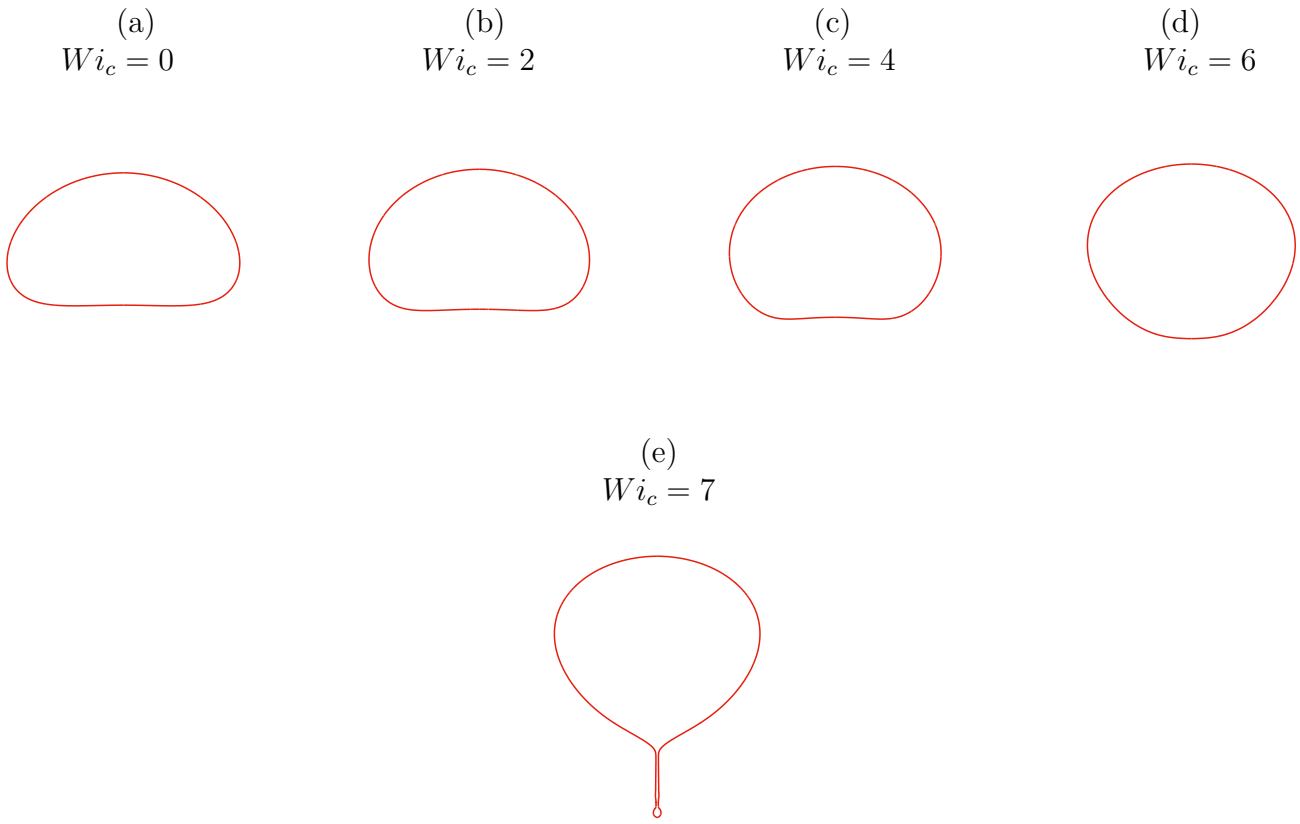

Figure 5.20: Drop shape at steady-state rise for $Fr = 200$, $\eta_r = 0.1$, $Bo = 20$, and $Wi_c = 0.0$ (a), 2 (b), 4 (c), 6 (d), and 7 (e).

In the case of the higher viscosity ratio scenario (blue line with triangles in Fig. 5.15), the drop velocity and width exhibit minimal variations with changes in Wi_c. This can be attributed to the boundary condition on the drop surface, which tends to resemble that of a solid sphere, resulting in a distinct stress field compared to the lower viscosity ratio case. Figure 5.21 presents the components τ_{rr} and τ_{zz} of the extra stress tensor for $\eta_r = 10$ and $Wi_c = 0$ and 6. Though τ_{rr} increases with increasing Wi_c on the upper hemisphere, it remains negative on the lower hemisphere. Additionally, τ_{zz} reaches its maximum value in the drop equator region, where shear is more pronounced, while its value at the drop trailing edge is relatively small. A similar stress field has been observed by Goyal and Derksen (2012) and Faroughi et al. (2020) for solid spheres in viscoelastic materials. Consequently, in the higher viscosity ratio case, the observed effect of Wi_c on drop width reduction and corresponding velocity increase is significantly less pronounced compared to the lower viscosity ratio case.

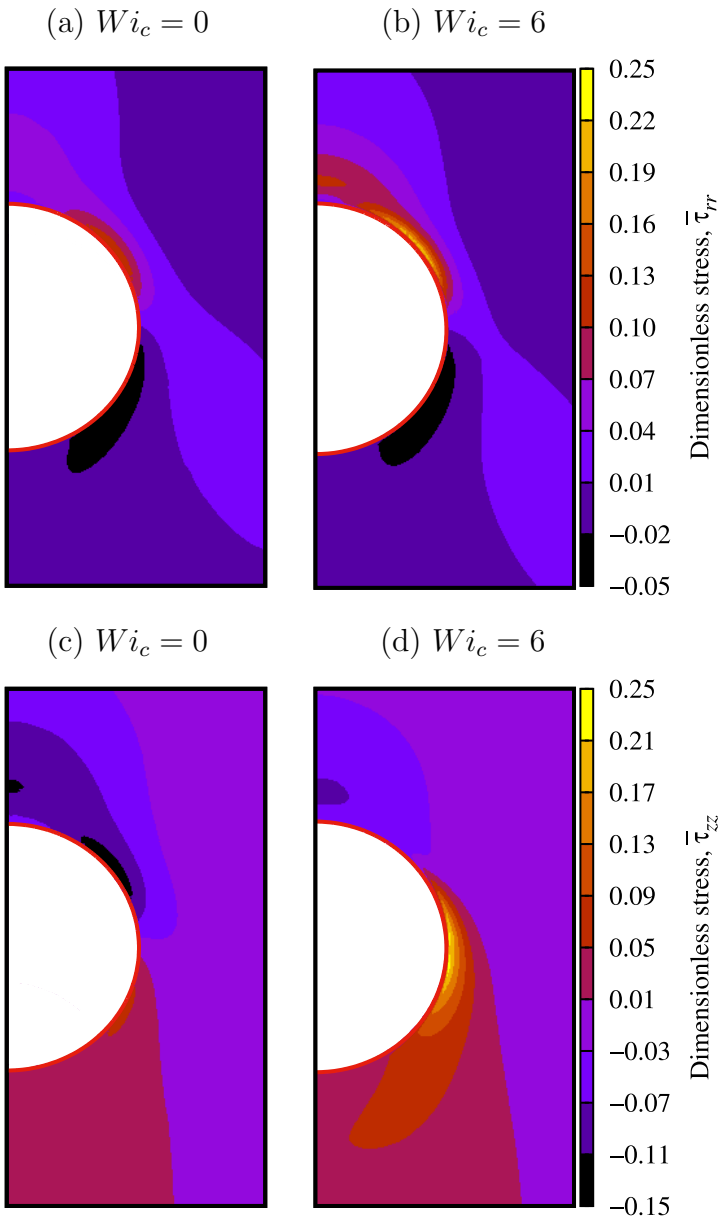

Figure 5.21: The dimensionless extra stress components (a,b) $\bar{\tau}_{rr}$ and (c,d) $\bar{\tau}_{zz}$ for $Wi_c = 0$ (a,c) and 6 (b,d), $Fr = 200$, $Bo = 2$, and $\eta_r = 10$.

5.2.4 Drop rise in elasto-viscoplastic materials

Real yield stress materials generally also exhibit elastic behavior. Elasticity and plasticity mutually influence the extent of each others' effect; for instance, the size and shape of the yield surface and the shape and rise velocity of the drop (Moschopoulos et al., 2021; Lopez et al., 2018; Frey et al., 2015). In this section, the dynamics of drop rise in elasto-viscoplastic materials are explored. The elasto-viscoplastic nature of the surrounding is modeled by the Saramito model. Due to the computationally intensive nature of the analysis, the focus of

the investigation is on presenting results obtained for the lower viscosity ratio cases, $\eta_r = 0.1$. The discussion commences with the examination of the interaction between Pl and Wi_c (and also $Wi(Wi_c, Pl)$), and concludes with the effects of Fr and Bo in EVP surroundings.

Figures 5.22(a) and (b) exhibit the drop dimensionless terminal velocity (multiplied by $Fr^{1/2}$) as a function of Wi_c (with a fixed $Pl = 0.04$) and Pl (with a fixed $Wi_c = 4$), respectively, for various values of Fr and Bo. From the results shown in Fig. 5.22(a), it can be observed that in a plastic medium, elastic effects lead to an increase in the rise velocity of the drop. The increase in velocity with respect to Wi_c is significantly greater compared to a surrounding medium without a yield stress. On the other hand, Fig. 5.22(b) demonstrates that in an elastic medium, an increase in the level of plasticity causes a reduction in the terminal velocity of the drop. However, the velocity reduction with increasing Pl is less prominent than that observed for an inelastic surrounding.

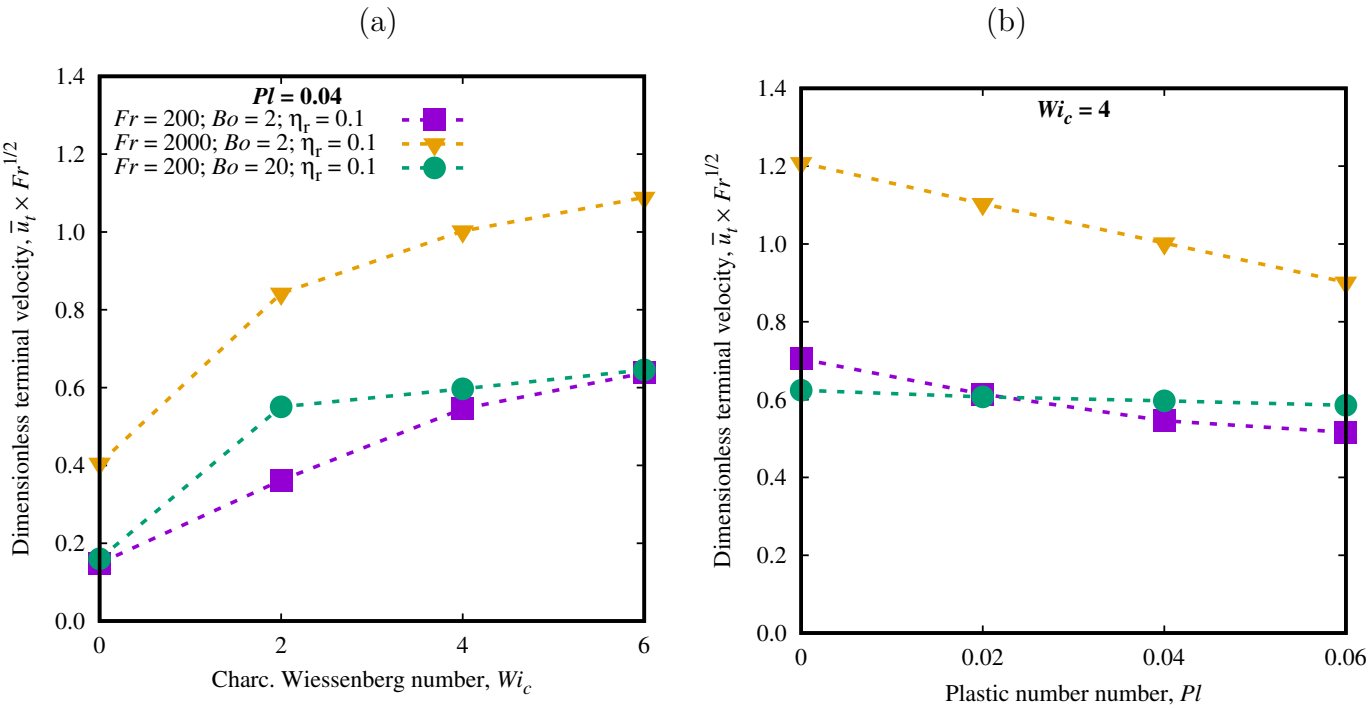

Figure 5.22: Drop dimensionless terminal velocity, $\bar{u}_t$ ($\times Fr^{1/2}$), as a function of (a) Wi_c for $Pl = 0.04$, and as a function of (b) Pl for $Wi_c = 4$, and different values of Fr and Bo. The viscosity ratio is $\eta_r = 0.1$ in all cases.

To gain deeper insights into the intricate relationship between elastic and plastic effects, it is instructive to revisit Eq. 3.7, which represents the dimensionless form of the extra stress equation. The elasticity of the material is indicated by the Weissenberg number, expressed

as

$$Wi = Wi_c \left[1 + Pl \left(\frac{1 - |\bar{\dot{\boldsymbol{\gamma}}}|}{|\bar{\dot{\boldsymbol{\gamma}}}|} \right) \right]. \tag{5.1}$$

Notably, Wi incorporates a contribution from the plastic number and the magnitude of the dimensionless strain rate tensor (a kinematic quantity). To elucidate this interaction, it is didactic to examine the mechanical analog of the model presented in Figure 3.2, which is reproduced here for the convenience of the reader.

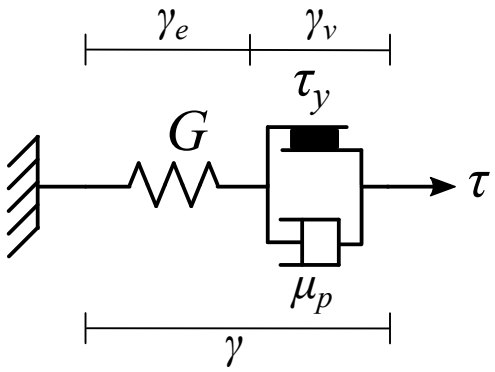

Figure 3.2: Mechanical analog of EVP model employed.

An increase in Pl results in a decrease in drop velocity, u_t (*e.g.*, $u_t \sim |\bar{\dot{\boldsymbol{\gamma}}}|$), which in turn leads to a general increase in the viscosity field, $\eta(|\dot{\boldsymbol{\gamma}}|)$. This amplifies the contribution of the spring element, experiencing the deformation rate $\dot{\gamma}_e$, to the total strain rate, $\dot{\gamma} = \dot{\gamma}_e + \dot{\gamma}_v$, in comparison to the contribution of the viscoplastic element, submitted to the deformation rate $\dot{\gamma}_v$. Therefore, considering that $|\bar{\dot{\boldsymbol{\gamma}}}| < 1$, an increase in Pl results in an increase in Wi *i.e.*, an enhancement of the material's elastic response. This influence of the plastic number is also reflected in the relaxation time of each fluid element $\lambda = \eta(|\dot{\boldsymbol{\gamma}}|)/G$, which, for a constant Wi_c (and, equivalently, G), tends to increase with an increase in Pl. Therefore, the increase in drop velocity observed in Fig. 5.22(a) is a result of the partial viscosity activation, which is enhanced by the plasticity of the material.

For the influence of Wi_c on the plastic response of the material, it can be observed that an increase in Wi_c signifies a decrease in G. This also enhances the elastic contribution, γ_e, to the total strain, $\gamma = \gamma_e + \gamma_v$, relative to the viscous contribution, γ_v. For instance, as Wi_c approaches infinity, $\dot{\gamma}_v$ tends to zero. Therefore, an increase in Wi_c diminishes the significance of the deformation of the viscoplastic element $\eta(|\dot{\boldsymbol{\gamma}}|)$. This diminishes the material's plastic response (rigidity) since it allows deformation in the unyielded state, elucidating the observed lesser drop velocity reduction with Pl in Fig. 5.22(b) when contrasted with the inelastic scenario.

The preceding discussion elucidates the observed behavior depicted in Fig. 5.22, which can be summarized as follows: i) plasticity amplifies elastic effects, as evidenced by the increase in drop velocity with respect to Wi_c in Fig. 5.22(a), and ii) elasticity diminishes plastic effects, as demonstrated by the comparatively less prominent reduction in velocity with increasing Pl in Fig. 5.22(b).

Figures 5.23(a) and (b) present the drop dimensionless terminal width for the same parameter settings as in Figs. 5.22(a) and (b), respectively. Figure 5.23(a) reveals an initial decrease in $\bar{D}_{tW}$ as Wi_c increases; however, with further increments in Wi_c, the drop width subsequently increases. The reduction in the initial width of the drop can be attributed to the plastic and elastic squeezing effects discussed in the Secs. 5.2.2 and 5.2.3, respectively. However, due to the substantial increase in the drop terminal velocity with higher values Wi_c, inertial effects also become important, resulting in a more oblate-shaped drop. Regarding the influence of Pl while maintaining Wi_c constant, Fig. 5.23(b) illustrates that the drop width decreases as Pl increases. This reduction is attributed to the plastic effects discussed in Sec. 5.2.2.

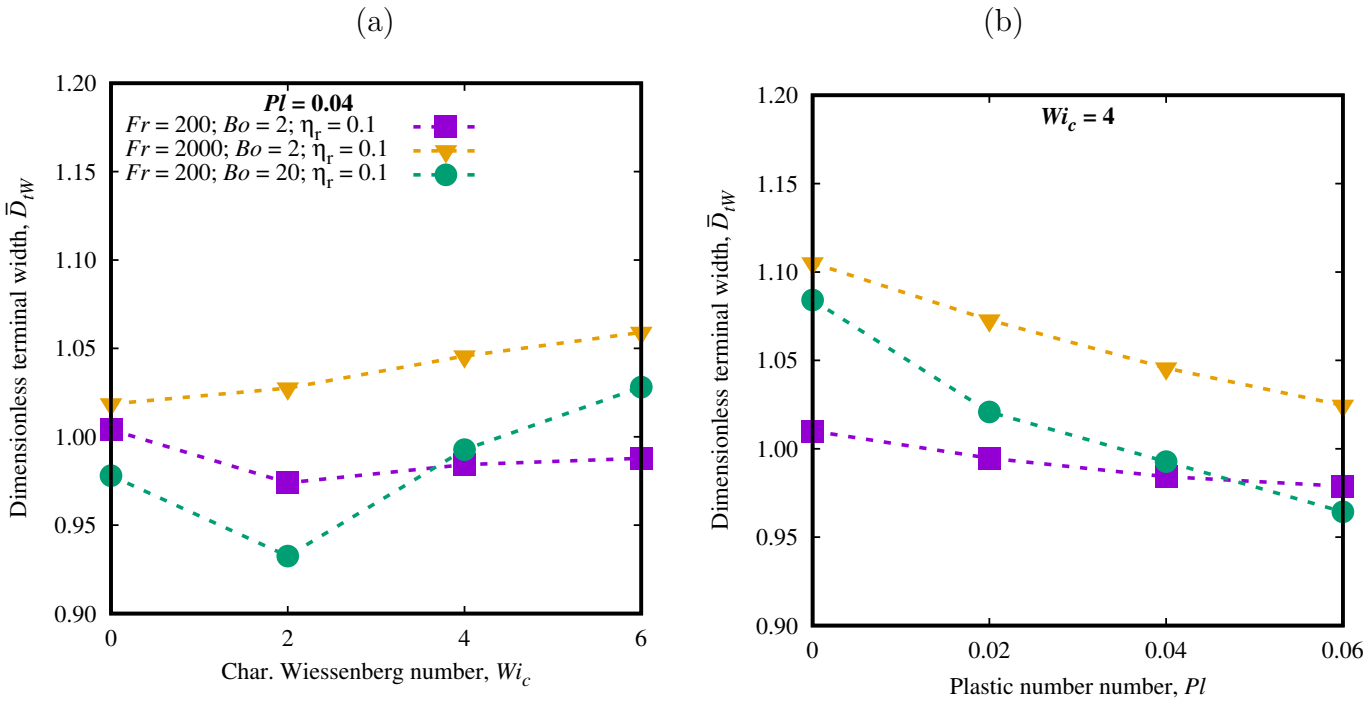

Figure 5.23: Drop dimensionless terminal width, $\bar{D}_{tW}$, as a function of (a) Wi_c for $Pl = 0.04$, and as a function of (b) Pl for $Wi_c = 4$, and different values of Fr and Bo. η_r is kept equal to 0.1 in all cases.

Figures 5.24 to 5.27 further explore the interaction between Wi_c and Pl in relation to the yield surface, velocity field, and drop shape. The discussion concerning the influence of

Fr and Bo is presented towards the end of this section. Figure 5.24 showcases the yield surface for $Wi_c = 0$, 2, 4, and 6. The remaining dimensionless parameters are $Pl = 0.04$, $Fr = 200$, $Bo = 2$, and $\eta_r = 0.1$. The presence of elasticity in the surrounding medium significantly impacts the shape and size of the yield surface. In Fig. 5.24(a), for $Wi_c = 0$, the inelastic Bingham model (Eq. 2.58) is employed, while the Saramito model (Eq. 3.2) is employed for the results in Figs. 5.24(b) to (d). The inclusion of elasticity leads to an expansion of the yielded region, which can be attributed to the contribution of elastic stresses to the von Mises criterion, facilitating yielding (Moschopoulos et al., 2021). The shape of the yield surfaces is different from that observed with the inelastic formulation, resembling the shapes observed by Moschopoulos et al. (2021) for EVP materials. Increasing Wi_c from 0 to 2 causes an enlargement of the yielded region upstream of the drop. As Wi_c increases further, the yielded region downstream of the drop expands, while the yield surface upstream

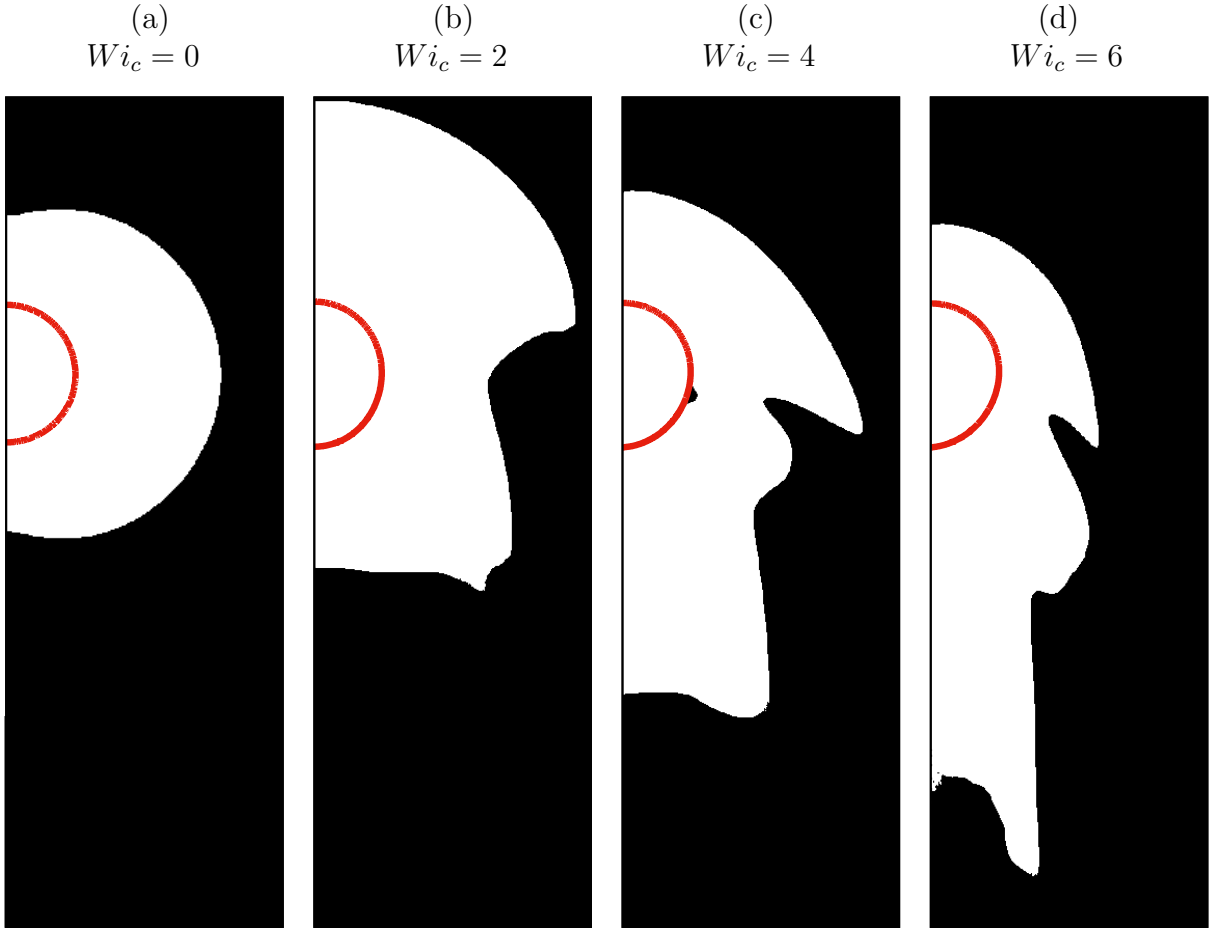

Figure 5.24: Yield (white) and unyielded (black) regions around drops at steady-state rise for $Pl = 0.04$, and $Wi_c = 0$ (a), 2 (b), 4 (c), and 6 (d). The interface is represented by the red line. The other dimensionless parameters are $Fr = 200$, $\eta_r = 0.1$, $Bo = 2$.

approaches the drop surface. This observation also aligns with the findings of Moschopoulos et al. (2021). According to the authors, the drop in the lesser elastic material has to yield the upstream material further away in order to achieve even a small velocity. However, here it is argued that the increase in Wi_c leads to an increase in the material's relaxation time, subsequently slowing down the development of elastic stresses. Simultaneously, the drop rises faster. As a result, upstream stresses exceed the yield stress at increasingly close distances from the drop surface. As the drop ascends, the surrounding material undergoes a process of yielding and subsequent relaxation. This relaxation process requires time for the material to return to the unyielded state. As the stress decays, the thinning Bingham viscosity of the viscoplastic element increases, *i.e.*, as $|\boldsymbol{\tau}| \to \tau_y$, $\eta_p \to \infty$ (or $\eta_p \to N\eta_c$ in the regularized version). Consequently, the relaxation time of the fluid element increases, forming a region of slow relaxation where the stress is slightly above the yield stress. This can be observed in Fig. 5.24, for $Wi_c = 6$, where a longer tail of yield materials is formed downstream of the drop.

Figure 5.25 shows the velocity vector field for $Wi_c = 4$ and $Pl = 0.00$, 0.02, 0.04, and 0.06. The vectors are colored based on the magnitude of the dimensionless velocity. In the absence of plasticity ($Pl = 0.00$), no negative wake is observed. However, a negative wake becomes apparent with the introduction of plasticity. The magnitude of the velocity in the negative wake is relatively small, indicated by the black color of the arrows. As the value of Pl increases, the negative wake approaches the drop, clearly demonstrating the amplification of elastic effects with an augmentation in the material's plasticity, despite keeping Wi_c constant.

Figures 5.26 and 5.27 showcase the drop shape for the higher Bond number condition ($Bo = 20$) with fixed parameters of $Fr = 200$ and $\eta_r = 0.1$. These figures explore the influence of characteristic Weissenberg and plastic numbers on the drop shape. Figure 5.26 illustrates that for a plastic surrounding, the drop acquires a cusp-shaped tail for lower values of Wi_c. The teardrop shape is observed at $Wi_c = 2$, whereas, in the absence of plasticity as discussed in Sec. 5.2.3, it is only observed at $Wi_c = 7$. Similarly, Fig. 5.27 also reveals that a cusp is already formed at the trailing edge of the drop for $Pl = 0.02$, indicating that the drop shape evolved from an oblate shape to a teardrop shape by changing Pl, while holding Wi_c constant.

The discussion now returns to Figs. 5.22 and 5.23, with a focus on the influence of Fr and Bo in the context of elasto-viscoplastic surroundings. To aid in the analysis, Fig. 5.28 showcases the shape of the drop for $Wi_c = 6$, $Pl = 0.04$ and and three different scenarios: (a) $Fr = 200$ and $Bo = 2$, (b) $Fr = 2000$ and $Bo = 2$, and (c) $Fr = 200$ and $Bo = 20$. In the baseline scenario depicted in Fig. 5.28(a), the drop exhibits a prolate shape with the cusp of its tail on the verge of formation. As the Froude number increases (Figure 5.28(b)), the

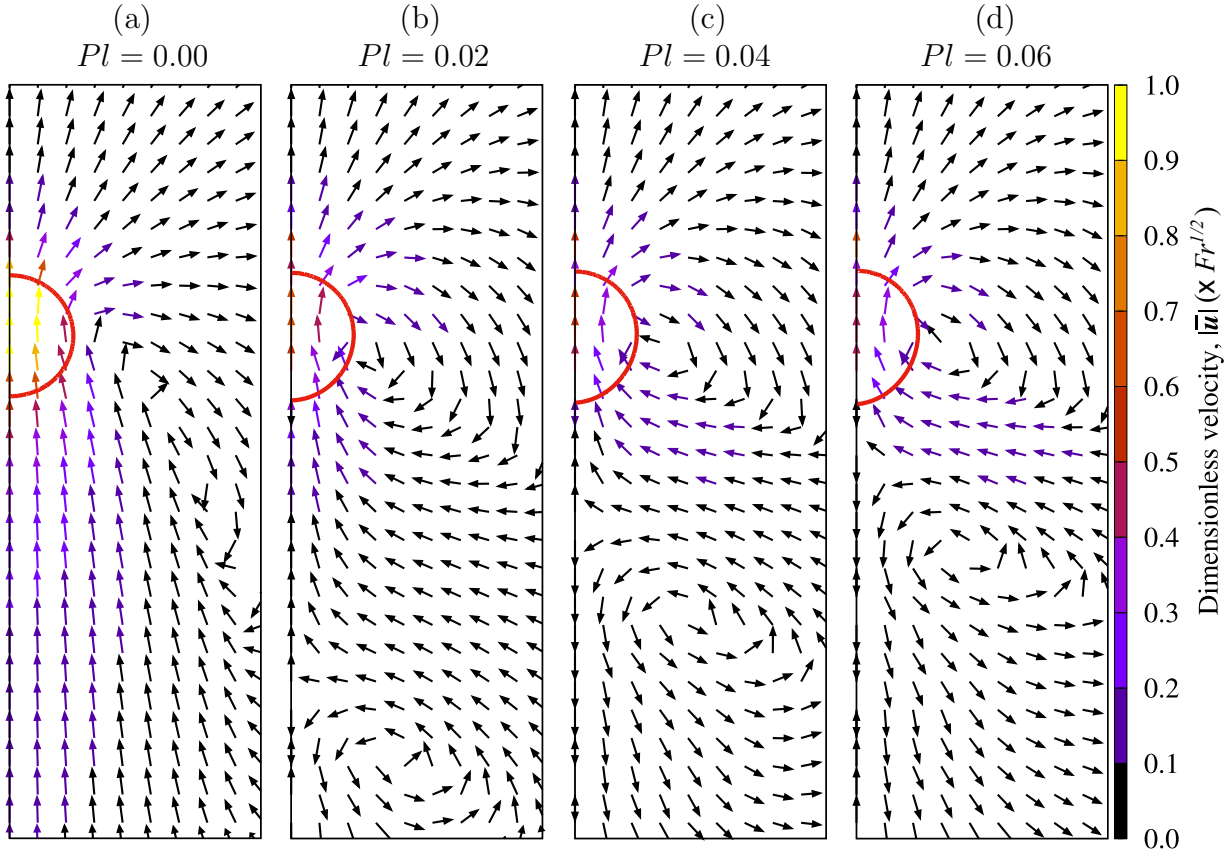

Figure 5.25: Velocity vector field for $Wi_c = 3$ and $Pl = 0.00$ (a), 0.02 (b), 0.04 (c), and 0.06 (d). The arrows are colored according to the magnitude of $|\bar{u}|(\times Fr^{1/2})$ and the interface is represented by the red line. The other dimensionless parameters are $Fr = 200$, $\eta_r = 0.1$, and $Bo = 2$.

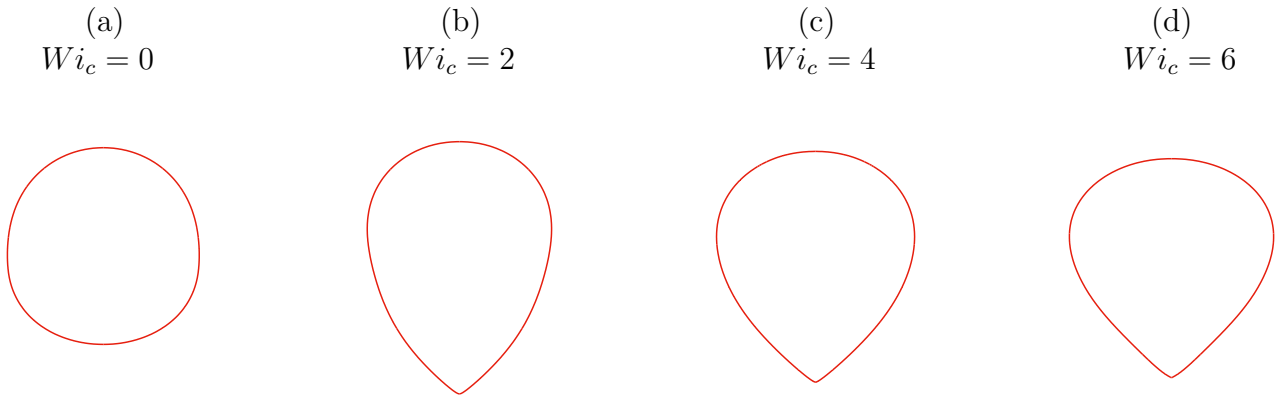

Figure 5.26: Drop shape at steady-state rise for $Fr = 200$, $\eta_r = 0.1$, $Bo = 20$, $Pl = 0.04$, and $Wi_c = 0.0$ (a), 2 (b), 4 (c), and 6 (d).

drop transitions to an oblate shape due to the amplified effect of inertial forces, necessitating a higher Weissenberg number for the formation of a cusp-shaped tail. The increase in drop

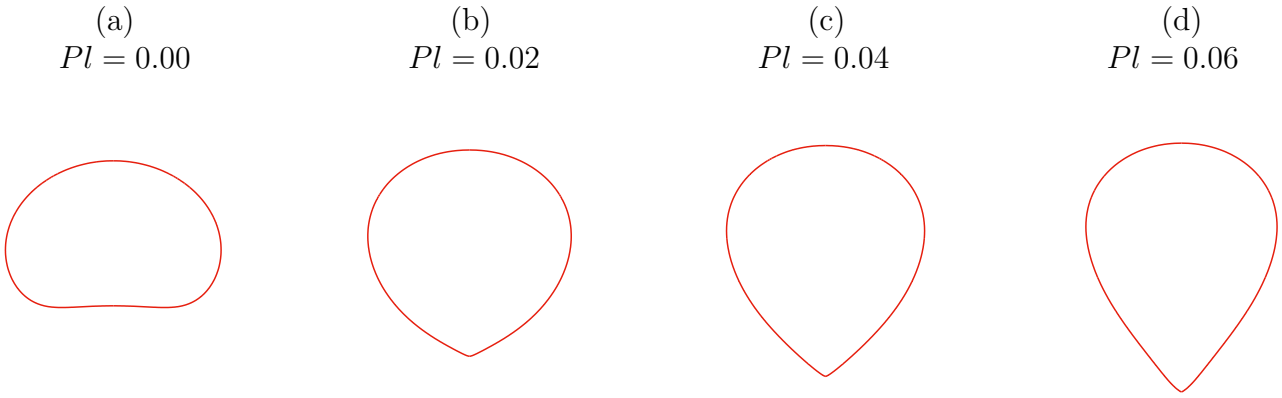

Figure 5.27: Drop shape at steady-state rise for $Fr = 200$, $\eta_r = 0.1$, $Bo = 20$, $Wi_c = 4$, and $Pl = 0.00$ (a), 0.02 (b), 0.04 (c), and 0.06 (d).

velocity and width is also evident from Figs. 5.22 and 5.23, respectively. The increased inertial effects for $Fr = 2000$ causes the drop diameter to monotonically increase with Wi_c in Fig. 5.23(a). In contrast, for $Fr = 200$ elastic effects are more substantial compared to inertial effects, and the drop width reduces when Wi_c increases from 0 to 2. The delayed formation of a cusp-shaped tail with increasing inertial effects has also been observed in the experimental work conducted by Lopez et al. (2018) and in the numerical investigation of Moschopoulos et al. (2021), where the ratio Re/De[1] was used to distinguish between flows dominated by inertia or elasticity. It is observed that the ratio $El = Fr/Wi$, denominated as elastic number, naturally emerges from the dimensionless form of the momentum equation (Eq. 3.6). El relates the significance of inertia to elasticity and is used in a similar context as Re/De in the authors' work. For high values of El, inertia dominates over elasticity, and vice versa. Consequently, an increase in Fr leads to an augment in El.

In contrast to the effect of increasing Fr, an increase in Bo facilitates the formation of a cusp-shaped tail, as demonstrated in Fig. 5.28(c). This behavior arises due to the limited capacity of surface tension forces to resist the deformation induced by elastic effects. As illustrated in Fig. 5.23, an increase in Bo causes a larger drop deformation with changes in Wi_c and Pl. Notably, the drop velocity remains relatively constant with changes in Pl for the scenario involving a higher Bond number, as observed in Fig.5.22(b). Such behavior can be ascribed to two key factors: the pronounced reduction in drop width and the influence of elastic effects (partial viscosity activation), which collectively facilitate the rise of drops through yield stress materials.

[1]The Reynolds and Deborah numbers in the works of Lopez et al. (2018) and Moschopoulos et al. (2021) have similar definitions to the Froude and Weissenberg numbers in the present work, respectively, but using the drop terminal velocity, u_t, and radius, R, as the characteristic velocity and length, respectively.

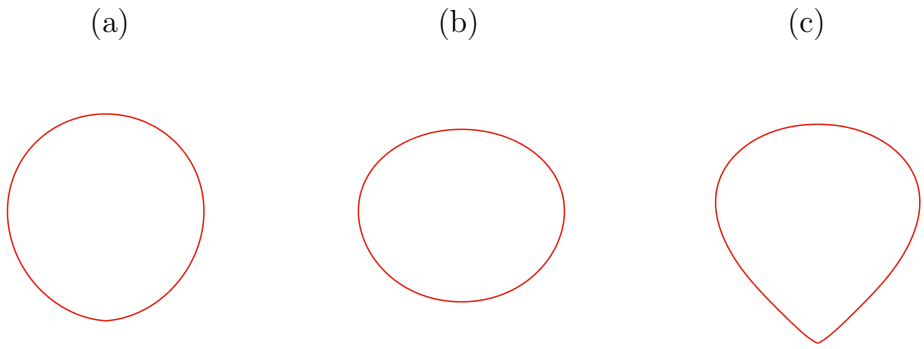

Figure 5.28: Drop shape at steady-state rise for $Wi_c = 6$, $Pl = 0.04$, $\eta_r = 0.1$, and (a) $Fr = 200$ and $Bo = 2$, (b) $Fr = 2000$ and $Bo = 2$, and (c) $Fr = 200$ and $Bo = 20$.

5.2.4.1 Entrapment condition in elasto-viscoplastic materials

Elasto-viscoplastic materials undergo deformation below the yield stress due to the spring deformation γ_e. No deformation is expected in the viscoplastic element submitted to the strain γ_v (in fact, only a small deformation due to the regularization approach). Therefore, predicting drop entrapment in elasto-viscoplastic materials is more challenging than for inelastic viscoplastic materials. The objective of this section is to demonstrate that the elasticity of the surrounding material influences the conditions for drop entrapment. This aspect may provide insight into the discrepancies observed between numerical and experimental studies.

Figure 5.29 displays the dimensionless velocity, $\bar{u}$ ($\times Fr^{1/2}$), as a function of dimensionless time, $\bar{t}$ ($/Fr^{1/2}$), for drops rising in elasto-viscoplastic media. The lowest value of the plastic number considered is $Pl = 0.08$, corresponding to $Y_g = 0.24$, which exceeds the threshold for drop rise in inelastic viscoplastic media ($Y_{gc} = 0.20 \pm 0.02$). The solvent to the total viscosity ratio was set to $\beta = 0.01$, since for high levels of plasticity, close to the entrapment condition, it has shown to improve the visualization of the yield surface. In all cases, the velocity of the drops initially increases, reaching a significant value, and subsequently decreases. For comparison, the dimensionless velocity of drops, $\bar{u}$ ($\times Fr^{1/2}$), with the regularized Bingham model for $Pl = 0.08$ is on the order of 10^{-4}, and no peak velocity is observed (not shown). Differently from the inelastic viscoplastic case, where the appearance (or not) of the yield envelope can be quickly verified, the entrapment condition for elasto-viscoplastic materials requires longer simulations and can not be based on the formation of a complete envelope of yielded material. Interestingly, the drop attains negative velocity during the deceleration phase for some combinations of Wi_c and Pl. This is caused by the development of elastic stresses which are enhanced by the larger values of the plastic number. Moreover, the initial

drop velocity suggests that, unlike inelastic viscoplastic surroundings, the critical plastic number Pl_c may depend on the Bond number for initially spherical drops, as the drop has the potential (opportunity) to deform and adopt a prolate shape.

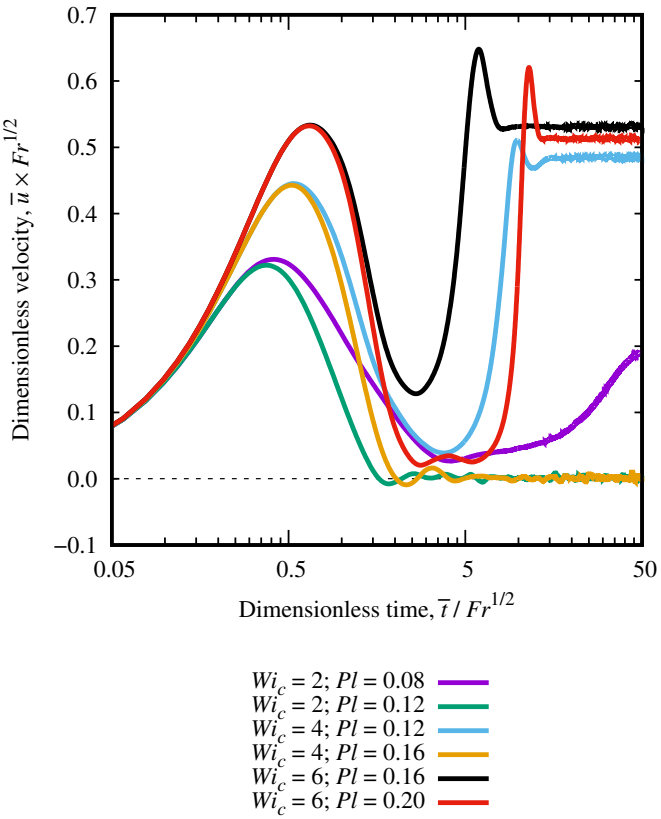

Figure 5.29: Drop dimensionless rise velocity, $\bar{u}(\times Fr^{1/2})$, with dimensionless time, $\bar{t}(/Fr^{1/2})$, in elasto-viscoplastic materials for different values of Pl and Wi_c. The other dimensionless parameters are $Fr = 200$, $Bo = 2$, $\eta_r = 0.1$, $\rho_r = 0.1$, and $\beta = 0.01$

For $Wi_c = 2$ and $Pl = 0.08$, the drop velocity increases again (after the first local maximum) to a significant value, indicating that the drop remains mobile. Increasing Pl to 0.12 slightly reduces the peak velocity reached after the initial acceleration and also causes the drop velocity to reach negative values during deceleration. It should be noted that after some velocity fluctuations, the velocity of the drop approaches zero, $\bar{u}(\times Fr^{1/2})$ is on the order of 10^{-3}. The yield surface of these drops is exhibited in Figs. 5.30(a) and (b) at $\bar{t}(/Fr^{1/2}) = 50$. For the former, a complete envelope of yield materials is formed, while for the latter only spots of yield materials, which appear and disappear over time, are observed. The drop for $Pl_c = 0.12$ is then considered entrapped. Higher values of Wi_c result in increased drop initial peak velocity. For $Wi_c = 4$ and $Pl = 0.12$, the drop is mobile, and a stable yielded region is formed around the drop, as depicted in Fig. 5.30(c). It should be noted that the

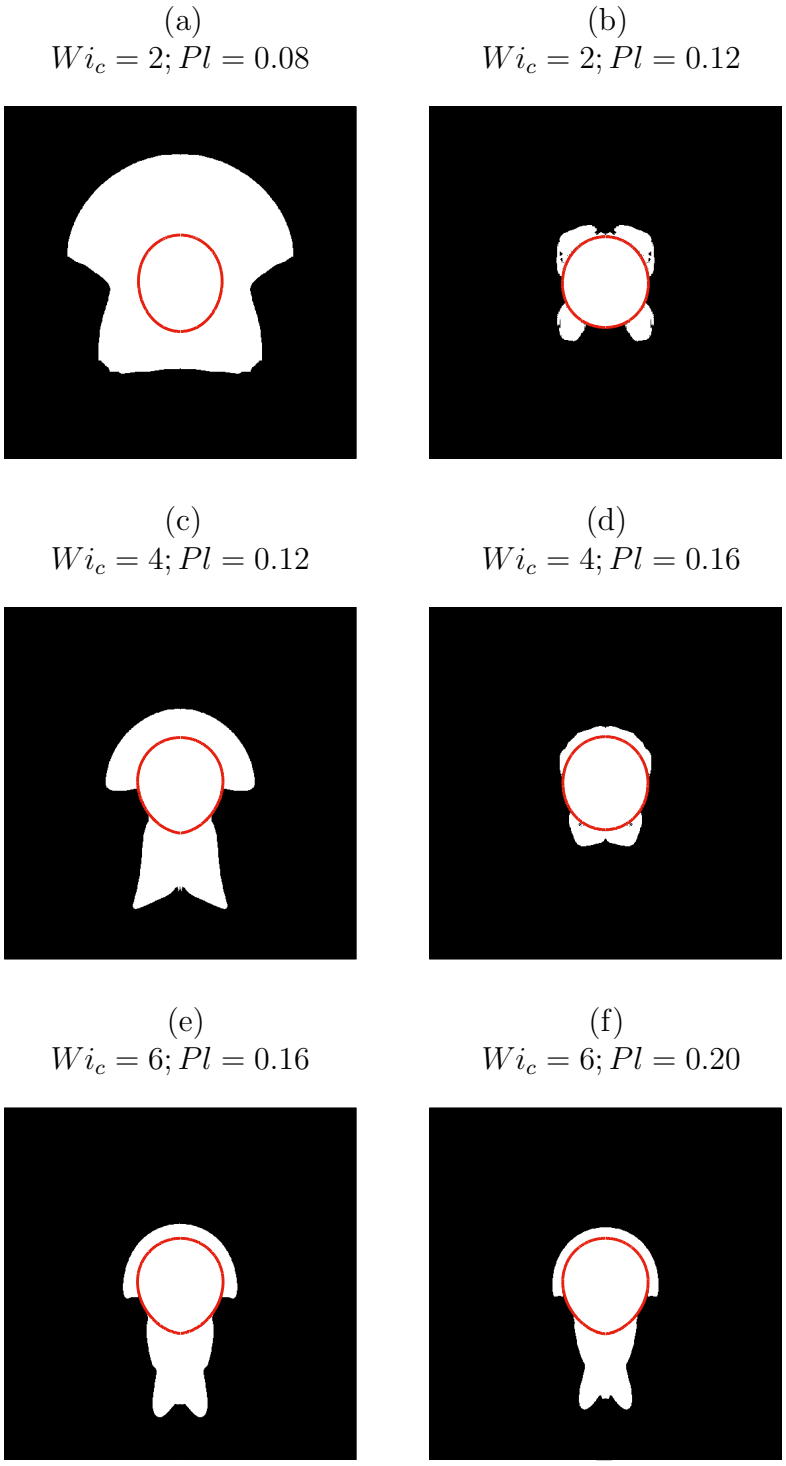

Figure 5.30: Snapshots of the drop interface (red line) and yielded (white)/unyielded (black) regions in EVP materials for different Wi_c and Pl. The other dimensionless parameters are $Fr = 200$, $Bo = 2$, $\eta_r = 0.1$, $\rho_r = 0.1$, and $\beta = 0.01$.

drop is considered mobile despite the fact that a close envelope of yielded materials is not formed. Increasing Pl to 0.16 results in the entrapment of the drop, as for $Wi_c = 2$ and $Pl = 0.12$. A fluctuating yielded region appears and disappears over time close to the drop surface (Fig. 5.30(d)). For $Wi_c = 6$ the drop does not become entrapped even for $Pl = 0.20$ ($Y_g = 0.60$). The yield surfaces for $Wi_c = 6$ and $Pl = 0.16$ and 0.20 are shown in Fig. 5.30(e) and (f), respectively, where a stable region, that does not completely involve the drop, is formed. The observations made by Sikorski et al. (2009) in Carbopol solutions revealed that the bubbles exhibited a teardrop shape, indicating the presence of significant elasticity in the surrounding material. In their study, the authors estimated the critical parameter Y_{gc} to have a value of 0.50 ± 0.04. This finding implies that for elasto-viscoplastic materials, the value of Y_{gc} depends on the elasticity of the material. However, determining the precise functional relationship between Y_{gc} and the elasticity of the surrounding material is beyond the scope of this thesis. Therefore, this section concludes by highlighting the dependence of Y_{gc} on the elasticity of the surrounding material.

5.3 Drop Coalescence Initiation

Drop collision dynamics (velocity and shape change) during the impact on the top layer interface, together with the rheological properties of the fluids, govern the film drainage process. This section specifically focuses on investigating the initial stages of drop interfacial coalescence taking into account the drop rise dynamics, discussed in Sec. 5.2, before collision. The section begins by presenting the results obtained for Newtonian surroundings (Sec. 5.3.1). Subsequently, the coalescence initiation for inelastic viscoplastic and viscoelastic surroundings is examined in Secs. 5.3.2 and 5.3.3, respectively. Lastly, the section concludes by investigating the coalescence initiation in elasto-viscoplastic surroundings in Sec. 5.3.4. To promote a more comprehensive discussion, the analysis is divided into two parts. The first part examines the influence of the surrounding fluid's rheology on drop collision dynamics, while the second part investigates the computational drainage time, denoted as Δt. The computational drainage time serves as a measure or an indication of how the dimensionless parameters impact the coalescence time (the time needed for the film to thin until the rupture thickness), which is larger than Δt. This division is undertaken for every formulation of the surrounding material, except for the Newtonian surrounding.

5.3.1 Drop collision and $\Delta\bar{t}$ in Newtonian materials

This section evaluates the effects of Fr, η_r, and Bo on drop collision dynamics and computational drainage time in Newtonian media. Figures 5.31(a) and (b) present the dimensionless drop velocity (multiplied by $Fr^{1/2}$), $\bar{u}$, and dimensionless width, $\bar{D}_W$, respectively, with dimensionless time (divided by $Fr^{1/2}$) $\bar{t}$. The results are for $Pl = 0.00$, $Wi = 0.00$, using the same sets of Fr, η_r, and Bo as shown in Fig. 5.9. The black dashed vertical line marks the time $\bar{t} = 0.0$ representing the moment the dimensionless minimum distance between the drop and the interface is $\bar{h}_{min} = 0.1$. Additionally, the colored dashed vertical lines mark the time at which $\bar{h}_{min} = 0.01$. The purple line, for $Fr = 200$, $\eta_r = 0.1$, and $Bo = 2$, serves as the base scenario, while individual variations in Fr, η_r, and Bo are considered to assess their respective effects. To aid in the discussion, two auxiliary figures are provided. Figure 5.32 shows the drop and top layer interface shape for $\bar{h}_{min} = 0.1$, 0.05, and 0.01 (the film's thinnest part is marked by a pair of black arrows) and Fig. 5.33 exhibits the draining film shape for $\bar{h}_{min} = 0.01$, respectively.

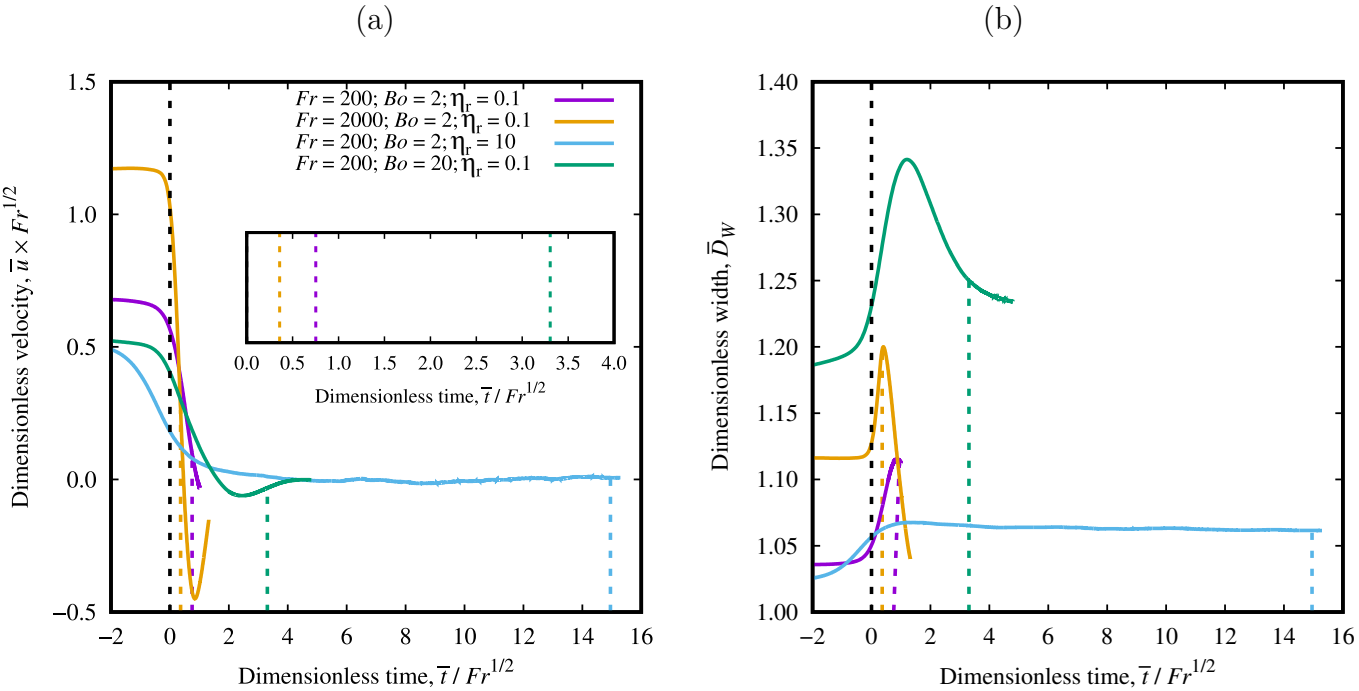

Figure 5.31: Drop (a) dimensionless velocity, $\bar{u}$ ($\times Fr^{1/2}$), and (b) dimensionless width, $\bar{D}_W$, versus dimensionless time, $\bar{t}$ ($/Fr^{1/2}$), for a Newtonian surrounding ($Pl = 0$ and $Wi = 0$) and different values of Fr, η_r, and Bo.

As the drop approaches the top layer interface, its velocity decelerates, and its width expands due to the conversion of kinetic energy to surface energy (see Fig. 5.31). Subse-

quently, the drop retracts and undergoes rebound. Throughout this process, a fraction of the kinetic energy dissipates due to viscous effects. By increasing the Froude number (comparing the purple line for $Fr = 200$ with the yellow line for $Fr = 2000$), the impact velocity of the droplet intensifies, consequently leading to an augmented width of the droplet during the collision stage. The higher impact energy results in a more substantial pressure growth within the film and a more extensive deformation of the interfaces. Consequently, the film length is more pronounced for $Fr = 2000$ in comparison to $Fr = 200$. This distinction can be observed by comparing the shapes of the drop and the top layer interface in Fig. 5.32(a) and (b) for $Fr = 200$ and 2000, respectively, as well as the film shapes represented by the purple and yellow lines in Fig. 5.33 for $Fr = 200$ and 2000, respectively. For $Fr = 200$, the film exhibits a spherical shape, while for $Fr = 2000$, it adopts a dimpled shape due to the heightened pressure accumulation. Although a larger film length tends to decelerate the drainage process, a decrease in Δt is observed for an increase in the Froude number, as indicated by the position of purple and yellow vertical dashed lines. This behavior can be attributed to the fact that an increase in the Froude number, as discussed in Sec. 5.2.1, enhances the relative significance of inertial forces compared to viscous forces. Consequently, the decrease in resistive viscous effects appears to compensate for the increase in inertial effects (which tend to increase the film length) within the range of parameters investigated. In both cases, the simulation's drainage time stopping criterion ($\bar{h}_{min} = 0.01$) is reached while the drops are still bouncing on the interface (the impact energy has not been fully dissipated by viscous effects). The phenomenon of coalescence during bouncing on the interface has been experimentally observed by Zawala and Malysa (2011), and Vakarelski et al. (2019) for bubbles in high-purity water.

Regarding the effect of the viscosity ratio, Fig. 5.31 illustrates that as η_r increases from 0.1 (purple line) to 10 (blue line), the change in drop velocity and width during the collision stage occurs at a slower rate. This can be attributed to higher viscous dissipation, which reduces the transfer rate of kinetic energy to surface energy. Figure 5.31(b) demonstrates that the increase in drop width is less pronounced for $\eta_r = 10$ compared to $\eta_r = 0.1$. Viscous dissipation dampens (smooths and slows down) the collision process, resulting in a monotonous decrease in the drop's velocity without rebounding. Despite the smaller width and impact velocity, the drainage time increases significantly with an increase in the viscosity ratio. During the collision stage, the drop remains mostly static ($\bar{u} \approx 0$) on the interface, while the film continues to drain. This behavior aligns with the experimental observations of Vakarelski et al. (2019), who investigated the effects of interface mobility on the coalescence of bubbles. They found that mobile-surface bubbles exhibited a shorter coalescence time but a higher bouncing amplitude compared to immobile-surface bubbles. For mobile-surface

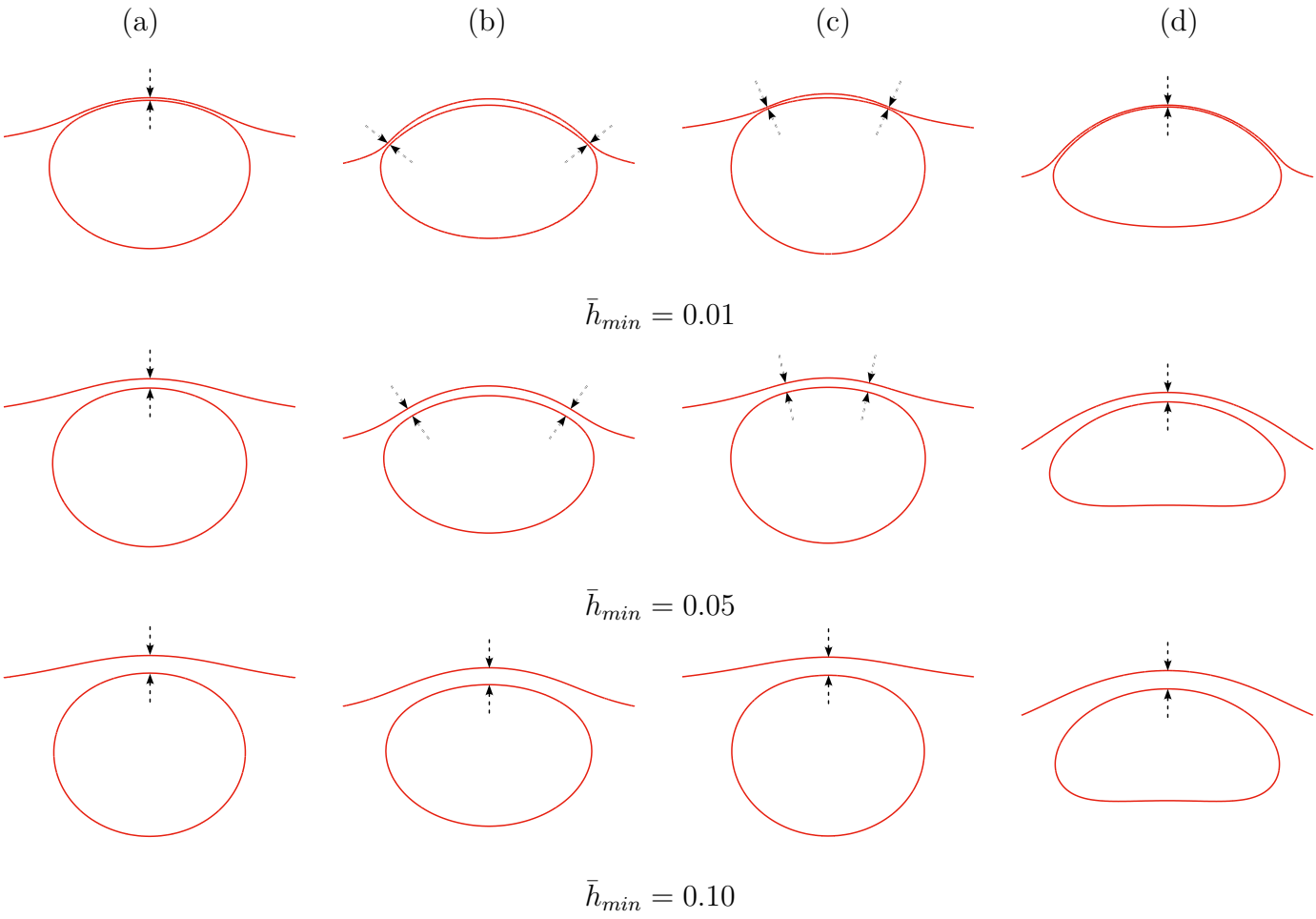

Figure 5.32: Drop and top layer interface shape for $\bar{h}_{min} = 0.10$ (third row), $\bar{h}_{min} = 0.05$ (second row), and $\bar{h}_{min} = 0.01$ (first row) for $Pl = 0.00$, $Wi = 0.00$, (a) $Fr = 200, Bo = 2$, and $\eta_r = 0.1$, (b) $Fr = 2000, Bo = 2$, and $\eta_r = 0.1$, (c) $Fr = 200, Bo = 2$, and $\eta_r = 10$, and (d) $Fr = 200, Bo = 20$, and $\eta_r = 0.1$. The film's thinnest part is marked by a pair of black arrows.

bubbles, a significant rebound of the drop was followed by rapid coalescence. Similar behavior was observed in the lower viscosity ratio cases simulated in Fig. 5.31 (purple and yellow lines), where the film's hydrodynamics boundary condition is closer to that of a bubble with a mobile surface. $\bar{h}_{min} = 0.01$ is reached while the drops are still bouncing on the interface. In contrast, immobile-surface bubbles exhibited weaker bouncing but remained on the interface for a longer time before coalescing. This behavior is similar to the higher viscosity ratio case (blue line), where the film's hydrodynamics boundary condition is closer to that of a bubble with an immobile surface. Vakarelski et al. (2019) attributed these behaviors to the lesser viscous dissipation in the mobile-surface case, allowing for a more pronounced conversion of kinetic energy to surface energy (resulting in stronger rebounding) but also faster drainage. Therefore, the film rapidly reaches smaller thicknesses during the collision

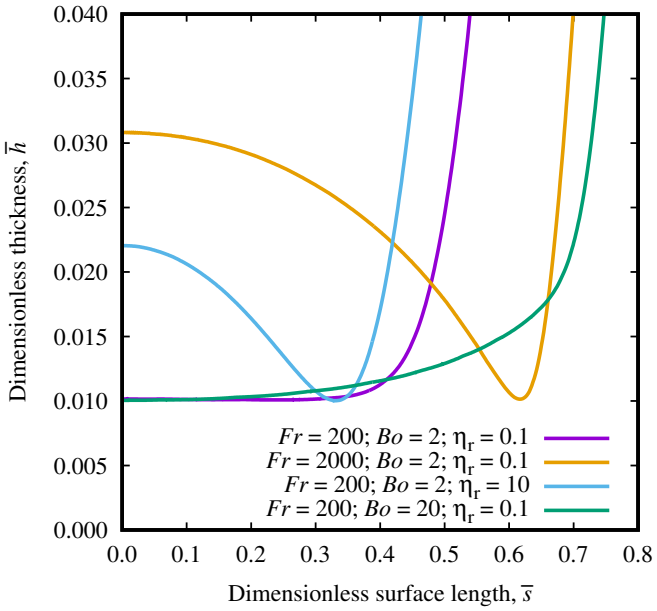

Figure 5.33: Film dimensionless thickness, $\bar{h}$, versus dimensionless surface length, $\bar{s}$, at $\bar{h}_{min} = 0.01$ for a Newtonian surrounding ($Pl = 0$ and $Wi = 0$) and different values of Fr, η_r, and Bo.

stage for lower viscosity ratios while the drop is bouncing on the interface. Conversely, for the higher viscosity ratio, the film thinning during the collision stage is minimal, and a significant portion of the drainage process occurs during the resting stage when the drop is nearly static. Moreover, the larger drop and top layer viscosity generate a stronger pressure gradient in the film, resulting in the formation of a dimple-shaped film. This configuration further hinders the drainage process due to restricted flow passage along the film periphery. The formation of dimpled films due to the coupling of hydrodynamics forces and interface deformation is also predicted by the lubrication theory (Chan et al., 2011). Figure 5.32(c) and the blue line in 5.33 demonstrate that for the higher viscosity ratio, $\eta_r = 10$, the film becomes dimpled, while for $\eta_r = 0.1$ (Fig. 5.32(a) and purple line in Fig. 5.33) the film assumes a spherical shape. This behavior is consistent with the findings of Aarts and Lekkerkerker (2008), and Chi and Leal (1989). The former experimentally observed that during the coalescence of bubbles (low viscosity ratios) and drops (high viscosity ratios), film rupture tends to occur at the film center (spherical-shaped films) and at the film periphery (dimple-shaped films), respectively. The numerical results presented by Chi and Leal (1989) also support these observations, indicating that an increase in the viscosity ratio tends to slow down the drainage process and promote the formation of a dimpled film. Therefore, an increase in η_r prolongs the drainage time due to enhanced viscous dissipation and the change in the film shape by the rheological

properties of the inner phase.

Lastly, in the scenario where the Bond number increases from 2 (purple line) to 20 (green line), the drop width increases during both the rise and collision stages. It is important to note that the viscosity of both phases is maintained constant. As a result, the length of the film increases, as illustrated in Fig. 5.32(d) and by the green line in Fig. 5.33. Due to the larger film area over which the buoyancy force is distributed, the pressure within the film decreases, resulting in a slower drainage process. For a Bond number of $Bo = 20$, the drop has sufficient time to complete almost one rebound before reaching $\bar{h}_{min} = 0.01$, whereas for $Bo = 2$, this is not the case. At lower values of the Bond number, surface tension plays a dominant role, causing less deformation of the drop by distorting forces. Consequently, a smaller film is formed, facilitating the thinning process of the film. These observations are in agreement with the experimental findings of Kočárková et al. (2013), who conducted experiments to measure the thinning rate of films formed during the interfacial coalescence of gas bubbles in Newtonian liquids. Additionally, the authors confirmed that the drainage time is influenced by the length (or area) of the film, which is directly related to the Bond number.

To summarize, in Newtonian media, an increase in Fr tends to reduce the drainage time due to the diminished viscous effects compared to inertial effects, despite the larger width and higher impact velocity of the drop. On the other hand, an increase in η_r has the opposite effect, leading to an increased drainage time despite the decrease in drop width and impact velocity. Moreover, an increase in the viscosity ratio contributes to the formation of dimpled films, which are harder to drain. Higher viscosities of the drop and top layer also promote a smoother collision process, causing the drainage occurring during the drop collision and resting stages to lose and gain significance, respectively. Lastly, an increase in the Bond number (Bo) results in an enlarged film length, leading to an increase in drop rebound amplitude and drainage time.

5.3.2 Drop collision and $\Delta\bar{t}$ in inelastic viscoplastic materials

Non-Newtonian behaviors introduce additional complexity to the inherently complex coalescence phenomenon. This section aims to investigate the effect of plasticity on the dynamics of drop collision, specifically pertaining to drop velocity and shape in Sec. 5.3.2.1. Additionally, the influence of the plastic number (Pl) on $\Delta\bar{t}$ is discussed in Sec. 5.3.2.2.

5.3.2.1 Drop collision in inelastic viscoplastic materials

This section is concerned with the influence of plastic effects on drop collision dynamics. Initially, the plastic number is varied while the other parameters are kept constant. Subsequently, an investigation is conducted to ascertain the influence of variations in Fr, η_r, and Bo on drop collision in scenarios where the surrounding material exhibits a yield stress.

Figures 5.34(a) and (b) display the dimensionless drop velocity (scaled by $Fr^{1/2}$), $\bar{u}$, and dimensionless width, $\bar{D}_W$, respectively, versus dimensionless time (divided by $Fr^{1/2}$). The results are presented for fixed parameters: $Fr = 200$, $Bo = 20$, $\eta_r = 0.1$, and varying values of $Pl = 0.00$, 0.02, 0.04, and 0.06. The vertical black dashed line denotes the time $\bar{t} = 0.0$ when $\bar{h}_{min} = 0.1$, while the colored dashed lines indicate the time when $\bar{h}_{min} = 0.01$ (further discussion on $\Delta\bar{t}$ will be provided in the subsequent section). In the case of a Newtonian surrounding medium (purple line in Fig. 5.34), the drop velocity consistently decreases while the drop width increases as it approaches the interface. However, a distinct behavior is observed for the viscoplastic scenarios (yellow, blue, and green lines). Here, the drop velocity increases while the drop width decreases during the approach to the interface. This behavior can be attributed to the interaction between the drop and the interface prior to the collision

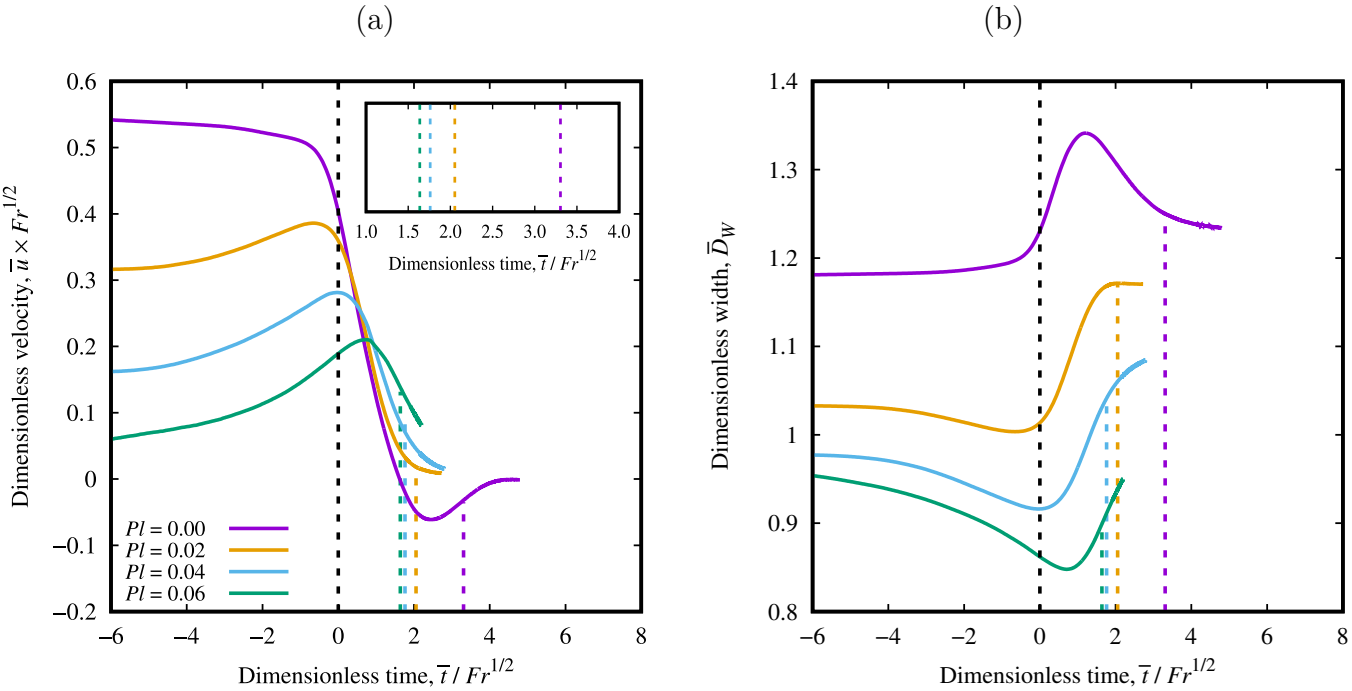

Figure 5.34: Drop (a) dimensionless velocity, $\bar{u}$ ($\times Fr^{1/2}$), and (b) dimensionless width, $\bar{D}_W$, versus dimensionless time, $\bar{t}$ ($/Fr^{1/2}$), for different values of Pl. The other dimensionless parameters are $Fr = 200$, $Bo = 20$, and $\eta_r = 0.1$.

event. To illustrate this phenomenon, Fig. 5.35 presents snapshots of a drop and the yield surface throughout the rise, collision, and resting stages. The depicted scenario corresponds to $Pl = 0.04$, $Fr = 200$, $Bo = 20$, and $\eta_r = 0.1$ (blue line in Fig. 5.34). Figure 5.35(a) presents the drop rising at steady-state, enveloped by a region of yielded material. As the drop nears the upper layer fluid (Figs. 5.35(b) and (c)), the latter begins to deform, facilitating further yielding of the material ahead of the drop. Consequently, the rising velocity of the drop increases, and its width decreases as it approaches the interface. During the progress of the collision, kinetic energy is converted into surface energy, leading to an expansion of the drop width, as depicted by Fig. 5.35(d), (e), and (f). In Fig. 5.35(f), the drop is approaching the resting stage ($\bar{u} \approx 0.0$), where it becomes nearly static on the interface while the drainage process continues and the size of the yielded region diminishes. Additionally, apart from the energy conversion, the buoyancy force exerted on the drop against the interface also contributes to the observed increase in drop width.

Figure 5.36 showcases the shapes of the drop and top layer interface for each condition presented in Fig. 5.34 at minimum film thicknesses: $\bar{h}_{min} = 0.10$, 0.05, and 0.01 (the film's thinnest part is marked by a pair of black arrows). It can be observed that an increase in the plastic number intensifies the reduction in drop width, consequently leading to a shorter film length. Additionally, Fig. 5.36 also conveys that plasticity promotes the formation of more spherical-shaped films. This tendency towards spherical films with increased plasticity can be attributed to two plastic effects that manifest during the rise stage. The first effect is the decrease in drop rising velocity with Pl, while the second effect is the reduction in drop width due to the viscosity field of the Bingham material. In Figs. 5.37(a) and (b), the dimensionless viscosity field, $\bar{\eta}_1$, is depicted in the film (using the (s, h) coordinate system) and in the area surrounding the drop outside the film (using the (r, z) coordinate system), respectively, at the moment $\bar{h}_{min} = 0.01$ for $Pl = 0.04$, $Fr = 200$, $Bo = 2$, and $\eta_r = 10$. Figure 5.37(a) demonstrates that the viscosity within the film increases with $\bar{s}$, resulting in a more rapid thinning of the film in the central region compared to the periphery. Moreover, Fig. 5.37(b) shows that the viscosity of the surrounding material near the drop equator is higher than that near the poles (similar to the rise stage). Therefore, the eventual increase in drop width during the collision stage appears to be impeded by the plastic effects of the surrounding material. A study conducted by Sanjay et al. (2021) examined bubble merging with a top layer gas in Bingham materials and observed a similar hindrance of capillary waves and shape change of the post-rupture cavity due to the yield stress of the surroundings. Figure 5.38 depicts the dimensionless position, $\bar{z}$, of the interface during the collision for various combinations of Pl and Bo values. The curves terminate at $\bar{h}_{min} = 0.01$. The results indicate that plasticity has a dampening effect on drop collision, leading to a decrease in the amplitude and rate

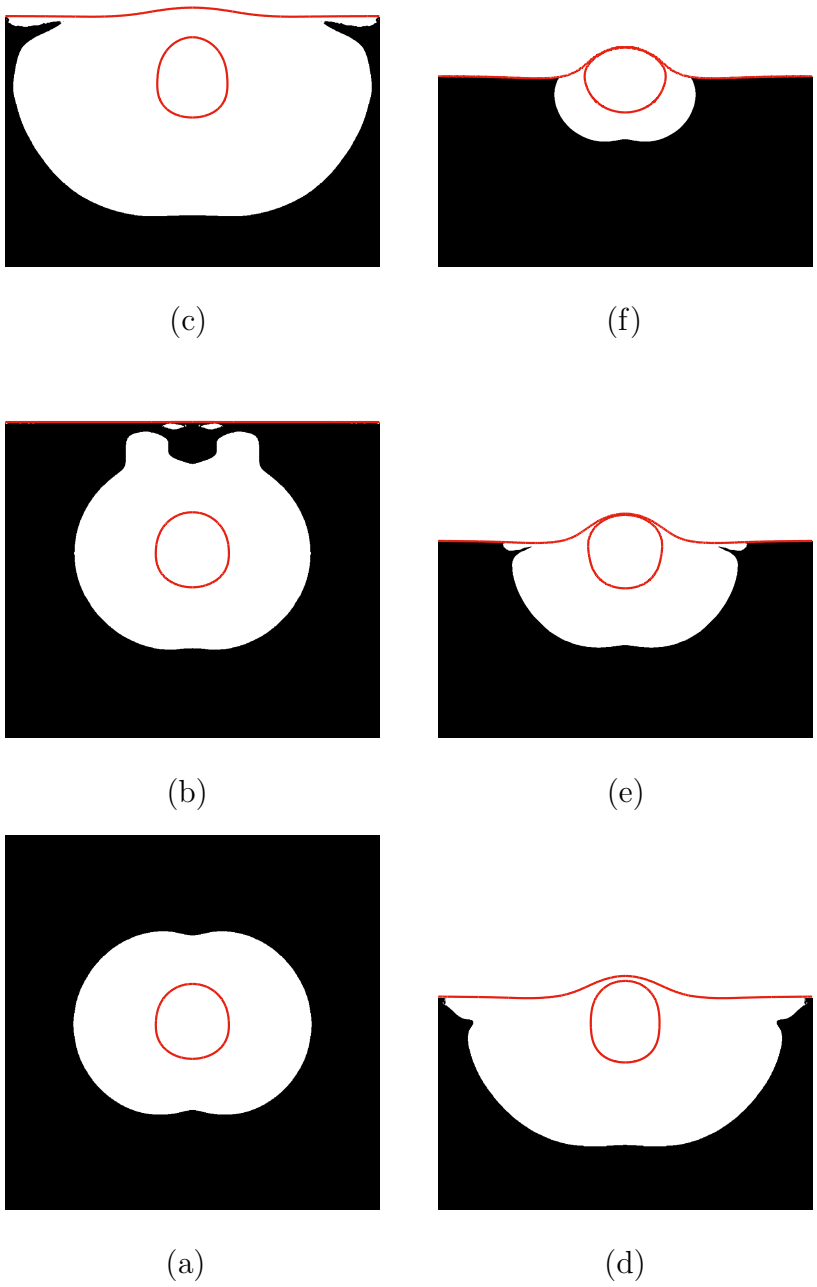

Figure 5.35: Yield surface around a drop rising and impacting on the top layer interface for $Pl = 0.04$, $Fr = 200$, $Bo = 20$, $\eta_r = 0.1$ at steady-state rise (a), approaching the interface at $\bar{t}(/Fr^{1/2})$ = -6.35 (b) and -1.60 (c), colliding on the interface at $\bar{t}(/Fr^{1/2}) = 0.30$ (d) and 1.25 (e), and resting on the interface at $\bar{t}(/Fr^{1/2}) = 2.75$ (f).

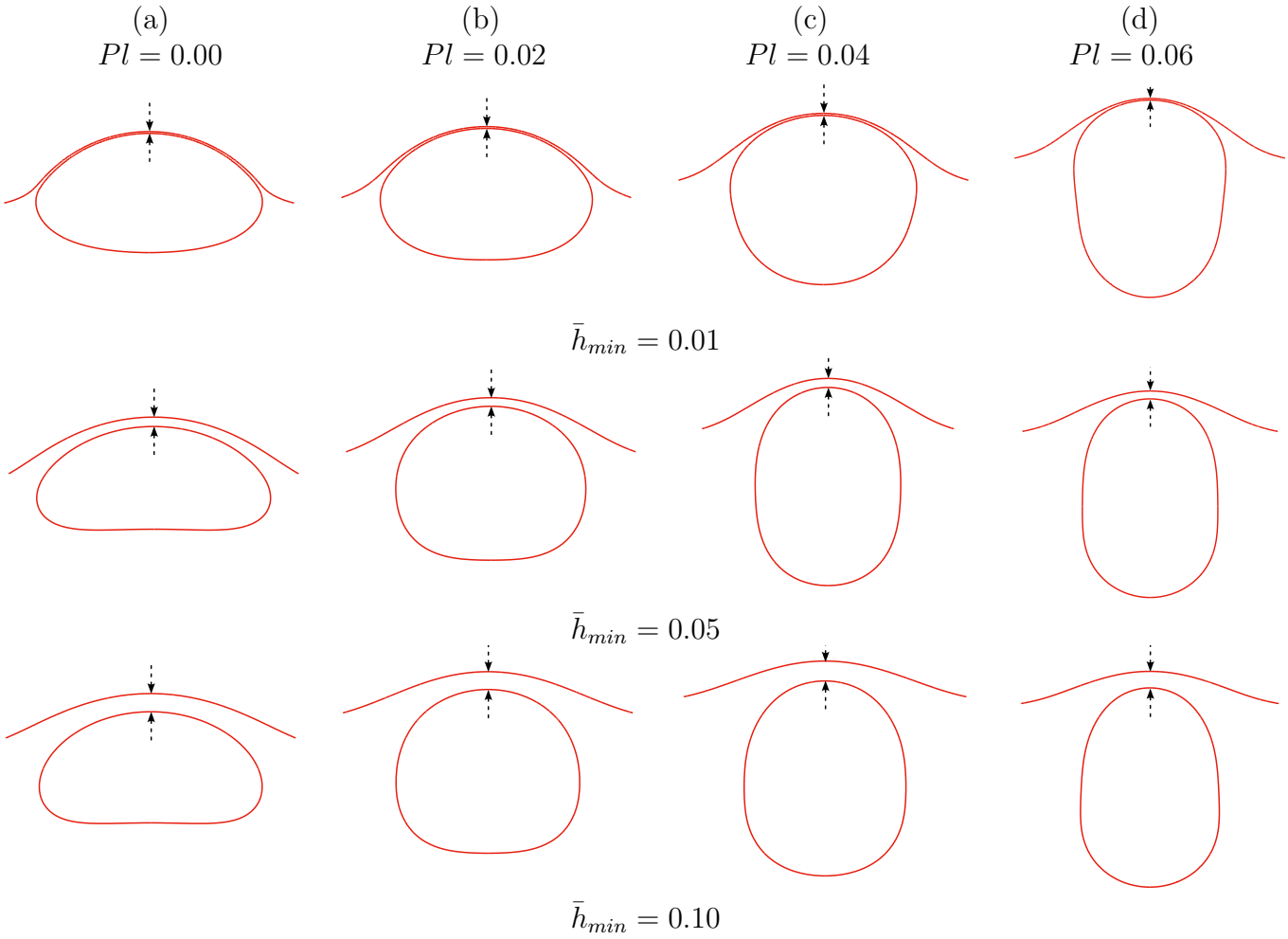

Figure 5.36: Drop and top layer interface shape for $\bar{h}_{min} = 0.10$ (third row), $\bar{h}_{min} = 0.05$ (second row), and $\bar{h}_{min} = 0.01$ (first row) for $Fr = 200, Bo = 20, \eta_r = 0.1$, and (a) $Pl = 0.00$, (b) $Pl = 0.02$, (c) $Pl = 0.04$, and (d) $Pl = 0.06$. The film's thinnest part is marked by a pair of black arrows.

of interface deflection regardless of the Bond number value. Furthermore, a decrease in the Bond number also reduces the maximum deformation of the interface due to its decreased deformability. Thus, our findings suggest that an increase in plasticity and/or surface tension results in diminished drop rebound, which is observed only for $Bo = 20$ and $Pl = 0.00$.

Figures 5.39(a) and (b) exhibit the dimensionless drop velocity (multiplied by $Fr^{1/2}$), $\bar{u}$, and dimensionless width, $\bar{D}_W$, respectively, with dimensionless time (divided by $Fr^{1/2}$), $\bar{t}$, for $Pl = 0.04$ and the same sets of Fr, η_r, and Bo in Fig. 5.31, for $Pl = 0.00$. Once again, the base scenario is represented by the purple line ($Pl = 0.04$, $Fr = 200$, $\eta_r = 0.1$, and $Bo = 2$) and the effects of Fr, η_r, and Bo are assessed by altering them individually. The black dashed line marks the time $\bar{t} = 0.0$ at which $\bar{h}_{min} = 0.1$, and the colored dashed lines indicate the time when $\bar{h}_{min} = 0.01$. Additionally, Fig. 5.40 illustrates the shape of the film at $\bar{h}_{min} = 0.01$.

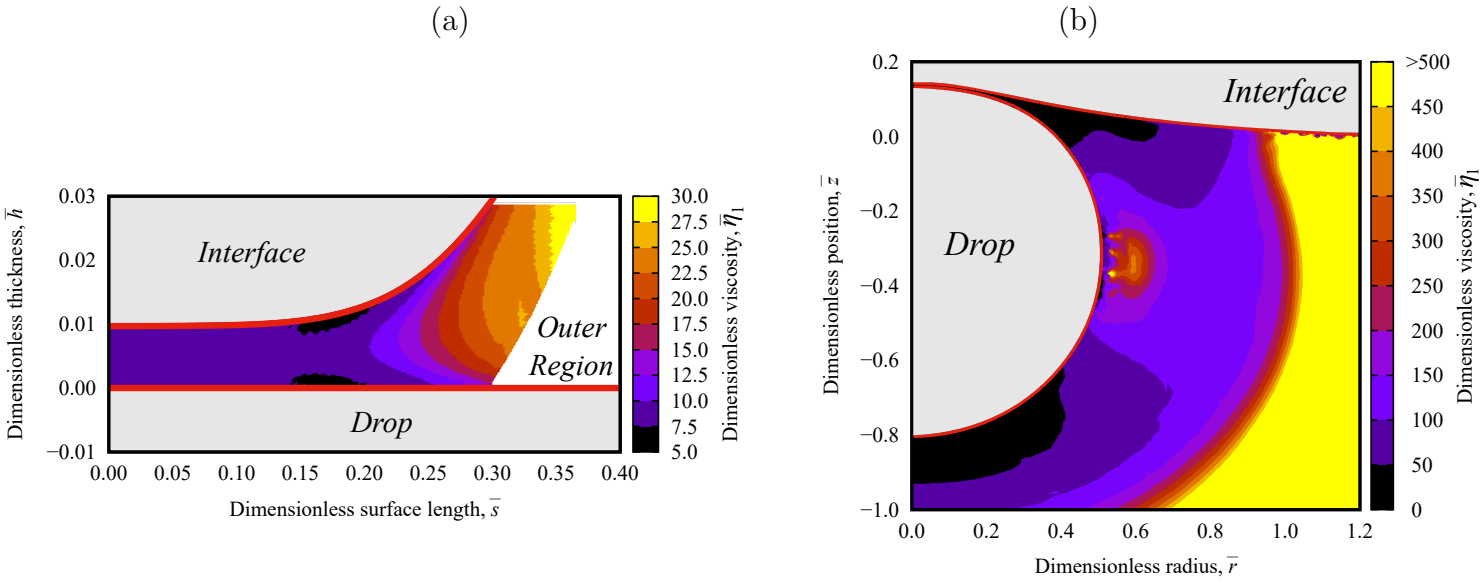

Figure 5.37: Dimensionless viscosity field, $\bar{\eta}_1$, (a) in the film in the (s, h) coordinate system and (b) around the drop in the (r, z) coordinate system at the moment $\bar{h}_{min} = 0.01$ for $Pl = 0.04$, $Fr = 200$, $Bo = 2$, and $\eta_r = 10$. Gray areas correspond to Fluid 2 (drop and top layer).

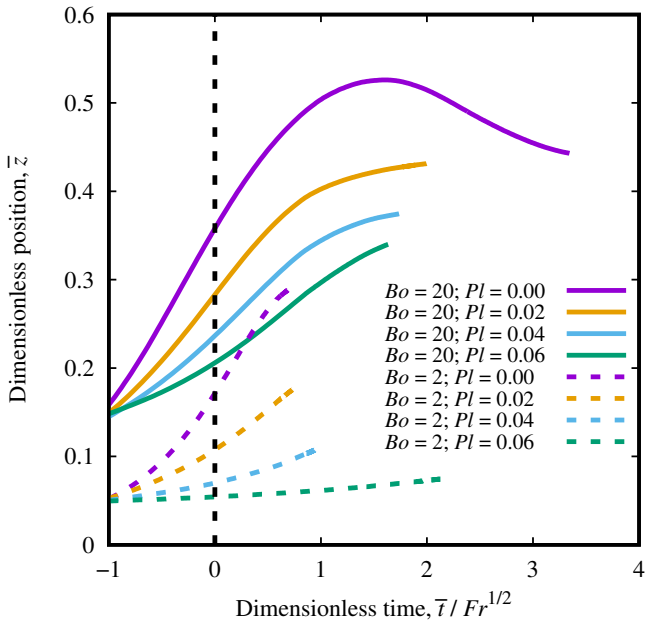

Figure 5.38: Interface dimensionless position, $\bar{z}$, with dimensionless time, $\bar{t}$ $(/Fr^{1/2})$, for $Fr = 200$, $\eta_r = 0.1$, $Bo = 20$ (solid lines) and 2 (dashed lines), and $Pl = 0.00$ (purple lines), 0.02 (yellow lines), 0.04 (blue lines), and 0.06 (green lines).

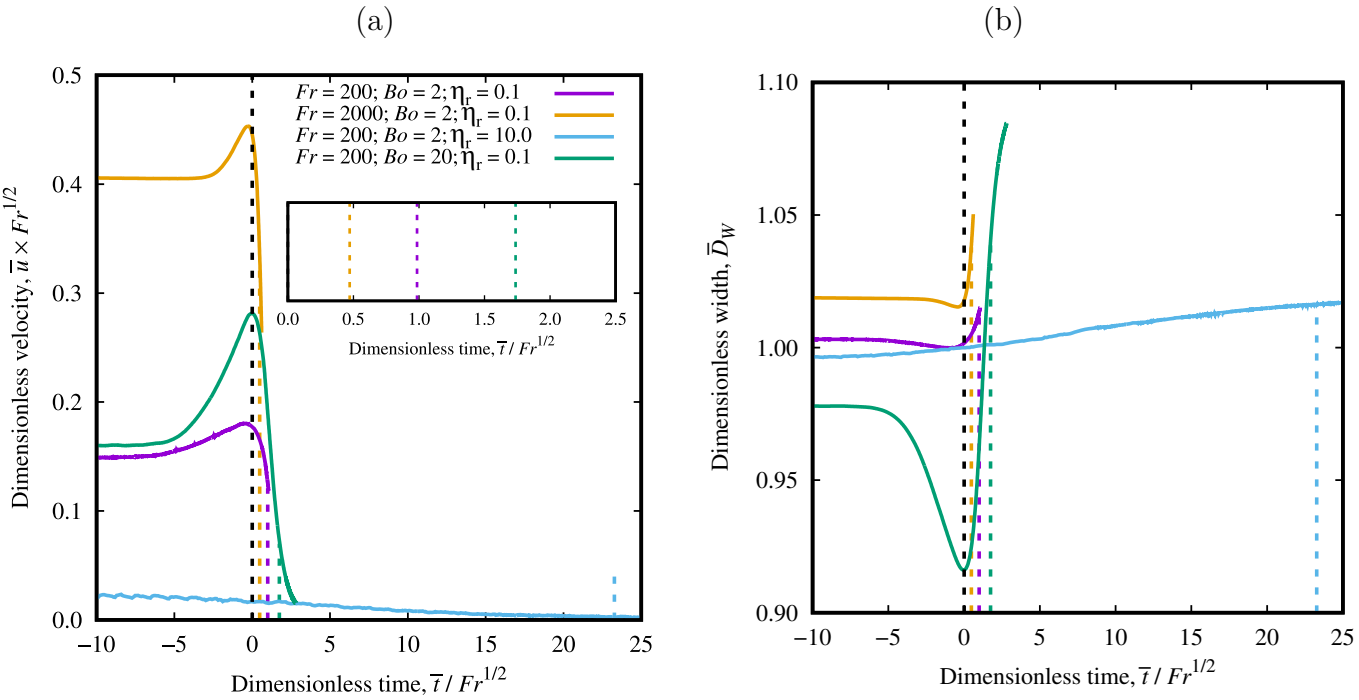

Figure 5.39: Drop (a) dimensionless velocity, $\bar{u}$ ($\times Fr^{1/2}$), and (b) dimensionless width, $\bar{D}_W$, as a function of the dimensionless time, $\bar{t}$ ($/Fr^{1/2}$), for different values of Fr, η_r, and Bo. The plastic number is equal to 0.04.

Except for $Pl = 0.04$, the other dimensionless parameters are the same as in Fig. 5.33. The changes in $\bar{u}$ and $\bar{D}_W$ for different values of Fr values (purple line for $Fr = 200$ and yellow line for $Fr = 2000$) exhibit similarities to the Newtonian case. The drop impact velocity and width increase with an increase in the Froude number. The film length also increases with the Froude number, as can be seen by comparing the purple and yellow lines in Fig. 5.40. However, in contrast to the Newtonian case, both films assume a spherical shape, while the film for $Fr = 2000$ in the Newtonian scenario forms a dimple. A similar behavior to the Newtonian case is observed for an increase in the viscosity ratio, where the changes in drop velocity and width during impact on the interface occur more smoothly and over a longer period. Moreover, the critical plastic number for drop entrapment starts to decrease with an increase in the viscosity ratio for $\eta_r \approx 10$. Therefore, in the case of a higher viscosity ratio (blue line in Fig. 5.39), the drop is closer to the entrapment condition compared to the lower viscosity ratio. Consequently, the velocity reduction with η_r is more pronounced than in the Newtonian scenario, and the drop rise velocity approaches zero for $Pl = 0.04$ and $\eta_r = 10$. The blue line in Fig. 5.40 for $\eta_r = 10$ demonstrates that the film remains spherical even for the higher viscosity ratio case. For an increase in the Bond number (purple and green lines for $Bo = 2$ and 20 in Fig. 5.39, respectively), the rise and impact velocities of the drop

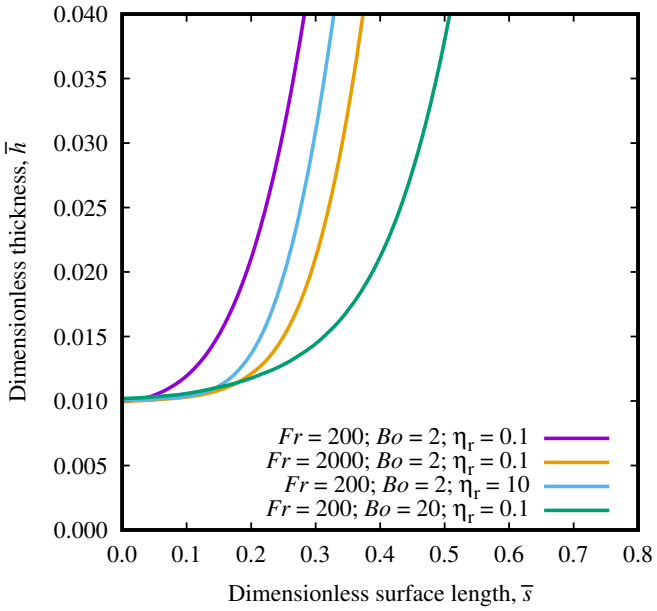

Figure 5.40: Film dimensionless thickness, $\bar{h}$, versus dimensionless surface length, $\bar{s}$, at $\bar{h}_{min} = 0.01$, for different values of Fr, η_r, and Bo, and $Pl = 0.04$.

($\bar{t} \lessapprox 0.0$) increase, exhibit an increment, in contrast to the $Pl = 0.00$ scenario. This behavior arises from the reduction in drop width caused by Pl, which becomes more pronounced for higher values of Bo. However, as the drop collision progresses and the conversion of kinetic energy to surface energy takes place, the drop width for $Bo = 20$ surpasses that of $Bo = 2$. Consequently, the film length corresponding to $Bo = 20$ eventually becomes more prominent than that of $Bo = 2$, as illustrated by the green line in Fig. 5.40.

5.3.2.2 The effect of plasticity on $\Delta\bar{t}$ in inelastic viscoplastic materials

The objective of this section is to assess the influence of plastic effects on the initial stage of the film drainage process. This influence is evaluated by analyzing the computational drainage time, Δt, which provides a measure of how plasticity influences the coalescence time.

Figure 5.41 shows the dimensionless computational drainage time (divided by $Fr^{1/2}$), $\Delta\bar{t}$, as a function of Pl, using the same sets of parameters Fr, η_r, and Bo as in Fig. 5.12. In the base scenario (purple line with squares) characterized by $Fr = 200$, $\eta_r = 0.1$, and $Bo = 2$, the computational drainage time exhibits an increasing trend with increasing Pl. This trend remains consistent for both the higher Froude number (yellow line with inverted triangles, $Fr = 2000$) and higher viscosity ratio scenarios (blue line with triangles, $\eta_r = 10$). The

variations in $\Delta\bar{t}$ with respect to Fr and η_r are consistent across all values of Pl. Specifically, an increase in Fr leads to a decrease in $\Delta\bar{t}$, while an increase in η_r results in an increase in $\Delta\bar{t}$. However, in the case of the higher Bond number scenario (green line with circles, $Bo = 20$), an inverse trend is observed, where $\Delta\bar{t}$ decreases as Pl increases.

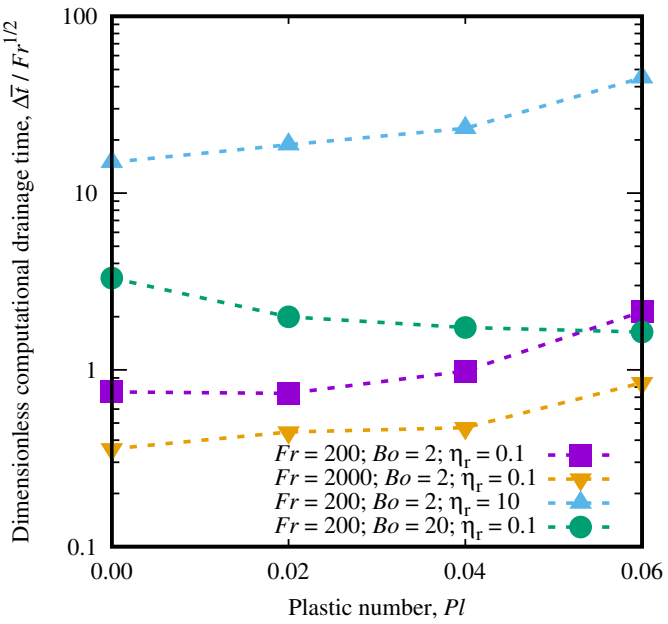

Figure 5.41: Dimensionless computational drainage time, $\Delta\bar{t}$ $(/Fr^{1/2})$, versus the plastic number, Pl.

As discussed in the preceding sections, the drainage time of the film is influenced by both the geometrical characteristics of the film (film length and shape) and the rheological properties of the phases involved, including interface mobility and viscous resistance. The presence of plastic effects has a dual impact: it facilitates coalescence by promoting the formation of prolate drops and spherical films, while simultaneously increasing resistance to flow within the film. To provide further insight into this phenomenon, Fig. 5.42 shows the dimensionless stress field within the film for $Fr = 200$, $Bo = 2$, $\eta_r = 10$, and $Pl = 0.00$, 0.02, 0.04, and 0.06, at $\bar{h}_{min} = 0.01$. This analysis aims to elucidate the changes in the film shape and the average magnitude of stress within the film, which is directly linked to the rheological properties of the materials, as Pl varies. The objective is to gain insight into the overall trends and tendencies rather than providing an exhaustive discussion concerning the detailed contours of the stress field. It is worth noting that $\bar{\tau}_y = Pl$. The gray area in the figure represents the region occupied by Newtonian fluids comprising the drop and the upper layer interface, while the white area on the right side corresponds to the surrounding material

outside the film. For the case of $Pl = 0.00$ (Fig. 5.42(a)), the film exhibits a dimpled shape, and a region of high stress is observed near the throat of the film, while the stress within the central region of the film is relatively low. This finding aligns with the theoretical predictions of Abid and Chesters (1994), who predicted that for dimpled films with partially mobile interfaces, the maximum shear stress is concentrated near the rim of the film. For $Pl = 0.02$ (Fig. 5.42(b)), a similar trend is observed, albeit with a smaller film length and dimple size. The stress within the central region of the film is slightly higher than the yield stress ($|\bar{\boldsymbol{\tau}}| \gtrapprox \bar{\tau}_y$). As Pl increases to 0.04 (Fig. 5.42(c)), the film length decreases, and it becomes spherical. The reduced film length concentrates the buoyancy force over a smaller area, leading to an increase in stress within the film, which remains slightly above the yield stress. This behavior persists for $Pl = 0.06$ (Fig. 5.42(d)), where the film becomes even shorter, and the stress within the film remains slightly above the yield stress. Thus, enhancing the plasticity of the surrounding materials results in a more spherical and shorter film, ultimately facilitating the drainage process. This mechanism is particularly pronounced for higher values of the Bond number, which explains the observed decrease in $\Delta\bar{t}$ with increasing Pl when $Bo = 20$. In all cases, the minimum stress within the film is slightly above the yield stress, indicating a low strain rate ($|\boldsymbol{\tau}| = \tau_y + \mu_p|\dot{\boldsymbol{\gamma}}| \gtrapprox \tau_y$, so $|\dot{\boldsymbol{\gamma}}| \approx 0.0$) and, consequently, a high viscosity (*e.g.*, $\eta_1 = \mu_p + \tau_y/|\dot{\boldsymbol{\gamma}}|$) within the film, rendering the drainage process more difficult. For lower values of Bo, the influence of surface tension is more pronounced, resulting in less deformation of the drop by distorting forces. In this scenario, the flow resistance imposed by the plasticity of the surrounding material outweighs the facilitation provided by the film geometry, resulting in an increase in $\Delta\bar{t}$ with increasing Pl. Therefore, the flow-arresting property of the yield stress is counterbalanced by the alterations in film geometry, thereby introducing challenges in determining the conditions that lead to film arrest.

Goel and Ramachandran (2017) conducted a study utilizing lubrication theory and scaling analyses to investigate the drainage of films composed of Bingham materials. In their research, the interfaces were immobile, and the drops approached each other with a constant velocity during a binary collision. Their study focused on the drainage time as a function of the capillary number $Ca = F/(\sigma R)$, where F represents the force exerted on the drops and R corresponds to the drop radius. In the present thesis, the deformation of the interfaces and film thicknesses investigated exceed those considered with the lubrication theory. Additionally, the constant force approach is deemed more suitable for analyzing interfacial coalescence compared to the constant velocity approach utilized by Goel and Ramachandran (2017). Nonetheless, an attempt is made to qualitatively compare their findings with the results obtained in this research. To begin with, the authors' findings indicate that the introduction of a yield stress to the film material led to an increase in the drainage time across

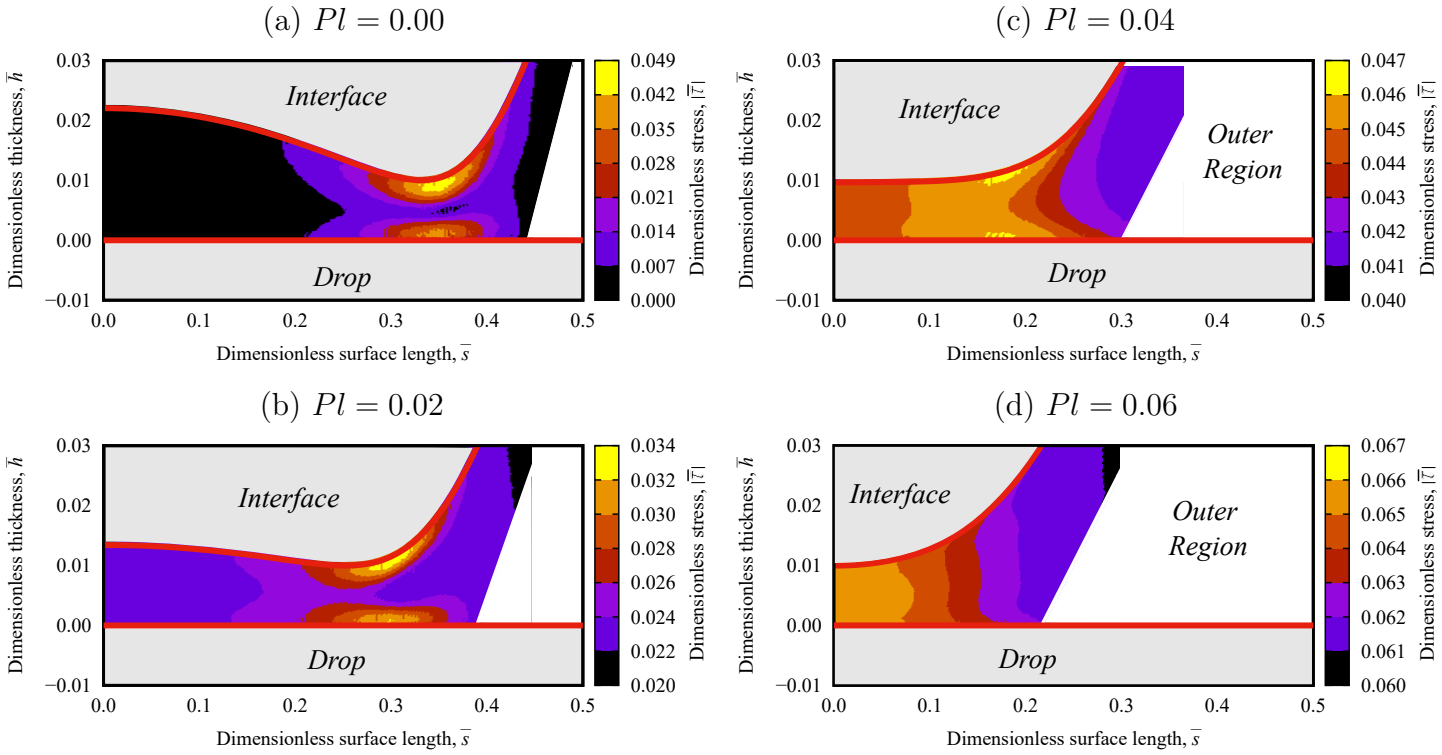

Figure 5.42: Dimensionless stress field $|\bar{\boldsymbol{\tau}}|$ at $\bar{h}_{min} = 0.01$ for $Fr = 200$, $Bo = 2$, $\eta_r = 10$, and $Pl = \bar{\tau}_y =$ (a) 0.00, (b) 0.02, (c) 0.04, and (d) 0.06. The gray areas correspond to Fluid 2 (Newtonian) and the white area corresponds to the region in Fluid 1 (viscoplastic) outside the film.

all capillary numbers. However, as pointed out by Thompson and Soares (2016), the yield stress possesses both viscous and plastic characteristics. This is evident in the definition of viscosity, $\eta = |\boldsymbol{\tau}|/|\dot{\boldsymbol{\gamma}}| = \tau_y/|\dot{\boldsymbol{\gamma}}| + \mu_p$, where an increase in τ_y (while holding μ_p constant) results in an increase in viscous resistive forces. Consequently, the observed increase in drainage time reported by the authors may be attributed to an elevation in viscous stresses within the film. This has a similar effect of both reducing the Froude number and increasing the plastic number in the present study, rather than solely increasing the level of plasticity (Pl). Differently, the present results have demonstrated that under low surface tension conditions, an increase in plasticity can lead to a reduction in the drainage time (at least the computational drainage time). This phenomenon is attributed to the formation of shorter and spherical films with an increase in Pl. Secondly, Goel and Ramachandran (2017) scaled the film length as $\sqrt{hR}$ for spherical films. Therefore, for a constant force F, the pressure gradient within the film increases due to the diminishing film length during the drainage process. Consequently, as the film thickness decreases, the magnitude of the stress increases, and according to the authors, preventing these films from being arrested by the yield stress.

In contrast, the present simulations have revealed an opposite trend, as depicted in Fig. 5.43, which displays the dimensionless stress field for $Fr = 200$, $Bo = 2$, $\eta_r = 10$, and $Pl = 0.04$ for different dimensionless minimum film thicknesses: $\bar{h}_{min} = 0.050$, 0.025, and 0.010. The figure indicates that, on average, the stress level within spherical films can decrease as the film thickness diminishes, suggesting that the drainage of spherical films is susceptible to arrestment by the yield stress. Lastly, the authors posited that plastic effects may exclusively freeze dimpled films since these exhibit a region of minor stress in the film center. However, considering the rise and collision dynamics, the present results indicate that the formation of

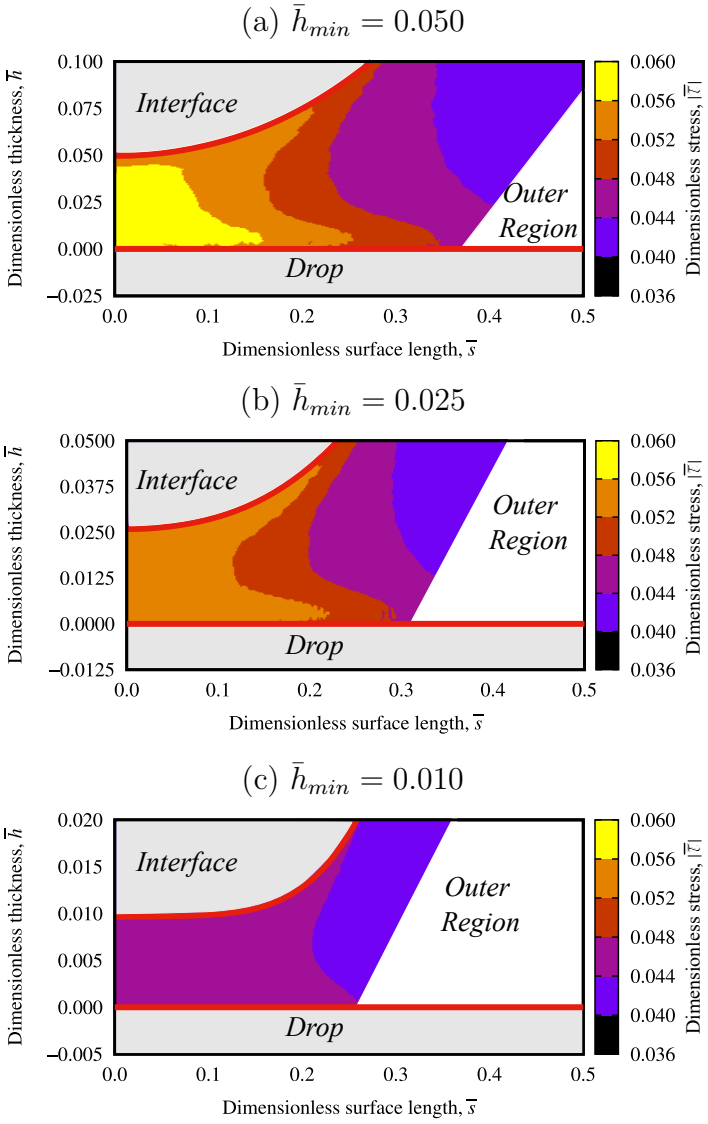

Figure 5.43: Dimensionless stress field $|\bar{\tau}|$ for $Fr = 200$, $Bo = 2$, $\eta_r = 10$, and $Pl = \bar{\tau}_y = 0.04$ at $\bar{h}_{min} = 0.050$ (a), 0.025 (b), and 0.010 (c). The gray areas correspond to Fluid 2 (Newtonian) and the white area corresponds to the region in Fluid 1 (viscoplastic) outside the film.

dimpled films tends to occur for low levels of plasticity, which may not be sufficient to arrest the drainage process. On the other hand, at higher levels of plasticity, the film assumes a spherical and shorter configuration, rendering the drainage process arrestment by the yield stress more difficult. Therefore, the dimpled films calculated for high values of τ_y in the work of Goel and Ramachandran (2017) may not be obtainable in the present simulations.

5.3.3 Drop collision and $\Delta\bar{t}$ in viscoelastic materials

This section investigates the influence of elasticity, quantified by the characteristic Weissenberg number, on the dynamics of drop collision (Sec. 5.3.3.1) and on $\Delta\bar{t}$ (Sec. 5.3.3.2) in viscoelastic materials.

5.3.3.1 Drop collision in viscoelastic materials

In this section, the influence of the characteristic Weissenberg number, as well as of Fr, η_r, and Bo, on drop collision in a viscoelastic medium is investigated. Figures 5.44(a) and (b) display the dimensionless velocity of the drop, $\bar{u}(\times Fr^{1/2})$, and dimensionless width, $\bar{D}_W$, with dimensionless time, $\bar{t}(/Fr^{1/2})$, for $Bo = 20$ and varying values of Wi_c. The dashed

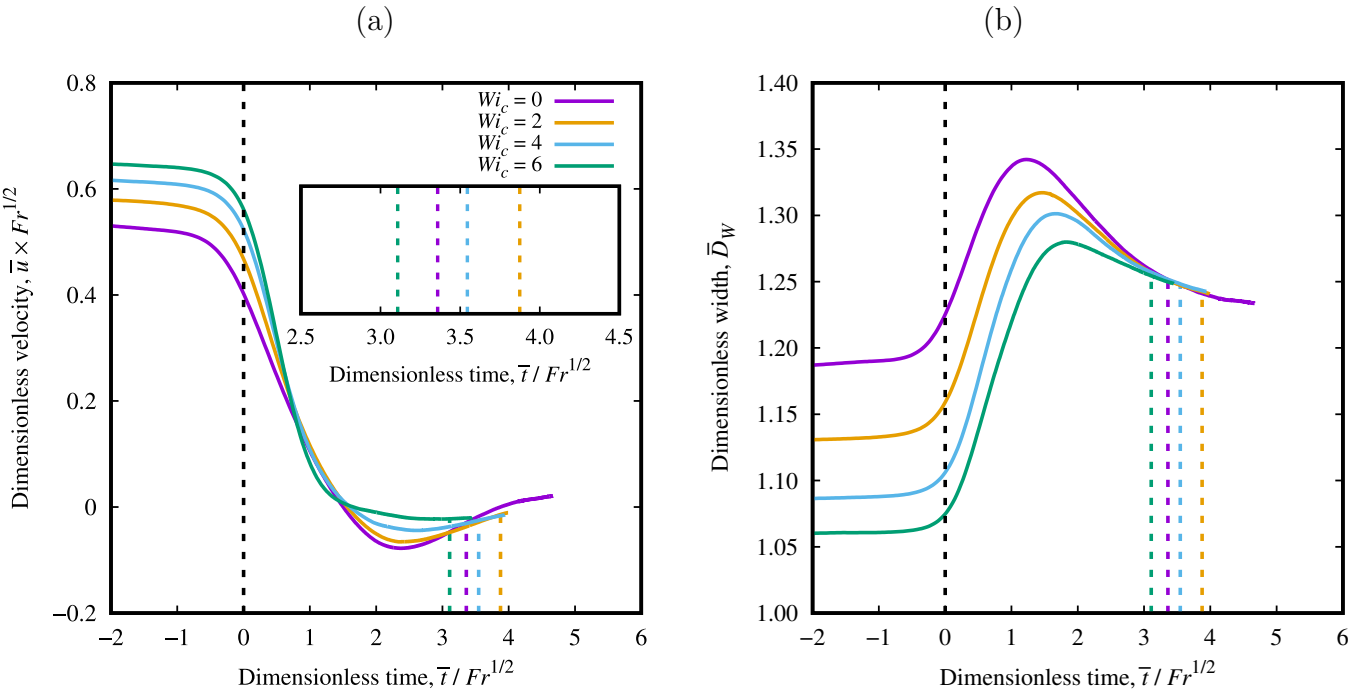

Figure 5.44: Drop (a) dimensionless velocity, $\bar{u}$ $(\times Fr^{1/2})$, and (b) dimensionless width, $\bar{D}_W$, versus dimensionless time, $\bar{t}$ $(/Fr^{1/2})$, for different values of Wi_c. The other dimensionless parameters are $Fr = 200$, $Bo = 20$, and $\eta_r = 0.1$.

black line marks the time $\bar{t} = 0$ and the colored dashed lines the moment $\bar{h}_{min}$ reaches 0.01. In contrast to the behavior observed in inelastic viscoplastic surroundings, the drop velocity decreases monotonically, while the width increases as the drop approaches the interface, similar to the cases with Newtonian surroundings. Figure 5.45 depicts the shapes of the drop and top layer interface for the same parameters as in Fig. 5.44, at $\bar{h}_{min} = 0.10$, 0.05, and 0.01. At $\bar{h}_{min} = 0.10$ the shape of the drop is still close to that at steady state rise (see Fig. 5.20 in Sec. 5.2.3). Due to the differences in the shapes of the impacting drops, the change in the center of mass position during collision also differs, resulting in a reduction and flattening of the drop rebound as Wi_c increases. Notably, Fig. 5.44(b) reveals a convergence of the drop width at later times for this particular value of the Bond number. Indeed, as demonstrated in Fig. 5.45, the shape of the drops and top fluid interfaces is similar for the

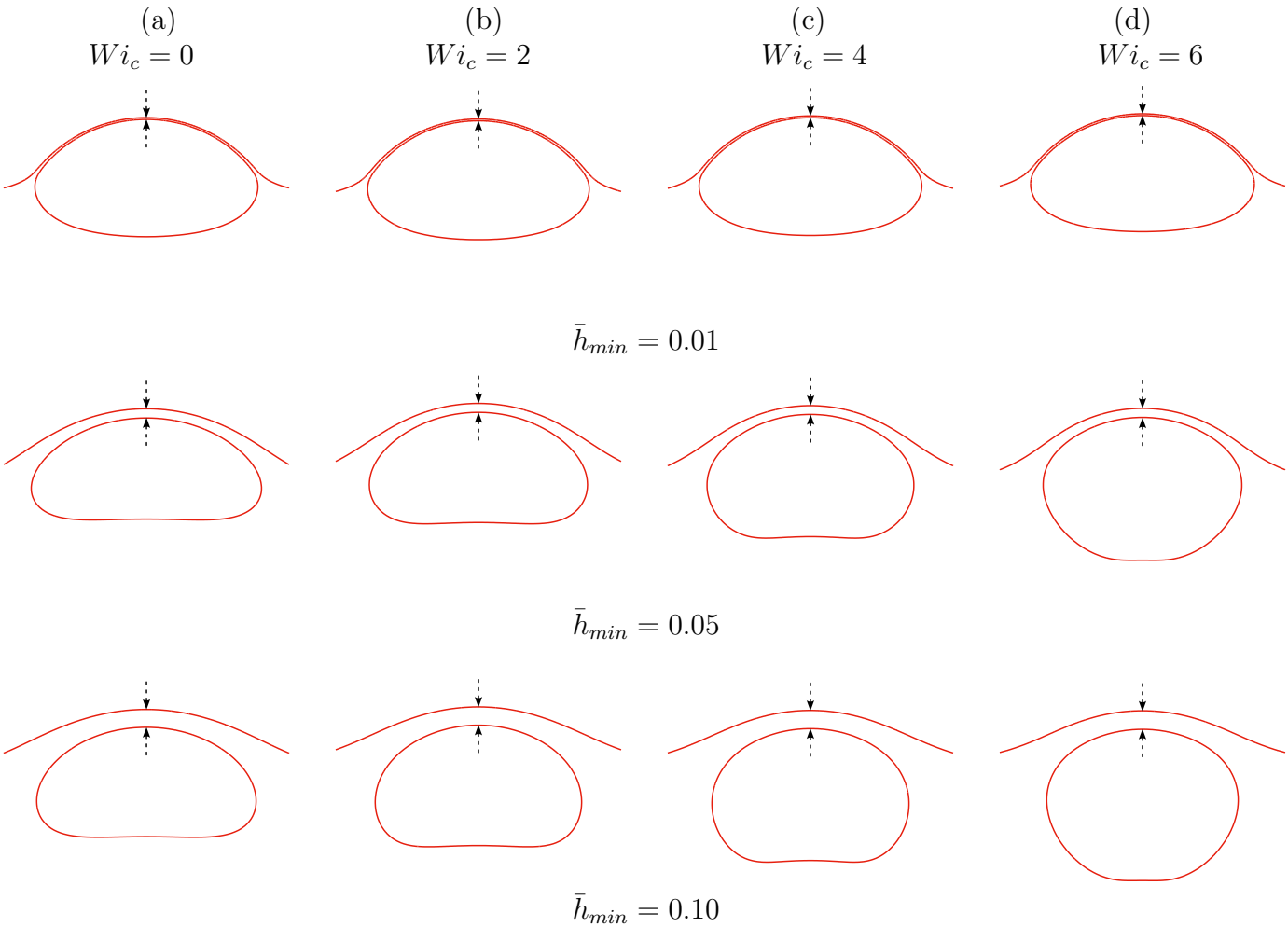

Figure 5.45: Drop and top layer interface shape for $\bar{h}_{min} = 0.10$ (third row), $\bar{h}_{min} = 0.05$ (second row), and $\bar{h}_{min} = 0.01$ (first row) for $Fr = 200, Bo = 20$, $\eta_r = 0.1$, and (a) $Wi_c = 0$, (b) $Wi_c = 2$, (c) $Wi_c = 4$, and (d) $Wi_c = 6$. The film's thinnest part is marked by a pair of black arrows.

different characteristic Weissenberg numbers at $\bar{h}_{min} = 0.01$.

Regarding the effect of the other dimensionless parameters (Fr, η_r, and Bo) in the context of viscoelastic media, Figs. 5.46(a) and (b) present the dimensionless drop velocity (multiplied by $Fr^{1/2}$), $\bar{u}$, and dimensionless width, $\bar{D}_W$, respectively, as a function of dimensionless time (divided by $Fr^{1/2}$), $\bar{t}$, for $Wi_c = 4$ and different values of Fr, η_r, and Bo. The obtained results closely resemble those observed for Newtonian surroundings in Fig. 5.31. Specifically, an increase in Fr leads to higher drop impact velocity and larger width, while an increase in η_r results in a smoother collision and reduced drop impact velocity. Furthermore, increasing Bo facilitates the drop and top layer deformation, resulting in a more pronounced drop rebound.

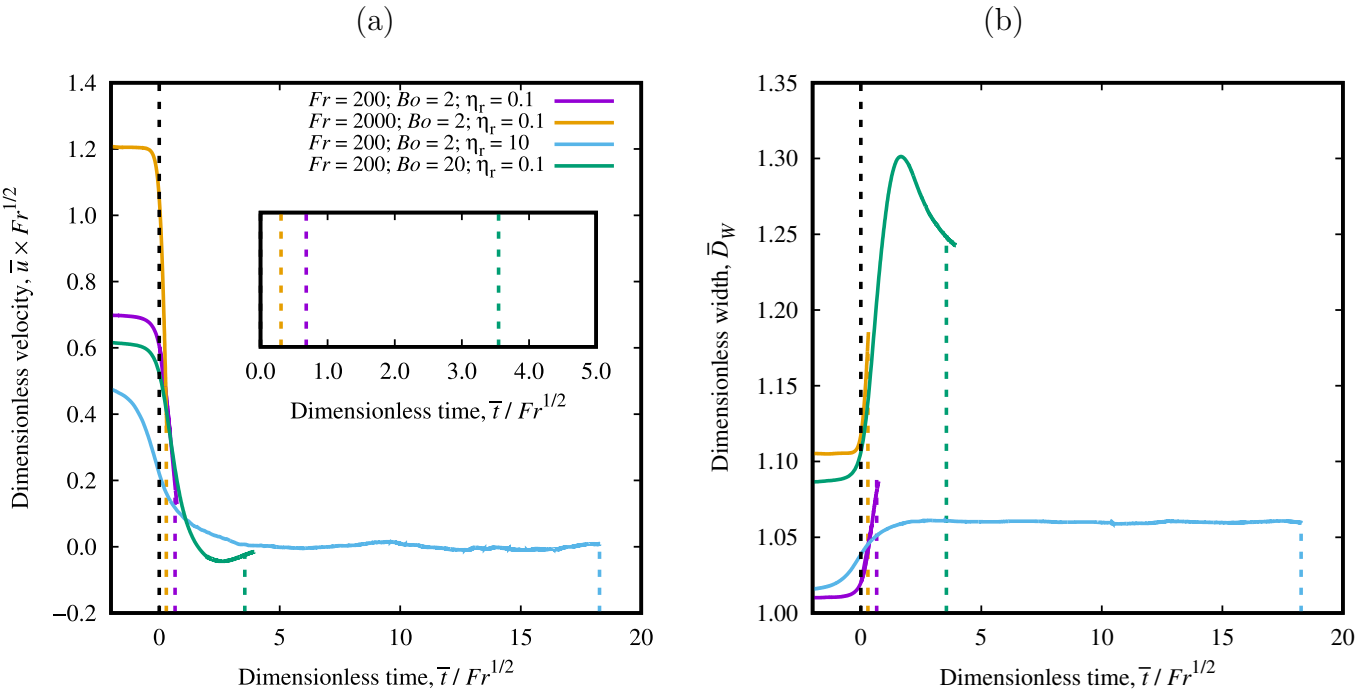

Figure 5.46: Drop (a) dimensionless velocity, $\bar{u}$ ($\times Fr^{1/2}$) and (b) dimensionless width, $\bar{D}_{tW}$, versus dimensionless time, $\bar{t}$ ($/Fr^{1/2}$) for $Wi_c = 4$ and different values of Fr, η_r, and Bo.

A slight deviation from the Newtonian scenario is also perceptible in the shape of the films, as shown in Fig. 5.47. The dimensionless parameters are the same as in Fig. 5.33 for Newtonian surroundings, except for $Wi_c = 4$. In the case of higher viscosity, a slight decrease in the film dimpling is observed. For the lower viscosity ratio cases, elastic effects appear to have a weak contribution to the dimpling of the films. The yellow line corresponding to $Fr = 2000$ indicates an increase in the size of the film dimple compared to the Newtonian counterpart in Fig. 5.33. For the base scenario (purple line), the film becomes slightly dimpled, while for the higher Bond number case (green line), the film is still spherical, but it exhibits a tendency toward a wimpled shape (the film shape at the periphery is flatter, or

less curved) compared with its counterpart in Fig. 5.33.

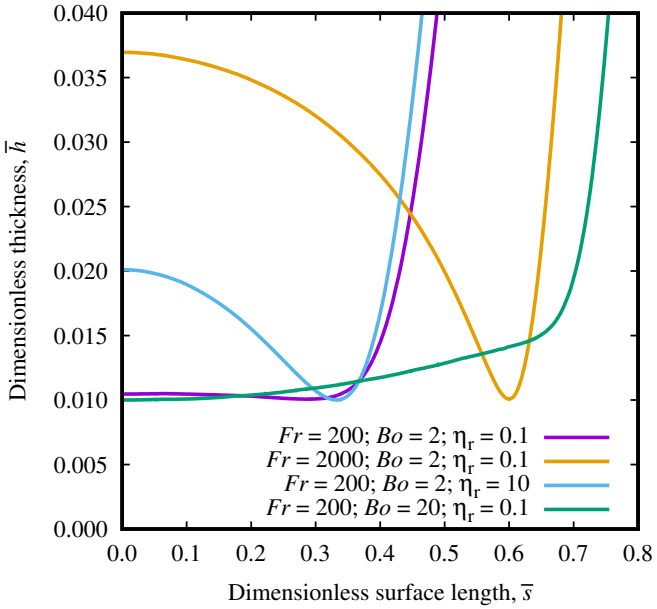

Figure 5.47: Film dimensionless thickness, $\bar{h}$, versus dimensionless surface length, $\bar{s}$, at $\bar{h}_{min} = 0.01$, for different values of Fr, η_r, and Bo, and $Wi_c = 4$.

5.3.3.2 The effect of elasticity on $\Delta\bar{t}$ in viscoelastic materials

This section begins by examining the influence of the parameters Fr, η_r, and Bo, derived from the Newtonian analysis, on the computational drainage time for viscoelastic surroundings. Subsequently, the focus of the discussion shifts to the effect of Wi_c on Δt. Figure 5.48 depicts the dimensionless computational drainage time, $\Delta\bar{t}$ (divided by $Fr^{1/2}$), as a function of Wi_c for different values of Fr, η_r, and Bo. Consistent with the previous analyses conducted for Newtonian and inelastic viscoplastic surroundings, an increase in the Froude number (indicated by the comparison between the yellow to the purple line for $Fr = 2000$ and $Fr = 200$, respectively) leads to a reduction in $\Delta\bar{t}$ due to the decrease in viscous forces relative to inertial forces. Furthermore, an increase in the viscosity ratio (represented by the comparison between the blue to the purple line for $\eta_r = 10$ and $\eta_r = 0.1$, respectively) results in a longer drainage time as the fluid interface approaches the immobile condition. Lastly, a higher Bond number (illustrated by the comparison between the green and purple lines for $Bo = 20$ and $Bo = 2$, respectively) leads to the formation of a longer film, which in turn leads to prolonged drainage times.

In the drainage stage, similar to the rise stage, the deviation from the Newtonian case

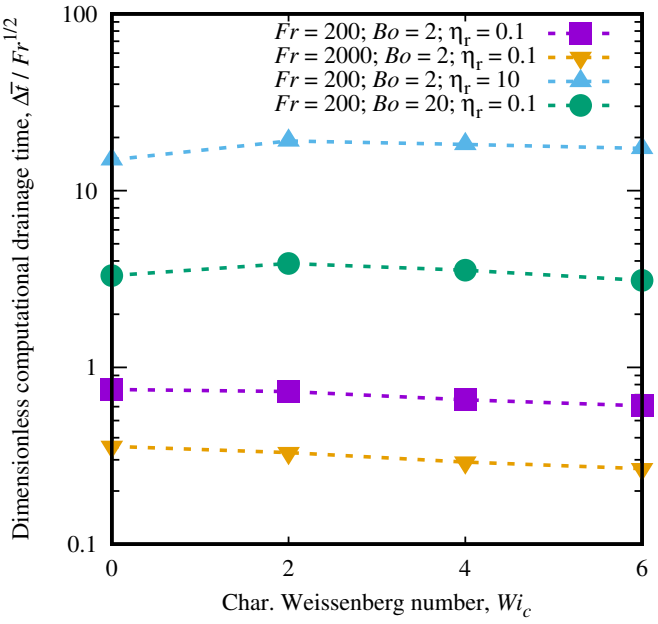

Figure 5.48: Dimensionless computational drainage time, $\Delta\bar{t}$ $(/Fr^{1/2})$, versus the characteristic Weissenberg number, Wi_c.

with respect to Wi_c is relatively mild. Interestingly, an initial increase in the surrounding's elasticity (increasing Wi_c from 0 to 2) resulted in an increase in the computational drainage time for the cases with higher viscosity ratio (blue line) and Bond number (green line). Additional simulations (not shown) for the base (purple line) and the higher Froude number (yellow line) scenarios also revealed a slight increase in Δt for $Wi_c = 1$ compared to the Newtonian case. However, for higher values of Wi_c, $\Delta\bar{t}$ decreases as Wi_c increases. Drop collision and film drainage in viscoelastic materials are complex and highly non-linear processes. The film drainage is influenced by the film shape and by the development of elastic stresses, which also influenced the drop rise dynamics (Sec. 5.2.3). To illustrate this, Fig. 5.49 exhibits $\Delta\bar{t}(/Fr^{1/2})$ (red line with filled circles) and the Deborah number (blue line with open circles) as a function of Wi_c. Here, De is defined for the coalescence process as $De = \lambda/\Delta t$ (Δt is taken as the time of observation and the slope of the line is $1/\Delta\bar{t}$). The value of the Bond number is $Bo = 0.2$, so the drops have a spherical shape. The other dimensionless parameters employed are $Fr = 200$ and $\eta_r = 0.1$. An initial increase in $\Delta\bar{t}$ is observed when Wi_c increases from 0 to 1, followed by a subsequent decrease in the computational drainage time as Wi_c further increases. Notably, the transition in the behavior of $\Delta\bar{t}$ occurs within the range of Wi_c between 1 and 2, which corresponds to De ranging from 0.32 to 0.67. Similar to the rise stage, the transition in the drainage stage also occurred for $De \sim 0.5$. Therefore,

for small values of Wi_c ($De \lesssim 0.5$), the development of elastic stresses results in an increase in $\Delta\bar{t}$.

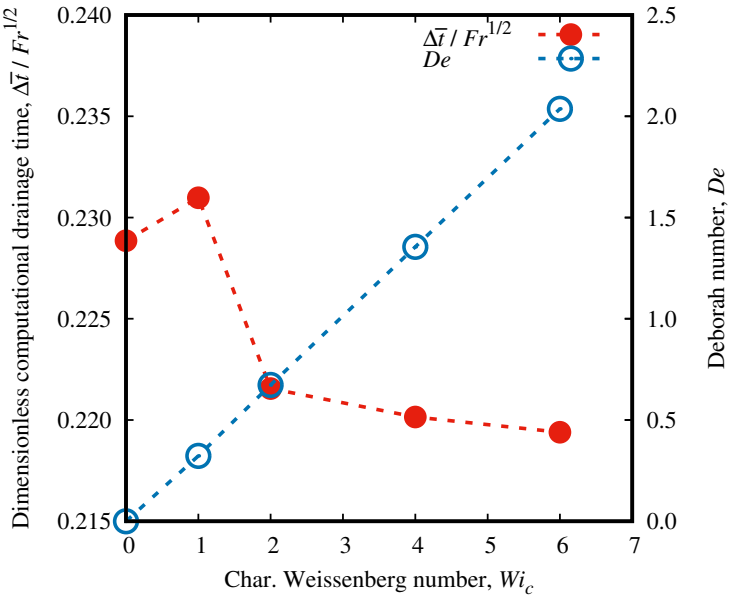

Figure 5.49: Dimensionless computational drainage time, $\Delta\bar{t}/Fr^{1/2}$ (red line with closed circles), and temporal ratio, $\Delta t/\lambda$ (blue line with open circles), versus the characteristic Weissenberg number, Wi_c. The other dimensionless numbers are $Fr = 200$, $\eta_r = 0.1$, and $Bo = 0.2$.

For lower surface tension regimes (*i.e.*, $Bo = 2$ and 20), these effects are counteracted by the reduction in film length. Figure 5.50 presents the film shape at $\bar{h}_{min} = 0.01$ for the base scenario ($Fr = 200$, $\eta_r = 0.1$, and $Bo = 2$) and different values of Wi_c. The graph shows that the film length decreases with an increase in Wi_c. This reduction in film length is caused by the elastic stresses that decrease the drop width during the rise stage, as discussed in Sec. 5.2.3. A slight dimpling effect is also observed for the viscoelastic cases. However, the dimpling does not appear to increase with Wi_c, most likely due to the width reduction effect, which increases the curvature of the drop surface in the film region. This, in turn, increases the surface tension force that resists the dimpling effect. The maximum difference in film thickness between the film center and film periphery in Fig. 5.50 is only about 4%. For sufficiently small values of Wi_c, the reduction in film length is not substantial, and elastic stresses lead to an increase in $\Delta\bar{t}$. For higher values of Wi_c, the film length reduction gains significance, leading to a reduction in the computational drainage time. In the case of the higher Bond number ($Bo = 20$), the film drainage takes longer, and the elastic stresses that slow down the drainage process have more time to develop and counterbalance the drop width

reduction with increasing Wi_c. As a result, the drainage time for $Wi_c = 2$ and 4 is longer than that for $Wi_c = 0$. Only for $Wi_c = 6$ does the draining time become shorter. Lastly, for the higher viscosity ratio, the boundary condition on the drop surface alters the stress field compared to the case with lower viscosity ratio, mitigating the drop width reduction effect observed in the latter case.

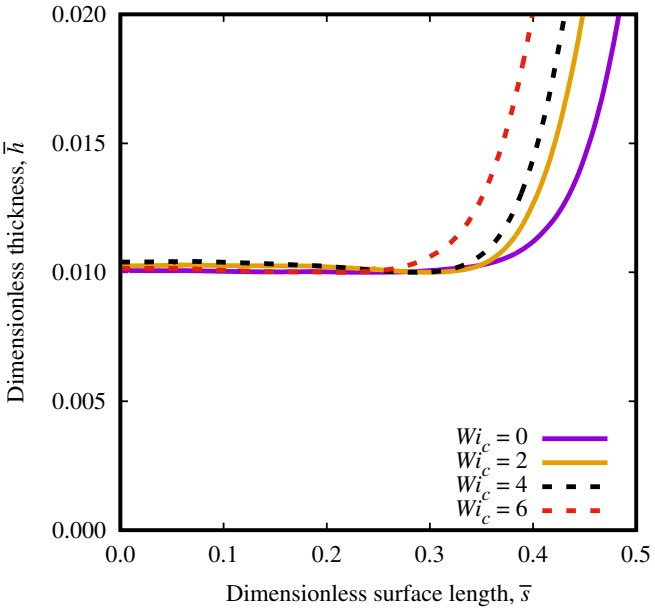

Figure 5.50: Film dimensionless thickness, $\bar{h}$, versus dimensionless surface length, $\bar{s}$, at $\bar{h}_{min} = 0.01$, for $Fr = 200$, $\eta_r = 0.1$, $Bo = 2$, and different values of Wi_c.

The obtained results suggest that the significantly increased difficulty in separating an oil-water mixture after polymer flooding in oilfields (Zheng et al., 2011; Wang et al., 2020) may be attributed to a combination of factors, as described below. Firstly, as demonstrated in Fig. 5.48, the introduction of a low level of elasticity ($Wi_c \sim 1$) leads to a relatively modest increase in the drainage time. Secondly, the addition of polymers also increases the viscosity of the surrounding medium, which has a similar effect of reducing the Froude number in the current study. Thirdly, polymer molecules may act as surfactants, rendering the interfaces immobile or even suppressing the attractive van der Waals forces during the film rupture process. As discussed in Sec. 5.3.1, an increase in the drop viscosity also reduces interface mobility, an effect similar to that of surfactants in this regard. To elucidate the combined influence of these factors, consider, for example, the rise and interfacial coalescence of a drop for the case of $Fr = 2000$, $\eta_r = 0.1$, $Bo = 2$, and $Wi_c = 0$, mimicking the behavior of an oil drop rising in pure water. Suppose a small amount of polymer molecules is added to the

water, leading to a new set of dimensionless parameters represented by $Fr = 200$, $\eta_r = 10$, $Bo = 2$, and $Wi_c = 2$. In this hypothetical scenario, Fig. 5.48 predicts a remarkable increase of approximately 50-fold in $\Delta\bar{t}$, illustrating the dramatic impact of the polymer addition. The findings of this study indicate that the challenges associated with separating these mixtures can be primarily attributed to the surfactant properties of the polymer molecules. These properties render the drop interface immobile and hinder film rupture through chemical interactions. Additionally, the viscosity enhancement of the surrounding materials plays a significant role, with the contribution of elastic stresses being relatively minor in comparison.

5.3.4 Drop collision and $\Delta\bar{t}$ in elasto-viscoplastic materials

This section examines the initiation of drop interfacial coalescence for surroundings that present both plastic and elastic behaviors. The influence of the surrounding rheological parameters on drop collision dynamics and computational drainage time is discussed in Secs. 5.3.4.2 and 5.3.4.2, respectively.

5.3.4.1 Drop collision in elasto-viscoplastic materials

This section presents the results of drop collision in elasto-viscoplastic materials and begins by examining the changes in drop velocity and width during the interfacial collision. Figures 5.51(a) and (b) showcases the drop dimensionless velocity, $\bar{u}(\times Fr^{1/2})$, and width, $\bar{D}_W$, respectively, as a function of dimensionless time, $\bar{t}(/Fr^{1/2})$, during interfacial collision for different values of Wi_c with fixed parameters $Pl = 0.04$, $Bo = 20$, $Fr = 200$, and $\eta_r = 0.1$. The figures illustrate the influence of elasticity on drop collision for yield stress surroundings. As shown in Fig. 5.51(a), the drop velocity increases and its width decreases as it approaches the interface, similar to the behavior observed for inelastic viscoplastic materials. However, this trend is attenuated with an increase in Wi_c. As discussed in Sec. 5.2.4, elastic effects tend to mitigate plastic effects by reducing the contribution of the viscoplastic element undergoing deformation, γ_v. The reduction in drop width prior to the collision ($t = 0$) is also suppressed by an increase in Wi_c. For instance, as depicted in Fig. 5.51(b), the drop width is smaller for $Wi_c = 0$ compared to $Wi_c = 2$ for most part of the collision, despite the opposite trend observed during the steady-state rise phase.

Figures 5.52(a) and (b) display the corresponding results for different values of Pl and fixed $Wi_c = 4$, showcasing the influence of plasticity in an elastic surrounding. Figure 5.52(a) demonstrates that the drop impact velocities are similar for all values of Pl, differently from the inelastic viscoplastic case (see Fig. 5.34), where a significant decrease in $\bar{u}$ is observed with increasing Pl. This similarity in impact velocities can be attributed to the suppression

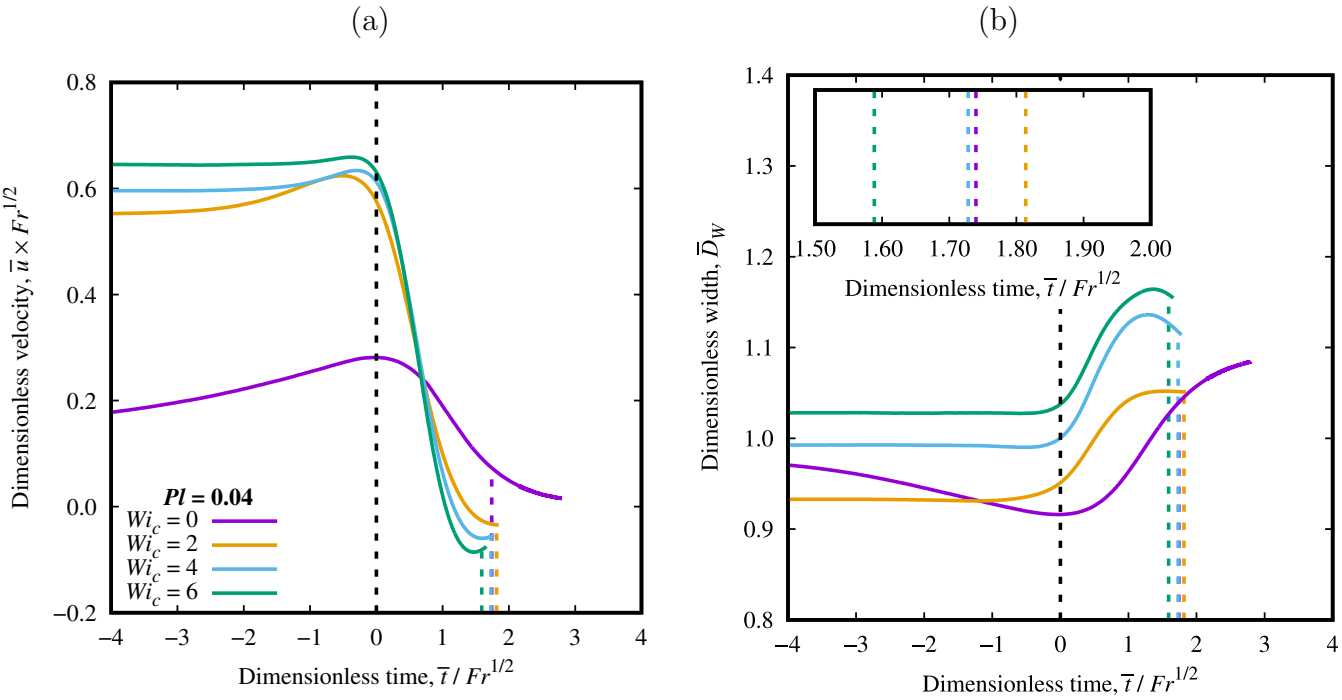

Figure 5.51: Drop (a) dimensionless velocity, $\bar{u}$ ($\times Fr^{1/2}$), and (b) dimensionless width, $\bar{D}_{tW}$, versus dimensionless time, $\bar{t}$ ($/Fr^{1/2}$), for $Pl = 0.04$ and different values of Wi_c. The other dimensionless parameters are $Fr = 200$, $Bo = 20$, and $\eta_r = 0.1$.

of plastic effects by the elasticity of the material, along with the reduction in drop width with increasing values of both Pl and Wi_c, as depicted in Fig. 5.52(b).

Figure 5.53 and 5.54 showcase the drop and interface shapes at $\bar{h}_{min} = 0.10$, 0.05, and 0.01, also for $Fr = 200$, $\eta_r = 0.1$, $Bo = 20$. In the former, the plastic number is fixed at 0.04 and the characteristic Weissenberg number varied, while in the latter, the characteristic Weissenberg number is fixed at 4 and the plastic number varied. Figure 5.53 demonstrates that the film length exhibits a progressive increase as Wi_c increases. This observed behavior can be attributed to the partial activation of the surrounding material's viscosity, which is enhanced for plastic materials, in conjunction with the suppression of plastic effects. These factors result in a greater impact velocity and width of the drop, consequently leading to an elongated film. In contrast, Fig. 5.54 reveals a progressive decrease in film length as Pl increases. Given that the drops experience approximately the same impact velocity, the reduction in width is attributed to the combined influences of plasticity and elasticity, rather than a decrease in inertial effects.

To investigate the influence of Fr and Bo in elasto-viscoplastic surroundings, Fig. 5.55(a) and (b) present the dimensionless drop velocity (multiplied by $Fr^{1/2}$), $\bar{u}$, and the dimensionless width, $\bar{D}_W$, respectively. These quantities are plotted as functions of dimensionless time

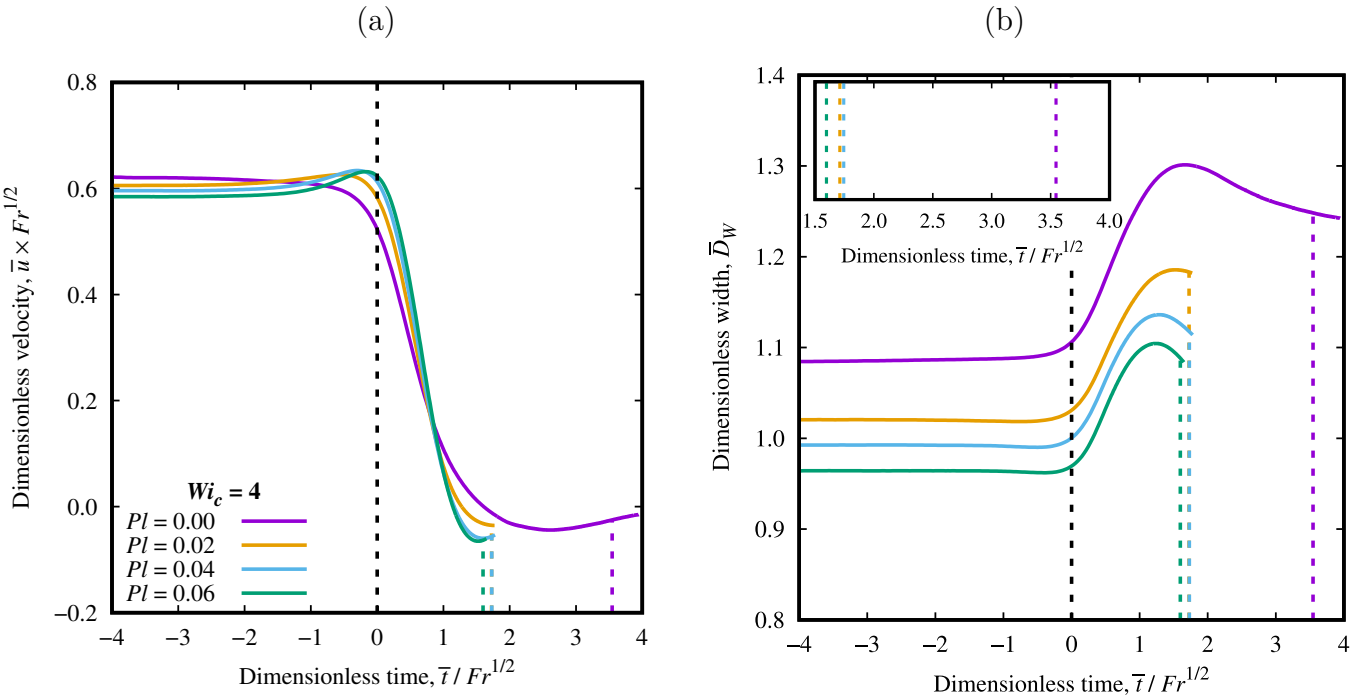

Figure 5.52: Drop (a) dimensionless velocity, $\bar{u}$ ($\times Fr^{1/2}$), and (b) dimensionless width, $\bar{D}_{tW}$, versus dimensionless time, $\bar{t}$ ($/Fr^{1/2}$), for $Wi_c = 4$ and different values of Pl. The other dimensionless parameters are $Fr = 200$, $Bo = 20$, and $\eta_r = 0.1$.

(divided by $Fr^{1/2}$), $\bar{t}$, for fixed values of $Wi_c = 4$ and $Pl = 0.04$, and for varying values of Fr and Bo. Consistent with expectations, the drop impact velocity and width increase with an increase in Fr. Notably, the changes in drop velocity and shape are more pronounced for $Bo = 20$ compared to $Bo = 2$. Prior to the collision, the drops for $Bo = 2$ and 20 have similar widths. However, due to the larger deformability and conversion of kinetic energy to surface energy, the drop for $Bo = 20$ becomes significantly wider, resulting in a longer film compared to the latter. Furthermore, Fig. 5.56 presents the film shape in the (s, h) coordinate system at $\bar{h}_{min} = 0.01$ for the same parameters as in Fig. 5.55. The observed film shape exhibits characteristics intermediate to those observed in inelastic viscoplastic and viscoelastic surroundings. Similar to the inelastic case, plastic effects reduce film dimpling and length, but the films remain slightly longer due to the elasticity of the material. Notably, the film for $Fr = 2000$ displays some dimpling, albeit to a lesser extent than the viscoelastic and Newtonian cases. For lower Froude number cases, the films exhibit a more spherical shape compared to the viscoelastic and Newtonian cases.

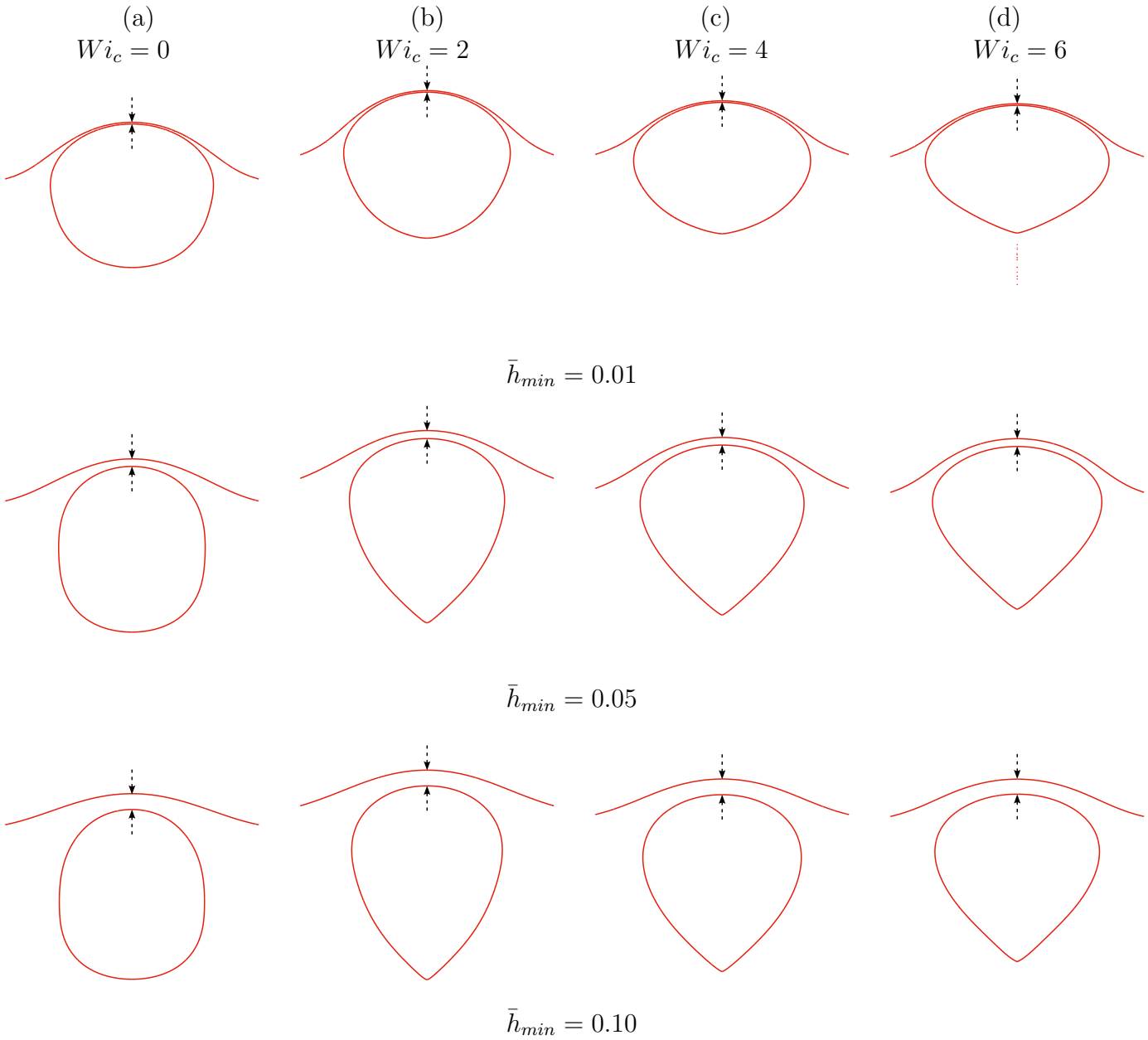

Figure 5.53: Drop and top layer interface shape for $\bar{h}_{min} = 0.10$ (third row), $\bar{h}_{min} = 0.05$ (second row), and $\bar{h}_{min} = 0.01$ (first row) for $Fr = 200, Bo = 20$, $\eta_r = 0.1$, and $Pl = 0.04$. The Weissenberg number is equal to $Wi_c = 0$ (a), 2 (b), 4 (c), and 6 (d). The film's thinnest part is marked by a pair of black arrows.

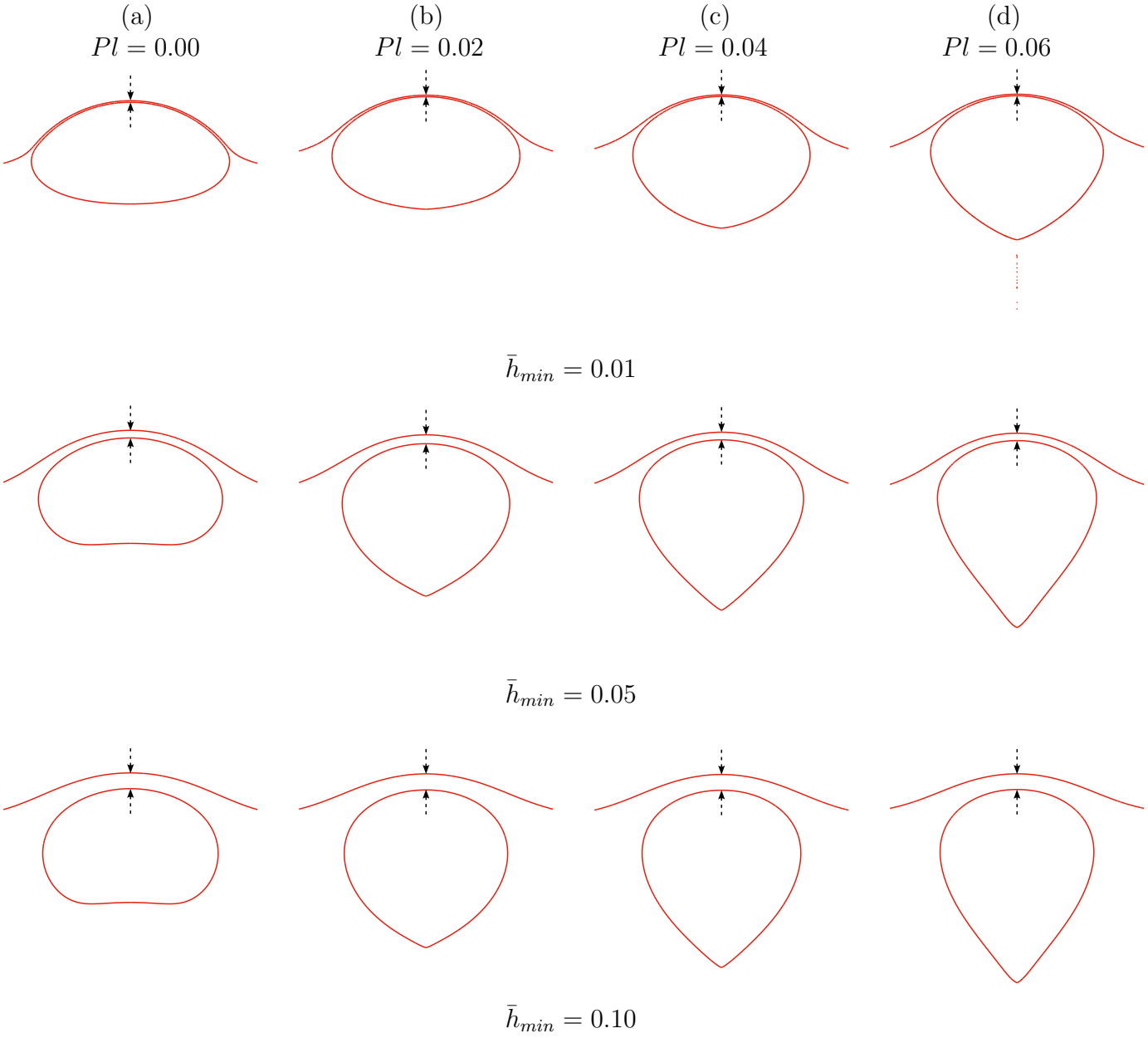

Figure 5.54: Drop and top layer interface shape for $\bar{h}_{min} = 0.10$ (third row), $\bar{h}_{min} = 0.05$ (second row), and $\bar{h}_{min} = 0.01$ (first row) for $Fr = 200, Bo = 20$, $\eta_r = 0.1$, and $Wi_c = 4$. The plastic number is equal to $Pl = 0.00$ (a), 0.02 (b), 0.04 (c), and 0.06 (d). The film's thinnest part is marked by a pair of black arrows.

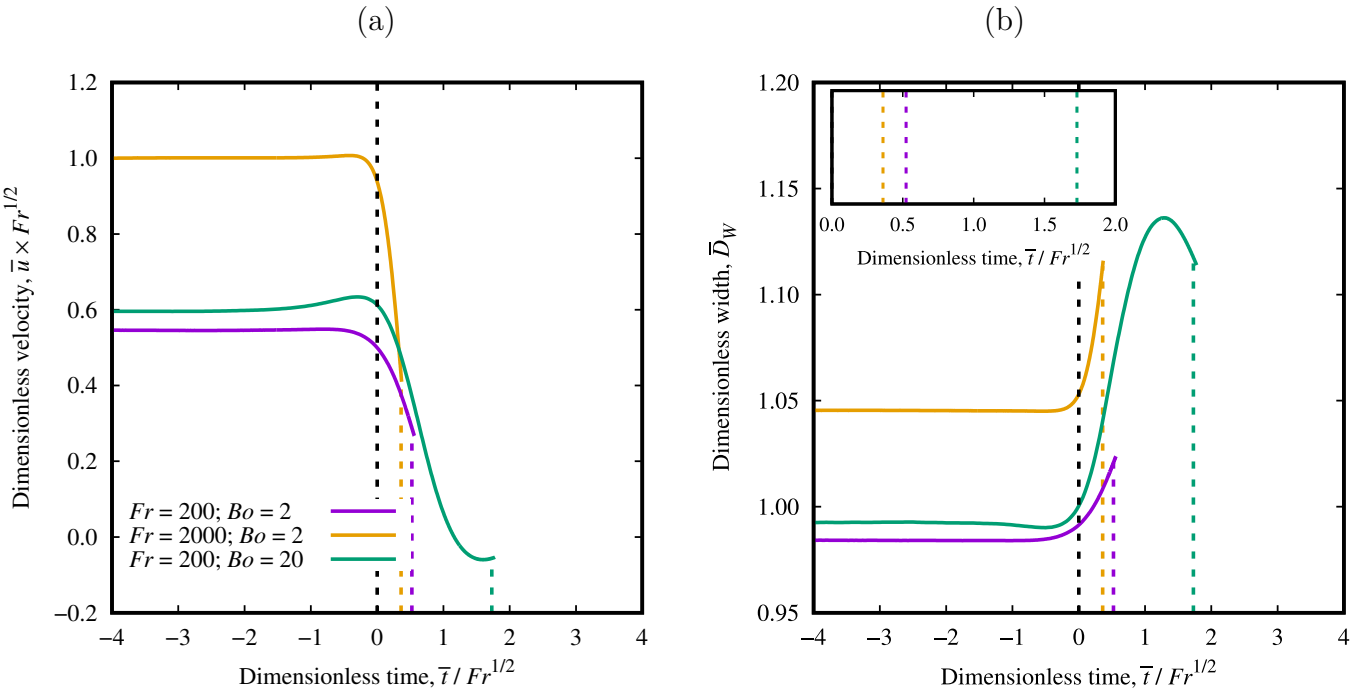

Figure 5.55: Drop (a) dimensionless velocity, $\bar{u}$ ($\times Fr^{1/2}$) and (b) dimensionless width, $\bar{D}_{tW}$, versus dimensionless time, $\bar{t}$ ($/Fr^{1/2}$). The dimensionless parameters are $Wi = 3$, $Pl = 0.04$, $\eta_r = 0.1$, $Fr = 200$ and 200, and $Bo = 2$ and 20.

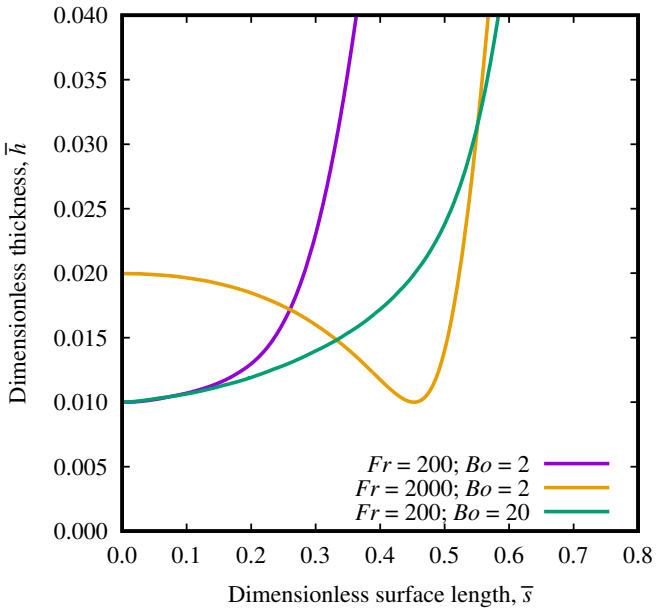

Figure 5.56: Film dimensionless thickness, $\bar{h}$, versus dimensionless surface length, $\bar{s}$, at $\bar{h}_{min} = 0.01$, for $Wi_c = 4$, $Pl = 0.04$, and $\eta_r = 0.1$, $Fr = 200$ and 2000, and $Bo = 2$ and 20.

5.3.4.2 The effect of elasticity and plasticity on $\Delta\bar{t}$ in elasto-viscoplastic materials

In this section, the interplay between elasticity and plasticity in relation to Δt is analyzed. As discussed in Sec. 5.3.3, the process of film drainage is characterized by dynamic and complex phenomena that arise from the intricate interplay of various forces. Figures 5.57(a) and (b) present the dimensionless computational drainage time (divided by $Fr^{1/2}$), $\Delta\bar{t}$, as a function of Wi_c and Pl, respectively. The overall effects of Fr and Bo align with previous analyses conducted on other types of material surroundings. In general, an increase in Fr leads to a decrease in the computational drainage time, primarily attributed to the reduction in viscous resistive forces. Conversely, an increase in Bo tends to elongate the film and consequently prolong the computational drainage time.

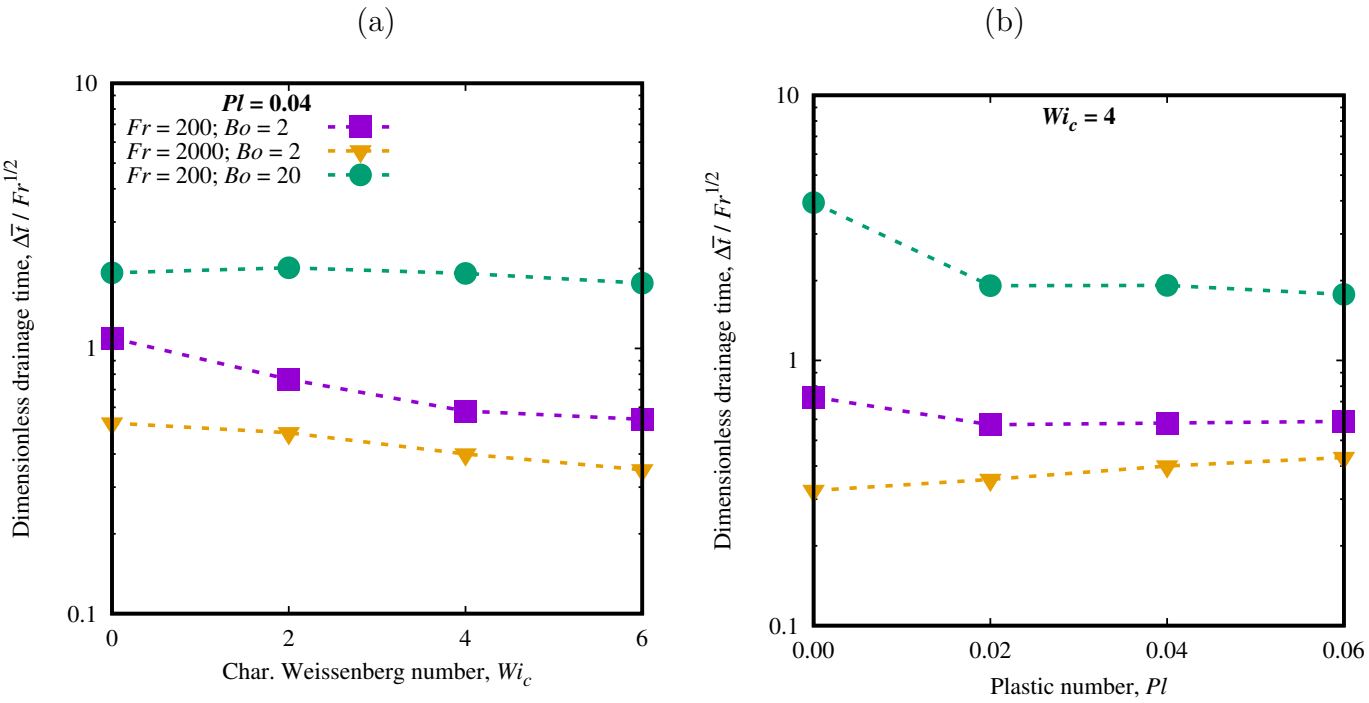

Figure 5.57: Dimensionless computational drainage time, $\Delta\bar{t}$ ($/Fr^{1/2}$), versus (a) the characteristic Weissenberg number, Wi_c, and (b) the plastic number, Pl.

Regarding the influence of Wi_c in a plastic medium, Fig. 5.57(a) demonstrates $\Delta\bar{t}$ exhibits a monotonic decrease with increasing Wi_c for the base scenario (indicated by the purple line with squares). This reduction in $\Delta\bar{t}$ is more pronounced compared to the viscoelastic case. As discussed in Sec. 5.2.4, the presence of a yield stress amplifies the effects of elasticity, resulting in a slower buildup of elastic stresses and partial activation of the material's viscosity. As a result, $\Delta\bar{t}$ decreases with increasing Wi_c despite the longer film, as shown in Fig 5.58(a).

The plot displays the film shape at $\bar{h}_{min} = 0.01$ for different values of Wi_c and the base scenario in Fig. 5.57(a). Notably, the films for $Wi_c = 0$ and 2 exhibit a close resemblance, while the films for $Wi_c = 4$ and 6 are longer. As discussed in the previous section, the width of the rising drop for $Wi_c = 0$ is greater than that for $Wi_c = 2$. However, during most of the collision stage, this trend is reversed due to the influence of plastic effects. Ultimately, as $\bar{h}_{min}$ approaches 0.01, the films for $Wi_c = 0$ and 2 converge towards each other. In the case of the higher Froude number scenario (indicated by the yellow line with inverted triangles), a similar behavior to the lower Froude number case is observed. For the higher Bond number scenario (depicted by the green line with circles), a slight increase in $\Delta\bar{t}$ is observed when Wi_c is increased from 0 to 2. Subsequently, with further increases in Wi_c, the computational drainage time experiences a slight decrease. In this particular scenario, the greater film length leads to an increase in the film drainage process, allowing more time for the development of elastic stresses. As a result, the interplay between film geometry and partial viscosity activation becomes more balanced. Initially, the increase in $\Delta\bar{t}$ can be attributed to the longer film. However, as Wi_c continues to increase and the material's viscosity is only partially activated, $\Delta\bar{t}$ decreases.

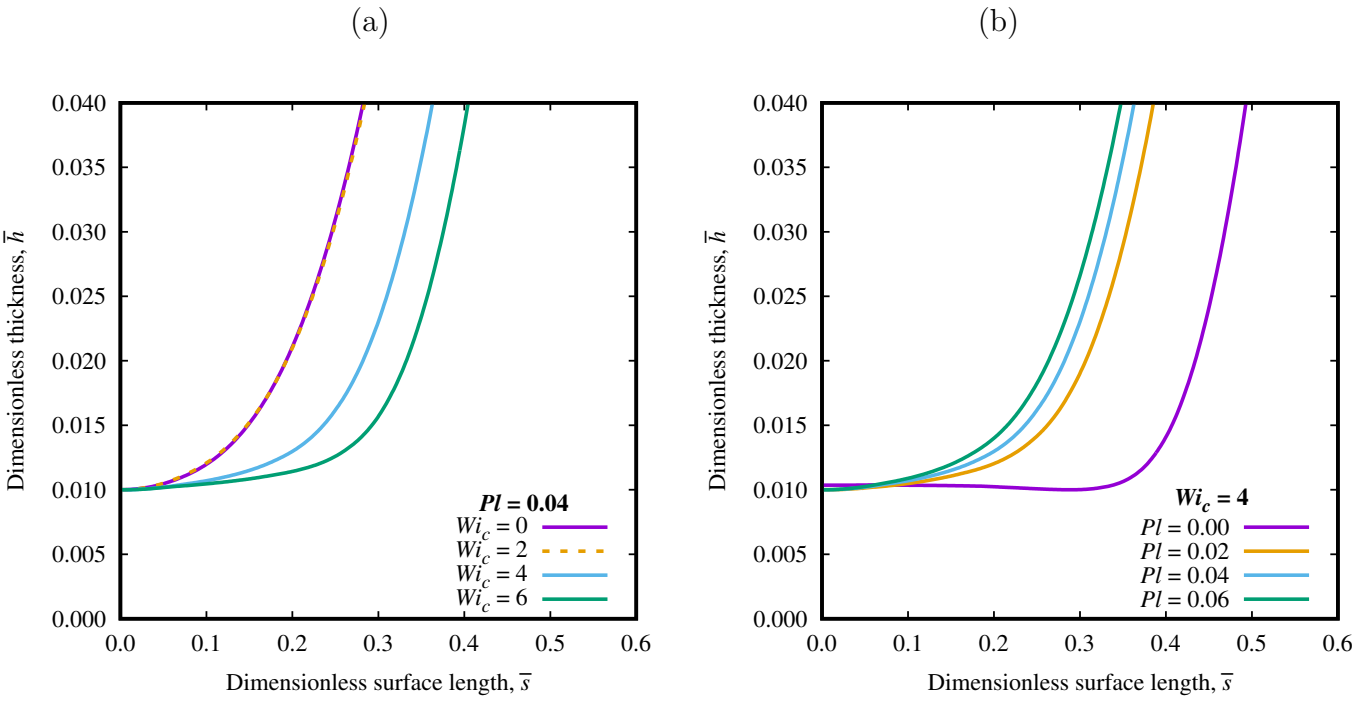

Figure 5.58: Film dimensionless thickness, $\bar{h}$, versus dimensionless surface length, $\bar{s}$, at $\bar{h}_{min} = 0.01$, for $Fr = 200$, $\eta_r = 0.1$, $Bo = 2$, and different values of Wi_c (a) and Pl (b).

An interesting behavior is also observed in the analysis of the influence of Pl in an elastic surrounding. Figure 5.57(b) reveals that for the lower Froude number cases (purple and green

lines), there is an initial decrease in $\Delta\bar{t}$ as Pl increases from 0.00 to 0.02. This behavior can be attributed to a substantial reduction in the drop width and, consequently, the film length, as depicted in Fig. 5.58(b). Moreover, films with $Pl \geq 2$ exhibit a more spherical shape compared to the film with $Pl = 0$, thereby facilitating the drainage process. Due to the suppression of plastic effects by the elasticity of the material, the impact velocity and width decrease are less substantial with increasing Pl compared to the inelastic viscoplastic scenario. Consequently, the film shapes for $Wi_c = 2$, 4, and 6 are similar. Thus, for $Pl \geq 2$, a slight increase in $\Delta\bar{t}$ is observed with an increase in Pl due to the augmentation of the forces that resist the film flow. In contrast, for the higher Froude number case, a monotonic increase in the computational drainage time with respect to Pl is observed. As discussed in Sec. 5.2.4, the elastic number, El, increases with an increase in Fr, which leads to a reduction in the influence of elastic effects compared to inertial effects. Consequently, the behavior of the drainage time differs for the higher Froude number case.

Chapter 6

Concluding Remarks

This thesis investigates the dynamics of Newtonian drop rise and interfacial coalescence initiation in complex materials using direct numerical simulations. The surrounding medium is characterized using progressively sophisticated constitutive material formulations, namely Newtonian, inelastic viscoplastic, viscoelastic, and elasto-viscoplastic. The non-Newtonian formulations are represented by the Bingham, Upper Convected Maxwell, and Saramito models, respectively. Prior to examining the phenomena of drop rise and coalescence, a condition for drop entrapment in inelastic viscoplastic fluids is established. An assessment of how elasticity impacts the entrapment condition is also carried out. The investigation proceeds with the drop at rest, attaining a steady-state rise, and subsequently colliding with a fluid-fluid interface. The investigation focuses on the influence of inertial, viscous, surface tension, plastic, and elastic effects, as well as their interplay, on key parameters such as drop velocity, drop shape, draining film shape, and drainage time. Their impact on the coalescence process is evaluated through the computational drainage time, which captures the initial stage of the film drainage process. Given the substantial computational expense associated with simulating up to the film rupture thickness, the computational drainage time indicates the ease or difficulty of coalescence occurrence.

The entrapment condition is assessed for initially spherical and non-spherical drops in Bingham materials in terms of the critical Yield-stress parameter, Y_{gc}. In the case of a spherical drop, the entrapment condition is observed to be independent of the Bond and Froude numbers, as well as the density ratio. The critical Yield-stress parameter also remains unaffected by variations in the viscosity ratio below a certain threshold ($\eta_r \approx 10$) and subsequently decreases with increasing viscosity ratio, ultimately converging to the asymptotic value of 0.143 for solid particles. For initially non-spherical drops, the role of surface tension force becomes significant in determining the final entrapment condition within the intermediate surface tension regime ($6 \lessapprox Bo \lessapprox 60$). In the low surface tension regime, the surface tension

force does not exert any influence on the final entrapment condition of non-spherical drops. In this regime, the critical plastic number for entrapment increases as the drop aspect ratio increases because of the change in the effective area on which the force exerted by the yield stress acts. Notably, by defining the Yield-stress parameter based on the radius of the maximum cross-sectional area of the drop (normal to buoyancy), Y_{gc} demonstrates an approximately constant value. In the high surface tension regime, the surface tension force completely yields the surrounding material, causing the drop to rise and approach a spherical shape. As a result of its final spherical configuration, the drop has the same critical plastic number as that of an initially spherical drop. Within the intermediate regime, surface tension can yield the surrounding material to a certain extent, reducing the drop deformation and initiating movement. However, the surface tension effect is insufficient to transform the drop into a perfectly spherical shape, resulting in the drop remaining in a deformed state. In this regime, prolate-shaped drops have a slightly higher critical plastic number than spherical drops, while oblate-shaped drops have a slightly lower critical plastic number than spherical drops. In the low viscous regime, by appropriately defining the Yield-stress parameter based on the radius of the final maximum cross-sectional area of the drop (normal to buoyancy), the entrapment criteria can be expressed as a constant value of the Yield-stress parameter given as $Y_{gc} = 0.20 \pm 0.02$. In case the surrounding yield stress material presents elasticity, the value of the critical Yield-stress parameters increases with the level of elasticity. The elastic nature of the material allows for deformation in the unyielded region, promoting initial drop movement even in cases of spherical entrapped drops.

Drop rise sets the initial condition for drop collision and the subsequent film drainage process. It is observed that an increase in the Froude number leads to an increase in drop terminal velocity and width for all formulations of the surrounding material studied. This behavior arises from the relatively reduced importance of viscous effects compared to inertial effects. Conversely, an increase in the viscosity ratio enhances viscous dissipation, thereby inducing a decrease in drop velocity. An increase in the Bond number facilitates the drop deformation by the dominating distorting forces, whereas a decrease in Bo compels the drop to assume a spherical shape. In the case of Newtonian surroundings, an increase in Bo makes the drop more oblate due to the increased dynamic pressure ahead of the drop. This leads to an increase in the drag coefficient and subsequent reduction in velocity. For inelastic viscoplastic media, plastic effects contribute to the formation of prolate-shaped drops. This can be attributed mainly to the lower viscosity regions near the poles of the drop, in contrast to the higher viscosity region along the drop's equator. Consequently, at higher values of the plastic number, the aspect ratio of the drop exhibits an increase with an augmentation in the Bond number. Drop rise in viscoelastic media is a fascinating, intricate, and dynamic

phenomenon. Elastic effects are found to be relatively mild for the range of parameters investigated (Wi_c from 0 to 6) and no negative wake and teardrop shape are observed. In the scenario of a lower viscosity ratio, the development of the elastic stress field drives a reduction in drop width, consequently contributing to an increase in drop velocity. The amplification of drop width reduction with the Weissenberg number is further intensified by an increase in the Bond number, where a more significant enhancement in velocity is observed with increasing levels of elasticity. In contrast, for the higher viscosity ratio, the change in the interfacial stress on the surface of the drop causes the elastic stress field to deviate from that of the lower viscosity ratio. As a result, the drop width reduction effect is reduced, and the drop velocity is little affected within the range of Wi assessed. Moreover, because of the non-instantaneous (delayed) nature of elastic stresses buildup and relaxation processes, elasticity can lead to the attainment of a higher or lower terminal velocity by the drop. Increasing the Weissenberg number decelerates the buildup and relaxation of elastic stress, while simultaneously increasing the maximum attainable stress magnitude. As a result, the drop initial acceleration increases with an increase in Wi. For high values of the Deborah number, defined upon the characteristic rise time of the drop, elastic stresses have sufficient time to develop, potentially resulting in "over" activation of the material's viscosity, and consequently causing a reduction in drop velocity. However, for low values of the Deborah number, a "partial" viscosity activation of the viscoelastic medium occurs, resulting in an increased drop velocity as the level of elasticity increases. The interaction between plastic and elastic effects in EVP materials yields interesting drop rise dynamics. Plastic and elastic effects are shown to influence each other extent. Specifically, an increase in the plastic number tends to enhance the ratio of elastic to viscous deformation, thereby amplifying elastic effects. This behavior is demonstrated by the emergence of the negative wake and the formation of teardrop-shaped drops as the plastic number increases while keeping the characteristic Weissenberg number (and, consequently, the elastic modulus) constant. In fact, the Weissenberg number, which characterizes the level of elasticity compared to viscous effects, explicitly depends on the plastic number. Therefore, increasing the plastic number contributes to a partial activation of the materials' viscosity and, consequently, to an increase in drop velocity. Conversely, the presence of elastic effects appears to impede the plastic response of the material by enabling the material to deform even in the unyielded state. As a result, a higher level of plasticity is required for the entrapment of drops when the surrounding material presents elastic behavior.

The drainage time, assessed based on the computational drainage time, depends on the film geometry (length and shape), which is influenced by the dynamics of drop rise and collision, as well as the rheological properties of the fluids. An augmentation in the Froude

number intensifies inertial effects, leading to an elongation of the film and contributing to the formation of dimple-shaped. However, the decrease in viscous effects are associated with an increase in Fr overcompensate for the rise in inertial effects, resulting in a decrease in the computational drainage time. Conversely, an increase in the viscosity ratio yields the opposite outcome by augmenting viscous dissipation and diminishing inertial effects. Furthermore, the change in the film boundary condition with an increase in the viscosity ratio contributes to the formation of dimpled films. Consequently, an increase in the viscosity ratio results in longer drainage times. Similar to the rising stage, the influence of the Bond number on the drainage time depends upon the prevailing distorting force. In the case of Newtonian surroundings, where the buoyancy force is predominantly balanced by inertial effects, an increase in Bo leads to an increase in the film length, subsequently causing an increase in Δt. The drop deformation caused by plastic effects tends to facilitate the film drainage process by reducing the film length and promoting the formation of spherical films. Conversely, the changes in the rheological parameters of the surrounding material tend to make the drainage process harder. Hence, the effect of Pl on Δt depends on the surface tension regime. For small values of Bo, where the interfaces are less distorted, the significance of the rheological properties of the phases, in relation to the film geometry, in determining the coalescence time becomes more pronounced. In this regime, an increase in the resistive force resulting from plasticity prolongs the drainage time, exhibiting a positive correlation with Pl. However, in the case of high values of Bo, the influence of the film geometry becomes more critical, and an increase in Pl facilitates the initial stage of the drainage process. The arrest of the film drainage by plastic effects depends on the balance between the film's geometry and the level of plasticity of the surrounding material. Despite the presence of low-stress regions within dimple-shaped films, such film configurations were observed only for low levels of plasticity, wherein the yield stress may not sufficiently hinder the drainage process. An escalation in the level of plasticity alters the film geometry in a manner that impedes its arrest. Consequently, the interplay of these two opposing plastic effects complicates the determination of the film's arresting condition. In the case of viscoelastic surroundings, the impact of elastic effects on the film drainage is relatively small for the range of parameters studied. An initial increase in the Weissenberg number caused an increase in the computational drainage time due to the development of elastic stresses. For higher levels of elasticity, the Deborah number of the coalescence process, defined based on Δt, increases, and the slower development of elastic stresses allows for a faster drainage. Moreover, increasing the level of elasticity also causes the film length to decrease, contributing to a reduction in the drainage time. The interplay between plastic and elastic effects on the film drainage in elasto-viscoplastic materials is complex. It also depends on the interaction with inertial and surface tension effects. For

a plastic surrounding in a high surface tension regime, an increase in the characteristic Weissenberg number facilitates the drainage process owing to the partial activation of the surrounding viscosity. In the case of low surface tension effects, the large variation in drop width and velocity (and consequently inertial effects), makes the drainage time not behave monotonically with an increase in the level of elasticity. For an elastic surrounding and low values of the Froude number (small inertia), the drainage time tends to first decrease with an addition of plasticity, but then to slightly increase as the plasticity of the material increases. The initial decrease is attributed to the significant drop width reduction and the smaller plastic response in an elastic medium. Lastly, an increase in the inertial effect, represented by an increase in the Froude number, reduces the importance of the material elastic response. As a result, the drainage time increases monotonically with an increase in the plastic number for high values of the Froude number.

Some specific future research directions are to investigate i) the particular case of bubbles for smaller minimum film thickness in high surface tension regime (where the low viscosity ratio and bubble shape allows for faster simulations), ii) the film drainage process arresting condition by the yield stress, iii) the drop entrapment condition in elasto-viscoplastic materials, iv) the effect of the rise distance, and v) the inclusion of thixotropic effects. Additionally, the implemented elasto-viscoplastic can be employed to model other flows involving drops and flows with free interfaces in general.

Bibliography

Aarts, D.G., Lekkerkerker, H.N., 2008. Droplet coalescence: drainage, film rupture and neck growth in ultralow interfacial tension systems. Journal of fluid mechanics 606, 275–294.

Abid, S., Chesters, A., 1994. The drainage and rupture of partially-mobile films between colliding drops at constant approach velocity. International journal of multiphase flow 20, 613–629.

Acharya, A., Ulbrecht, J., 1978. Note on the influence of viscoelasticity on the coalescence rate of bubbles and drops. AIChE Journal 24, 348–351.

Albadawi, A., Donoghue, D., Robinson, A., Murray, D., Delauré, Y., 2014. On the assessment of a vof based compressive interface capturing scheme for the analysis of bubble impact on and bounce from a flat horizontal surface. International journal of multiphase flow 65, 82–97.

Allouche, M., Frigaard, I.A., Sona, G., 2000. Static wall layers in the displacement of two visco-plastic fluids in a plane channel. J. Fluid Mech. 424, 243–277.

Astarita, G., Apuzzo, G., 1965. Motion of gas bubbles in non-newtonian liquids. AIChE Journal 11, 815–820.

Balmforth, N.J., Frigaard, I.A., Ovarlez, G., 2014. Yielding to stress: recent developments in viscoplastic fluid mechanics. Annual Review of Fluid Mechanics 46, 121–146.

Barnes, H.A., Hutton, J.F., Walters, K., 1989. An introduction to rheology. volume 3. Elsevier.

Basilisk, . URL: `http://basilisk.fr/`.

Batchelor, G.K., 1967. An introduction to fluid mechanics. Cambridge University Press, Cambridge.

Bell, J.B., Colella, P., Glaz, H.M., 1989. A second-order projection method for the incompressible navier-stokes equations. Journal of computational physics 85, 257–283.

Beris, A., Tsamopoulos, J., Armstrong, R., Brown, R., 1985. Creeping motion of a sphere through a bingham plastic. Journal of Fluid Mechanics 158, 219–244.

Bhaga, D., Weber, M., 1981. Bubbles in viscous liquids: shapes, wakes and velocities. Journal of fluid Mechanics 105, 61–85.

Bingham, E.C., 1922. Fluidity and Plasticity. McGraw-Hill, New York.

Bird, R.B., Armstrong, R.C., Hassager, O., 1987a. Dynamics of Polymeric Liquids. second ed., John Wiley & Sons, New York. Vol. 1.

Bird, R.B., Curtiss, C.F., Armstrong, R.C., Hassager, O., 1987b. Dynamics of polymeric liquids, volume 2: Kinetic theory. Wiley.

Bothe, D., Niethammer, M., Pilz, C., Brenn, G., 2022. On the molecular mechanism behind the bubble rise velocity jump discontinuity in viscoelastic liquids. Journal of Non-Newtonian Fluid Mechanics 302, 104748.

Brackbill, J.U., Kothe, D.B., Zemach, C., 1992. A continuum method for modeling surface tension. Journal of computational physics 100, 335–354.

Brown, T., Lemay, B., Bursten, B., Murphy, K., Woodward, P., 2012. Liquids and intermolecular forces.

Burrill, K., Woods, D., 1973. Film shapes for deformable drops at liquid-liquid interfaces. ii. the mechanisms of film drainage. Journal of Colloid and Interface Science 42, 15–34.

Bush, J.W.M., 2013. Interfacial phenomena. Lecture Notes.

Cano-Lozano, J.C., Martinez-Bazan, C., Magnaudet, J., Tchoufag, J., 2016a. Paths and wakes of deformable nearly spheroidal rising bubbles close to the transition to path instability. Physical Review Fluids 1, 053604.

Cano-Lozano, J.C., Tchoufag, J., Magnaudet, J., Martínez-Bazán, C., 2016b. A global stability approach to wake and path instabilities of nearly oblate spheroidal rising bubbles. Physics of Fluids 28, 014102.

Chan, D.Y., Klaseboer, E., Manica, R., 2011. Film drainage and coalescence between deformable drops and bubbles. Soft Matter 7, 2235–2264.

Chandran Suja, V., Kannan, A., Kubicka, B., Hadidi, A., Fuller, G., 2020. Bubble coalescence at wormlike micellar solution–air interfaces. Langmuir 36, 11836–11844.

Charin, A.H., Lage, P.L., Silva, L.F.L., Tuković, Ž., Jasak, H., 2019. On the dynamic behavior of rising droplets. International Journal of Multiphase Flow 110, 165–178.

Chatzigiannakis, E., Jaensson, N., Vermant, J., 2021. Thin liquid films: Where hydrodynamics, capillarity, surface stresses and intermolecular forces meet. Current Opinion in Colloid & Interface Science 53, 101441.

Chatzigiannakis, E., Vermant, J., 2021. Dynamic stabilisation during the drainage of thin film polymer solutions. Soft Matter 17, 4790–4803.

Chesters, A., 1991. Modelling of coalescence processes in fluid-liquid dispersions: a review of current understanding. Chemical engineering research and design 69, 259–270.

Chi, B., Leal, L., 1989. A theoretical study of the motion of a viscous drop toward a fluid interface at low Reynolds number. Journal of Fluid Mechanics 201, 123–146.

Chirco, L., Maarek, J., Popinet, S., Zaleski, S., 2022. Manifold death: a volume of fluid implementation of controlled topological changes in thin sheets by the signature method. Journal of Computational Physics 467, 111468.

Clift, R., Grace, J., Weber, M., Bubbles, D., 1978. Particles.

Czarnecki, J., Tchoukov, P., Dabros, T., Xu, Z., 2013. Role of asphaltenes in stabilisation of water in crude oil emulsions. The Canadian Journal of Chemical Engineering 91, 1365–1371.

De Malmazet, E., Risso, F., Masbernat, O., Pauchard, V., 2015. Coalescence of contaminated water drops at an oil/water interface: Influence of micro-particles. Colloids and Surfaces A: Physicochemical and Engineering Aspects 482, 514–528.

Dealy, J.M., 2010. Weissenberg and deborah numbers—their definition and use. Rheology Bulletin 79.

Deka, H., Pierson, J.L., Soares, E.J., 2019. Retraction of a viscoplastic liquid sheet. Journal of Non-Newtonian Fluid Mechanics 272, 104172.

Deka, H., Pierson, J.L., Soares, E.J., 2020. Retraction criteria of viscoplastic drops and sheets: Long-wave approximations. Journal of Non-Newtonian Fluid Mechanics 284, 104352.

Deoclecio, L.H.P., da Cunha Ribeiro, D., Meneguelo, A.P., 2020. Cfd modeling of the creaming zone of batch gravity separation with coalescence. Journal of Dispersion Science and Technology 41, 674–689. doi:10.1080/01932691.2019.1611436.

Dimakopoulos, Y., Pavlidis, M., Tsamopoulos, J., 2013. Steady bubble rise in herschel–bulkley fluids and comparison of predictions via the augmented lagrangian method with those via the papanastasiou model. Journal of Non-Newtonian Fluid Mechanics 200, 34–51.

Duarte, A., Miranda, A.I., Oliveira, P.J., 2008. Numerical and analytical modeling of unsteady viscoelastic flows: The start-up and pulsating test case problems. Journal of non-newtonian fluid mechanics 154, 153–169.

Dubash, N., Frigaard, I., 2004. Conditions for static bubbles in viscoplastic fluids. Physics of fluids 16, 4319–4330.

Dubash, N., Frigaard, I., 2007. Propagation and stopping of air bubbles in carbopol solutions. Journal of non-newtonian fluid mechanics 142, 123–134.

Engquist, B., Tornberg, A.K., Tsai, R., 2005. Discretization of dirac delta functions in level set methods. Journal of Computational Physics 207, 28–51.

Faroughi, S., Fernandes, C., Nóbrega, J.M., McKinley, G., 2020. A closure model for the drag coefficient of a sphere translating in a viscoelastic fluid. Journal of Non-Newtonian Fluid Mechanics 277, 104218.

Fortuna, A.d.O., 2012. Técnicas Computacionais para Dinâmica dos Fluidos.

Fox, R.W., McDonald, A.T., 1998. Introduction to Fluid Mechanics. Fifth ed., J. Wiley and Sons, New York.

Fraggedakis, D., Dimakopoulos, Y., Tsamopoulos, J., 2016a. Yielding the yield-stress analysis: a study focused on the effects of elasticity on the settling of a single spherical particle in simple yield-stress fluids. Soft matter 12, 5378–5401.

Fraggedakis, D., Dimakopoulos, Y., Tsamopoulos, J., 2016b. Yielding the yield stress analysis: A thorough comparison of recently proposed elasto-visco-plastic (evp) fluid models. Journal of Non-Newtonian Fluid Mechanics 236, 104–122.

Fraggedakis, D., Pavlidis, M., Dimakopoulos, Y., Tsamopoulos, J., 2016c. On the velocity discontinuity at a critical volume of a bubble rising in a viscoelastic fluid. Journal of Fluid Mechanics 789, 310–346.

Frey, S.L., Naccache, M.F., de Souza Mendes, P.R., Thompson, R.L., dos Santos, D.D., Link, F.B., Fonseca, C., 2015. Performance of an elasto-viscoplastic model in some benchmark problems. Mechanics of Time-Dependent Materials 19, 419–438.

Frigaard, I., Nouar, C., 2005. On the usage of viscosity regularisation methods for visco-plastic fluid flow computation. Journal of Non-Newtonian Fluid Mechanics 127, 1 – 26. doi:https://doi.org/10.1016/j.jnnfm.2005.01.003.

Fröhlich, A., Sack, R., 1946. Theory of the rheological properties of dispersions. Proceedings of the Royal Society of London. Series A. Mathematical and Physical Sciences 185, 415–430.

Garcia, C.G., Kiick, K.L., 2019. Methods for producing microstructured hydrogels for targeted applications in biology. Acta biomaterialia 84, 34–48.

de Gennes, P.G., Brochard-Wyart, F., Quéré, D., et al., 2004. Capillarity and wetting phenomena: drops, bubbles, pearls, waves. volume 315. Springer.

Glowinski, R., 1983. Numerical Methods for Nonlinear Variational Problems.

Goel, S., Ng, S., Acosta, E., Ramachandran, A., 2018. The roles of contact time and contact pressure on the coalescence of water droplets suspended in concentrated bitumen solutions. Fuel 223, 486–495.

Goel, S., Ramachandran, A., 2017. The suppression of droplet-droplet coalescence in a sheared yield stress fluid. Journal of colloid and interface science 492, 199–206.

Goyal, N., Derksen, J., 2012. Direct simulations of spherical particles sedimenting in viscoelastic fluids. Journal of Non-Newtonian Fluid Mechanics 183, 1–13.

Hadamard, J., 1911. Mouvement permanent lent d'une sphere liquid et visqueuse dans un liquide visqueux. CR Hebd. Seances Acad. Sci. Paris 152, 1735–1738.

Hartland, S., Jeelani, A., 1987. Drainage in thin planar non-newtonian fluid films. The Canadian Journal of Chemical Engineering 65, 382–390.

Hartland, S., Jeelani, S.A., 1986. Drainage of thin dimpled non-newtonian fluid films. The Journal of Physical Chemistry 90, 6054–6059.

Henschke, M., Schlieper, L.H., Pfennig, A., 2002. Determination of a coalescence parameter from batch-settling experiments. Chemical Engineering Journal 85, 369–378.

Holenberg, Y., Lavrenteva, O.M., Nir, A., 2011. Interaction of viscous drops in a yield stress material. Rheologica acta 50, 375–387.

Izbassarov, D., Tammisola, O., 2020. Dynamics of an elastoviscoplastic droplet in a newtonian medium under shear flow. Physical Review Fluids 5, 113301.

Jeffreys, H., 1929. The Earth. Cambridge University Press.

Kamp, J., Villwock, J., Kraume, M., 2017. Drop coalescence in technical liquid/liquid applications: A review on experimental techniques and modeling approaches. Reviews in Chemical Engineering 33, 1–47.

Keiller, R., 1992. Numerical instability of time-dependent flows. Journal of non-newtonian fluid mechanics 43, 229–246.

Kemiha, M., Frank, X., Poncin, S., Li, H.Z., 2006. Origin of the negative wake behind a bubble rising in non-newtonian fluids. Chemical Engineering Science 61, 4041–4047.

Kočárková, H., Rouyer, F., Pigeonneau, F., 2013. Film drainage of viscous liquid on top of bare bubble: Influence of the bond number. Physics of Fluids 25, 022105.

Kulkarni, A.A., Joshi, J.B., 2005. Bubble formation and bubble rise velocity in gas- liquid systems: a review. Industrial & engineering chemistry research 44, 5873–5931.

Lagrée, P.Y., Staron, L., Popinet, S., 2011. The granular column collapse as a continuum: validity of a two-dimensional navier-stokes model with a [mu](i)-rheology. Journal of Fluid Mechanics 686, 378.

Lai, W.M., Rubin, D.H., Rubin, D., Krempl, E., 2009. Introduction to continuum mechanics. Butterworth-Heinemann.

Lavrenteva, O.M., Holenberg, Y., Nir, A., 2009. Motion of viscous drops in tubes filled with yield stress fluid. Chemical engineering science 64, 4772–4786.

Liao, Y., Lucas, D., 2010. A literature review on mechanisms and models for the coalescence process of fluid particles. Chemical Engineering Science 65, 2851–2864.

Liu, B., Manica, R., Liu, Q., Klaseboer, E., Xu, Z., Xie, G., 2019. Coalescence of bubbles with mobile interfaces in water. Physical review letters 122, 194501.

Liu, B., Manica, R., Zhang, X., Bussonniere, A., Xu, Z., Xie, G., Liu, Q., 2018. Dynamic interaction between a millimeter-sized bubble and surface microbubbles in water. Langmuir 34, 11667–11675.

Liu, Y., Liao, T., Joseph, D., 1995. A two-dimensional cusp at the trailing edge of an air bubble rising in a viscoelastic liquid. Journal of Fluid Mechanics 304, 321–342.

Lopez, W.F., Naccache, M.F., de Souza Mendes, P.R., 2018. Rising bubbles in yield stress materials. Journal of Rheology 62, 209–219.

López-Herrera, J., Popinet, S., Castrejón-Pita, A., 2019. An adaptive solver for viscoelastic incompressible two-phase problems applied to the study of the splashing of weakly viscoelastic droplets. Journal of Non-Newtonian Fluid Mechanics 264, 144–158.

Macosko, C.W., 1994. Rheology: principles, measurements, and applications. VCH.

Maldonado, M., Quinn, J., Gomez, C., Finch, J., 2013. An experimental study examining the relationship between bubble shape and rise velocity. Chemical Engineering Science 98, 7–11.

Martin, A.N., Sinko, P.J., Singh, Y., 2006. Martin's physical pharmacy and pharmaceutical sciences: physical chemical and biopharmaceutical principles in the pharmaceutical sciences. Wolters Kluwer.

Maxwell, J.C., 1867. Iv. on the dynamical theory of gases. Philosophical transactions of the Royal Society of London , 49–88.

Mendes, P.R.S., Naccache, M.F., Varges, P.R., Marchesini, F.H., 2007. Flow of viscoplastic liquids through axisymmetric expansions-contractions. J. Non-Newtonian Fluid Mech. 142, 207–217.

Mendes, P.R.S., Thompson, R.L., 2012. A critical overview of elasto-viscoplastic thixotropic modeling. J. Non-Newt. Fluid Mech. 187-188, 8–15.

Mendes, P.R.S., Thompson, R.L., 2013. A unified approach to model elasto-viscoplastic thixotropic yield-stress materials and apparent-yield-stress fluids. Rheol Acta 52, 673–694.

Mendes, P.S., 2011. Thixotropic elasto-viscoplastic model for structured fluids. Soft Matter 7, 2471–2483.

Metzner, A., White, J., Denn, M., 1966. Constitutive equations for viscoelastic fluids for short deformation periods and for rapidly changing flows: significance of the deborah number. AIChE Journal 12, 863–866.

Mitrias, C., Jaensson, N.O., Hulsen, M.A., Anderson, P.D., 2019. Head-on collision of newtonian drops in a viscoelastic medium. Microfluidics and Nanofluidics 23, 1–11.

Mitsoulis, E., Tsamopoulos, J., 2017. Numerical simulations of complex yield-stress fluid flows. Rheologica Acta 56, 231–258.

Mohamed-Kassim, Z., Longmire, E.K., 2003. Drop impact on a liquid–liquid interface. Physics of Fluids 15, 3263–3273.

Moschopoulos, P., Spyridakis, A., Varchanis, S., Dimakopoulos, Y., Tsamopoulos, J., 2021. The concept of elasto-visco-plasticity and its application to a bubble rising in yield stress fluids. Journal of Non-Newtonian Fluid Mechanics 297, 104670.

Mougin, N., Magnin, A., Piau, J.M., 2012. The significant influence of internal stresses on the dynamics of bubbles in a yield stress fluid. Journal of Non-Newtonian Fluid Mechanics 171, 42–55.

Mujumdar, A., Beris, A.N., Metzner, A.B., 2002. Transient phenomena in thixotropic systems. J. Non-Newtonian Fluid Mech. 102, 157–178.

Nomena, E.M., Remijn, C., Rogier, F., van der Vaart, M., Voudouris, P., Velikov, K.P., 2018. Unravelling the mechanism of stabilization and microstructure of oil-in-water emulsions by native cellulose microfibrils in primary plant cells dispersions. ACS Applied Bio Materials 1, 1440–1447.

Oishi, C.M., Martins, F.P., Thompson, R.L., 2020. Gravitational effects in the collision of elasto-viscoplastic drops on a vertical plane. Fluids 5, 61.

Oishi, C.M., Thompson, R.L., Martins, F.P., 2019. Normal and oblique drop impact of yield stress fluids with thixotropic effects. Journal of Fluid Mechanics 876, 642–679.

Oldenziel, G., Delfos, R., Westerweel, J., 2012. Measurements of liquid film thickness for a droplet at a two-fluid interface. Physics of Fluids 24, 022106.

Oldroyd, J.G., 1947. A rational formulation of the equations of plastic flow for a bingham solid. Proc. Cambridge Philos. Soc. 43, 100–105.

Oldroyd, J.G., 1950. On the formulation of rheological equations of state. Proceedings of the Royal Society of London. Series A. Mathematical and Physical Sciences 200, 523–541.

Oldroyd, J.G., 1953. The elastic and viscous properties of emulsions and suspensions. Proceedings of the Royal Society of London. Series A. Mathematical and Physical Sciences 218, 122–132.

Ortiz, S.L., Lee, J.S., Figueroa-Espinoza, B., Mena, B., 2016. An experimental note on the deformation and breakup of viscoelastic droplets rising in non-newtonian fluids. Rheologica Acta 55, 879–887.

Ozan, S.C., Hosen, H.F., Jakobsen, H.A., 2021. On the prediction of coalescence and rebound of fluid particles: A film drainage study. International Journal of Multiphase Flow 135, 103521.

Papanastasiou, T.C., 1987. Flows of materials with yield. J. Rheology 31, 385–404.

Pawliszak, P., Ulaganathan, V., Bradshaw-Hajek, B.H., Manica, R., Beattie, D.A., Krasowska, M., 2019. Mobile or immobile? rise velocity of air bubbles in high-purity water. The Journal of Physical Chemistry C 123, 15131–15138.

Phan-Thien, N., Mai-Duy, N., 2013. Understanding viscoelasticity: an introduction to rheology. Springer.

Pillapakkam, S.B., Singh, P., Blackmore, D., Aubry, N., 2007. Transient and steady state of a rising bubble in a viscoelastic fluid. Journal of Fluid Mechanics 589, 215–252.

Pilz, C., Brenn, G., 2007. On the critical bubble volume at the rise velocity jump discontinuity in viscoelastic liquids. Journal of non-newtonian fluid mechanics 145, 124–138.

Poole, R.J., 2012. The Deborah and Weissenberg numbers. Rheology Bulletin 53.

Popinet, S., 2003. Gerris: a tree-based adaptive solver for the incompressible euler equations in complex geometries. Journal of computational physics 190, 572–600.

Popinet, S., 2009. An accurate adaptive solver for surface-tension-driven interfacial flows. Journal of Computational Physics 228, 5838–5866.

Popinet, S., 2018. Numerical models of surface tension. Annual Review of Fluid Mechanics 50, 49–75.

Potapov, A., Spivak, R., Lavrenteva, O.M., Nir, A., 2006. Motion and deformation of drops in bingham fluid. Industrial & engineering chemistry research 45, 6985–6995.

Pourzahedi, A., Chaparian, E., Roustaei, A., Frigaard, I.A., 2022. Flow onset for a single bubble in a yield-stress fluid. Journal of Fluid Mechanics 933, A21.

Pourzahedi, A., Zare, M., Frigaard, I., 2021. Eliminating injection and memory effects in bubble rise experiments within yield stress fluids. Journal of Non-Newtonian Fluid Mechanics 292, 104531.

Premlata, A., Tripathi, M.K., Karri, B., Sahu, K.C., 2017. Dynamics of an air bubble rising in a non-newtonian liquid in the axisymmetric regime. Journal of non-Newtonian fluid mechanics 239, 53–61.

Rajagopal, K.R., Srinivasa, A.R., 2000. A thermodynamic frame work for rate type fluid models. Journal of Non-Newtonian Fluid Mechanics 88, 207–227.

Reiner, M., 1964. The deborah number. Physics today 17, 62.

Reynolds, O., 1883. An experimental investigation of the circumstances which deter- mine whether the motion of water shall be direct or sinuous, and of the law of resistance in parallel channels. Philosophical Transactions of the Royal Society of London. 174, 935–982.

Ribeiro, C.P., Mewes, D., 2006. On the effect of liquid temperature upon bubble coalescence. Chemical Engineering Science 61, 5704–5716.

Ribeiro, C.P., Mewes, D., 2007. The effect of electrolytes on the critical velocity for bubble coalescence. Chemical Engineering Journal 126, 23–33.

Rybczynski, W., et al., 1911. On the translatory motion of a fluid sphere in a viscous medium. Bull. Acad. Sci., Cracow, Series A 40, 33–78.

Saien, J., Jafari, F., 2019. Mass transfer intensification strategies for liquid–liquid extraction with single drop investigations. International Journal of Heat and Mass Transfer 144, 118603.

Sanjay, V., Lohse, D., Jalaal, M., 2021. Bursting bubble in a viscoplastic medium. Journal of fluid mechanics 922, A2.

dos Santos, D.D., Frey, S.L., Naccache, M.F., Mendes, P.R.S., 2014. Flow of elasto-viscoplastic liquids through a planar expansion-contraction. Rheol Acta 53, 31–41.

Saramito, P., 2007. A new constitutive equation for elastoviscoplastic fluid flows. J. Non-Newt. Fluid Mech. 145, 1–14.

Saramito, P., 2009. A new elastoviscoplastic model based on the Herschel–Bulkley viscoplastic model. J. Non-Newt. Fluid Mech. 158, 154–161.

Sharaf, D., Premlata, A., Tripathi, M.K., Karri, B., Sahu, K.C., 2017. Shapes and paths of an air bubble rising in quiescent liquids. Physics of Fluids 29, 122104.

Shi, X., Rodríguez-Hakim, M., Shaqfeh, E.S., Fuller, G.G., 2021. Instability and symmetry breaking in binary evaporating thin films over a solid spherical dome. Journal of Fluid Mechanics 915.

Sikorski, D., Tabuteau, H., de Bruyn, J.R., 2009. Motion and shape of bubbles rising through a yield-stress fluid. J. Non-Newtonian Fluid Mech. 159, 10–16.

Singh, J.P., Denn, M.M., 2008. Interacting two-dimensional bubbles and droplets in a yield-stress fluid. Physics of Fluids 20, 040901.

Sussman, M., Smereka, P., Osher, S., 1994. A level set approach for computing solutions to incompressible two-phase flow. Journal of Computational physics 114, 146–159.

Sweby, P.K., 1984. High resolution schemes using flux limiters for hyperbolic conservation laws. SIAM journal on numerical analysis 21, 995–1011.

Syrakos, A., Dimakopoulos, Y., Tsamopoulos, J., 2020. A finite volume method for the simulation of elastoviscoplastic flows and its application to the lid-driven cavity case. Journal of Non-Newtonian Fluid Mechanics 275, 104216.

Tabuteau, H., Coussot, P., de Bruyn, J.R., 2007. Drag force on a sphere in steady motion through a yield-stress fluid. Journal of rheology 51, 125–137.

Tchoukov, P., Yang, F., Xu, Z., Dabros, T., Czarnecki, J., Sjöblom, J., 2014. Role of asphaltenes in stabilizing thin liquid emulsion films. Langmuir 30, 3024–3033.

Thien, N.P., Tanner, R.I., 1977. A new constitutive equation derived from network theory. Journal of Non-Newtonian Fluid Mechanics 2, 353–365.

Thompson, R.L., Oishi, C.M., 2021. Reynolds and weissenberg numbers in viscoelastic flows. Journal of Non-Newtonian Fluid Mechanics 292, 104550.

Thompson, R.L., Soares, E..J., 2016. Viscoplastic dimensionless numbers. Journal of Non-Newtonian Fluid Mechanics 241, 60–69.

Tripathi, M.K., Sahu, K.C., Govindarajan, R., 2014. Why a falling drop does not in general behave like a rising bubble. Scientific reports 4, 4771.

Tripathi, M.K., Sahu, K.C., Govindarajan, R., 2015a. Dynamics of an initially spherical bubble rising in quiescent liquid. Nature communications 6, 1–9.

Tripathi, M.K., Sahu, K.C., Karapetsas, G., Matar, O.K., 2015b. Bubble rise dynamics in a viscoplastic material. Journal of Non-Newtonian Fluid Mechanics 222, 217–226.

Tryggvason, G., Scardovelli, R., Zaleski, S., 2011. Direct numerical simulations of gas–liquid multiphase flows. Cambridge university press.

Tsamopoulos, J., Dimakopoulos, Y., Chatzidai, N., Karapetsas, G., Pavlidis, M., 2008. Steady bubble rise and deformation in newtonian and viscoplastic fluids and conditions for bubble entrapment. Journal of Fluid Mechanics 601, 123.

Vakarelski, I.U., Langley, K.R., Yang, F., Thoroddsen, S.T., 2022. Interferometry and simulation of the thin liquid film between a free-rising bubble and a glass substrate. Langmuir 38, 2363–2371.

Vakarelski, I.U., Yang, F., Tian, Y.S., Li, E.Q., Chan, D.Y., Thoroddsen, S.T., 2019. Mobile-surface bubbles and droplets coalesce faster but bounce stronger. Science advances 5, eaaw4292.

Versteeg, H.K., Malalasekera, W., 2007. An introduction to computational fluid dynamics: the finite volume method. Pearson education.

Wang, Z., Xu, Y., Liu, Y., Liu, X., Rui, Z., 2020. Molecular dynamics-based simulation on chemical flooding produced emulsion formation and stabilization: A critical review. Arabian Journal for Science and Engineering 45, 7161–7173.

Wegener, M., Kraume, M., Paschedag, A.R., 2010. Terminal and transient drop rise velocity of single toluene droplets in water. AIChE journal 56, 2–10.

Weheliye, W.H., Dong, T., Angeli, P., 2017. On the effect of surfactants on drop coalescence at liquid/liquid interfaces. Chemical Engineering Science 161, 215–227.

White, F.M., 1998. Fluid mechanics, 4th edition. Mcgraw-Hill College .

White, J.L., 1964. Dynamics of viscoelastic fluids, melt fracture, and the rheology of fiber spinning. Journal of Applied Polymer Science 8, 2339–2357.

Xue, S.C., Tanner, R., Phan-Thien, N., 2004. Numerical modelling of transient viscoelastic flows. Journal of non-newtonian fluid mechanics 123, 33–58.

Yaminsky, V.V., Ohnishi, S., Vogler, E.A., Horn, R.G., 2010. Stability of aqueous films between bubbles. part 1. the effect of speed on bubble coalescence in purified water and simple electrolyte solutions. Langmuir 26, 8061–8074.

Yiantsios, S.G., Davis, R.H., 1990. On the buoyancy-driven motion of a drop towards a rigid surface or a deformable interface. Journal of Fluid Mechanics 217, 547–573.

Yuan, W., Zhang, M., Khoo, B.C., Phan-Thien, N., 2020. Dynamics and deformation of a three-dimensional bubble rising in viscoelastic fluids. Journal of Non-Newtonian Fluid Mechanics 285, 104408.

Yuan, W., Zhang, M., Khoo, B.C., Phan-Thien, N., 2021. On peculiar behaviours at critical volumes of a three-dimensional bubble rising in viscoelastic fluids. Journal of Non-Newtonian Fluid Mechanics 293, 104568.

Yue, P., Feng, J.J., Liu, C., Shen, J., 2005. Diffuse-interface simulations of drop coalescence and retraction in viscoelastic fluids. Journal of Non-Newtonian Fluid Mechanics 129, 163–176.

Zawala, J., Malysa, K., 2011. Influence of the impact velocity and size of the film formed on bubble coalescence time at water surface. Langmuir 27, 2250–2257.

Zawala, J., Malysa, K., Kowalczuk, P.B., 2020. On importance of external conditions and properties of the interacting phases in formation and stability of symmetrical and unsymmetrical liquid films. Advances in Colloid and Interface Science 276, 102085.

Zheng, F., Quiroga, P., Sams, G.W., 2011. Challenges in processing produced emulsion from chemical enhanced oil recovery-polymer flood using polyacrylamide, in: SPE Asia Pacific Enhanced Oil Recovery Conference, SPE. pp. SPE–144322.

Appendix A

Appendix

A.1 Non-dimensionalization of the Momentum Conservation Equation

The scaling analyses presented in Sec. 3.3 is used to write the momentum equation in terms of the non-dimensional governing parameters

$$(\bar{r}, \bar{z}) = (r/D, z/D),\ \bar{\mathbf{u}} = \mathbf{u}/U,\ \bar{t} = t/t_c,\ \bar{p} = p/\rho_1 U^2,\ \bar{\dot{\boldsymbol{\gamma}}} = \dot{\boldsymbol{\gamma}}/\dot{\gamma}_c,$$
$$\bar{\rho} = \rho/\rho_1,\ \bar{\eta} = \eta/\eta_c,\ \bar{\boldsymbol{\tau}} = \boldsymbol{\tau}/\tau_c,\ \bar{\lambda} = \lambda/\lambda_c.$$

Also, recall the characteristic variables:

$$\begin{aligned} &U = \sqrt{Fr|\rho|gD/\rho_1},\ t_c = D/U,\ \dot{\gamma}_c = 1/t_c = U/D, \\ &\tau_c = \eta_p \dot{\gamma}_c,\ \eta_c = \mu_p + \tau_y/\dot{\gamma}_c,\ \lambda_c = \eta_c/G. \end{aligned} \tag{A.1}$$

For simplicity, the non-dimensionalization is done using the one-dimension of the momentum equation,

$$\rho\left[\frac{\partial u}{\partial t} + u\frac{\partial u}{\partial x}\right] = -\frac{\partial p}{\partial x} + \frac{\partial}{\partial x}\left[\tau_s + \tau_p\right] + \sigma\kappa n\delta_s - \rho g \tag{A.2}$$

Using the above scaling results in:

$$\rho_1\frac{U^2}{D}\bar{\rho}\left[\frac{\partial \bar{u}}{\partial t} + \bar{u}\frac{\partial \bar{u}}{\partial \bar{x}}\right] = -\rho_1\frac{U^2}{D}\frac{\partial \bar{p}}{\partial \bar{x}} + \eta_c\frac{U}{D^2}\frac{\partial}{\partial \bar{x}}\left[\bar{\eta}\bar{\dot{\gamma}} - \bar{\eta}\frac{\eta_c}{G}\frac{U}{D}\frac{\partial \bar{\tau}}{\partial \bar{t}}\right] + \frac{\sigma}{D^2}\bar{\kappa}n\delta_s - \rho_1\bar{\rho}g,$$

$$\bar{\rho}\left[\frac{\partial \bar{u}}{\partial t}+\bar{u}\frac{\partial \bar{u}}{\partial \bar{x}}\right]=-\frac{\partial \bar{p}}{\partial \bar{x}}+\frac{\eta_c}{\rho_1 U D}\frac{\partial}{\partial \bar{x}}\left[\bar{\eta}\bar{\dot{\gamma}}-\bar{\eta}\frac{\eta_c}{G}\frac{U}{D}\frac{\partial \bar{\tau}}{\partial \bar{t}}\right]+\frac{\sigma}{\rho_1 U^2 D}\bar{\kappa}n\delta_s-\frac{D}{U^2}\bar{\rho}g. \tag{A.3}$$

Replacing $\eta_c = |\Delta\rho|gD^2/U$ and $U=\sqrt{Fr|\Delta\rho|gD/\rho_1}$ in the second and third terms of the right hand side, respectively, yields

$$\bar{\rho}\left[\frac{\partial \bar{u}}{\partial t}+\bar{u}\frac{\partial \bar{u}}{\partial \bar{x}}\right]=-\frac{\partial \bar{p}}{\partial \bar{x}}+\frac{1}{Fr}\frac{\partial}{\partial \bar{x}}\left[\bar{\eta}\bar{\dot{\gamma}}-\bar{\eta}Wi_c\frac{\partial \bar{\tau}}{\partial \bar{t}}\right]+\frac{1}{FrBo}\bar{\kappa}n\delta_s-\frac{1}{Fr}\frac{\bar{\rho}}{1-\rho_r}. \tag{A.4}$$

Additionally, an expression for $\bar{\eta}$ can be obtained by doing

$$\eta=\mu_p+\frac{\tau_y}{\dot{\gamma}}, \tag{A.5}$$

$$\bar{\eta}\eta_c=\mu_p+\frac{\tau_y}{\bar{\dot{\gamma}}\dot{\gamma}_c}, \tag{A.6}$$

$$\bar{\eta}=\frac{\mu_p}{\eta_{pc}}+\frac{\tau_y}{\bar{\dot{\gamma}}\dot{\gamma}_c\eta_{pc}}. \tag{A.7}$$

But

$$\eta_c=\mu_p+\frac{\tau_y}{\dot{\gamma}_c}, \tag{A.8}$$

$$1=\frac{\mu_p}{\eta_c}+\frac{\tau_y}{\eta_c\dot{\gamma}_c}, \tag{A.9}$$

$$\eta_c=\frac{\mu_p}{1-Pl}. \tag{A.10}$$

Therefore,

$$\bar{\eta}=1-Pl+\frac{Pl}{\bar{\dot{\gamma}}}. \tag{A.11}$$

Rearranging,

$$\bar{\eta}=1+Pl\frac{(1-\bar{\dot{\gamma}})}{\bar{\dot{\gamma}}}. \tag{A.12}$$